

Delft University of Technology
Stevin Laboratory for Steel Structures
Stevinweg 1
2628 CN Delft
The Netherlands

Stevin Report 6.93.27-A1/11.07
TNO-Bouw Report 93-CON-R0832

CONFIDENTIAL

SEMI-RIGID CONNECTIONS BETWEEN I-BEAMS AND TUBULAR COLUMNS

DRAFT FINAL REPORT

ECSC CONVENTION 7210-SA/611 (F 6.6/90)

DISTRIBUTION

a. Directorate General XII, Research Science, Developments.
(R.V. Salkin)

b. Executive Committee F6 Steel Research and Development Committee

Bijl C.L.	Staalbouw Instituut SBI
Bijlaard	F.S.K.TNO-BOUW
Borchgraeve	P.CBLIA
Bozzo	E.SIDERCAD SPA
Correia da Cruz A.	Instituto de Soldadura e Qualidade
Defourny J.	Centre de Recherches Métallurgiques
Demuth J.	Europrofil S.A.
Eaton K.J.	The Steel Construction Institute
Hüller V.	Studiengesellschaft Stahlanwendung
Ioannidis G.	National Technical University
Karamanos A.	Hellenic Steel Co.
Martin M.A.	ENSIDESA
Martin D.M.	British Steel Technical
Mudry F.	USINOR SACILOR S.A.
Neste J. van	Convention Européenne de la Construction
Parmentier M.	CTICM
Ramirez J.L.	Labein
Salkin R.V.	Commission of the European Communities
Schleich J.B.	Profilarbed-Recherches
Walley M.	Irish Steel Ltd.
Wardenier J.	Technische Universiteit Delft (Chairman)
Zandonini R.	Universita di Trento

c. Members of Research team
(13 copies)

d. Sponsors:
(6 copies)

SEMI-RIGID CONNECTIONS BETWEEN I-BEAMS AND TUBULAR COLUMNSResearch teams:Delft University of Technology, Stevin Laboratory, The Netherlands

Mr. A. Verheul

Dr. G.S. Frater

Ir. H.D. Rink

Ms.Ir. L.H. Lu

Ir. G.D. de Winkel

Dr. Eur.-Ing. R.S. Puthli

Prof.Dr.Ir. J. Wardenier (Project Leader)

TNO Building and Construction Research, Rijswijk, The Netherlands

Mr. C.H.M. de Koning

Ir. R.J. van Foeken

Dr. Eur.-Ing. R.S. Puthli

Rheinisch-Westfälischen Technischen Hochschule Aachen, Germany

Dipl.-Ing. D. Grotmann

Prof.Dr.-Ing. G. Sedlacek

British Steel Welded Tubes S.H.S. International, U.K.

Mr. N.F. Yeomans

Mannesmannröhren-Werke AG Düsseldorf, Germany

Dipl.-Ing. D. Dutta

ABSTRACT

This report presents an investigation of the static-strength and behaviour of multiplanar connections between I-section beams or plates and circular or rectangular hollow section columns.

Semi-rigid connections between I-section beams and tubular columns can be used economically for buildings and offshore structures. The lack of stiffening plates allows the fabrication of these connections in a cost effective way. By filling the tubular column with reinforced concrete sufficient fire resistance can be achieved and the strength will also be increased. The strength and stiffness of the connection can be further increased by the use of a composite steel-concrete floor.

This research programme consists of an experimental and numerical investigation on the static-strength and behaviour of multiplanar connections between I-section beams or plates and circular or rectangular hollow section columns, where the influence of a reinforced concrete infill in columns, a composite floor or a steel floor are also considered.

The experiments, including detail tests, interaction tests and overall tests are carried out at the laboratories of the Delft University of Technology and TNO Building and Construction Research.

Throughout this work, the columns are either circular hollow sections (CHS) of size $\varnothing 324 \times 9.5$ or rectangular hollow sections (RHS) of size $300 \times 300 \times 10$. The multiplanar joints are made up of plates representing individual flanges or I-beams (120×10 or 170×12) for axial load combinations and I-beams (IPE 240 or IPE 360) for moment loaded combinations. The testing is carried out and reported in four series (detail tests on axially loaded welded plates; interaction tests on two levels of axially loaded welded plates; moment loaded tests using welded I-beams; and moment loaded tests on bolted I-beams with a composite floor).

The numerical (Finite Element) work is carried out at Delft University of Technology and RWTH Aachen to simulate the experimental work and to calibrate the finite element (F.E.) models. In general, there is good agreement found between the experimental and numerical results.

The experimental and numerical results are also compared with existing design formulae, if available.

The results show that no maximum peak is reached for all the tested connections with an RHS column, except those with a composite column. All tested connections with a CHS column show a peak load.

To determine the strength of connections without a peak load, further studies are needed to derive a ultimate deformation criterion. None of the currently available deformation criteria can generally be applied.

Based on this research project calibrated finite element models can be used for parametric studies. This is being carried out at Delft University of Technology in the framework of two Ph.D. research programmes [1,2]. In Aachen a numerical approach will be developed to derive load deformation characteristics for design purpose.

The results of this project show that the fabrication friendly connections have a considerable strength, which can reduce the overall structural costs.

For design either characterisations of the moment rotation diagrammes are necessary or the strength should be presented in such a way that it indirectly covers a deformation or rotation criterion. These aspects have to further investigated before design recommendations can be given.

It was envisaged to design the connections with a composite floor in such way, that the reinforcement would be decisive for failure. However, it has been shown that the cold formed reinforcement bars does not have sufficient deformation capacity. This aspect needs further study. Thus for such connections it is essential that hot rolled concrete reinforcement is used.

CONTENTS

	ABSTRACT	vii
	TABLE OF SYMBOLS	xix
	OBJECTIVES OF THE RESEARCH PROGRAMME	xxi
1	INTRODUCTION	1
2	RESEARCH PROGRAMME	3
	2.1 Participating ECSC countries and laboratories	3
	2.2 Overview of the experimental work	3
	2.3 Overview of the numerical work	4
3	DEFINITION OF VARIOUS CHARACTERISTICS	5
4	TEST SPECIMEN, TEST RIG AND MEASUREMENT DETAILS	7
	4.1 Design of composite steel-concrete CHS and RHS columns	7
	4.2 Design of composite floor comprising a deep steel deck (PMF CF46) and a 110 mm deep concrete slab for series 4 tests with CHS and RHS columns	7
	4.2.1 Design philosophy	7
	4.2.2 Design of floor	8
	4.3 Welding details	9
	4.4 Mechanical properties	9
	4.4.1 Steel members	9
	4.4.2 Weld material	10
	4.4.3 Reinforced concrete filling to CHS and RHS columns	10
	4.4.3.1 Concrete composition for the composite columns	10
	4.4.3.2 Concreting operations of the columns	11
	4.4.3.3 Properties of cured concrete cubes for the composite columns	11
	4.4.4 Composite floor comprising a deep steel deck (PMF CF46) and a 110 mm deep concrete slab for series 4 tests with CHS and RHS columns	12
	4.4.4.1 Construction of test specimens	12
	4.4.4.2 Concrete composition of composite floors	13
	4.4.4.3 Concreting operations for the composite floor	14
	4.4.4.4 Properties of cured concrete cubes for the composite floors	14
	4.5 Measured dimensions	15
	4.6 Weld measurements	15
	4.7 Test rigs and testing procedures	16
	4.7.1 Connections with axially loaded plates and beams and CHS/RHS columns (series 1 and 2)	16
	4.7.2 Connections with moment loaded beams and CHS/RHS columns (series 3 and 4)	17
	4.8 Measurements	19
	4.8.1 Strains	19
	4.8.1.1 Strain measurements for series 1	19
	4.8.1.2 Strain measurements for series 2	19
	4.8.1.3 Strain measurements for series 3	20
	4.8.1.4 Strain measurements for series 4	21
	4.8.2 Column indentations for the axially loaded specimens (series 1	

	and 2)	21
	4.8.2.1 Transducer measurements for series 1	22
	4.8.2.2 Transducer measurements for series 2	22
	4.8.3 Transducer measurements for series 3	23
	4.8.4 Transducer measurements for series 4	23
	4.8.5 Determination of beam rotation	23
5	GENERAL DETAILS FOR THE NUMERICAL FE WORK	25
	5.1 Method of analyses	25
	5.2 Method of modelling	26
6	CONNECTIONS WITH CHS COLUMNS	27
	6.1 Experimental research	27
	6.2 Comparison of numerical and experimental results	28
	6.3 Discussion of results	29
	6.3.1 Plate to CHS connections	29
	6.3.2 Interaction effects	30
	6.3.3 Beam to column connections	30
	6.3.4 Effect of concrete infill in the CHS column	30
	6.3.5 Effect of a steel floor	31
	6.3.6 Comparison with existing strength formulae	31
	6.3.6.1 Plate to CHS column connections	31
	6.3.6.2 Interaction effects	32
	6.3.6.3 In-plane bending test	32
	6.3.6.4 Bolted connections with a composite steel concrete floor	32
7	CONNECTIONS WITH RHS COLUMNS	35
	7.1 Experimental research	35
	7.2 Definition of the maximum load	37
	7.3 Comparison of numerical and experimental results	38
	7.4 Discussion of results	39
	7.4.1 Plate to RHS connections	39
	7.4.2 Interaction effects	39
	7.4.3 Beam to column connections	40
	7.4.4 Effect of concrete infill in the RHS column	40
	7.4.5 Effect of a steel floor	40
	7.4.6 Comparison with existing strength formulae	41
	7.4.6.1 Plate to RHS column connections	41
	7.4.6.2 I-beam to RHS column connections	41
	7.4.6.3 Bolted connections with a composite steel concrete floor	42
8	CONCLUSIONS AND PRELIMINARY RECOMMENDATIONS	45
	8.1 General connection behaviour	45
	8.2 Finite element modelling of plate or I-beam to CHS or RHS column connections	45
	8.3 Welded Connections with a CHS column	46
	8.3.1 Plate to CHS column connections under axial loading	46
	8.3.2 Interaction effects	47
	8.3.3 I-Beam to CHS column connections under in-plane bending	47
	8.4 Welded Connections with a RHS column	48
	8.4.1 Plate to RHS column connections under axial loading	48
	8.4.2 Interaction effects	48

8.4.3	I-beam to RHS column connections under In-plane bending	49
8.5	Bolted connections with a composite floor	49
8.5.1	Connection behaviour	49
8.5.2	Design aspects	50
9	ACKNOWLEDGEMENTS	51
10	REFERENCES	53

LIST OF TABLES

Table 2-1	: Overview of the test specimens with CHS columns
Table 2-2	: Overview of the test specimens with RHS columns
Table 4-1a	: Mechanical properties
Table 4-1b	: Mechanical properties
Table 4-2	: Concrete cube properties for composite columns
Table 4-3	: Concrete cube properties of batch 1 used for composite floor of specimens 4C1, 4C2, 4R1 and 4R2
Table 4-4	: Concrete cube properties of batch 2 used for composite floor of specimens 4C3, 4C4, 4R3 and 4R4
Table 4-5	: Material properties of concrete and steel reinforcement in columns and floors
Table 4-6	: Nominal dimensions test series with CHS column \varnothing 323.9*9.5, 1800 long
Table 4-7	: Nominal dimensions test series with RHS column 300*300*10, 1800 long
Table 4-8	: Average measurements for each stock number in CHS
Table 4-9	: Average measurements for each stock number in RHS
Table 4-10	: Average measurements for each stock number from IPE sections
Table 4-11	: Average measurements for each stock number from plates 120*10, 170*10 and steel floor
Table 6-1	: Comparison of the experimental and numerical results (series 1 and 2) with CHS column
Table 6-2	: Comparison of the experimental and numerical results (series 3 and 4) with CHS column
Table 7-1	: Comparison of the experimental and numerical results (series 1 and 2) with RHS column
Table 7-2	: Comparison of the experimental and numerical results (series 3 and 4) with RHS column
Table 8-1	: Main results and conclusions for plate to CHS column connections under axial load
Table 8-2	: Main results and conclusions for axial loading interaction effects (CHS)
Table 8-3	: Main results and conclusions for I-beam to CHS column connections under in-plane bending
Table 8-4	: Main results and conclusions for plate to RHS column connections under axial load
Table 8-5	: Main results and conclusions for axial loading interaction effects (RHS)
Table 8-6	: Main results and conclusions for I-beam to RHS column connections under in-plane bending
Table 8-7	: Main results and conclusions for the tests on bolted connections with a composite floor (CHS column)

Table 8-8 : Main results and conclusions for the tests on bolted connections with a composite floor (RHS column)

LIST OF FIGURES

- Fig. 1-1 : Semi-rigid welded beam-to-column connections
 Fig. 1-2 : Semi-rigid bolted beam-to-column connections
 Fig. 4-1 : CHS columns with reinforced concrete filling
 Fig. 4-2 : RHS columns with reinforced concrete filling
 Fig. 4-4 : Reinforcement details for series 4 test specimens with CHS/RHS columns
 Fig. 4-5 : Standard arrangement of shear studs for series 4 tests (CHS/RHS)
 Fig. 4-6 : Web plate welded to columns (typical) for specimens 4C1 to 4C4
 Fig. 4-7 : Specific details of web plate welded to columns (typical) for specimens 4C1 to 4C4
 Fig. 4-8 : Ring plate to be bolted to I-beam bottom flanges for specimens 4C1 to 4C4 (typical)
 Fig. 4-9 : Typical details of bolt holes in columns for fire protection, web plate and cleats for connection to I-beams, for specimens 4R1 to 4R4
 Fig. 4-10 : Specific details of web plates and cleats for connections to I-beams, for specimens 4R1 to 4R4
 Fig. 4-11 : Details of bolt holes in I-beams for specimens 4C1 to 4C4 and 4R1 to 4R4 in side elevation
 Fig. 4-12 : Details of bolt holes in I-beams for specimens 4C1 to 4C4 and 4R1 to 4R4 in plane
 Fig. 4-13 : Welding details (welding process for all the welds : SMAW)
 Fig. 4-14 : Weld measurements for series 1 and 2 with CHS and RHS columns
 Fig. 4-15 : Weld measurements for series 3 with CHS and RHS columns
 Fig. 4-16 : Position of weld measurements for web plates and angle cleats of series 4 with CHS and RHS columns
 Fig. 4-18 : Test rig for specimens 3C3 and 3R3 having CHS or RHS columns with primary beams under hogging moments and secondary beams under sagging moments
 Fig. 4-19 : Test rig for specimens 4C3, 4C4, 4R3 and 4R4 having CHS or RHS columns with all beams only under hogging moments
 Fig. 4-20 : Typical strain gauge details for series 1 (CHS)
 Fig. 4-21 : Typical strain gauge details for series 1 (RHS)
 Fig. 4-22 : Strain gauges on beams for series 2 in CHS (22 for 2C1 and 2C3, 16 for 2C2)
 Fig. 4-23 : Strain gauges provided on column only for 2C1 (8 locations)
 Fig. 4-24 : Strain gauges on beams for series 2 in RHS (30 for 2R1 and 2R2, 22 for 2R3)
 Fig. 4-25 : Strain gauges provided on column only for 2R1 (8 locations)
 Fig. 4-26 : Strain gauging for 3C1 (28 on primary beams and 4 on column)
 Fig. 4-27 : Strain gauging for 3R1 (28 on primary beams and 8 on column)
 Fig. 4-28 : Strain gauges on beam for 3C2 (60 No.)
 Fig. 4-29 : Strain gauges on column for 3C2 (4 No.)
 Fig. 4-30 : Strain rosettes for steel floor of 3C2 (9 locations)
 Fig. 4-31 : Strain gauges on beams for 3R2 (38 No.)
 Fig. 4-32 : Strain gauges on column for 3R2
 Fig. 4-33 : Strain gauges on beams for 3C3 and 3C4 (16 No. each)
 Fig. 4-34 : Strain gauges on column for 3C3 (7 No.)
 Fig. 4-35 : Strain gauges on beam for 3R3 and 3R4 (16 No. each)

- Fig. 4-36 : Strain gauges on column 3R3 (8 No.)
- Fig. 4-37 : Strain gauge on beams for specimens under uniplanar loading (4C1,4C2, 4R1 and 4R2)
- Fig. 4-38 : Strain gauge on beams for specimens under uniplanar loading (4C3,4C4, 4R3 and 4R4)
- Fig. 4-39 : Typical schematic details of transducers for series 1 (CHS)
- Fig. 4-40 : Typical schematic details of transducers for series 1 (RHS)
- Fig. 4-41 : Typical schematic details of transducers for series 2 (2C1-2C3, 2R1-2R3)
- Fig. 4-42 : Typical schematic details of transducers for series 3 (3C1-3C4, 3R1-3R4)
- Fig. 4-43 : Typical schematic details of transducers for series 4 (4C1, 4C2, 4C3 and 4C4)
- Fig. 4-44 : Typical schematic details of transducers for series 4 (4R1, 4R2, 4R3 and 4R4)
- Fig. 4-45 : Definition of connection rotation
- Fig. 5-1 : Typical stress-strain relationship
- Fig. 5-2 : Weld simulation with shell elements
- Fig. 6-1 : Data sheet for test 1C1
- Fig. 6-2 : Data sheet for test 1C2
- Fig. 6-3 : Data sheet for test 1C3
- Fig. 6-4 : Data sheet for test 1C4
- Fig. 6-5 : Data sheet for test 1C5
- Fig. 6-6 : Data sheet for test 1C6
- Fig. 6-7 : Data sheet for test 1C7
- Fig. 6-8 : Data sheet for test 1C8
- Fig. 6-9 : Data sheet for test 2C1
- Fig. 6-10 : Data sheet for test 2C2
- Fig. 6-11 : Data sheet for test 2C3
- Fig. 6-12 : Data sheet for test 3C1
- Fig. 6-13 : Data sheet for test 3C2
- Fig. 6-14 : Data sheet for test 3C3
- Fig. 6-15 : Data sheet for test 3C4
- Fig. 6-16 : Data sheet for test 4C1
- Fig. 6-17 : Data sheet for test 4C2
- Fig. 6-18 : Data sheet for test 4C3
- Fig. 6-19 : Data sheet for test 4C4
- Fig. 6-20 : Experimental and numerical load-deformation diagram for 1C1
- Fig. 6-21 : Experimental and numerical load-deformation diagram for 1C2
- Fig. 6-22 : Experimental and numerical load-deformation diagram for 1C3
- Fig. 6-23 : Experimental and numerical load-deformation diagram for 1C4
- Fig. 6-24 : Experimental and numerical load-deformation diagram for 1C5
- Fig. 6-25 : Experimental and numerical load-deformation diagram for 1C6
- Fig. 6-26 : Experimental and numerical load-deformation diagram for 1C7
- Fig. 6-27 : Experimental and numerical load-deformation diagram for 1C8
- Fig. 6-28 : Experimental and numerical load-deformation diagram for 2C1
- Fig. 6-29 : Experimental and numerical load-deformation diagram for 2C2
- Fig. 6-30 : Experimental and numerical load-deformation diagram for 2C3
- Fig. 6-31 : Experimental and numerical moment-rotation diagram for 3C1
- Fig. 6-32 : Experimental and numerical moment-rotation diagram for 3C2
- Fig. 6-33 : Experimental and numerical moment-rotation diagram for 3C3
- Fig. 6-34 : Experimental and numerical moment-rotation diagram for 3C4

- Fig. 6-35 : Deformation finite element mesh of model 1C2
Fig. 6-36 : Deformation finite element mesh of model 1C3
Fig. 6-37 : Deformation finite element mesh of model 1C5
Fig. 6-38 : Deformation finite element mesh of model 2C1
Fig. 6-39 : Deformation finite element mesh of model 3C1
Fig. 6-40 : Deformation finite element mesh of model 3C2
Fig. 6-41 : Multiplanar effect axial loading tests series 1
Fig. 6-42 : Multiplanar effect in-plane bending tests series 3
Fig. 7-1 : Data sheet for test 1R1
Fig. 7-2 : Data sheet for test 1R2
Fig. 7-3 : Data sheet for test 1R3
Fig. 7-4 : Data sheet for test 1R4
Fig. 7-5 : Data sheet for test 1R5
Fig. 7-6 : Data sheet for test 1R6
Fig. 7-7 : Data sheet for test 1R7
Fig. 7-8 : Data sheet for test 1R8
Fig. 7-9 : Data sheet for test 2R1
Fig. 7-10 : Data sheet for test 2R2
Fig. 7-11 : Data sheet for test 2R3
Fig. 7-12 : Data sheet for test 3R1
Fig. 7-13 : Data sheet for test 3R2
Fig. 7-14 : Data sheet for test 3R3
Fig. 7-15 : Data sheet for test 3R4
Fig. 7-16 : Data sheet for test 4R1
Fig. 7-17 : Data sheet for test 4R2
Fig. 7-18 : Data sheet for test 4R3
Fig. 7-19 : Data sheet for test 4R4
Fig. 7-20 : Experimental and numerical load-deformation diagram for 1R1
Fig. 7-21 : Experimental and numerical load-deformation diagram for 1R2
Fig. 7-22 : Experimental and numerical load-deformation diagram for 1R3
Fig. 7-23 : Experimental and numerical load-deformation diagram for 1R4
Fig. 7-24 : Experimental and numerical load-deformation diagram for 1R5
Fig. 7-25 : Experimental and numerical load-deformation diagram for 1R6
Fig. 7-26 : Experimental and numerical load-deformation diagram for 1R7
Fig. 7-27 : Experimental and numerical load-deformation diagram for 1R8
Fig. 7-28 : Experimental and numerical load-deformation diagram for 2R1
Fig. 7-29 : Experimental and numerical load-deformation diagram for 2R2
Fig. 7-30 : Experimental and numerical load-deformation diagram for 2R3
Fig. 7-31 : Experimental and numerical moment-rotation diagram for 3R1
Fig. 7-32 : Experimental and numerical moment-rotation diagram for 3R2
Fig. 7-33 : Experimental and numerical moment-rotation diagram for 3R3
Fig. 7-34 : Experimental and numerical moment-rotation diagram for 3R4
Fig. 7-35 : Deformation finite element mesh of model 1R2
Fig. 7-36 : Deformation finite element mesh of model 1R3
Fig. 7-37 : Deformation finite element mesh of model 1R5
Fig. 7-38 : Deformation finite element mesh of model 2R1
Fig. 7-39 : Deformation finite element mesh of model 3R1
Fig. 7-40 : Deformation finite element mesh of model 3R2
Fig. 7-41 : Multiplanar effect axial loading tests series 1
Fig. 7-42 : Multiplanar effect in-plane bending tests series 3
Fig. 7-43 : Experimental and numerical load-deformation diagram for 1R1 (Aachen)
Fig. 7-44 : Experimental and numerical load-deformation diagram for 1R3 (Aachen)

- Fig. 7-45 : Experimental and numerical load-deformation diagram for 1R5 (Aachen)
Fig. 7-46 : Experimental and numerical load-deformation diagram for 1R6 (Aachen)
Fig. 7-47 : Experimental and numerical load-deformation diagram for 1R7 (Aachen)
Fig. 7-48 : Experimental and numerical load-deformation diagram for 1R8 (Aachen)
Fig. 7-49 : Experimental and numerical load-deformation diagram for 2R1 (Aachen)
Fig. 7-50 : Experimental and numerical load-deformation diagram for 2R3 (Aachen)
Fig. 7-51 : Experimental and numerical moment-rotation diagram for 3R1 (Aachen)
Fig. 7-52 : Experimental and numerical moment-rotation diagram for 3R3 (Aachen)
Fig. 7-53 : Experimental and numerical moment-rotation diagram for 3R4 (Aachen)

LIST OF PHOTOS

- Photo 4-1 : Placement of reinforcement cages of typical RHS columns
Photo 4-2 : Placement of reinforcement cages of typical CHS columns
Photo 4-3 : Reinforcement arrangement inside CHS columns
Photo 4-4 : Reinforcement arrangement inside RHS columns
Photo 4-5 : Beams bolted to CHS columns
Photo 4-6 : Beams bolted to RHS columns
Photo 4-7 : Placement of steel decks on specimen in CHS
Photo 4-8 : Placement of steel decks on specimen in RHS
Photo 4-9 : Laying reinforcement
Photo 4-10 : Concreting
Photo 4-11 : Test rig for connections with axially loaded plates and beams in CHS and RHS columns (series 1 and 2)
Photo 4-12 : Test rig for connections with axially loaded plates and beams in CHS and RHS columns (series 1 and 2)
Photo 4-13 : Test rig for series 1 and 2, specimen 1C4, with composite CHS column and primary members (plates) in compression
Photo 4-14 : Test rig for series 1 and 2, specimen 1C4, with composite CHS column and primary members (plates) in compression
Photo 4-15 : Test rig for series 1 and 2, specimen 2C1, with CHS column and primary beams in compression
Photo 4-16 : Test rig for series 1 and 2, specimen 2C1, with CHS column and primary beams in compression
Photo 4-17 : 2R2 in tensile testing machine used for testing specimens 1C2, 2C2, 1R2 and 2R2
Photo 4-18 : 2R2 in tensile testing machine used for testing specimens 1C2, 2C2, and 2R2
Photo 4-19 : Test rig for series 3 and 4 with beams under hogging moment only (all except 3C3 and 3R3)
Photo 4-20 : Test rig for series 3 and 4 with 3R2 during testing
Photo 4-21 : Test rig for series 4 with 4C3
Photo 4-22 : Some transducers and column rosettes for 1C1
Photo 4-23 : Some transducers and column rosettes for 1C1
Photo 4-24 : 1C3 fully instrumented in test rig
Photo 4-25 : 1C3 fully instrumented in test rig
Photo 4-26 : 1R4 showing transducers
Photo 4-27 : 1R4 showing transducers
Photo 4-28 : 2C1 showing transducers
Photo 4-29 : 2C1 showing transducers
Photo 4-30 : 2R1 showing transducers

- Photo 4-31 : 2R1 showing transducers
Photo 4-32 : Instrumentation on 3R1 at failure
Photo 4-33 : Instrumentation on 3R1 at failure
Photo 4-34 : Instrumentation on 3C2
Photo 4-35 : Instrumentation on 3C2 and lateral supports to column
Photo 4-36 : Instrumentation on 3C3 and 3R3 at failure
Photo 4-37 : Instrumentation on 3C3 and 3R3 at failure
Photo 4-38 : Instrumentation on 4R2 at failure
Photo 4-39 : Crack width meters on 4R2 at failure
Photo 4-40 : Instrumentation below composite floor for 4C3
Photo 6-1 : Specimen 1C1 after failure
Photo 6-2 : Details of specimen 1C1 after failure
Photo 6-3 : Specimen 1C2 after failure
Photo 6-4 : Details of specimen 1C2 after failure
Photo 6-5 : Specimen 1C3 after failure
Photo 6-6 : Details of specimen 1C3 after failure
Photo 6-7 : Specimen 1C4 after failure
Photo 6-8 : Details of specimen 1C4 after failure
Photo 6-9 : Specimen 1C5 after failure
Photo 6-10 : Details of specimen 1C5 after failure
Photo 6-11 : Specimen 1C6 after failure
Photo 6-12 : Details of specimen 1C6 after failure
Photo 6-13 : Specimen 1C7 after failure
Photo 6-14 : Details of specimen 1C7 after failure
Photo 6-15 : Specimen 1C8 after failure
Photo 6-16 : Details of specimen 1C8 after failure
Photo 6-17 : Specimen 2C1 after failure
Photo 6-18 : Details of specimen 2C1 after failure
Photo 6-19 : Details of specimen 2C2 after failure
Photo 6-20 : Details of specimen 2C2 after failure
Photo 6-21 : Specimen 2C3 after failure
Photo 6-22 : Details of specimen 2C3 after failure
Photo 6-23 : Specimen 3C1 after failure
Photo 6-24 : Details of specimen 3C1 after failure
Photo 6-25 : Specimen 3C2 after failure
Photo 6-26 : Details of specimen 3C2 after failure
Photo 6-27 : Specimen 3C3 after failure
Photo 6-28 : Details of specimen 3C3 after failure
Photo 6-29 : Specimen 3C4 after failure
Photo 6-30 : Details of specimen 3C4 after failure
Photo 6-31 : Specimen 4C1 after failure
Photo 6-32 : Details of specimen 4C1 after failure
Photo 6-33 : Specimen 4C2 after failure
Photo 6-34 : Details of specimen 4C2 after failure
Photo 6-35 : Specimen 4C3 after failure
Photo 6-36 : Details of specimen 4C3 after failure
Photo 6-37 : Specimen 4C4 after failure
Photo 6-38 : Details of specimen 4C4 after failure
Photo 7-1 : Specimen 1R1 after failure
Photo 7-2 : Details of specimen 1R1 after failure
Photo 7-3 : Details of specimen 1R2 after failure
Photo 7-4 : Details of specimen 1R2 after failure

Photo 7-5 : Specimen 1R3 after failure
Photo 7-6 : Specimen 1R4 after failure
Photo 7-7 : Details of specimen 1R4 after failure
Photo 7-8 : Specimen 1R5 after failure
Photo 7-9 : Details of specimen 1R5 after failure
Photo 7-10 : Specimen 1R6 after failure
Photo 7-11 : Details of specimen 1R6 after failure
Photo 7-12 : Specimen 1R7 after failure
Photo 7-13 : Details of specimen 1R7 after failure
Photo 7-14 : Specimen 1R8 after failure
Photo 7-15 : Details of specimen 1R8 after failure
Photo 7-16 : Specimen 2R1 after failure
Photo 7-17 : Specimen 2R1 after failure
Photo 7-18 : Details of specimen 2R2 after failure
Photo 7-19 : Details of specimen 2R2 after failure
Photo 7-20 : Specimen 2R3 after failure
Photo 7-21 : Details of specimen 2R3 after failure
Photo 7-22 : Specimen 3R1 after failure
Photo 7-23 : Details of specimen 3R1 after failure
Photo 7-24 : Specimen 3R2 after failure
Photo 7-25 : Details of specimen 3R2 after failure
Photo 7-26 : Specimen 3R3 after failure
Photo 7-27 : Details of specimen 3R3 after failure
Photo 7-28 : Specimen 3R4 after failure
Photo 7-29 : Details of specimen 3R4 after failure
Photo 7-30 : Specimen 4R1 after failure
Photo 7-31 : Details of specimen 4R1 after failure
Photo 7-32 : Specimen 4R2 after failure
Photo 7-33 : Details of specimen 4R2 after failure
Photo 7-34 : Specimen 4R3 after failure
Photo 7-35 : Details of specimen 4R3 after failure
Photo 7-36 : Specimen 4R4 after failure
Photo 7-37 : Details of specimen 4R4 after failure

TABLE OF SYMBOLS

b_i	- Width of beam i ($i = 1$ to 4)
b_o	- Outer width of RHS columns
d_o	- Outer diameter of CHS column
f_c	- Concrete cube crushing strength
f_t	- Concrete splitting strength
f_u	- Ultimate stress
f_{ub}	- Ultimate stress in bolts
$f_{ui,w}$	- Ultimate stress in the beam (i ($i = 1$ to 4) web material
$f_{ui,f}$	- Ultimate stress in the beam (i ($i = 1$ to 4) flange material
f_{u0}	- Ultimate stress in the column material
$f_{yi,f}$	- Yield stress in the beam flange material
$f_{yi,w}$	- Yield stress in the beam web material
f_{y0}	- Yield stress in the column material
h_i	- Height of beam i ($i = 1$ to 4)
l_o	- Column length
l_i	- Length of beam i ($i = 1$ to 4)
r_1	- Corner radius of the beam
t_f	- Beam flange wall thickness
t_o	- Wall thickness of the column
t_p	- Thickness of plate
t_w	- Beam web wall thickness
w_i	- Width of plate i ($i = 1$ to 4)
A_i	- Cross-sectional area of the beam or plate i ($i = 1$ to 4)
A_o	- Cross-sectional area of the column
A_s	- Area of steel reinforcement
A_t	- Total area of concrete + steel reinforcement
E_c	- Modulus of elasticity of concrete
F_1	- Vertical load on main (or primary) beam
F_2	- Vertical load on secondary beam
M	- Bending moment in the beam at the column face
M_1	- Bending moment in the main (or primary) beams at the column face due to F_1
M_2	- Bending moment in the secondary beams at the column face due to F_2
$M_{d,c}$	- the design moment resistance according to the RHS column side wall failure
$M_{d,e}$	- the design moment resistance according to the effective width failure
$M_{d,p}$	- the design moment resistance according to the punching shear failure
$M_{d,y}$	- the design moment resistance according to the RHS column face yielding failure mode
M_{max}	- Maximum bending moment in the beam at the column face
N_1	- Axial force on main (or primary) beams
N_2	- Axial force on secondary beams
N_p	- Squash load of beam ($= A_i f_{yi}$)
N_{u1}	- Axial force on main (or primary) beams at the ultimate capacity of the connection
N_{u2}	- Axial force on secondary beams at the ultimate capacity of the connection
β	- Beam flange width to column diameter (or width) ratio
δ_{u1}	- Average ultimate indentation into the column due to the main (or primary) beams
δ_{u2}	- Average ultimate indentation into the column due to the secondary beams
δ_1	- Average indentation into the column due to the main (or primary) beams

- δ_2 - Average indentation into the column due to the secondary beams
 ϵ_0 - Maximum strain in the column material
 $\epsilon_{1,f}$ - Maximum strain in the beam flange material
 $\epsilon_{1,w}$ - Maximum strain in the beam web material
 η - beam height to column diameter (or width) ratio
 θ - Beam rotation at column face
 2γ - Column wall thickness to diameter (or width) ratio
 τ - Plate or beam flange thickness to column wall thickness ratio

- CHS - Circular Hollow Section
RHS - Rectangular Hollow Section
FE - Finite Element

- ECSC - European Coal and Steel Community
NCF - Stichting Nederlandse Computer Faciliteit
SARA - Stichting Academisch Rekencentrum Amsterdam
STW - Stichting Technische Wetenschappen

OBJECTIVES OF THE RESEARCH PROJECT

The overall objective of this project is to reduce the global costs of structural steelwork. This can be achieved by using fabrication friendly unstiffened beam-to-column connections.

The aim of this project is to develop guidance and preliminary design recommendations for unstiffened connections between I-beams and hollow section columns. This includes welded as well as bolted connections. Steel grades with nominal yield stresses of 355 N/mm² are used, since high strength steel hollow sections could not be supplied at the start of the project.

Furthermore it is intended to show the effect of a reinforced concrete infill in the columns (composite columns) and the influence of steel floors and composite steel-concrete floors on the connection behaviour.

1 INTRODUCTION

This investigation is carried out for buildings and offshore deck structures, where steel can be economically used by employing I section beams (or trusses) in combination with tubular columns. The elements are then optimally used, with beams or trusses taking the bending moments and shears, while the tubes take the compression as columns. Furthermore, the design will be most economical if the connections are simple, avoiding fabrication intensive stiffening plates. Such connections can be classified as rigid, semi-rigid or pin-ended, on the basis of the stiffness of the connection. For the economical connections investigated in this research programme, the connection characteristics are non-existent, hampering the use of such structural steel framing systems.

I-section columns are optimal for framing systems in one plane. Tubular columns offer considerable advantages for multiplanar connections, in addition to the fact that they are more effective for compression loading. Also, filling the tubular columns with reinforced concrete allows composite action and also offers sufficient fire resistance.

The use of a steel flooring or composite floor (comprising a deep steel deck and a concrete slab) can also increase the strength and stiffness of the connection, if their structural behaviour is taken into account. In this way, the tensile forces on top of the I-beam can also be taken up by the steel floor or the steel reinforcement in the concrete slab.

In the design of steel structures, it is still customary to regard the connections as pinned or rigid. Pinned connections can lead to fabrication friendly designs and heavier beams, while rigid connections result in material savings at the expense of careful detailing which involve use of stiffeners to develop the full moment capacity of the members. To get an optimum solution, fabrication friendly designs should be considered, using the structural moment resistance of such connections in the design of a structure.

For the present research work, the connections considered in general are the welded joints shown in figure 1-1 which offer considerable cost savings for offshore deck modules, whereas the bolted joints shown in figure 1-2 are preferred for building structures to allow for simple jointing and assembly, while permitting sufficient clearance and adjustment to accommodate practical imperfections. In figure 1-2a, for circular hollow section columns, a ring plate bolted solely to the bottom flanges of the I-beams (no welding to the columns) is considered to transfer axial loading across the column. However, for rectangular hollow section columns, angle cleats welded to the column face are considered, which are connected to the bottom flanges of the I-beams with bolts, as shown in figure 1-2(b). For transferring the shear loading from the beams to the columns for the bolted connections, single plates are welded vertically to the tubular column and the I-beam webs bolted to these plates. Although the present work considers semi-rigid behaviour, this is not included in Eurocode 4 [5], where the design is based on pin-ended connections.

The connection behaviour is studied in a systematic way, reflected by detail tests, interaction tests and complete connection tests. The load-deformation behaviour of every part of the connection is studied, such as:

- the influence of only the bottom flanges with each other and with the column
- the interaction between the top and bottom flanges
- the influence of a steel or composite floor
- the multiplanar effect on loading
- the effect of a reinforced concrete infill in the steel columns, i.e. composite columns).

All these combined effects result in a description of the moment-rotation behaviour of the connection and the contribution of the various components. The results of the tests are used for evaluating and calibrating finite element simulations which include material and geometrical non-linearity. On the basis of analytical formulae combined with statistical parameter analyses, design equations should be developed for the design strength of the connection. Also, the moment-rotation characteristics are stored in data sheets, which can be used on a larger European SERICON [13] data base for semi-rigid connections.

The complete research programme consists of:

- A review of literature, to consider existing information and design rules.
- Simple detail testing using circular and rectangular hollow section columns, on the behaviour of individual or both the I-beam flanges, either loaded in compression or tension. Interaction and multiplanar effects are also considered, as well as the influence of composite (reinforced concrete infilled tubular) columns. The tests are carried out for various joint geometries and loading conditions (see tables 2-1 and 2-2). Series 1 consider individual I-beam flanges (or plates), while series 2 considers interaction tests with both I-beam flanges (no web influence).
- Series 3 considers overall connection tests on I-beams welded to circular and rectangular hollow section columns where the influence of a reinforced concrete infill in the column (composite column) and the influence of the steel floor plating are also considered.
- Series 4 considers overall connection tests on I-beams bolted to circular and rectangular hollow section columns with a composite floor comprising a deep steel deck and a concrete slab. Both steel and composite (reinforced concrete infilled) columns are considered.
- Finite element simulation of all the tests, considering material and geometrical non-linearity. This simulation is to form a basis for further numerical parametric studies using the calibrated models established in the comparison between experimental and numerical work.
- Preparation of design guidance on the basis of the experimental, numerical (F.E.) and analytical studies, in conjunction with existing guidelines.

2 RESEARCH PROGRAMME

2.1 Participating ECSC countries and laboratories

The experimental tests are carried out at:

- TNO Building and Construction Research Laboratories Rijswijk, where the detail and interaction tests are carried out.
- Delft University of Technology, Stevin Laboratory, where the overall connection tests are carried out.

The numerical work using non-linear finite element analyses is carried out at:

- Delft University of Technology, Stevin Laboratory, where all the simulations with circular hollow section columns are carried out. Additionally, simulations are also carried out for the specimens with rectangular hollow section columns.
- Rheinisch-Westfälische Technische Hochschule, Aachen, where some simulations with rectangular hollow section columns are carried out as a comparison with the modelling procedures at Delft.

Additionally, British Steel, Tubes and Pipes. International, Corby and Mannesmannröhren-Werke AG Düsseldorf have participated in the project groups of the programme.

2.2 Overview of the experimental work

Tables 2-1 and 2-2 give an overview of the experimental work. Table 2-1 shows the series of tests (series 1 to 4), with various loading combinations to be carried out on multiplanar joints using I-beams (IPE 240 or IPE 360) or plates representing individual flanges of I-beams (120 x 10 or 170 x 12), and circular hollow section (CHS) columns (\varnothing 324 x 9.5), where in some cases the columns are composite (with reinforced concrete infill) as shown shaded inside the columns in table 2-1. For welded beams, a 5 mm¹ thick steel floor is considered for one test specimen, while a composite floor comprising a deep steel deck and a concrete slab is provided for all the bolted connections. Table 2-2 shows an identical series of tests (series 1 to 4), where only rectangular hollow section (RHS) columns (300 x 300 x 10) are used. The I-beams or plates are the same as those used for CHS columns.

The series 1 detail tests (1C1 to 1C8 in table 2-1 and 1R1 to 1R8 in table 2-2) and the series 2 interaction tests (2C1 to 2C3 in table 2-1 and 2R1 to 2R3 in table 2-2) add up

¹ 5 mm has been chosen as the lowest thickness for these scale tests to limit distortions due to welding. In offshore practice, a thickness of 8-10 mm is used with larger columns (deck legs).

to a total of 22 tests. The tests on complete moment connections using welded beams with and without a steel floor plate (3C1 to 3C4 in table 2-1 and 3R1 to 3R4 in table 2-2) and with bolted beams with a composite floor (4C1 to 4C4 in table 2-1 and 4R1 to 4R4 in table 2-2) add up to a total of 16 tests.

2.3 Overview of the numerical work

Numerical simulation of all the experimental work in tables 2-1 and 2-2 is carried out, to show that finite element (F.E.) models can be well calibrated. Parametric studies can then be carried out in the framework of other programmes such as: the STW (Technology Foundation) research grant DCT 99.1904 [1] supported by the Netherlands government for circular hollow section columns in combination with I-beams and plates; the "Beek" Project of the Delft University of Technology [2] for rectangular hollow sections in combination with I-beams and plates; and the German DFG project "Raumliche vervormbare Verbindungen" [3].

For all the simulations, careful measurements of dimensions and mechanical properties of the test specimens are carried out, which are used in the F.E. models.

The comparisons with experiments are then a true representation of the simulation.

3 DEFINITION OF VARIOUS CHARACTERISTICS

Throughout the text, several characteristics are mentioned that need to be clearly defined. These are all listed below:

Indentation

Indentation is defined as the average displacement of a beam or plate into the column face under axial load.

Average indentation

Average indentation is defined as the mean value of the indentations of the two plates or beams in the same plane (on either side of a column).

Moment at column face

The moment at column face is defined as the reaction at a beam support multiplied by the distance between the support and the column face, for moment loaded connections.

Average moment at column face

The average moment at column face is defined as the mean value of the moments (at column face) for the two beams in the same plane (on either side of a column) for moment loaded connections.

Beam rotation

The beam rotation is defined as the in-plane rotation of the beam from its original axis for moment loaded connections. The method of measurement is described in chapter 4.8.5. and figure 4-45.

Average beam rotation

The average beam rotation is defined as the mean value of the beam rotations of the beams in the same plane (on either side of a column)

Ultimate load

As ultimate load is taken the first maximum in the load-displacement or moment rotation curve. In case without a maximum, the load is taken at which the average indentation is equal to $1.2 t_0$.

4 TEST SPECIMEN, TEST RIG AND MEASUREMENT DETAILS

4.1 Design of composite steel-concrete CHS and RHS columns

The design is restricted due to availability of materials and requirements for comparison with hollow steel columns, although every attempt is made to keep to established design practice. Steel reinforcement arrangement is chosen as given in figure 4-1 for the \varnothing 324*9.5 CHS columns and in figure 4-2 for the 300*300*10RHS columns, the steel percentages are:

$$\text{CHS: } A_s/A_t = 2512/72976 = 3.44\%$$

$$\text{RHS: } A_s/A_t = 2512/78400 = 3.2\%$$

where A_s = total area of steel reinforcement

A_t = total area of concrete + steel reinforcement.

The composite steel-concrete columns with a concrete quality C35/45 according to Eurocode 2 [9], are designed for a fire resistance of 60 minutes, according to Eurocode 4 Parts 1.1 [5] and 1.2 [6] which are based upon design recommendations in the ECCS Technical Note [7].

Photos 4-1 and 4-2 show the reinforcement cages being placed into typical CHS and RHS columns, while photos 4-3 and 4-4 show the reinforcement in more detail after placement of the cages, prior to the concreting operations.

For the composite column with composite floor tests (4C2, 4C4, 4R2, 4R4), eight M 16-8.8 bolts, 100 mm long, are provided on the column walls, one on each side of the four beams at the web mid-height, embedded in the concrete filling to satisfy fire resistance requirements, in accordance with work at British Steel [8].

The bolts are threaded through 18 mm diameter holes in the hollow section wall and tack welded, at 33 mm from the web plate on the side where the beam web is bolted to the web plate and 24 mm from the web plate on the other side.

4.2 Design of composite floor comprising a deep steel deck (PMF CF46) and a 110 mm deep concrete slab for series 4 tests with CHS and RHS columns

4.2.1 Design philosophy

Usual practice is to design the I-beam and composite floor as simply supported at the column, with reinforcement at the support only to control the crack width in the concrete. However, for the present work, because it is economically attractive to include the resulting positive bending moments, the resistance of the reinforcement provided adjacent to the column is taken into account.

The column and beam members for the composite connections are taken the same as

for the as-welded connections in order to allow comparisons. This choice results in composite columns that are relatively heavy in relation to the beams. Also, the I-beams are the same in the primary and secondary directions, despite the fact that the composite floor is designed to transfer loads predominantly in one direction, between primary beams.

The design of the composite floor is also restricted due to the availability of materials, although every attempt is made to keep to established design practice.

4.2.2 Design of floor

A column spacing of 5.4 x 7.2 m is chosen for the design, with primary beams at 7.2 m centres (over columns) and secondary beams at standard spacing of 2.7 m centres, supported alternatively at columns and mid-spans of primary beams. This arrangement is chosen on the basis of standard spacings which are in relation to the maximum span of the deep steel deck between secondary beams. Because of availability, deep steel deck PMF CF46/0.9 mm (see figure 4-3) having a 0.9 mm sheet thickness is used instead of 1.2 mm required for 2.7 m spacing. To ensure adequate rotation capacity so that the mid-span moment may develop and to have adequate warning of failure after reaching ultimate moment, bolt failure in the bottom flange is not allowed to govern.

The design of the composite floor is according to Eurocode 4 [6]. For the design, concrete strength class C 20/25 according to Eurocode 2 [9] is chosen and 8 no. 8 mm \emptyset grade B500H reinforcing bars are provided in the vicinity of the columns and grade B500N reinforcing bars at 150 mm centres, both with a concrete cover of 15 mm. The steel reinforcement is on the basis of a permissible crack width of 0.3 mm for high bond bars, according to clause 5.3.2 of Eurocode 4 [5]. The nominal yield stress of the IPE 240 beams 355 N/mm². For an ultimate strength design only B500H bars are taken into account because only these bars have the required ductility (Eurocode 4, Clause 4.2.1 (3)). Clause 4.4.1.2 of Eurocode 4 [5] and Staal-Beton Liggers [12] are used to determine design resistance of the composite floor.

3 No. M16-8.8 bolts ($f_{ub} = 800 \text{ N/mm}^2$) are provided to resist the web shear.

6 No. M12-10.9 bolts are provided in the flange to give a shear resistance through the shank area which is larger than the tensile strength of 6 No. 6 mm \emptyset within the effective width of the secondary beams at the support according to Clause 4.2.2.1 of Eurocode 4) and 8 No. 8 mm \emptyset bars. This ensures that the composite slab will fail before the bolts.

For practical reasons, 6 No. ST37-3K NELSON headed shear studs according to DIN 17150 are used on each beam of the test specimens with composite floors (series 4), although smaller diameter studs would suffice in resisting the tensile force in the

8 No. 8 \emptyset bars and 6 No. 6 \emptyset bars within the beam effective width. The shear connector design resistance is according to Clause 6.3.2.1 of Eurocode 4 [5], with $f_u = 500 \text{ N/mm}^2$ and a height of 100 mm. Figure 4-4 gives the reinforcement details, and figure 4-5 the standard shear stud arrangement.

The web plate size is 180 x 81 x 6 mm, with a projection of 81 mm from the column face (see figures 4-6 and 4-7, showing 3 No. 18 \emptyset bolt holes for M16-8.8 bolts). The size of the ring plate for bolting the I-beam flanges to each other around the CHS columns is 638 mm outside diameter, 326 mm inside diameter and 10 mm thick (see figure 4-8). 24 No. 13 mm \emptyset holes are provided for M12-10.9 bolts on the ring plate (6 No. on each beam, 3 on either side at 45 mm spacing). Figure 4-8 shows the details. The flange cleats for the I-beam bolted connection to the RHS columns have the same thickness as the beam flange, and are 160 x 80 x 10 mm angle sections, 120 mm long. 6 No. 13 mm \emptyset holes are provided for the M12-10.9 bolts (see figures 4-9 and 4-10). The details of bolt holes in the beams for all specimens 4C1 to 4C4 and 4R1 to 4R4 are given in figures 4-11 and 4-12.

4.3 Welding details

All test specimens are welded with basic electrodes (trade name Kryo 1 for butt welds and NF 52 for fillet welds) in accordance with ASME SFA-5.5, E9018G, DIN 8529 and EY 5562 1 Ni MoBH5 standards. The plates and beam flanges are welded to the CHS and RHS columns with butt welds. All weld design is to full capacity as used for offshore work, as shown in fig. 4-13. The webs of beams are welded to the column on both sides of the web with fillet welds (section I-I in fig. 4-13). The web plates are also similarly fillet welded to the columns (section D-D in fig. 4-13). There are no starts or stops of the welding process at the flange corners and there is a smooth transformation of the fillet welds in the web to the sealing welds on the inner face of the flanges. All welding is carried out using shielded metal arc welding (SMAW), in welding position 2G (axis of weld horizontal) for butt welds, and horizontal position 2F for fillet welds, in accordance with section 5.8 of ANSI/AWS D1.1-90, Structural Welding Code for Steel [10]. These details have been chosen such that the specimens can be considered as "scale tests" for offshore applications, whereas this has no effect for the application as used for building design. Only the effect of fillet welds as generally used for buildings have to be considered later on with numerical models.

4.4 Mechanical properties

4.4.1 Steel members

The 300 x 300 x 10 rectangular hollow sections used as columns for the tests are hot finished, steel grade Fe 510 D, in accordance with Euronorm prEN 0210 (draft) for hot

- The expected control cube strength of 50 N/mm² at 28 days is achieved.
- The hardened cube strength in the period of testing increased to 60.3 N/mm².
- The average hardened splitting tensile strength over the testing period is 4.39 N/mm².

Finally, table 4-5 summarizes the mechanical properties of the steel reinforcement and concrete at time of testing.

4.4.4 Composite floor comprising a deep steel deck (PMF CF46) and a 110 mm deep concrete slab for series 4 tests with CHS and RHS columns

The concrete strength class for the concrete floor is C 20/25 in accordance with Eurocode 2 [9]. Eurocode 2 [9] refers to the (draft) prEN 10080 [11] for the hot rolled ribbed 8 mm \varnothing steel reinforcement to grade B500H that is used, which states that they have high ductility (characteristic value of elongation at maximum load > 5% and characteristic value of $f_u/f_y > 1.08$, are weldable and have projected rib factors of not less than 0.045 for 8 mm \varnothing bars. The 6 mm \varnothing reinforcing net is grade B500N, with cold formed normal ductility plain bars.

4.4.4.1 Construction of test specimens

The beams are first bolted to the columns as shown in photos 4-5 and 4-6, for specimens 4C1 to 4C4 and 4R1 to 4R4 at the concreting site for the composite floor. The deep steel decks (PMF CF46) with a 0.9 mm wall thickness are then placed over the beams as shown in photos 4-7 and 4-8. Since the standard widths are 900 mm, they are placed next to each other with an overlap of one upper flange. Close observation of photo 4-7 shows one overlap on the upper flange immediately next to the beam, on the right hand side. Two other overlaps about 900 mm on either side are also present. The overlapping sections are connected together with pop rivets.

The ends of the beams as well as the PMF CF46 steel deck are then supported before further operations. The shear studs are then welded to the steel beams through the PMF CF46 steel decks. The formwork is then erected around the edges of the deep steel deck. Photo 4-9 shows the reinforcement meshes placed into position, using spacers to provide the required cover of 15 mm from the upper surface of the concrete floor. Photo 4-10 shows the ready mixed concrete being poured with a skip, which is then compacted with needle and surface vibrators. Finally, the surface is trowelled flat.

The composite floors are erected and constructed in two different batches on separate dates. Specimens 4C1, 4C2, 4R1 and 4R2 are constructed first, followed by 4C3, 4C4, 4R3 and 4R4. Photo 4-9 shows the 4 specimens for one of these batches.

4.4.4.2 Concrete composition of composite floors

Ready mixed concrete of quality C20/25 is used for pouring into the formwork for the floors of the specimens for series 4. Two mixes of concrete are used for pouring the concrete floors for two series of specimens. The first mix is for specimens 4C1, 4C2, 4R1 and 4R2 and the second mix for the specimens 4C3, 4C4, 4R3 and 4R4.

Concrete composition for the first mix

- maximum particle size = 16 mm
 - cement content = 320 kg/m³ HC-A , consistency = 3 according to NEN 5950 (ISO 4103 (1979) class S3-S4), where necessary achieved with a superplastifier
 - water content = 130 litres
water cement (w/c) ratio = 0.41
- The following properties of the concrete are determined:
- slump according to NEN 5956 (ISO 4109 (1980)⁴) = 210 mm
 - flow according to NEN 5957 (ISO 9812⁵) = 490 mm
 - density of fresh concrete according to NEN 5959 (ISO 6276, 1982) = 2374 kg/m³
 - air content of fresh concrete according to NEN 5962 (ISO 4848, 1980)
= 0.4 % v/v

Concrete composition for the second mix

- maximum particle size = 16 mm
- cement content = 320 kg/m³ HC-A consistency = 3 according to NEN 5950 (ISO 4103 (1979) class S3-S4), where necessary achieved with a superplastifier
- water content = 130 litres
water cement (w/c) ratio = 0.41

The following properties of the concrete are determined:

- slump according to NEN 5956 (ISO 4109 (1980)⁶) = 180 mm
- flow according to NEN 5957 (ISO 9812⁷) = 470 mm
- density of fresh concrete according to NEN 5959 (ISO 6276, 1982)
= 23471 kg/m³

⁴ The compaction for NEN 5956 is less intensive than for ISO 4109

⁵ The cone capacity for NEN 5957 is larger than for ISO 9812

⁶ The compaction for NEN 5956 is less intensive than for ISO 4109

⁷ The cone capacity for NEN 5957 is larger than for ISO 9812

- air content of fresh concrete according to NEN 5962 (ISO 4848, 1980)
= 1.6 % v/v

4.4.4.3 Concreting operations for the composite floor

The formwork for the floors is prepared with reinforcement bars and meshes, the ready mixed concrete is then poured by a skip (see photos 4-9 and 4-10). After pouring, the concrete is then compacted by a needle and surface vibrators and the surface is trowelled flat.

The formwork and reinforcement bars and meshes are positioned in such a way that the thickness of the floor after trowelling the concrete surface smooth, is 110 mm and the cover to the reinforcement bars is 15 mm.

From each mix (see 4.4.4.2) twenty 150*150*150cubes and one 75*75*150prism are cast according to NEN5956 (ISO 2736/2 (1986)). All the cubes and the prism are cured in a humidity chamber at 20° and 95% relative humidity. These cubes are used for or determination of the cube strength and the cube splitting tensile strength, whereas for the determination of the E modulus the prism is used.

4.4.4.4 Properties of cured concrete cubes for the composite floors

At the start of testing each series of four specimens, the following properties are determined: The cube compression strength according to NEN 5968 (ISO 4102 (1978)) (3 cubes); the splitting tensile strength according to NEN 5969 (ISO 4108 (1980)) (3 cubes); the modulus of elasticity according to NEN 3880, Part G, Clause 609.2.1, page 463, using the 75 x 75 x 150 mm prism (one prism). At the start testing of the third specimen, the compression strength of 3 cubes and the splitting tensile strength of 3 cubes are carried out. When the last specimen is tested, the compression strength of 3 cubes and the splitting tensile strength of 3 cubes are again repeated.

The results of the cube and prism tests are given in table 4-3 for the specimens 4C1, 4C2, 4R1 and 4R2 whereas for specimens 4C3, 4C4, 4R3 and 4R4 they are given in table 4-4. The following observations are made:

- The expected control cube strength of 25 N/mm² at 28 days is achieved.
- The hardened cube strength in the period of testing increased to 41 N/mm².
- The average hardened splitting tensile strength over the testing period is 3.61 N/mm².

Finally, table 4-5 summarizes the mechanical properties of the steel and concrete at the time of testing.

4.5 Measured dimensions

Tables 4-6 and 4-7 give all the relevant details, including the nominal sizes and lengths of members used in test specimens with CHS and RHS columns, respectively.

The actual dimensional measurements are done on stubs from stock sizes which have been used for material data, with the exception of CHS columns, where additional measurements of thickness around the circumference have also been made on individual specimens, mainly for series 1 and 2, where imperfection sensitivity is observed.

The stock numbers for the members of each test specimen are also identified in tables 4-6 and 4-7.

Tables 4-8, 4-9, 4-10 and 4-11 give the average actual measurements for the stubs from each stock number, for the CHS, RHS, IPE and plate (including floor) sections, respectively. The cross-sectional areas of the specimens are based upon weights of the stubs from each stock length (approximately 700 mm long), measured up to an accuracy of 0.01 kg. A density of 7580 kg/m³ is used and the stock lengths accurately measured, to calculate the cross-sectional areas.

For each of the stubs from the different stock lengths, a number of measurements are taken of the different components to obtain the average thickness. Table 4-8 shows the diameter of CHS sections measured in two orthogonal directions and the thickness at 4 locations around the circumference. However, as mentioned above, for a number of specimens, 16 equally spaced locations are chosen for thickness measurements instead of 4, because of imperfection sensitivity of the CHS sections subjected to axial load from the plate and beam sections. Table 4-9, for RHS sections, shows the widths measured at two cross-sections in the two orthogonal directions and the thickness at the centre of each of the four sides. Additionally, all corner thicknesses at 3 locations of each corner (see figure in table 4-9) and the inner and outer corner radii at each corner are also measured. For the I-sections, table 4-10 shows that 4 locations are taken in each flange and 3 locations in the web for the thickness measurements. The I-beam heights are measured at three locations and the widths of both flanges are also measured. All 4 fillet radii are also measured to an accuracy of 0.5 mm with gauges. Table 4-11 shows 3 measurements of plate thicknesses and 4 measurements of steel floor thickness from the stubs, used to determine the average thickness.

4.6 Weld measurements

The weld measurements are also given as average values, but in contrast to dimensional measurements of member sizes, are measured individually for each specimen and the average values given in the data sheets. (figures 6-1 to 6-19 for connections with CHS columns and figures 7-1 to 7-19 for connections with RHS columns). The measurements

made are "horizontal" and "vertical" leg lengths (a_h and a_v), representing leg lengths on beams (or plates) and the columns, respectively.

For series 1 using CHS and RHS with axially loaded plates (see figure 4-14), measurements of a_h and a_v are made for the butt welds on one side of the plate and the sealing run on the other side at 3 positions of the plate width. The weld sizes at the two plate corners are also measured. For series 2 using CHS and RHS columns with axially loaded beams, the same measurements are made as for series 1, but for both the flange plates which are welded to the columns. For series 3 using CHS and RHS columns with beams in bending, 20 measurements are made for a_h and a_v around each I-beam as shown in figure 4-15 (the 2 corners, 3 positions on outer face and 2 positions on inner face of each flange, and 3 positions on each side of the web). For series 4 with a composite floor in bending, the web plate welds for specimens with CHS and RHS columns are measured at the top corner and 3 positions along the web plate length (see figure 4-16). For the series 4 angle cleats used for seating the I-beams only for specimens with RHS columns, a_h and a_v are measured at 6 positions (2 along each horizontal weld and 1 along each vertical weld), as shown in figure 4-16. For the CHS columns, the circular plate is only bolted to the lower flanges of the beams and a gap left between the circular plate and the CHS column.

4.7 Test rigs and testing procedures

4.7.1 Connections with axially loaded plates and beams and CHS/RHS columns (series 1 and 2)

A schematic drawing of the test rig for specimens 1C1, 1C3 to 1C8, 2C1 to 2C3, 1R1, 1R3 to 1R8, and 2R1 to 2R3 is shown in figure 4-17. This includes all specimens in series 1 and 2 except 1C2, 2C2, 1R2 and 2R2, which are tested in a tensile testing machine. The test specimens are placed in the test rig with the CHS or RHS columns in a horizontal position. The ends of the vertically positioned primary members (plates or beams) are pin-ended. During the test, the column is maintained horizontal by using a servo controlled hydraulic jack to displace the column vertically at one end of the column. The vertical displacement is measured at both ends of the column with displacement transducers, so that if a difference is noted, the column is automatically balanced into a horizontal position. The out-of-plane displacement of the loaded plates and beams is prevented at one-third and two-third positions of the member (plate or beam) lengths by using lateral supports that allow longitudinal displacements.

This prevents buckling of these members under compression loading. The axial load in the vertical direction is applied vertically on the lower member using a servo controlled hydraulic jack, while the upper member is pin-supported to the reaction frame through a dynamometer, which measures the axial load. The load is applied by force control until the first occurrence of non-linearity, after which displacement control is applied for the uniplanar load situations. For multiplanar load cases, the ratio of horizontal to vertical

load is always maintained constant. Photo 4-11 shows a test in operation, while photo 4-12 shows the test rig prior to installation of a test specimen. The horizontal (multiplanar) load is applied by means of a hydraulic jack mounted in an independent frame in the horizontal direction along the horizontal members, as shown in figure 4-17 (which shows the situation for tensile loads in the horizontal members). For horizontal members subjected to compression, section I-I in figure 4-17 shows the space for the hydraulic jack in the loading frame. The horizontal load is measured with a dynamometer fitted in the end of the frame opposite to the jack end, as shown in sections I-I and II-II of figure 4-17. The ends of the horizontal members, when loaded, are adjustably supported in such a way that during the test, eccentric loading is prevented. This is controlled by means of displacement transducers measuring the indentations into the columns. The column indentations in the two directions is measured through displacement measurements at three locations of each of the 4 members. These locations are in the middle and the two edges of the members, at a distance of 25 mm from the column face. In addition, strain gauge measurements are made on the members. Photos 4-13 and 4-13 show test rig details for specimen 1C4 with a composite CHS column and compression only on primary plate members. In photos 4-15 and 4-16, test rig details for specimen 2C1 with a CHS steel column and only primary beams under compression load are shown. Photos 4-17 and 4-18 show the specimen, where composite RHS columns are employed, in a 1000 kN tensile testing machine. Only the primary members (plates or beams, respectively) are subjected to tension, while the secondary members are left unloaded and free. Specimens 1C2 and 2C2 are also tested similarly.

4.7.2 Connections with moment loaded beams and CHS/RHS columns (series 3 and 4)

A schematic drawing of the test rig is shown in figures 4-18 and 4-19. The test specimens are placed in the test rig with the column always in a vertical position. The configuration of the test rig in figure 4-18 is for test specimens 3C3 and 3R3, where the beams in the two orthogonal planes are loaded in an opposite direction to each other, while figure 4-19 shows the test rig configuration for specimens 4C3, 4C4, 4R3 and 4R4. The test rig configuration for all other connections in series 3 and 4 are similar. For 3C3 and 3R3 (figure 4-18), the primary beams are pulled downwards at their ends by a servo controlled hydraulic jack and spreader beam system as shown in the right half of figure 4-18. The reaction is taken by tension bars to the top of the test rig frame, through the secondary beams which are orthogonal to the primary beams, as shown on the left side of figure 4-18. The forces and reactions on the primary and secondary beams are transmitted through roller bearings to ensure only vertical loads. Hinges are provided at the ends of all the tension bars. Also, load cells are provided at the ends of all tension bars to record loads on each of the four individual beams.

A load cell is also provided at the location of the hydraulic jack to record the total applied load. The jack stroke is also recorded. The jack load is applied in small steps using displacement control.

For all other tests, as shown in figure 4-19, the load is applied in compression to the lower end of the column through the servo controlled hydraulic jack and the test specimen is supported at the ends of the I-beams. Roller bearings are provided between the I-beams and the reaction frame at the top of the test rig. For test specimens 3C1, 3C2, 4C1, 4C2, 3R1, 3R2, 4R1 and 4R2, where uniplanar loading is applied to the primary beams, only the primary beams are supported, as shown in photo 4-19. For test specimens 3C4, 4C3, 4C4, 3R4, 4R3 and 3R4, where all beams are equally loaded downwards, to give a moment with tension on the top flange, all four beams are supported at equal distances away from the face of the column, to give the same moments at the column face. The bending moment in the connection throughout this report is taken at the chord wall face. Again, load cells are provided at the supports to measure reaction forces at the beam ends, and one load cell between the jack and the test specimen. The jack stroke is also recorded.

For all test specimens, the column is supported in the two directions by lateral supports to prevent lateral displacements in any direction. For beams, lateral displacement is also prevented by lateral supports at the unrestrained flanges of the loaded beam ends. Photo 4-19 gives a typical illustration.

The vertical displacements of the beams are recorded at two locations, at approximately one-third and two-third positions of the beam length, using displacement transducers, as discussed in Section 4.8. The indentation of the beam flanges into the column is also measured, by using displacement transducers, as discussed in Section 4.8.

These measurements are taken by measuring the movement between beams in one plane. This movement is recorded on the top and bottom flanges, at a distance of 40 mm from the column face along the centre line of the beam flange. This measurement therefore gives the sum of the indentations due to the two beams in one place. The average indentation is therefore obtained by dividing this value by two.

Additionally, strain gauge measurements are carried out on the beam flanges and column face as described in Section 4.8.

For 3C3 and 3R3, the test rig arrangement has to be changed. Photo 4-20 shows 3R2 in the test rig with only the primary beams supported. Photo 4-21 shows 4C3 in the test rig, with all four beams under hogging moment.

4.8 Measurements

4.8.1 Strains

Strain gauges are provided at a number of cross-sections of members, so that the forces and moments in the member may be determined in order to control the applied jack loads measured by the dynamometers. Any lack of symmetry in the loading is also controlled by the strain gauges during the loading process. Also, the strains are used for comparison of the numerical work.

4.8.1.1 Strain measurements for series 1

Figures 4-20 and 4-21 show strain gauges provided on the braces for Series 1 specimens with CHS columns (1C1 to 1C8) and RHS columns (1R1 to 1R8), respectively. For 1C1 to 1C4 and 1R1 to 1R4, where secondary members are unloaded and primary members are under axial load, 3 strain gauges in the top surface and 2 on the bottom surface are provided at one cross-section of each primary member. In this way, the variation of strain across the width and thickness can be determined, so that the in-plane and out-of-plane bending in the members (plates) can be calculated. For 1C5 to 1C8 and 1R5 to 1R8, where all members (primary and secondary) are subjected to axial load, sufficient confidence in the testing procedure allowed the provision of strain gauges along the plate edges at mid-thickness instead of on the surfaces, so that each member has only 2 strain gauges, giving a total of 8 per specimen.

Rosettes are provided at 3 locations in one quadrant of the column only in the first test specimens (1C1 and 1R1) as shown in figures 4-20 and 4-21 and was not found to be necessary in subsequent tests in series 1.

4.8.1.2 Strain measurements for series 2

Figures 4-22 and 4-24 show strain gauges provided on the beams for series 2 specimens with CHS columns (2C1 to 2C3) and RHS columns (2R1 to 2R3), respectively. The strain gauges are only provided on the primary beams, since all the secondary beams in series 2 are unloaded and free. The strain assist maintenance of concentric the axial loads. Also, by providing strain gauges on both sides of each flange, the influence of flange bending due to the eccentricity created by the single bevelled butt weld on the outer face of the flanges can be measured for comparison with the numerical work. Strain gauges are also provided at a cross-section 300 mm from the end of the beam for some specimens.

As for series 1, strain gauges are provided on the column for the first test specimens of series 2 (2C1 and 2R1) as shown in figures 4-23 and 4-25, for possible use in comparing numerical results when discrepancies are observed.

4.8.1.3 Strain measurements for series 3

For this series, the beams are subjected to bending moments. Figures 4-26 and 4-27 show the arrangement for 3C1 and 3R1, where the strain gauging in the primary beams is identical. No strain gauges are provided on the secondary beams, which are unloaded for 3C1 and 3R1. Three cross-sections are strain gauged as shown, at 25 mm, 350 mm and 750 mm from the column face for both primary beams, in order to measure the variation in the bending moment along the beams.

Four strain gauges are provided on the column for 3C1 and 3R1, one directly underneath each beam, at 450 mm from the bottom of the column, so as to derive the axial load from the measured strains and control the dynamometer measurement of the jack load. For 3R1, 4 additional strain gauges are also provided on the column surface, 25 mm away from the top and bottom flanges on the primary beams.

Specimens 3C2 and 3R2 have a 5 mm thick steel floor fillet welded to the beam flanges. As this would result in a shift of the neutral axis, the strain gauging on the beams are extensive, with 60 for 3C2 and 38 for 3R2, as shown in figures 4-28 and 4-31, respectively. As for 3C1 and 3R1, four strain gauges are provided on the column for 3C2 and 3R2 (see figures 4-29 and 4-32) at 450 mm from the bottom of the column, in order to control the jack load.

Figure 4-30 shows the arrangement of rosettes for 3C2 on the steel floor upper surface, for use in comparison with finite element work. Rosettes are also provided for the steel floor on 3R2, which are arranged in a similar manner.

3C3, 3C4, 3R3 and 3R4 have primary and secondary beams subjected to bending moments. Again, sufficient confidence in the testing procedure allows the use of fewer strain gauges on the beams for 3C3 and 3C4 (figure 4-33) and 3R3 and 3R4 (figure 4-35). Only sufficient strain gauges are provided to ensure symmetric loading and control the bending moments at one cross-section of each of the loaded beams.

Strain gauges on the column are only provided for 3C3 and 3R3 (see figures 4-34 and 4-36, respectively). The method of loading 3C3 and 3R3 is quite different from that for the other specimens, because the primary and secondary beams are subjected to identical bending moments but in opposite directions, so that no loads are transmitted through the column (see tables 2-1 and 2-2, and figure 4-18). Therefore, strain gauges are provided on the column cross-section at 450 mm from the end of the column, to observe the influence of the column deformation on the strain variation at this cross-section, although there should be no resultant total stress at the cross-section.

4.8.1.4 Strain measurements for series 4

For this series, the beams, together with the composite floor are subjected to bending moments. For the specimens where only primary beams are loaded and the secondary beams unloaded (4C1, 4C2, 4R1 and 4R2), one of the primary beams (beam 1 in figure 4-37) is provided with 10 strain gauges. For determination of the bending moment and shift of the neutral axis of the beam, a cross-section at 460 mm from the column face is provided with seven strain gauges. For determination of the bending moment variation along the length of the beam the remaining three strain gauges are attached to the middle of the flange at various distances from the column face. For monitoring the symmetry of loading, the other primary beam (beam 2 in figure 4-37) is provided with only 4 strain gauges at the same cross-section as for beam 1.

The secondary beams and the column are not strain gauged.

For the specimens where both primary and secondary beams are loaded (4C3, 4C4, 4R3 and 4R4) the primary beams are provided with 10 strain gauges on beam 1, and 4 strain gauges on beam 2, as before. For determination of the bending moments and shift of the neutral axis of the secondary beams, these beams are also provided with strain gauges. The strain gauges are attached at similar locations as for the primary beams, giving 10 strain gauges on beam 3 and 4 strain gauges on beam 4 (see figure 4-38).

4.8.2 Column indentations for the axially loaded specimens (series 1 and 2)

During the tests, the column indentations are measured and recorded for all the specimens in series 1 and 2, using electrical transducers. Also, problems of stability are encountered with the detail and interaction tests comprising series 1 and 2, where the specimens are always tested with the column in a horizontal position. Therefore, electrical transducers are provided at the ends of the column to ensure that the vertical displacements at the column ends are the same. Any difference is adjusted by a jack at one end that applies small compressive or tensile forces to bring the column back to the horizontal position. For those tests, where multiplanar loading is applied, so that the secondary members are also subjected to load, this same problem can occur due to bending moments created by the ends of the secondary beams not being in line with the direction of force. Therefore, for cases with secondary members under load (1C5 to 1C8 and 1R5 to 1R8), transducers are also used at the ends of these members to measure their displacements and correct them with a jack at the ends of the two secondary members. A further explanation is given below.

4.8.2.1 Transducer measurements for series 1

Figures 4-39 and 4-40 give schematic details of the transducers used in series 1. For the primary members which are placed vertically and the column horizontally in the test rig, transducers 1 and 2 (figure 4-39) measure the vertical displacements of the column ends so that any variation from the horizontal may be corrected by tensile or compressive forces from the jack at one end.

For the specimens where both primary and secondary members are loaded (1C5 to 1C8 and 1R5 to 1R8), the transducers 10 and 11 also help in maintaining the ends of the secondary members at one level so as not to introduce bending moments in them.

Transducers 3, 4 and 5 (figures 4-39 and 4-40) measure the central and two edge displacements on the two primary members at positions 40 mm from the column face. This effectively measures the sum of the indentations due to the two primary members into the column. Transducers 6, 7 and 8 for specimens 1C1, 1C5 to 1C8, 1R1, and 1R5 to 1R8 make similar measurements to transducers 3, 4 and 5, but in the horizontal direction between the secondary members. However, for specimens 1C2 to 1C4, and 1R2 to 1R4, where the secondary members are unloaded, transducer measurements are only made along the centre line, on both sides of the secondary members (plates).

Photos 4-22 to 4-27 show some of the instrumentation, and transducers in particular, used in series 1.

4.8.2.2 Transducer measurements for series 2

Figure 4-41 gives the schematic details for the transducers used in series 2. Transducers 1 and 2 in figure 4-41 serve the same function of maintaining the column horizontal by measuring the column end deflections, as for series 1. Transducers 3, 4 and 5 measure the central and two edge displacements between positions at 40 mm from the column face on the flanges which are on one side of the neutral axis of the two primary members. Transducers 7, 8 and 9 do the same on the flanges which are on the other side of the neutral axis of the two primary members. Transducer 6 measures the flange centre line displacement between the secondary members at positions 40 mm away from the column face on one flange, while transducer 10 does so on the other flange. These two measurements are adequate for series 2, where all of the secondary beams are unloaded.

Photos 4-28 to 4-31 show all the relevant transducer instrumentations for specimens 2C1 and 2R1, representative for series 2.

4.8.3 Transducer measurements for series 3

Four electrical transducers are used to measure and record column indentations for all the specimens in series 3, as shown by transducer numbers 9 to 12 in figure 4-42. The indentation measurements are the same as for series 1 and 2. At approximately one-third and two-third positions of each beam length on both primary and secondary beams, displacements during load application are also measured by 8 electrical transducers, identified by numbers 1 to 8 in figure 4-42. Photos 4-32 to 4-37 show the transducers used for series 3.

4.8.4 Transducer measurements for series 4

For measuring the horizontal displacements of the concrete floor adjacent the column wall, the concrete floor has been provided with two transducers (79, 95) in the two main directions (see figure 4-44 and 4-45). For measuring and recording column indentations, four transducers are used. The positions of the transducers (80, 403, 95 and 404) are given in these figures.

The slip between the angle cleats or stiffener ring and the bottom flange of the primary beams is determined by the transducers 80 and 403. For the secondary beams, the slip is determined by the transducers 96 and 404. For measuring the rotation at the column wall, the specimens are provided with transducers 405, 406, 407 and 408.

At approximately one-third and two-third positions of each beam length on both primary and secondary beams, displacements during load application are also measured by 8 electrical transducers, identified by numbers 48, 47, 63, 64, 32, 31, 143 and 114, in figures 4-44 and 4-45.

Photos 4-38 to 4-40 show the instrumentation during the tests. The transducers described above can all be seen in the photographs for the series 4 tests. Also, as shown in photos 4-38 and 4-39 for 4R2 at the end of the test, the deformations at the column face, and around the beam and composite slab can be seen, together with the dial gauges used for crack width measurements.

4.8.5 Determination of beam rotation

The first method of calculating the beam rotations is by using the two recorded displacements at their one-third and two-third positions, corrected by the elastic deformations of the beam, and dividing by the distance between the displacement transducers, as shown in figure 4-45. The rotation is also calculated in a second manner, by adding the transducer measurements to be used in calculating column indentation at the upper and lower flange locations, and dividing by the distance between the measurement points of the upper and lower flanges. Both methods give the same results for this type of connection because there is no plastic deformation in the

beams, and the elastic deformations in the beams are small. Therefore, all the moment-rotation diagrams, the first method, without correction for the elastic beam deformation, is employed.

5 GENERAL DETAILS FOR THE NUMERICAL FE WORK

5.1 Method of analyses

The numerical work with finite element simulations of test series 1, 2 and 3 are carried out at the Delft University of Technology. Also, finite element simulations of test specimens with an RHS column, but without concrete, are carried out at RWTH Aachen. For the FE models, eight noded thick (Delft) or thin (Aachen) shell elements are used, with four integration points at Gauss locations in seven (Delft) or five (Aachen) layers across the thickness using Simpson integration (a maximum of 28 integration points). It is shown for the elements as used in Delft in a preliminary study [1] and also by Vegte et al [16] that using these elements with a proper mesh grading can give good agreement with experimental results. For the thin shell elements, as used for the Aachen part, it is shown, that using this elements with a proper mesh grading may give good results compared with experimental results [30].

At theoretical point of view, thick shell elements with at least 7 layers and a reduced integration scheme provide the best simulation of the plastic behaviour of connections with tubular members. Results obtained with thin shell elements will be less accurate, but computer time can be saved.

The experimentally determined engineering stress-strain curves, obtained with tensile coupon tests, are translated to the true-stress - true-strain relationships, using the Ramberg-Osgood relationship [17]. Figure 5-1 shows typical stress-strain curves for the steel used for a CHS column and an IPE 240 flange.

The load is applied using either displacement or load control, similar to the experimental procedure.

For the finite element solution procedure, the updated Lagrange method for the Delft part and the by Riks and Wemper modified Newton-Raphson algorithm for the Aachen part is used, both allowing large curvatures during deformations [14, 15 and 19].

During the tests on specimen with composite columns, the column wall near the plate under tension load is observed to pull away from the concrete infill. The concrete infill is therefore modelled as a rigid contact surface. The characteristics of the rigid contact surface are to provide full resistance against compression and no resistance to tension. The linear elastic deformations of the concrete infill and the adhesive bond between the concrete infill and the column are neglected with this approach. However, in reality, these influences are small in comparison to the total ovalization for the tensile load cases (1C2, 1R2, 2C2 and 2R2). For the test specimen under compression (1C4 and 1R4) the deformations and indentations in the composite columns are observed to be negligible in comparison to the plastic buckling deformation of the plates. Therefore, the numerical modelling assumes a rigid concrete infill in the composite column also for tests 1C4 and 1R4, with plates under compression.

For the modelling, the pre- and post processor SDRG-IDEAS Level V [18] is used for the Delft part and the at the RWTH Aachen developed program Profil [20] is used for the

Aachen part. The finite element analyses are carried out with the general purpose finite element computer programs MARC versions K4.2 and K5 (Delft). and ABAQUS version 4.9 (Aachen). For interfacing between IDEAS and MARC the MENTAT 5.4.3 computer program is used.

5.2 Method of modelling

The finite element modelling uses the averaged values of the measured dimensions for each component of a test specimen. The influence of the welds is also simulated, by using shell elements. Figure 5-2 shows how the magnitude of the dimensional measurements and thicknesses of the shell elements, modelling the welds, are obtained for model 3C3. The welds of all other models are modelled using the same method. In a preliminary study on the influence of weld modelling [1] it is shown that not taking the welds into account in the modelling would give lower ultimate strengths and initial stiffnesses than the experiments. Furthermore, solid elements could also be used for weld modelling. However, a FE model with solid elements leads to an unacceptable amount of computer time for the non-linear FE calculations.

For the modelling, symmetry planes are used where possible. Two different stress-strain curves are used for the FE analysis of each connection, one for the column and one for the I-section beam or plate. For the RHS columns, a third stress-strain curve is used for the corners. It should be noted that the yield stress of the beam web is considerably higher than the yield stress of the beam flanges (see Tables 4-1a and 4-1b). However, since there is no significant plastification in the beam web, the material properties of the flanges are also used for the web.

6 CONNECTIONS WITH CHS COLUMNS

6.1 Experimental research

The results of all tested specimens with CHS columns in series 1 to 4 are given in figures 6-1 to 6-19. The following information is given in these figures:

- specimen type
- type of loading
- type of column (if composite, the inside cross-section is shown shaded)
- reinforcement details for concrete floor
- average weld sizes
- average column, beam and floor dimensional measurements
- mechanical properties of steel and concrete components
- curves showing average load versus average indentation plots for axially loaded plates or beams, and average moment at column face versus average rotation plots for beams loaded by in-plane bending.

For axially loaded plates and beams (series 1 and 2), the average column indentation represents the average of the indentations into the column due to the two members (plates or beams) in the same plane. For beams under in-plane bending moment, the rotations plotted are the average rotation of the two beams in the same plane. The moments given in the plots are at the column face at the crown position. The definition for average loads and moments are given in chapter 3.

For the axially loaded connections, the testing is stopped when the average indentation is approximately 10% of the column diameter, even if the maximum load is already registered, so that information on the deformation capacity and possible failure modes is obtained. For beams subjected to bending moments, the testing is stopped when the average beam rotation is approximately 0.15 radians.

For the series 1 tests (1C1 to 1C8), all the connections without a concrete infill in the columns (1C1, 1C3, 1C5 to 1C8) failed by column wall yielding (see photos 6-1, 6-2, 6-5, 6-6 and 6-9 to 6-16). Specimen 1C2, with a composite column, primary plate members in tension and secondary members unloaded, failed by plate yielding followed by punching shear in the column wall, at the weld toes of the primary plate member corners (see photos 6-3 and 6-4). Specimen 1C4, also with a concrete infill, but with primary plate members in compression and unloaded secondary members, failed by buckling of the primary plate members under compression. The maximum load for this test is 15% below the squash load of the primary plate member, which could be due to a combination of bending and axial force. Theoretically it can be shown that an eccentricity of 3.4 mm is required to give a 15% lower ultimate load than the squash load. The strain gauge measurements also show a considerable amount of plate

bending, which is unavoidable because of the one-sided single V butt welds between the plate members and the column.

For the series 2 tests (2C1 to 2C3), the connections 2C1 and 2C3 without a concrete infill failed by column wall plastic yielding (see photos 6-17 to 6-18, and 6-21 to 6-22). Specimen 2C2, with a composite column, primary beams in tension and secondary beams unloaded, failed by punching shear in the column wall, at the weld toes of the flange corners of the primary beams (see photos 6-19 and 6-20).

For series 3 (specimens 3C1 to 3C4), all specimens failed by column wall yielding (see photos 6-23 to 6-30). For some specimens, cracks are observed at weld toes of the tension flanges (see photo 6-24). These small cracks occur far into the plastic region of the moment rotation curves. There is no drop in the moment capacity after visual observation of the cracks. For the connection with the steel floor (3C2), a larger stiffness and slightly larger ultimate strength is observed than for the identical specimen 3C1 without a steel floor and which is subjected to an identical loading condition.

For series 4 (specimens 4C1 to 4C4), all specimens failed by cracking of the concrete in the composite floor, followed by failure of the concrete reinforcement (see photos 6-31 to 6-38).

From the start of testing of the uniplanar loaded specimens small cracks occurred in the concrete floor face. The cracks first appeared on the surface of the concrete floor on both sides of the secondary beams close to the column and developed parallel to the secondary beams. When the main cracks above the sides of the flange had a width of about 6 mm the reinforcement mesh failed, starting from the edge of the floor towards the column. The failure of the reinforcement mesh was followed by failure of the main bars (see photos 6-31 to 6-34). For the multiplanar loaded specimens the surface cracks fan out from the column face. Towards the end of the test the main cracks develop parallel to the secondary beams above the sides of the flange. Also here, the reinforcement mesh failed from the edges of the floor towards the column followed by failure of the main bars (see photos 6-35 to 6-38).

6.2 Comparison of numerical and experimental results

In general, for series 1 there is good agreement between the experimental and numerical results (see Figures 6-20 to 6-27). The deformed shapes of the test specimens and the finite element models agree well. The differences between the results of the numerical models and the experimental tests are quantified in Table 6-1. The largest difference between the experimental and numerical results is found for test 1C4. The ultimate load of the test specimen is $.85 * N_p$, due to eccentricity effects (see also Section 6.1), while the FE model even exceeds the squash load N_p , with increase of load in the FE model, due to the work hardening behaviour of steel. The numerical results are up to 9% higher

than the experimental results. The differences are acceptable. Examples of typical finite element meshes of series 1 are shown in Figures 6-35 to 6-37.

There is a less good agreement for the test specimens of series 2 with plates in two planes. The deformed shapes of the test specimens and the finite element models agree well. The differences between the results of the numerical models and the experimental tests are quantified in Table 6-1. The largest difference between the experimental and numerical results is found for test 2C1, namely 16 %. The load-displacement curves are shown in Figures 6-28 to 6-30. An example of a typical finite element mesh of series 2 is shown in Figure 6-38. Despite a thorough analysis of the experimental data and additional thickness measurements, no reasons could be found for the larger difference between the experimental and numerical results of tests 2C1 and 2C3 in comparison with the other tests. The ultimate loads of these two tests are lower than found in the numerical work, in the same way as for series 1, probably also due to sensitivity to stability.

There is good agreement between the experimental and numerical results for series 3 (see Figures 6-31 to 6-34). Also, the deformed shapes of the test specimens and the finite element models agree well. The variations between the results of the numerical models and the experimental tests is shown in Table 6-2. For one test, namely 3C3, the experimental ultimate moment is about 12% lower than the predicted ultimate value. This difference is attributed to the fact that two of the I-section beams were not properly aligned when welded to the column, but slightly rotated about the beam axes and not totally perpendicular to the column face. Typical finite element meshes of series 3 are shown in Figures 6-39 and 6-40.

6.3 Discussion of results

In general, the experimental values are discussed, with numerical values given within brackets.

6.3.1 Plate to CHS connections

There is a considerable multiplanar effect observed on the strength of the connections. For the case load ratio $N_2/N_1 = -1$ and $\beta = 0.37$ the ultimate strength is 29% (26%) lower than the uniplanar load case. For the case with load ratio $N_2/N_1 = +1$ and $\beta = 0.37$ the ultimate load is 23% (23%) higher than the uniplanar load case. With increasing β this effect becomes stronger. For $\beta = 0.52$ these values are -32% (-33%) and +54% (42%), respectively. Figure 6-41 gives a pictorial illustration. The relationship between the load ratio N_2/N_1 and the connection strength N_u is almost linear for the parameters considered in the present work, as can be seen in Figure 6-41.

6.3.2 Interaction effects

Test series 2, with two levels of plates (flanges), which represents the interaction tests, are compared with test series 1 with only one level of plates. This comparison is done, because in the experimental tests of series 2 both β and η are varied at the same time. The β influence is determined in series 1, so that it is possible to isolate the influences. If the distance between the "flanges" in series 2 is infinitely, it can be expected that the ultimate load for series 2 is two times that for a corresponding specimen in series 1. However, for the case where $\eta = 0.74$ and $\beta = 0.37$ (2C1) the ultimate load is 1.79 times the ultimate load of the corresponding test of series 1 (1C1) as can be calculated from the values as in Table 6-1. For $\eta = 1.1$ and $\beta = 0.52$ (2C3), the ultimate load is 1.73 times that of the corresponding tests of series 1 (1C3).

6.3.3 Beam to column connections

For the connections of series 3, subjected to in-plane bending, with a multiplanar moment ratio $M_2/M_1 = -1$, a decrease of 27% (34%) has been observed, in comparison to the uni-planar load case. For the load case $M_2/M_1 = +1$ a small decrease of 4% (2%) has been found, in comparison to the uniplanar load case. There is a multiplanar loading effect on the stiffness of the connections. A reduction of approximately 43% (32%) has been found for the load case $M_2/M_1 = -1$ and for the load case $M_2/M_1 = 1$ an increase of over 150% (138%), with respect to the uni-planar load case. See Figure 6-42 for illustration. The relationship between the load ratio and the ultimate strength is almost parabolic for the tested specimens, as shown in Figure 6-42. The shape of the parabola is dependent of the geometrical parameters of the connection and cannot be applied generally on such connections. For relatively small β ratios the ultimate loads for the load cases $M_2/M_1 = 0$ and $M_2/M_1 = +1$ are almost the same. This is due to the fact that the yield line pattern is governed by local deformations. These local deformations are about the same for both load cases. For load case $M_2/M_1 = -1$ the yield line pattern is governed by more global deformations.

6.3.4 Effect of concrete infill in the CHS column

For the axially loaded test specimens with a compression load (1C2 and 1C4), the stiffness of the connection becomes almost infinite. There is no crushing of the concrete infill observed. The plates under axial compression loading failed by local plastic buckling, after reaching almost full plasticification. The axially loaded test specimen under tension load (2C2) failed by punching shear. After plastification of the CHS wall, cracks at either side of the plates or beam flanges start to grow in a direction parallel to the column axis. This failure mode with cracks could not be modelled with the finite element program at present.

6.3.5 Effect of a steel floor

In comparison with the test specimen without a steel floor the provision of a steel floor increases the strength by 6% (5%) and the initial stiffness by 11% (30%).

6.3.6 Comparison with existing strength formulae

Currently only design formulae exist for uniplanar plate to CHS column connections under axial or bending moment loading. Currently, EUROCODE 3 [21] does not give any formulae for these type of connections. An overview of existing design formulae is provided by the CIDECT Design guide for CHS connections [22]. In other publications [23, 24] similar formulae are given, only the constants in the formulae are differing slightly. Also, in the AIJ recommendations for tubular structures [25] design formulae are given for these connections. In the formulae of the AIJ recommendations a γ influence is taken also into account.

The formulae for uniplanar connections cannot directly be applied to multiplanar connections. However, comparing the experimental and numerical results with these design formulae can give indications of the multiplanar influences.

6.3.6.1 Plate to CHS column connections

The experimentally obtained ultimate loads of the specimens loaded under compression 1C1, 1C3, 2C1 and 2C3 are compared with the CIDECT formula [22]:

$$N_u = \frac{5}{1 - 0.81\beta} (1 + 0.25\eta) f_y t_0^2$$

with $\eta = 0$, for connections with plates in one layer.

The results are also compared with the Japanese code formula [25]:

$$N_u = 6 \left(\frac{1 + 0.25\eta}{1 - 0.81\beta} \gamma^{-0.1} + \frac{0.55}{1 - 0.92\beta} \eta \gamma^{-0.3} \right) f_y t_0^2$$

with $\eta = 0$, for connections with plates in one layer.

The AIJ Recommendations make a distinction between allowable and maximum loads. The formula given above is for the maximum load, which is 2.14 times the allowable load. The f_y in the AIJ formula is based on the mean yield strength for cold-formed tubes. This mean yield strength is in the formula included as:

$$f_y = 1.4 F' \gamma^{-0.073}, \text{ with } F' = 330 \text{ N/mm}^2$$

The results of the comparison are listed in Table 6-3. For the yield stress the actual measured values are used in the formulae. The comparison is only made for the uniplanar loaded connections, because an obvious multiplanar loading effect is observed (see section 6.3.1). The AIJ formula, although developed for uniplanar connections, shows a reasonable agreement with the experimental tests, if the actual yield stresses are used. The CIDECT formula applied on multiplanar plate to CHS columns connections, with plates at one layer, give values close to the experimental results. EUROCODE 3 [21] prescribes a partial safety factor $\gamma_m = 1.1$, between the characteristic values and

the design value. However, in the design values the nominal specified yield stresses should be used, whereas the actual yield stresses are used here for the test results. As shown in Table 6-3, the test results for 1C1 and 1C3 are close to the design values, if the actual yield strength is used. The CIDECT design formula for uniplanar connections is based on experiments with fillet welds, where the results are expected to be higher than for butt welded specimens, as used in the programme.

6.3.6.2 Interaction effects

The experimental results of test 2C1 and 2C3 are compared with the design formula in the previous section. As shown in Table 6-3, there is a reasonable agreement between the experimentally obtained results and the formulae.

6.3.6.3 In-plane bending test

The results of test 3C1, loaded with uniplanar in-plane bending are compared with the formulae provided by CIDECT [22] and the Japanese code [25]. The formulae are based on the formulae given in the previous section, where the formulae for uniplanar axial load are multiplied by the I-section beam height and $\eta = 0$ is assumed. The η influence in the formulae is only valid for axial loading, not for in-plane bending. The CIDECT formula, based on design strength and the AIJ Recommendation formula, based on ultimate strength give both conservative maximum loads in comparison with the experimentally obtained maximum loads (see Table 6-3).

6.3.6.4 Bolted connections with a composite steel concrete floor

All test specimens failed as expected, namely by (progressive) failure of the reinforcement bars. Before failure of the main reinforcement bars, some of the reinforcement bars of the mesh failed, due to the smaller ultimate elongation. The concrete infill gives a small increase in connection strength, especially for the multiplanar load case, as shown in Table 8-4. The multiplanar loading $F_2/F_1 = +1$ decreases the connection strength with about 30%. The bending of the concrete slab in two directions causes an earlier failure of reinforcement bars. Since the connections failed by failure of the reinforcement bars, the theoretical strength can be determined easily. As described in section 4.2.2, for design only the main reinforcement, namely the 8 Φ 8 reinforcing bars, were taken into account. Thus, the connection strength can be calculated by multiplying the force in the reinforcement bars by the distance between the bolted connection at the bottom flange and the reinforcement ($h = 335$ mm).

If the nominal yield stress, $f_y = 500 \text{ N/mm}^2$ is used, and only $8\Phi 8$ is taken into account:

$$M_u = 67 \text{ kNm (design strength)}$$

If the actual ultimate stresses, $f_u = 645 \text{ N/mm}^2$ for $8\Phi 8$ and $f_u = 627 \text{ N/mm}^2$ for $16\Phi 6$ is taken into account:

$$M_u = 182 \text{ kNm (theoretical ultimate strength)}$$

For the tests the lowest ultimate strength is found for test 4C3, the multiplanar loaded connection without a concrete filled column. The ultimate strength found in the test, 117.5 kNm is 1.75 times the design strength. The highest strength is found for test 4C2, uniplanar loaded and with a concrete filled column. The ultimate strength found in this test, 186.8 kNm is about equal to the theoretical ultimate strength, as calculated above.

7 CONNECTIONS WITH RHS COLUMNS

7.1 Experimental research

The results of all tested specimens with RHS columns in series 1 to 4 are given in figures 7-1 to 7-19. The following information is given in these series:

- specimen type
- type of loading
- type of column (if composite, the inside cross-section is shown shaded)
- average weld sizes
- average column, beam and floor dimensional measurements
- mechanical properties of steel and concrete components
- curves showing load deflection plots for axially loaded plates or beams, and moment versus average rotation plots for beams loaded by in-plane bending.

For axially loaded plates and beams (series 1 and 2), the average column indentation represents the average of the indentations into the column due to the two members (plates or beams) in the same plane. For beams under in-plane bending moment, the rotation plotted is the average rotation of the two beams in the same plane.

The moments given in the plots are at the column face.

For the axially loaded connections, the testing is stopped when the total column deformation is approximately 10% of the column width, so that information on the deformation capacity and possible failure modes can be obtained. For beams subjected to bending moments, the testing is stopped when the average beam rotation is approximately 0.15 radians.

For the series 1 tests (1R1 to 1R8), all the connections without a concrete infill in the columns (1R1, 1R3, 1R5 to 1R8) gave no peak load during the tests. The maximum load achieved is accompanied by plastic yielding of the column wall (see photos 7-1, 7-2, 7-5, and 7-8 to 7-15). For specimen 1R7 with the larger β value of 0.57, where primary members are in compression and secondary members in tension, cracks are observed at the weld toes of the secondary (tensile) members at the plate edges (see photos 7-12 and 7-13). These small cracks, which occur far into the plastic region of the load deflection curves, cause no drop in the load capacity after visual observation of the cracks. Specimen 1R2 with a composite column, primary plate members in tension and secondary plate members unloaded, failed by plastification of the RHS wall followed by punching shear in the column wall, at the weld toes of the primary plate members in the plate corners (see photos 7-3 and 7-4). Specimen 1R4, also with a composite column but with primary plate members in compression and unloaded secondary plate members, failed by buckling of the primary plate members under compression. The maximum load for this test is 11% below the squash load of the primary plate

member, which could be due to a combination of bending and axial force. Theoretically, it can be shown that an eccentricity of less than 3 mm is required to give an ultimate load which is 11% lower than the squash load. The strain gauge measurements also show a considerable amount of plate bending, which is unavoidable because of the one sided single V butt welds between the plate members and the column.

For the series 2 tests (2R1 to 2R3), the connections 2R1 and 2R3 without a concrete infill do not exhibit a peak load during the tests. No failure modes are observed. The tests are stopped after sufficient deformation is reached. The relative large deformations in the RHS wall causes plastification of the RHS wall around the flanges (see photos 7-16, 7-17, 7-20 and 7-21). Specimen 2R2, with a composite column, primary beams in tension and unloaded secondary beams, failed by punching shear in the column wall, at the weld toes of the primary beam flanges in the flange corners (see photos 7-18 to 7-19).

For series 3 (specimens 3R1 to 3R4), (see photos 7-22 to 7-29), the tests are stopped after sufficient beam rotation is reached. The relative large deformations in the RHS wall causes plastification of the RHS wall at the areas above the top flanges and below the bottom flange of the loaded I-beam. For all specimens except specimen 3R2 (steel floor) cracks are observed at weld toes of the tension flanges (see photo 7-29). These small cracks occur far into the plastic region of the moment rotation curves. There is no drop in the moment capacity after visual observation of the cracks. For the connection with the steel floor (3R2), a larger stiffness is observed than for the identical specimen 3R1 without a steel floor and which is subjected to an identical loading condition.

For series 4 (specimens 4R1 to 4R4), all specimens (except specimen 4R3) failed by cracking of the concrete in the composite floor, followed by failure of the concrete reinforcement (see photos 7-30 to 7-33, 7-36 and 7-37).

From the start of testing of the uniplanar loaded specimens small cracks occurred in the concrete floor face. The cracks first appeared on the surface of the concrete floor on both sides of the secondary beams close to the column and developed parallel to the secondary beams. When the main cracks above the sides of the flange had a width of about 6 mm the reinforcement mesh failed, starting from the edge of the floor towards the column. Failure of the reinforcement mesh was followed by failure of the main bars. For the multiplanar loaded specimens the surface cracks commence adjacent to the corners of the column.

For specimen 4R3 no failure of the reinforcement bars occurred, probably due to the indentation of the column wall (no concrete infill of the column) at the bottom flange, so that the beam rotates close to the floor. Also for multiplanar loaded specimens the crack pattern in the concrete floor is more scattered than the crack pattern for the uniplanar loaded specimens.

The test was stopped when a beam rotation of 0.16 rad. was reached.

Towards the end of test of specimen 4R4 the main cracks develop parallel to the secondary above the sides of the flange. Also here the reinforcement mesh failed from the edges of the floor towards the column followed by failure of the main bars (see photos 7-34 to 7-37).

7.2 Definition of the maximum load

At this moment, several ultimate deformation limits are available for hollow section joints.

In some codes, in plastic design, a beam is considered to fail if the deflection at the midspan exceeds $l_1/50$ [31]. If it would be used as a deformation limit, a rotation of $\phi = 0.04$ rad. is then obtained at the ends of the simply supported beams. From the moment - rotation curves obtained, it can be seen that the strength of the connections between I-beams and RHS columns is still increasing after this rotation, the strength of the connection at this deformation limit gives a conservative estimate of the actual strength of the connection.

According to Yura [32], the ultimate moment for tubular joint in CHS is considered to be obtained if the rotation of the connection reaches four times the rotation when first yielding occurs. It can be shown that this is equal to $80 \cdot f_{y,0}/E$. This deformation limit gives very large rotations for these connections. These deformation limits give different local column wall deflection for various η ratios.

Korol and Mirza [26] propose a local deflection of the chord face $\Delta = 1.2t_0$ as a deformation limit for axially loaded T-joints in RHS. This deformation limit has been used also by Lu for plate to RHS column connections [33], which shows that it could be a suitable deformation limit for axially loaded connections. Applied to I-beam to RHS column connections with different chord thickness t_0 , and assuming that the local deformations in the tension and compression zone are the same, the rotation deformation limit will be $\phi = 2 \cdot 1.2t_0/h_1 = 1.2/\eta$.

Another criterion considered by Lu [34] is based on the initiation of punching shear cracks at the flange tips found in experiments. For these experiments it has been observed that for the connections, cracking occurs when the local deformation Δ at the intersection of the I-beam flange and the RHS wall reaches about 12 mm, which is about $0.04b_0$ (or $1.2t_0$, which agrees with the proposal of Korol and Mirza). It has to be mentioned that after crack initiation occurs, the static strength of the connections does not decrease because of the membrane action. If failure is considered to occur when the local deformation at the RHS column wall reaches $\Delta = 0.04b_0$, and supposing that the local deformation in the tension and compression zones are the same, a deformation limit of $\phi = 0.08b_0/h_1 = 0.08/\eta$ is obtained.

It may be concluded that a general criterion based on a fixed rotation leads to considerable local different deformations of the chord face and is therefore not appropriate, i.e. the Yura deformation limit and a fixed limit of $\phi = 0.04$ rad.

Adopting a fixed local deformation of the chord face as basis seems an acceptable choice. The deformation limit has to be further discussed. In this report, for indication only, the deformation and rotation limit of Korol is used.

7.3 Comparison of numerical and experimental results

This work is carried out at Delft University of Technology and RWTH Aachen. The main results from Delft University are presented in Figures 7-20 to 7-34 and from RWTH Aachen in Figures 7-43 to 7-53.

As no maximum peak loading is obtained in the numerical calculations, and as the definition of the deformation limit as a failure criterion is not yet established for these connections, various deformation limit criteria for static loading have been investigated. The most appropriate criterion for the present work for axially loaded connections seems that given by Korol and Mirza [26], where a value of $1.2t_0$ is used as the failure criterion for the connections loaded by axial forces. For $t_0 = 10$ mm, the deformation limit is then 12 mm. If it is also used for the connections loaded by bending, then the rotation limit at the intersection at this moment can be determined by $2 * 1.2 * t_0 / h_1$. With $t_0 = 10$ mm and $h_1 = 240$ mm, a rotation of 0.1 rad. is obtained as the deformation limit of the connection.

In general, for series 1 there is good agreement between the experimental and numerical results (see Figures 7-20 to 7-27). The deformed shapes of the test specimens and the finite element models agree well. For all the numerical results the initial stiffness agrees well with those found in the experimental tests. The slope of the strain hardening modulus for the connections is slightly overestimated, so that the resistance of the connections calculated numerically are always greater than those found in the experimental results. The differences between the results of the numerical models and the experimental tests are quantified in Table 7-1. The mean difference is smaller than 10% for all connections except for 1R4, where the largest difference between the experimental and numerical results is found. The numerical result is 18% higher than the experimental results, due to the local buckling of the plate as described in 7.1, see Table 7-1. Examples of typical deformed finite element meshes of series 1 are shown in Figures 7-35 to 7-37.

There is also good agreement for the test specimens of series 2 with plates in two levels. The deformed shapes of the test specimens and the finite element models agree well. The differences between the results of the numerical models and the experimental tests are quantified in Table 7-1. The load-displacement curves are shown in Figures 7-

28 to 7-30. An example of a typical finite element mesh of series 2 is shown in Figure 7-38. The ultimate loads in the experiments of these two specimens are 5% lower than found in the numerical work, in the same way as for series 1, due to sensitivity to stability.

There is good agreement between the experimental and numerical results for series 3 (see Figures 7-31 to 7-34). Also, the deformed shapes of the test specimens and the finite element models agree well. The variations between the results of the numerical models and the experimental tests is 3 - 5% as shown in Table 7-2. Examples of the typical finite element mesh of series 3 with or without a steel plate are shown in Figures 7-39 and 7-40.

7.4 Discussion of results

In general, the experimental values are discussed. Numerical values are given within brackets.

7.4.1 Plate to RHS connections

There is a considerable multiplanar effect observed on the strength of the connections. For the load ratio $N_2/N_1 = -1$ and $\beta = 0.4$, the strength at a deformation limit of $1.2t_0$ is 29% (30%) lower than that of the uniplanar load case $N_2/N_1 = 0$. For the load ratio $N_2/N_1 = +1$ and $\beta = 0.4$, the strength at the deformation limit of $1.2t_0$ is only 4.4% (7.6%) higher than that of the uniplanar load case $N_2/N_1 = 0$. With increasing β this effect becomes somewhat stronger. For $\beta = 0.57$ these values are -35% (33%) for load ratio $N_2/N_1 = -1$ and +2% (8.5%) for a load ratio $N_2/N_1 = +1$. Figure 7-41 gives the numerically determined load - deflection curves for specimens with $\beta = 0.4$ and three load ratios ($N_2/N_1 = -1, 0, +1$). The comparison for $\beta = 0.6$ is similar. For the load case $N_2/N_1 = -1$, the restraint of the RHS walls on the adjacent faces is reduced, while for $N_2/N_1 = +1$, initially, the restraint is reinforced, so that the initial stiffness and the strength of the connections are increased.

7.4.2 Interaction effects

Test series 2, with two levels of plates (flanges), which represents the interaction tests, are compared with test series 1 with only one level of plates. In the experimental tests of series 2 both β and η are varied at the same time. However, the β influence is determined in series 1, so that it is possible to isolate the influence of η . If the distance between the "flanges" in series 2 is infinitely, it can be expected that the strength for series 2 is two times that for a corresponding specimen in series 1.

However, for smaller η values, the strength of the connections is lower than 2 times that for a corresponding specimen in series 1. In the case where $\eta = 0.8$ and $\beta = 0.4$ (2R1) the strength at a deformation limit of $1.2t_0$ is 1.61 (1.60) times the ultimate load of the corresponding test of series 1 (1R1) as can be calculated from the values in Table 7-1. For $\eta = 1.2$ and $\beta = 0.57$ (2R3), the strength at a deformation limit of $1.2t_0$ is 1.87 (1.92) times that of the corresponding tests of series 1 (1R3).

7.4.3 Beam to column connections

For the connections of series 3, subjected to in-plane bending, with a multiplanar moment loading ratio $F_2/F_1 = -1$, a decrease of 34% (32%) has been observed, in comparison to the uniplanar load case $F_2/F_1 = 0$. For the load case $F_2/F_1 = +1$ a small decrease of 5% (3%) has been found, in comparison with the uniplanar load case $F_2/F_1 = 0$. There is also a multiplanar loading effect on the stiffness of the connections. A reduction of the stiffness has been found for the load case $F_2/F_1 = -1$ and an increase of the stiffness has been found for the load case $F_2/F_1 = +1$, with respect to the uniplanar load case $F_2/F_1 = 0$. See Figure 7-42 for illustration. Some yield line models have been derived by Lu et al [27] for three different load cases. For the load case $F_2/F_1 = -1$, yield lines do not occur adjacent to the corners of the RHS columns, so that the stiffness and the strength of the connection is significantly decreased. For the case of $F_2/F_1 = +1$, the same chord face yield model may be used as for the connection with $F_2/F_1 = 0$. However, for the case $F_2/F_1 = +1$, the restraint is reinforced, so that the initial stiffness and the strength of the connections are increased.

7.4.4 Effect of concrete infill in the RHS column

For the axially loaded test specimen with a compression load, the stiffness of the connection becomes almost infinite. The failure of the connection is caused by buckling of the plates, and there is no crushing of the concrete infill observed. The axially loaded test specimens with a tension load failed by punching shear in the RHS column wall. After plastification of the RHS wall, cracks at both sides of both plates or beam flanges start to grow in a direction parallel to the column axis, see photo's 7-3, 7-4 and 7-18, 7-19. This failure mode with cracks cannot yet be modelled with the finite element program at present.

7.4.5 Effect of a steel floor

In comparison with the test specimen without a steel floor the provision of a steel floor increases the strength at a deformation limit of $1.2t_0$ by 56% (56%). Although it appears that in this case the increase in strength is much more than for CHS columns, the strength here is more dictated by the deformation criterion.

7.4.6 Comparison with existing strength formulae

Comparisons with existing strength formulae have been done only for the connections without composite columns.

7.4.6.1 Plate to RHS column connections

Numerically determined maximum loads of the connections $N_{u,num}$ at the chosen deformation limit of $1.2t_0 = 12$ mm have also been compared with the design values according to the CIDECT formulae for effective width failure, which governs for the plate to RHS column connection for $\beta \leq 0.85$ [29]. The CIDECT effective width formula is given below :

$$N_1^* = f_{y1} t_1 b_e$$

$$b_e = \frac{10}{b_0/t_0} \cdot \frac{f_{y0} t_0}{f_{y1} t_1} \cdot b_1 \quad \text{but } \leq b_1$$

In table 7-3, the formula is compared with the experimental and numerical results. It can be seen that for connections with either one level or two levels of plates, the ratio of $N_{cidect} / N_{u,exp}$ ($N_{u,num}$) varies between 0.88 and 1.11.

The CIDECT formula for effective width for axially loaded uniplanar connections (1R1 and 1R3), give results of the design formula which are about 12% lower than the experimental results. Considering the partial safety factor, the scatter in the test results and the used actual yield stresses, the CIDECT design formula gives reasonable results for the one level plate connections for the chosen deformation limit of $1.2t_0$.

The formulae for connections with one level of plates cannot be used for the connections with two level of plates, by simply using twice the value of these formulae, because for smaller η ratios unsave results may be obtained. As discussed in section 7.3.2 a considerable interaction effect is found for $\eta = 0.8$. For indication only, in Table 7-3 the design values for 2R1 and 2R3 are taken twice the values of the connections with plates in one layer.

Further, it is obvious that the formula should be modified for multiplanar loading (1R5 to 1R8).

7.4.6.2 I-beam to RHS column connections

The connection moment resistance for I-beam to RHS column connections can be obtained by multiplying the plate axial force resistance by the beam depth ($h_1 - t_1$), because the plates can be used to represent the flanges of I-beams [29]. Several possible failure modes are considered for axially loaded plate to RHS connections, namely, punching shear, chord side wall failure, effective width failure and chord face yielding failure [28]. For the present work, due to the presence of the steel plate for 3R2

and the different loading cases for 3R1, 3R3 and 3R4, it becomes necessary to make different chord face yield models to investigate whether the steel plate or the loads on the out-of-plane I-beams have an influence on the connection failure. With this aim, three different chord face yield line models have been developed for 3R1, 3R2 and 3R3 [27].

In table 7-4, the values obtained from these design formulae, with inclusion of the welds between the flanges of I-beams and RHS columns, are given.

The design resistance moments obtained from formulae for various failure modes are also given in table 7-4. The formulae for punching shear and chord side wall failure give higher design resistances than those according to the effective width criterion [24], so that it can be concluded that the design resistance formulae for RHS column face yielding and effective width are the governing criteria. However, they are conservative in strength compared to the experiments. On the other hand, the actual strength of the connection cannot be used, since the rotation will be too large. The limitation for rotation as failure criterion needs further study and evaluation.

7.4.6.3 Bolted connections with a composite steel concrete floor

All test specimens failed as expected, namely by (progressive) failure of the reinforcement bars. Before failure of the main reinforcement bars, some of the reinforcement bars of the mesh failed, due to the smaller ultimate elongation. The concrete infill gives a considerable increase (50-67%) in connection strength, as shown in Table 8-8. The indentation of the RHS column face at the bottom flange in compression for the connections without a concrete filled column is relative large. Due to this indentation the local curvature in the concrete slab is much larger than for the connections with the concrete filled columns. This causes also extra bending in the reinforcement bars and therefore the reinforcement bars fail at a lower load.

The multiplanar loading decreases the connection strength with 14-28%. The bending of the concrete slab in two directions causes an earlier failure of reinforcement bars.

Since the connections failed by failure of the reinforcement bars, the theoretical strength can be determined easily. As described in section 4.2.2, for design only the main reinforcement, namely the 8Φ8 reinforcing bars, were taken into account. Thus, the connection strength can be calculated by multiplying the force in the reinforcement bars by the distance between the bolted connection at the bottom flange and the reinforcement ($h = 335$ mm).

If the nominal yield stress, $f_y = 500$ N/mm² is used, and only 8Φ8 is taken into account:

$$M_u = 67 \text{ kNm (design strength)}$$

If the actual ultimate stresses, $f_u = 645 \text{ N/mm}^2$ for $8\Phi 8$ and $f_u = 627 \text{ N/mm}^2$ for $16\Phi 6$ is taken into account:

$M_u = 182 \text{ kNm}$ (theoretical ultimate strength)

For the tests the lowest ultimate strength is found for test 4R3, the multiplanar loaded connection without a concrete filled column. The ultimate strength found in the test, 85.7 kNm is 1.28 times the design strength. The highest strength is found for test 4R2, uniplanar loaded and with a concrete filled column. The ultimate strength found in the test, 167.3 kNm is about 8% lower than the theoretical ultimate strength, as calculated above.

8 CONCLUSIONS AND PRELIMINARY RECOMMENDATIONS

The main results and conclusions have been summarized in Tables 8-1 to 8-8.

8.1 General connection behaviour

The results show that no maximum peak is reached for all the tested connections with an RHS column, except those with a composite column. All tested connections with a CHS column show a peak load.

To determine the strength of connections without a peak load, further studies are needed to derive a ultimate deformation criterion. None of the currently available deformation criteria can generally be applied.

Based on this research project calibrated finite element models will be used for parametric studies in Delft. In Aachen a numerical approach will be developed to derive load deformation characteristics for design purpose. These works will be published at the end of 1994.

As I-sections or plates are welded on CHS or RHS columns, the behaviour of the connections is really ductile, if the weld are designed to be stronger than the plates.

8.2 Finite element modelling of plate or I-beam to CHS or RHS column connections

To get a good agreement between experimental tests and numerical simulations eight noded thin or thick elements should be used. It is found that thick shell elements give, in general, a small overestimation of the static strength, thin shell elements give a small underestimation of the static strength. In the finite element calculations options which allow for large displacements, were used.

However, at theoretical point of view, thick shell elements with at least 7 layers and a reduced integration scheme provide the best simulation of the plastic behaviour of connections with tubular members. Results obtained with thin shell elements will be less accurate, but computer time can be saved.

The deformation shapes of the test specimens can be successfully simulated.

In this research, the modelling of the welds has influence on both the strength and initial stiffness of the connections. The actual weld sizes will be in most cases larger than the nominal dimensions. Therefore it is important to use actual measured weld sizes in the finite element models for calibration. Also, the actual measured thicknesses of the members should be used. Differences in wall thickness of the CHS column in the circumference may give asymmetric failure modes, if the load is applied using load control.

For calibration, actual measured mechanical properties should be used, because the actual measured yield stress and ultimate stress can be much higher than the nominal values. Also, workhardening effects are included in the numerical models.

The influence of the concrete infill can be simulated by the use of a rigid surface. This modelling method is fast, without a large increase of the size of the finite element model. The penalty is an increase of computer time with factor 3. However, if the concrete infill is modelled with solid elements, the computer time would increase even more.

The tension loaded test specimens with a composite column failed by punching shear. Currently, this failure mode could not be included in the finite element model.

8.3 Welded Connections with a CHS column

Based on the results of the FE analyses and the comparison with the experimental results and the design formulae, some conclusions are obtained. The summary of the conclusions are given in Table 8-1 to 8-3.

8.3.1 Plate to CHS column connections under axial loading

For connections with $N_2/N_1 = +1$, the stiffness and static strength is increased compared to connections with $N_2/N_1 = 0$ (see Table 8-1).

For connections with $N_2/N_1 = -1$, the stiffness and static strength is decreased compared to connections with $N_2/N_1 = 0$.

The relation between the load ratio and the connection strength is almost linear for the tested specimens (see Table 8-1).

An increase of β results in an increase of the stiffness and static strength of the connections.

The stiffness and static strength of the connections is considerably increased by the concrete filling in the CHS columns.

The strength of the connections with composite CHS columns, loaded by compression on the plates, are determined by the plate strength instead of the connection itself.

The connections with composite CHS columns, loaded by tension on the plates, fail by punching shear.

The existing formulae for uniplanar connections between plates and CHS columns under axial loading give reasonable agreement with the experimentally and numerically obtained results. However, if the present design formulae for uniplanar connections are used to determine the ultimate strengths for the multiplanar connections, the results may be not always conservative, when the appropriate safety factors are applied.

Since a limited amount of connections was investigated, no general conclusion can be drawn. Further parametric studies are needed to complete this work. The in the framework of this research project calibrated finite element models can be used for this parametric studies.

8.3.2 Interaction effects

The tendencies found in the experiments and the numerical work are in agreement with the existing design formulae for uniplanar joints, although the design formulae seem to be conservative for the interaction effects (see Table 8-2). Since only two experimental tests were done, no final conclusions can be drawn. Further (numerical) parameter investigations are necessary to develop design equations. The calibrated models as developed in the framework of this research can form the basis for these parameter investigations.

8.3.3 I-Beam to CHS column connections under in-plane bending

The existing formulae for uniplanar connections between I-beams and CHS columns under axial loading give much lower values (>30%) than the experimental results of the multiplanar test specimen with unloaded out-of-plane beams.

Considerable multiplanar loading effects are observed for the test specimen with the load ratio $F_2/F_1 = -1$. This moment ratio is chosen to provide a lower bound extreme for the strength. Of course, this load situation will only rarely occur in practice situations. The strength of the connections with moment ratios $F_2/F_1 = 0$. and $F_2/F_1 = +1$. is almost the same, although the initial stiffness of the connection with $F_2/F_1 = +1$. is higher (see Table 8-3).

All experimental tests show a obvious peak load. At large deformations the load increases further, due to membrane action effects.

An additional steel floor, welded to the top flanges of the I-beams, gives a small increase in ultimate strength and an obvious increase in initial stiffness.

Since only a few experimental tests have been carried out, no general conclusions can be made yet. The calibrated models can be used for further parametric investigation.

8.4 Welded Connections with a RHS column

Based on the results of the FE analyses and the comparison with the experimental results and the design formulae, some conclusions are obtained. The summary of the conclusions are given in Table 8-4 to 8-6.

8.4.1 Plate to RHS column connections under axial loading

For connections with $N_2/N_1 = +1$, the stiffness and static strength is increased compared to connections with $N_2/N_1 = 0$ (see Table 8-4).

For connections with $N_2/N_1 = -1$, the stiffness and static strength is decreased compared to connections with $N_2/N_1 = 0$.

An increase of β results in an increase of the stiffness and static strength of the connections.

The stiffness and static strength of the connections is considerably increased by the concrete filling in the RHS columns.

The strength of the connections with composite RHS columns, loaded by compression on the plates, are determined by the plate strength instead of the connection itself.

The strength of the connections with composite RHS columns, loaded by tension on the plates failed by punching shear at the RHS column face.

8.4.2 Interaction effects

The strength of the connections with $h_1/b_0 = 0.8$ and 1.21 of I-beam flanges (with two levels of plates) is about 1.61 (1.60) to 1.87 (1.92) times the strength of the connections with one level of plates, see Table 7-3 and 8-5.

Since only two experimental tests were done, no final conclusions can be drawn. Further (numerical) parameter investigations are necessary to develop design equations. The calibrated models as developed in the framework of this research can form the basis for these parameter investigations.

8.4.3 I-beam to RHS column connections under In-plane bending

The stiffness and the strength of the multiplanar connections, loaded by in-plane bending on the I-beams in one plane, is increased by the structural action of a steel floor.

Considerable multiplanar loading effects are observed for the test specimen with the load ratio $F_2/F_1 = -1$, which results in a decrease of the stiffness and the strength of the connection compared to $F_2/F_1 = 0$. However, this moment ratio is chosen to provide a lower bound extreme for the strength. Of course, this load situation will only rarely occur in practice situations.

The strength of the connections with moment ratios $F_2/F_1 = 0$ and $F_2/F_1 = +1$ is almost the same, although the initial stiffness of the connection with $F_2/F_1 = +1$ is higher.

The limitation for rotation under serviceability needs further study and evaluation.

8.5 Bolted connections with a composite floor

8.5.1 Connection behaviour

The main failure mode that is observed is progressive failure of the reinforcement bars.

For all connections with a CHS column a strength is found larger than 1.75 times the design strength. The multiplanar loading $F_2/F_1 = +1$ causes a reduction in strength of 30%, in comparison with the uniplanar loaded connections. The concrete infill causes a small increase in connection strength.

For all connections with a RHS column a strength is found larger than 1.28 times the design strength. The multiplanar loading $F_2/F_1 = +1$ causes a reduction in strength of 14-28%, in comparison with the uniplanar loaded connections. The concrete infill causes a considerable increase in connection strength.

The connections with the CHS column, by a ring, connecting the bottom flanges, and the RHS connections with a concrete filled column show a relatively rigid behaviour, with a limited rotation capacity, due to the low ultimate elongation of the concrete reinforcement.

The concrete filled columns are almost incompressible in radial direction. Therefore, the

deformations in the concrete floor (in tension) are relative large.

For the test specimens cold formed Φ 6 reinforcement bars were used. To improve rotation capacity the use of hot formed reinforcement bars is highly recommended.

8.5.2 Design aspects

EUROCODE 4 does not allow currently semi-rigid behaviour into account, but the design is based on pin-ended connections. The experimental tests show that the strength of semi-rigid connections can be used, if the maximum elongation of the reinforcement bars is sufficient.

The connection strength can easily be determined:

The shear force is transferred to the bolted connections between the web plates and the web of the I-beams. The bending moment is transferred at the bottom to the bolted connection between the bottom flanges and the ring or angles and at the top through the shear connectors to the reinforcement bars. Therefore, all these structural parts have to be designed separately.

The strength of the bolted connections at the bottom flanges should be stronger than the reinforcement bars, to prevent a brittle failure mode of the connection.

The shear studs providing the connection between the I-beams and the concrete deck were not subject of examination for this research, and therefore designed in such way that they never would be critical during testing. In practice, the amount of shear studs could be optimized.

If the bolted connection at the bottom flange is including the connection with the column, is designed in such way that the reinforcement will be critical, the design is easy. However, hot rolled concrete reinforcement bars should be used to provide sufficient deformation capacity.

The main results and conclusions have been summarized in Tables 8-1 to 8-8.

9 ACKNOWLEDGEMENTS

The research team wishes to extend their appreciation to:

"Van Leeuwen Buizen" - Zwijndrecht, for donation of the hollow sections used in this programme;

Meerhof - boutlas techniek b.v. - Gorssel, for donation and welding of the shear studs;

Profiel 2000 - Tiel, for donation of the deep steel decks (PMF CF46);

Rijkswaterstaat, for their financial support;

Grootint b.v. - Zwijndrecht, for their financial support;

Stichting Nationale Computer Faciliteiten (NCF)- for making available computer time for this project; and

IBM Nederland NV - for making available an RS/6000 model 350 workstation in the framework of a study contract.

10 REFERENCES

- [1] Stichting Technische Wetenschappen (Dutch Technology Foundation) Research Programme DCT99.1904 "Semi-stijve balk-kolom verbindingen (Semi-rigid beam to column connections)", 1990-1994.
- [2] Beek Project "Constructieve vaardigheden bij het detailleren van staal-beton verbindingen voor civiele constructies en gebouwen". Research programme sponsored by Commission Beek, Delft University of Technology.
- [3] Forschungsantrag an die Deutsche Forschung Gemeinschaft (DFG). "Raumliche vervormbare Verbindungen", Prof.Dr.-Ing. G. Sedlacek, RWTH Aachen, Aachen 1991 (in German).
- [4] The review of literature on beam to CHS/RHS column connections will be published in the framework of two Ph.D projects [1] and [2] at the end of 1994.
- [5] Eurocode 4, ENV 1994-1-1: 1992 "Design of composite steel and concrete structures - Part 1-1: General rules and rules for buildings". European Committee for Standardization (CEN).
- [6] Eurocode 4, CEN/TC 250/SC 4 N 39 prENV 1994-1-2 "Design of composite steel and concrete structures - Part 1.2: Structural fire design". Second draft 1992.
- [7] ECCS - Technical Committee 3 - Fire Safety of Steel Structures, Technical Note "Calculation of the fire resistance of centrally loaded composite steel-concrete columns exposed to the standard fire", First Edition, 1988.
- [8] British Steel Technical, Corby Technical Centre "Fire tests on cleat connections to concrete filled RHS columns (first and second phase tests). B.S. Project No. 800/0226/1, CIDECT Report No. 15H-90/15-E, Final Report, August 1990.
- [9] Eurocode 2, ENV 1992-1:1991 "Design of concrete structures - Part 1: General rules and rules for buildings". European Committee for Standardization (CEN).
- [10] Structural Welding Code - Steel, American National Standard ANSI/AWS D1.1-90, American Welding Society, 1990.
- [11] prEN 10080:1991 (Draft) "Steel for the reinforcement of concrete weldable ribbed reinforcing steel B500 - Technical delivery conditions for bars, coils and welded fabric, European Committee for Standardization (CEN).

- [12] Staal-beton liggers - Praktijkvoorbeelden voor ontwerp en berekening (Composite steel and concrete beams - examples of design and calculation in practice), CUR-Committee C 61/CS-Working Group 3, Jointly published by Staalbouwkundig Genootschap, Rotterdam, Centrum Staal Rotterdam and Civiel Technisch Centrum Uitvoering Research en Regelgeving, Gouda, ISBN 9037600263, 119 pages.
- [13] Weynand, K. (1992), SERICON Datenbank-system on semi-rigid joints, ECCS TC 10; Institute of steel construction, RWTH Aachen, Version 1.1.
- [14] MARC Manual (1990), volume A, revision K4.2, Marc Analysis Research Corporation
- [15] MARC Manual (199-), volume A, revision K5, Marc Analysis Research Corporation
- [16] Vegte G.J. van der, Koning C.H.M. de, Puthli R.S., Wardenier J. (1991), "The Static Strength and Stiffness of Multiplanar Tubular Steel X-Joints." Internat. Journal Offshore and Polar Eng., ISOPE, Vol. 1, No. 1, pp. 42-52.
- [17] Eurocode No. 3 (1989), "Design of Steel Structures, Part 1: General rules and rules for buildings, Chapter 3: Design against brittle fracture, background documentation
- [18] SDRC (1990), "I-Deas Finite Element Modelling User's Guide", Structural Dynamics Research Corporation, Ohio, USA.
- [19] ABAQUS, "User's Manual", Version 4.9, Karlsson & Sörensen Inc.
- [20] Profil-FEM-3D (1991), "Elektronischer Simulator für Versuche mit Bauteilen aus Stahl", Lehrstuhl für Stahlbau, RWTH Aachen, Version 1.0, Aachen, Germany.
- [21] Eurocode 3, Design of Steel Structures, (1992) Part 1: General Rules and Rules for Buildings.
- [22] Wardenier, J., Kurobane, Y., Packer, J.A., Dutta, D. Yeomans, N. (1991), "Design Guide for Circular Hollow Section (CHS) joints under predominantly static loading", CIDECT, Köln, Germany.
- [23] Kurobane, Y. (1981), "New Developments and practices in tubular joint design", IIW Doc XV-488-81 and XIII-1004-81, IIW, Kumamoto, Japan.

- [24] Wardenier, J. (1982), "Hollow Section Joints", Delft University Press, Delft.
- [25] AIJ (1990), "Recommendations for the design and fabrication of tubular structures in steel", Architectural Institute of Japan, Japan (in Japanese).
- [26] Korol, R.M., Mirza, F.A. (1982), "Finite Element Analysis of RHS T-Joints", ASCE, pp2081-2098.
- [27] Lu, L.H., Puthli, R.S, Wardenier, J. (1992), "The Static Strength of Multiplanar Connections between I-beams and Rectangular Hollow Section Columns", Stevin Report 6.93.17/A1/11.10, Delft.
- [28] Lu, L.H., Puthli, R.S, Wardenier, J. (1992), "The Influence of Reinforced Concrete Infill in RHS Columns on The Static Strength of Plate to Rectangular Hollow Section Columns", Stevin Report 6.93.39/11.10, Delft.
- [29] Packer, J.A., Wardenier, J., Kurobane, Y., Dutta, D., Yeomans, N. (1992) "Design Guide for Rectangular Hollow Section (RHS) Joints under Predominantly Static Loading", Published by Verlag TÜV Rheinland GmbH, Köln.
- [30] G. Sedlacek; R. Spangemacher; W. Dahl; R. Hubo; P. Langenberg Untersuchung der Auswirkung unterschiedlicher Streckgrenzenverhältnisse auf das Rotationsverhalten von I-Trägern; Projekt 169, Studiengesellschaft Stahlanwendung e.V.
- [31] NEN 6772, Staalconstructies TGB 1990.
- [32] Yura JA, Zettlemyer N, Edwards IF (1980). "Ultimate Capacity Equations for Tubular Joints," OTC Proceedings, Vol 1, No 3690.
- [33] Lu, LH, Puthli, RS, Wardenier, J (1993b). "Semi-Rigid Connections between Plates and Rectangular Hollow Section Columns," Tubular Structures V, E & FN SPON.
- [34] Lu, L.H., Wardenier, J. (1994), "Ultimate Deformation Criteria for Uniplanar Connections between I-Beams and RHS Columns under In-plane Bending", Proc. ISOPE 1994 Conference, Osaka, Japan.

TABLES

Table 2-1 : Overview of the test specimens with CHS columns

<p>1C1</p> <p>$\beta = 0.37$</p>	<p>1C2</p> <p>$\beta = 0.37$</p>	<p>1C3</p> <p>$\beta = 0.52$</p>	<p>1C4</p> <p>$\beta = 0.52$</p>
<p>1C5</p> <p>$N_2/N_1 = -1$ $\beta = 0.37$</p>	<p>1C6</p> <p>$N_2/N_1 = +1$ $\beta = 0.37$</p>	<p>1C7</p> <p>$N_2/N_1 = -1$ $\beta = 0.52$</p>	<p>1C8</p> <p>$N_2/N_1 = +1$ $\beta = 0.52$</p>
<p>2C1</p> <p>$\beta = 0.37$</p>	<p>2C2</p> <p>$\beta = 0.37$</p>	<p>2C3</p> <p>$\beta = 0.52$</p>	
<p>3C1</p> <p>$\beta = 0.37$</p>	<p>3C2</p> <p>$\beta = 0.37$</p>	<p>3C3</p> <p>$F_2/F_1 = -1$ $\beta = 0.37$</p>	<p>3C4</p> <p>$F_2/F_1 = +1$ $\beta = 0.37$</p>
<p>4C1</p> <p>$\beta = 0.37$</p>	<p>4C2</p> <p>$\beta = 0.37$</p>	<p>4C3</p> <p>$F_2/F_1 = +1$ $\beta = 0.37$</p>	<p>4C4</p> <p>$F_2/F_1 = +1$ $\beta = 0.37$</p>

Table 2-2: Overview of the test specimens with RHS columns

<p>1R1</p> <p>$\beta = 0.4$</p>	<p>1R2</p> <p>$\beta = 0.4$</p>	<p>1R3</p> <p>$\beta = 0.57$</p>	<p>1R4</p> <p>$\beta = 0.57$</p>
<p>1R5</p> <p>$N_2/N_1 = -1$ $\beta = 0.4$</p>	<p>1R6</p> <p>$N_2/N_1 = +1$ $\beta = 0.4$</p>	<p>1R7</p> <p>$N_2/N_1 = -1$ $\beta = 0.57$</p>	<p>1R8</p> <p>$N_2/N_1 = +1$ $\beta = 0.57$</p>
<p>2R1</p> <p>$\beta = 0.4$</p>	<p>2R2</p> <p>$\beta = 0.4$</p>	<p>2R3</p> <p>$\beta = 0.57$</p>	
<p>3R1</p> <p>$\beta = 0.4$</p>	<p>3R2</p> <p>$\beta = 0.4$</p>	<p>3R3</p> <p>$F_2/F_1 = -1$ $\beta = 0.4$</p>	<p>3R4</p> <p>$F_2/F_1 = +1$ $\beta = 0.4$</p>
<p>4R1</p> <p>$\beta = 0.4$</p>	<p>4R2</p> <p>$\beta = 0.4$</p>	<p>4R3</p> <p>$F_2/F_1 = +1$ $\beta = 0.4$</p>	<p>4R4</p> <p>$F_2/F_1 = +1$ $\beta = 0.4$</p>

Section mm	Stock no	Coupon no	From:	f_y N/mm ²	$f_{y\text{ aver.}}$ N/mm ²	f_u N/mm ²	$f_{u\text{ aver.}}$ N/mm ²	ϵ %	$\epsilon_{\text{ aver.}}$ %
CHS 323.9*9.5	1	1	Circumference	387	392	510	512	26	27
		2		397		513		28	
	2	1	Circumference	386	387	513	510	31	30
2	2	387		507		28			
RHS 300*300*10	1	1	Flat side At the corner	431	434	562	560	30	30
		2		437		558		29	
	2	1	Flat side At the corner	447	453	572	575	30	30
		2		458		578		30	
3	1	Flat side At the corner	433	439	564	565	32	32	
	2		444		566		31		
4	1	Flat side At the corner	438	438	557	559	29	30	
	2		437		561		31		
IPE-240	1	1	Flange	417	421	514	516	32	33
		2	Flange	425		517		33	
		3	Web	487		-		565	
	2	1	Flange	429	433	525	526	32	33
		2	Flange	436		526		33	
		3	Web	502		-		573	
	3	1	Flange	419	420	521	520	30	32
		2	Flange	420		518		33	
		3	Web	480		-		633	
	4	1	Flange	417	421	514	515	33	33
		2	Flange	424		515		32	
		3	Web	470		-		541	
	5	1	Flange	417	419	519	519	31	32
		2	Flange	420		519		32	
		3	Web	473		-		553	
	6	1	Flange	440	440	527	525	31	31
		2	Flange	440		523		30	
		3	Web	518		-		564	
	7	1	Flange	436	436	526	528	32	32
		2	Flange	435		529		31	
		3	Web	483		-		556	
	8	1	Flange	440	431	527	523	30	31
		2	Flange	422		518		32	
		3	Web	490		-		550	
	9	1	Flange	449	432	534	530	30	31
		2	Flange	414		526		31	
		3	Web	503		-		558	
IPE-360	1	1	Flange	401	399	499	497	31	32
		2	Flange	396		494		33	
		3	Web	442		-		532	
	2	1	Flange	404	404	497	496	33	34
		2	Flange	404		495		34	
		3	Web	442		-		540	

Mechanical properties determined with tensile coupon tests.

Table 4-1a : Mechanical properties

Section mm	Stock no	Coupon no	From:	f_y N/mm ²	$f_{y\text{ aver.}}$ N/mm ²	f_u N/mm ²	$f_{u\text{ aver.}}$ N/mm ²	ϵ %	$\epsilon_{\text{ aver.}}$ %
Plate: 10*120	1	1	Longitudinal direction	396	-	521	-	29	-
	2	1		389	-	514	-	31	-
	3	1		398	-	529	-	29	-
	4	1		388	-	509	-	30	-
Plate: 12*170	1	1	Longitudinal direction	392	-	516	-	31	-
Steel floor (5 mm)	1	1	Longitudinal direction	427	-	516	-	29	-
		2	Transverse direction	436	-	531	-	30	-
Ring stiffener)	-	1	-	355	-	510	-	22	-
Angle cleat	-	1	Longitudinal direction	372	377	522	526	29	29
		2		382		530		28	
Web plate)	-	1	-	355	-	510	-	22	-

Mechanical properties determined with tensile coupon tests.
*) Nominal values

Table 4-1b :Mechanical properties

Cube No.	Specimen No.	Age (days)	Control cube strength in climate chamber (N/mm ²)	Hardened cube strength at test site (N/mm ²)	Hardened splitting tensile strength at test site (N/mm ²)	Density (kg/m ³)	Modulus of elasticity (N/mm ²)
1	-	7	37.5	-	-	2354	-
13	-	7	35.9	-	-	2349	-
5	-	14	42.4	-	-	2362	-
17	-	14	42.2	-	-	2361	-
9	-	28	51.0	-	-	2362	-
20	-	28	50.5	-	-	2353	-
2	1C4	24	-	-	-	-	27000
3	and	24	-	49.5	-	2340	-
4	1R4	24	-	-	4.15	2335	-
6	4C4	326	-	-	-	-	28100
7	and	326	-	57.7	-	2318	-
8	4R4	326	-	-	5.12	2315	-
10	2C2	67	-	-	-	-	27200
11	and	67	-	54.7	-	2321	-
12	2R2	67	-	-	3.88	2321	-
14	1C2	54	-	-	-	-	25100
15	and	54	-	56.6	-	2351	-
16	1R2	54	-	-	4.82	2348	-
18	4C2	196	-	60.3	-	2312	-
19	and 4R2	196	-	-	4.00	2315	-

Table 4-2 : Concrete cube properties for composite columns

Cube No.	Age (days)	150*150*150 Cube strength of specimens in 95% R.H. climate chamber		150*150*150 Cube splitting tensile strength of specimens in 95% R.H. climate chamber		Modules of Elasticity of 100*100*400 Prism	
		(N/mm ²)	(N/mm ²) _{aver.}	(N/mm ²)	(N/mm ²) _{aver.}	(N/mm ²)	(N/mm ²) _{aver.}
7210	28	35.88					
7211	28	36.01	35.84				
7212	28	35.62					
7213	28			3.71			
7214	28			3.46	3.49		
7215	28			3.30			
7228	28					36380	
7229	28					34180	36500
7230	28					38940	
7216	41	37.90					
7217	41	38.36	37.64				
7218	41	36.66					
7219	41			3.38			
7220	41			3.48	3.58		
7221	41			3.89			
7222	73	42.11					
7223	73	39.38	40.64				
7224	73	40.42					
7225	73			3.75			
7226	73			3.85	3.79		
7227	73			3.77			

Table 4-3 : Concrete cube properties of batch 1 used for composite floor of specimens 4C1, 4C2, 4R1 and 4R2

Cube No.	Age (days)	150*150*150 Cube strength of specimens in 95% R.H. climate chamber		150*150*150 Cube splitting tensile strength of specimens in 95% R.H. climate chamber		Modules of Elasticity of 100*100*400 Prism	
		(N/mm ²)	(N/mm ²) _{aver.}	(N/mm ²)	(N/mm ²) _{aver.}	(N/mm ²)	(N/mm ²) _{aver.}
7312	28	36.59					
7313	28	33.54	34.59				
7314	28	34.71					
7316	28			3.77			
7317	28			2.90	3.34		
7330	28					35650	
7331	28					37330	36447
7332	28					36360	
7318	67	41.91					
7319	67	39.10	40.18				
7320	67	39.45					
7321	67			3.71			
7322	67			3.96	3.84		
7323	67			3.85			
7324	106	41.59					
7325	106	41.07	40.72				
7326	106	39.51					
7327	106			3.63			
7328	106			3.57	3.60		
7329	106			3.60			

Table 4-4 : Concrete cube properties of batch 2 used for composite floor of specimens 4C3, 4C4, 4R3 and 4R4

Series	Test specimen	Concrete filled column marked X	Concrete floor Marked X	Concrete quality		Concrete curing time (days)		Steel reinf. quality		Material properties (N/mm ²)					
				Column	Floor	Column	Floor	Column) ¹	Floor) ²	Concrete (column)			Concrete (floor)		
										f _c	f _t	E _c	f _c	f _t	E _c
1	1.C.2	X		C35/45		54		B500H		56.5	4.82	25100			
	1.C.4	X		C35/45		24		B500H		49.5	4.15	27000			
	1.R.2	X		C35/45		54		B500H		56.5	4.82	25100			
	1.R.4	X		C35/45		24		B500H		49.5	4.15	27000			
2	2.C.2	X		C35/45		67		B500H		54.7	3.88	27200			
	2.R.2	X		C35/45		67		B500H		54.7	3.88	27200			
4	4.C.1		X		C20/25		41	B500H/N	B500H/N				37.64	3.58	36500
	4.C.2	X	X	C35/45	C20/25	196	51	B500H	B500H/N	60.3	4.00	-	37.64	3.58	36500
	4.C.3		X		C20/25		105		B500H/N				40.72	3.60	36447
	4.C.4	X	X	C35/45	C20/25	326	96	B500H	B500H/N	57.7	5.12	28100	40.18	3.84	36447
	4.R.1		X		C20/25		64		B500H/N				37.64	3.58	36500
	4.R.2	X	X	C35/45	C20/25	196	72	B500H	B500H/N	60.3	4.00	-	40.64	3.79	36500
	4.R.3		X		C20/25		68		B500H/N				40.18	3.84	36447
	4.R.4	X	X	C35/45	C20/25	326	81	B500H	B500H/N	57.7	5.12	28100	40.18	3.84	36447

)¹ Measured for B500H 20 Øbars as f_y = 565 N/mm², f_u = 644 N/mm², ε = 9%

)² Measured for B500N 8 Øbars as f_y = 570 N/mm², f_u = 645 N/mm², ε = 24%

Measured for B500H 6 Øbars as f_y = 615 N/mm², f_u = 627 N/mm², ε = 17%

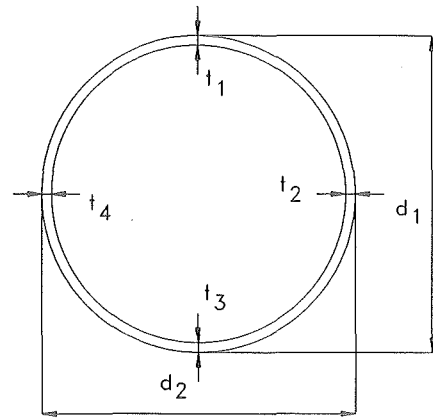
Table 4.5 : Material properties of concrete and steel reinforcement in columns and floors

Series	Test spec.	Configuration	Sizes and Lengths of Plates or Beams	β	2γ	τ	N_2/N_1 or F_2/F_1	Concrete filled column marked X	Type of loading	Comments (unless stated N_1 in compr.)	Stock No.	
											Column	Plates or Beams
1	1C1		10*120*615	0.37	34	1.05	0	X	Axial (simple test)	-	1	1
	1C2		10*120*615	0.37		1.05	0			N1 in tension	1	1
	1C3		12*170*780	0.52		1.26	0			-	1	1
	1C4		12*170*780	0.52		1.26	0			-	1	1
	1C5		10*120*615	0.37		1.05	-1			N_2 in tension	1	2
	1C7		12*170*780	0.52		1.26	-1			N_2 in tension	1	1
	1C6		10*120*615	0.37		1.05	1			N_2 in compr.	1	2
	1C8		12*170*780	0.52		1.26	1			N_2 in compr.	2	1
2	2C1		IPE 240-600	0.37	34	1.03	0	X	Axial (interaction test)	-	2	3
	2C2		IPE 240-600	0.37		1.03	0			N_1 in tension	2	3
	2C3		IPE 360-800	0.52		1.34	0			-	3	1
3	3C1		IPE 240-1200	0.37	34	1.03	0	-	Bending (welded connections)	-	2	1
	3C2		IPE 240-1200	0.37		1.03	0			With steel floor	2	1
	3C3		IPE 240-1200	0.37		1.03	-1			-	2	2
	3C4		IPE 240-1200	0.37		1.03	1			-	2	2
4	4C1		IPE 240-1200	0.37	34	1.03	0	X	Bending (bolted connections)	With concr. floor	3	6
	4C2		IPE 240-1200	0.37		1.03	0			"	3	6
	4C3		IPE 240-1200	0.37		1.03	1			"	3	7
	4C4		IPE 240-1200	0.37		1.03	1			"	3	7

Table 4-6 : Nominal dimensions test series with CHS column \varnothing 323.9*9.5, 1800 long

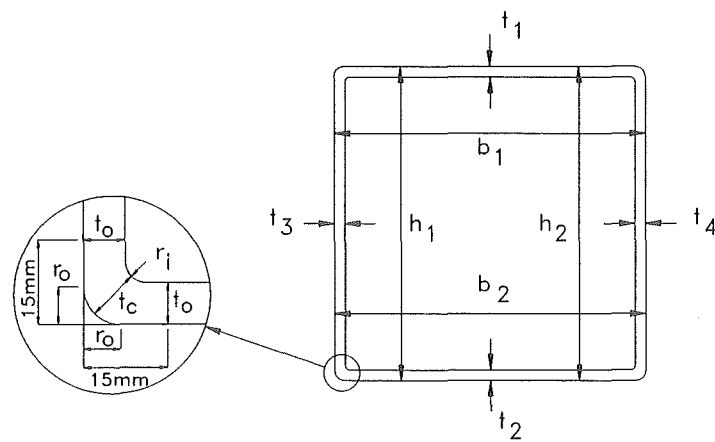
Series	Test spec.	Configuration	Sizes and Lengths of Plates or Beams	β	2γ	τ	N_2/N_1 or F_2/F_1	Concrete filled column marked X	Type of loading	Comments (unless stated N_1 in compr.)	Stock No.	
											Column	Plates or Beams
1	1R1		10*120*615	0.40	30	1.00	0		Axial (simple test)	-	1	3
	1R2		10*120*615	0.40		1.00	0	X		N1 in tension	1	3
	1R3		12*170*780	0.57		1.20	0			-	1	1
	1R4		12*170*780	0.57		1.20	0	X		-	1	1
	1R5		10*120*615	0.40		1.00	-1			N_2 in tension	1	4
	1R7		12*170*780	0.57		1.20	-1			N_2 in tension	1	1
	1R6		10*120*615	0.40		1.00	1			N_2 in compr.	1	4
	1R8		12*170*780	0.57		1.20	1			N_2 in compr.	2	1
2	2R1		IPE 240-600	0.40	30	0.98	0		Axial (interaction test)	-	2	3
	2R2		IPE 240-600	0.40		0.98	0	X		N_1 in tension	2	3
	2R3		IPE 360-800	0.57		1.27	0			-	2	2
3	3R1		IPE 240-1200	0.40	30	0.98	0		Bending (welded connections)	-	3	4
	3R2		IPE 240-1200	0.40		0.98	0			With steel floor	3	4
	3R3		IPE 240-1200	0.40		0.98	-1			-	3	5
	3R4		IPE 240-1200	0.40		0.98	1			-	3	5
4	4R1		IPE 240-1200	0.40	30	0.98	0		Bending (bolted connections)	With concr. floor	3	8
	4R2		IPE 240-1200	0.40		0.98	0	X		"	3	8
	4R3		IPE 240-1200	0.40		0.98	1			"	4	9
	4R4		IPE 240-1200	0.40		0.98	1	X		"	4	9

Table 4-7 : Nominal dimensions for test series with RHS column 300*300*10, 1800 long



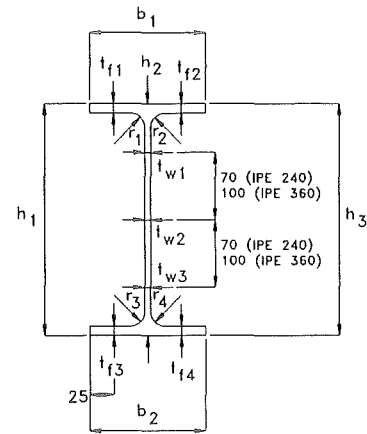
Stock No.	d_{av} (mm)	t_{av} from 16 measurements instead of 4 (mm)	Cross-sectional area (mm ²)
1	324.4	9.48	9521
2	324.3	9.44	9393
3	324.2	9.30	9320

Table 4-8 : Average measurements for each stock number in CHS



Stock No.	Cross-sectional area (mm ²)	b or h (mm)	t_{1-4} (mm)	t_o (mm)	t_c (mm)	r_o (mm)	r_i (mm)
1	11487	299.94	9.82	11.23	12.99	8.06	3.75
2	11380	299.97	9.74	11.13	12.48	9.06	4.00
3	11456	300.01	9.76	10.95	12.47	8.94	5.00
4	11497	299.90	9.88	9.94	12.85	9.03	3.75

Table 4-9 : Average measurements for each stock number in RHS



Type of beam	Stock No.	t_f (mm)	t_w (mm)	b (mm)	h (mm)	r (mm)	Cross-sectional area (mm ²)
IPE 240	1	9.82	6.59	120.02	242.13	15.13	3969
	2	9.80	6.58	120.41	242.02	15.25	3988
	3	9.74	6.42	120.00	242.08	15.25	3934
	4	9.72	6.64	119.74	241.87	15.00	3955
	5	9.63	6.57	119.02	241.75	15.25	3913
	6	9.87	6.83	119.90	242.33	15.63	3996
	7	9.83	6.64	119.80	242.33	15.88	3928
	8	9.72	6.48	119.60	242.20	15.75	3893
	9	9.83	6.53	120.25	242.47	16.00	3943
IPE 360	1	12.84	8.15	169.69	363.79	15.75	7282
	2	12.89	8.34	169.23	363.37	15.38	7344

Table 4-10 : Average measurements for each stock number from IPE sections

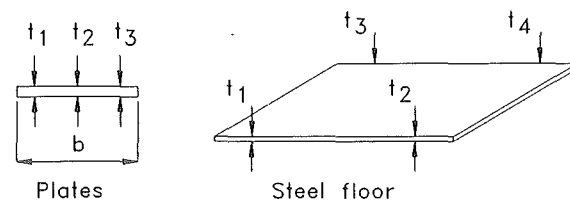


Plate width	Stock No.	Thickness (mm)	Width (b) (mm)	cross-sectional area (mm ²)
120	1	9.90	119.9	1187
	2	9.97	119.7	1193
	3	9.89	119.6	1183
	4	10.03	120.5	1209
170	1	11.53	170.0	1960
Steel floor	1	4.93	-	-

Table 4-11 : Average measurements for each stock number from Plates 120*10, 170*12 and steel floor

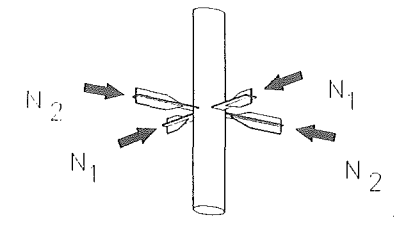
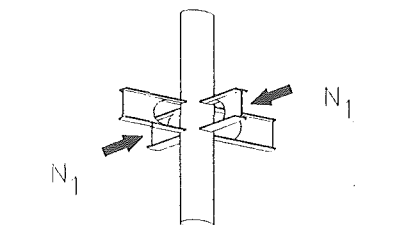
	TEST	β	Concrete infill in column	$\frac{N_2}{N_1}$	N_1 in Compr. or Tens.	N_u <i>Expt.</i>	$\frac{N_{u,num}}{N_{u,expt}}$
							[kN]
	1C1	.37	no	0	C	245.3	1.05
	1C2	.37	yes	0	T	510.8	1.06
	1C3	.52	no	0	C	325.0	1.08
	1C4	.52	yes	0	C	670.8	1.12
	1C5	.37	no	-1	C	175.6	1.08
	1C6	.37	no	+1	C	300.8	1.05
	1C7	.52	no	-1	C	220.1	1.07
	1C8	.52	no	+1	C	499.9	1.00
	2C1	.37	no	0	C	350.6	1.16
	2C2	.37	yes	0	T	971.8	1.07
	2C3	.52	no	0	C	456.0	1.12

Table 6-1 Comparison of experimental and numerical results (series 1 and 2) with a CHS column

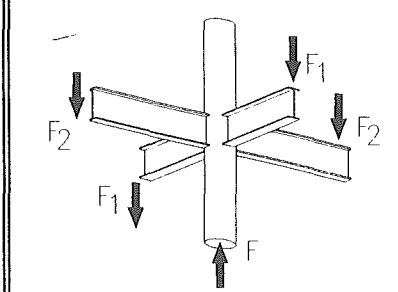
	TEST	β	Concrete infill in column	$\frac{F_2}{F_1}$	Steel or Concrete Floor	M_u <i>Expt.</i>	$\frac{M_{u,num}}{M_{u,expt}}$
							[kNm]
	3C1	.37	no	0		82.5	0.99
	3C2	.37	no	0	S	87.6	0.98
	3C3	.37	no	-1		54.1	1.12
	3C4	.37	no	+1		79.0	1.01

Table 6-2 Comparison of experimental and numerical results (series 3) with a CHS column

$F_2/F_1 = 0$	β	η	$N_{u,expt}$	$M_{u,expt}$	CIDECT/Expt (CIDECT/Num)	AIJ/Expt (AIJ/Num)
			[kN]	[kNm]		
1C1	0.37	0	245.3		1.025 (0.976)	0.930 (0.886)
1C3	0.52	0	325.0		0.940 (0.870)	0.850 (0.787)
2C1	0.37	0.74	350.6		0.854 (0.736)	0.931 (0.803)
2C3	0.52	1.11	456.0		0.856 (0.764)	1.007 (0.899)
3C1	0.37	0.74		82.5	0.664 (0.671)	0.735 (0.742)

Table 6-3 Comparison experimental and numerical results with design formulae

Remarks: The CIDECT formula is based on design strength [22]
The AIJ formula is based on maximum strength [25]

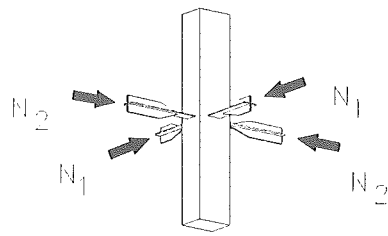
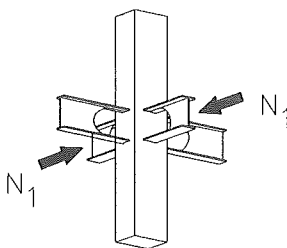
	TEST	β	Concrete infill in column	$\frac{N_2}{N_1}$	N_1 in Compr. or Tens.	$N_{u, Expt}$	$\frac{N_{u, num}}{N_{u, expt}}$
							[kN]
	1R1	.4	no	0	C	191.15	1.06
	1R2	.4	yes	0	T	264.91	1.10
	1R3	.57	no	0	C	254.75	1.04
	1R4	.57	yes	0	C	683.80	1.18
	1R5	.4	no	-1	C	135.58	1.04
	1R6	.4	no	+1	C	199.5	1.09
	1R7	.57	no	-1	C	165.21	1.06
	1R8	.57	no	+1	C	259.83	1.09
	2R1	.4	no	0	C	308.25	1.05
	2R2	.4	yes	0	T	509.80	1.05
	2R3	.57	no	0	C	477.62	1.05

Table 7-1 Comparison of experimental and numerical results (series 1 and 2) with a RHS column

Remarks:
 Maximum loads $N_{u,num}$ and $N_{u,expt}$ are based on $1.2t_0$ indentation of the I-beam flanges into the column face, because there were no maxima observed during the tests. A maximum peak load is only found for specimen 1R4.

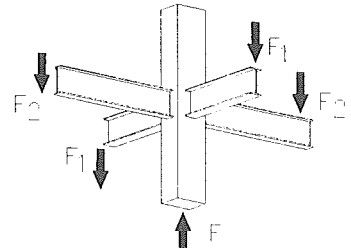
	TEST	β	Concrete infill in column	$\frac{F_2}{F_1}$	Steel or Concrete Floor	$M_{u, Expt}$	$\frac{M_{u, num}}{M_{u, expt}}$
							[kNm]
	3R1	.4	no	0		58.0	1.03
	3R2	.4	no	0	S	90.8	1.03
	3R3	.4	no	-1		38.4	1.05
	3R4	.4	no	+1		55.0	1.05

Table 7-2 Comparison of experimental and numerical results (series 3 and 4) with a RHS column

Remarks:
 Maximum moments $M_{u,num}$ and $M_{u,expt}$ are based on $1.2t_0$ indentation of the I-beam flanges into the column face.

Connections	$N_{u,exp}$ ($N_{u,num}$) [kN]	CIDECT [kN]	CIDECT/ $N_{u,exp}$ (CIDECT/ $N_{u,num}$)
1R1	191.15 (202.10)	167.29	0.88 (0.83)
1R3	254.75 (260.85)	237.78	0.88 (0.91)
2R1	308.25 (323.66)	340.77	1.11 (1.05)
2R3	477.62 (501.50)	480.48	1.00 (0.96)

Table 7-3 Comparison of the Numerically Determined Maximum Loads with Design Values for Plate to RHS Column Connections

Remark:

¹ Maximum moments $N_{u,num}$ and $N_{u,exp}$ are based on $1.2t_0$ indentation of the I-beam flanges into the column face

Connections	F_2/F_1	Maximum Moment in [kNm]	Design Moment Resistance in kNm			
		$M_{u,exp}$ ($M_{u,num}$)	$M_{d,e}$	$M_{d,y}$	$M_{d,p}$	$M_{d,c}$
3R1	0	58.0 (59.6)	38.91^2	59.26	87.67	152.50
3R2	0	90.8 (93.2)	39.33^2	76.59	82.73	148.69
3R3	-1	38.4 (40.4)	38.32	37.22^2	82.63	148.17
3R4	1	55.0 (58.0)	38.32^2	55.64	84.21	152.14

Table 7-4 Comparison of the Numerically Determined Maximum Loads with Design Values for I-beam to RHS Column Connections

¹ $M_{u,num}$, $M_{u,exp}$ are based on $1.2t_0$ indentation of the I-beam flanges into the column face

² Governing design strength of connection

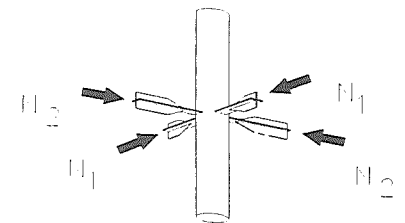
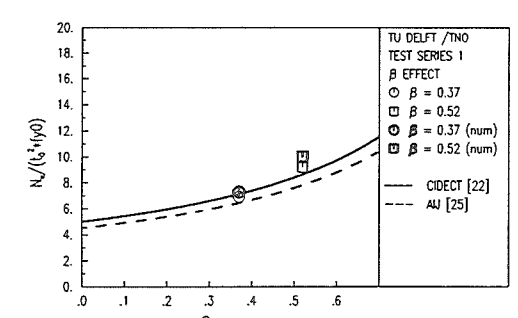
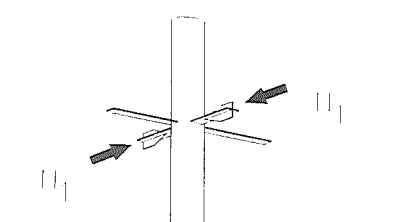
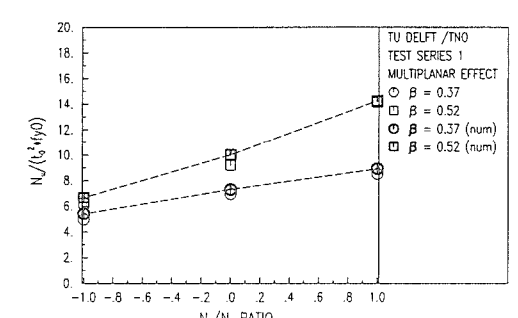
		Conclusions
 <p>- concrete infill</p>		<ul style="list-style-type: none"> - Failure mode: Chord face yielding - An increase of β results in an increase of N_u and initial stiffness <p>Notes: CIDECT [22] on basis of design strength AIJ [25] on basis of ultimate strength</p>
	 <p>+ concrete infill</p>	
	<p>N_1 in tension:</p>	<p>N_1 in tension:</p> <ul style="list-style-type: none"> - Failure mode: Punching shear at chord face, parallel to column axis - The location of the cracks are different from those for unfilled columns, therefore the existing formula for punching shear cannot be used for concrete filled columns.
	<p>N_1 in compression: $N_u = b_1 * t_1 * f_y$</p>	<p>N_1 in compression:</p> <ul style="list-style-type: none"> - Failure mode: Plate yielding + local buckling of plate - The concrete infill increases the N_u and the initial stiffness becomes almost infinite.

Table 8-1 Main results and conclusions for plate to CHS column connections under axial load

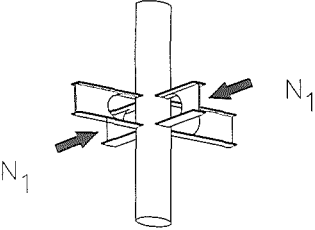
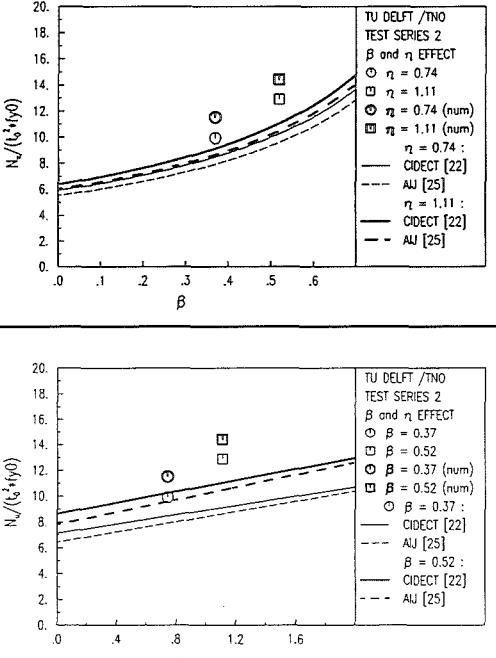
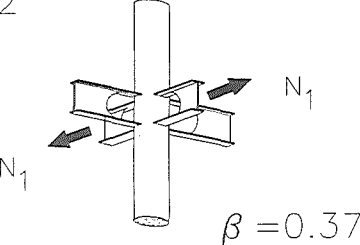
		Conclusions
 <p>- concrete infill</p>		<ul style="list-style-type: none"> - Failure mode: Chord face yielding - An increase of β gives a larger N_u and initial stiffness <ul style="list-style-type: none"> - For $\eta = 0$ the $N_u = N_u(\text{plate at one level})$ - For large η the $N_u = 2 * N_u(\text{plate at one level})$ - For smaller η the $N_u < 2 * N_u(\text{plate at one level})$ <p>Notes: CIDECT [22] on basis of design strength AIJ [25] on basis of ultimate strength</p>
<p>2C2</p>  <p>+ concrete infill</p>		<ul style="list-style-type: none"> - Failure mode: Punching shear at chord face, parallel to column axis - The location of the cracks are different from those for unfilled columns, therefore the existing formula for punching shear cannot be used for concrete filled columns. - Probably a fracture mechanics approach could be used to determine the connection strength, since the failure mode is similar to the K_{III} ("tearing") mode as used in fracture mechanics.

Table 8-2 Main results and conclusions for axial loading interaction effects (CHS)

	<p>TU DELFT / TNO TEST SERIES 3 MULTIPLANAR EFFECT</p> <ul style="list-style-type: none"> ○ Expt. □ Expt. + Steelfloor ● Num. ■ Num. + Steelfloor 	<p>Conclusions</p> <ul style="list-style-type: none"> - Failure mode: Chord face yielding - For $F_2/F_1 = +1$ the initial stiffness is larger than for load case $F_2/F_1 = 0$ - For $F_2/F_1 = +1$ is $M_u \approx M_u(F_2/F_1 = 0)$ - For $F_2/F_1 = -1$ the M_u and initial stiffness is smaller than for $F_2/F_1 = 0$ - The relation between F_2/F_1 and M_u is almost parabolic
	<p>TU DELFT / TNO TEST SPECIMEN JC1/3C2</p> <p>$F_2 / F_1 = 0$ $\beta = 0.37$ $2\gamma = 34$</p> <ul style="list-style-type: none"> — EXPT. — EXPT. + STEEL PLATE 	<ul style="list-style-type: none"> - Failure mode: Chord face yielding - The steel plate increases the M_u and the initial stiffness

Table 8-3 Main results and conclusions for I-beam to CHS column connections under in-plane bending

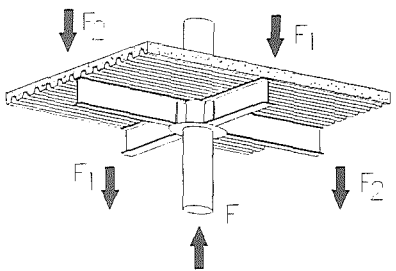
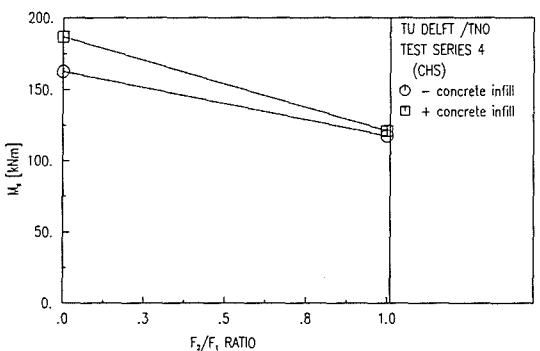
		Conclusions
	 <p>TU DELFT / TNO TEST SERIES 4 (CHS) ○ - concrete infill □ + concrete infill</p>	<p>- Failure mode: progressive failure of the reinforcement bars</p> <p>- The concrete filled column gives a small increase of the connect strength, especially for $F_2/F_1 = +1$.</p> <p>- The multiplanar load ratio $F_2/F_1 = +1$ gives a considerable smaller connection strength than for ($F_2/F_1 = 0$)</p> <p>Design strength: On basis of nominal yield stress reinforcement bars: $M_u = 67 \text{ kNm}$, if only $8\Phi 8$ are taken into account</p> <p>Theoretical strength: On basis of actual ultimate stress reinforcement bars: $M_u = 182 \text{ kNm}$, if $8\Phi 8$ and $16\Phi 6$ are taken into account</p>

Table 8-4 Main results and conclusions for the bolted connections with a composite floor (CHS column)

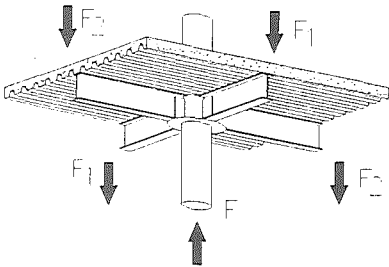
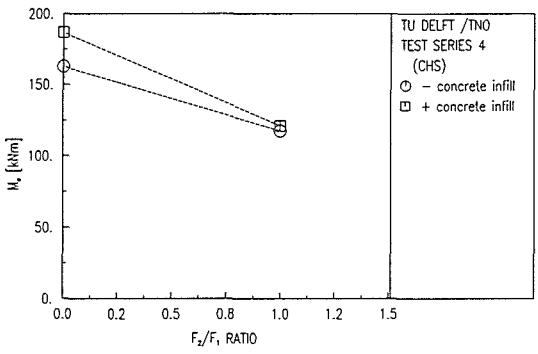
		Conclusions
	 <p>TU DELFT / TNO TEST SERIES 4 (CHS) ○ - concrete infill □ + concrete infill</p>	<p>- Failure mode: progressive failure of the reinforcement bars</p> <p>- The concrete filled column gives a small increase of the connect strength, especially for $F_2/F_1 = +1$.</p> <p>- The multiplanar load ratio $F_2/F_1 = +1$ gives a considerable smaller connection strength than for ($F_2/F_1 = 0$)</p> <p>Theoretical strength: On basis of nominal yield stress reinforcement bars: $M_u = 67$ kNm, if only $8\Phi 8$ are taken into account $M_u = 143$ kNm, if $8\Phi 8$ and $16\Phi 6$ are taken into account</p> <p>On basis of actual ultimate stress reinforcement bars: $M_u = 182$ kNm, if $8\Phi 8$ and $16\Phi 6$ are taken into account</p>

Table 8-4 Main results and conclusions for the bolted connections with a composite floor (CHS column)

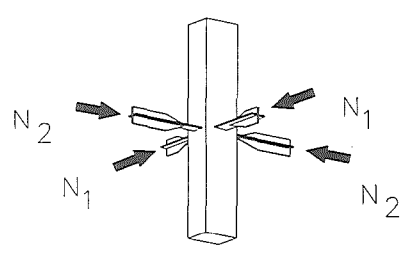
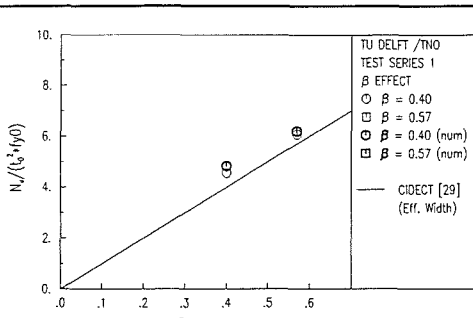
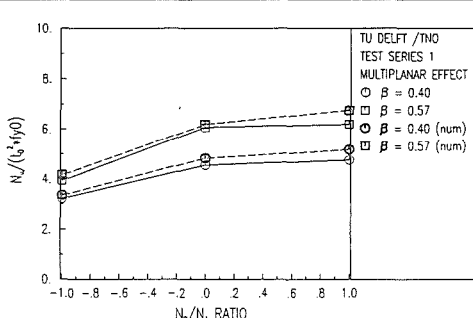
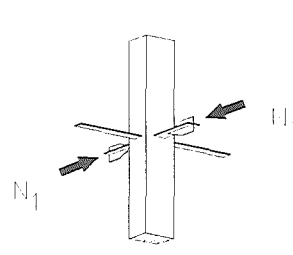
		Conclusions
 <p>- concrete infill .</p>		<ul style="list-style-type: none"> - Failure mode: Chord face yielding - An increase of β results in an increase of N_u and initial stiffness
		<ul style="list-style-type: none"> - For load ratio $N_2/N_1 = +1$ the N_u and initial stiffness is larger than for $N_2/N_1 = 0$ - For load ratio $N_2/N_1 = -1$ the N_u and initial stiffness is smaller than for $N_2/N_1 = 0$ - For larger β the multiplanar loading effect is larger
 <p>+ concrete infill</p>	<p>N_1 in tension:</p> $N_u = \frac{f_y o t_o}{\sqrt{3}} (2t_1 + 2b_{ep})$ $b_{ep} = \frac{10}{b_d t_o} \cdot b_1 \text{ but } \leq b_1$	<p>N_1 in tension:</p> <ul style="list-style-type: none"> - Failure mode: Punching shear at chord face - The concrete infill increases the N_u and the initial stiffness
	<p>N_1 in compression:</p> $N_u = b_1 * t_1 * f_y$	<p>N_1 in compression:</p> <ul style="list-style-type: none"> - Failure mode: Plate yielding + local buckling of plate - The concrete infill increases the N_u and the initial stiffness becomes almost infinite.

Table 8-5 Main results and conclusions for plate to RHS column connections under axial load

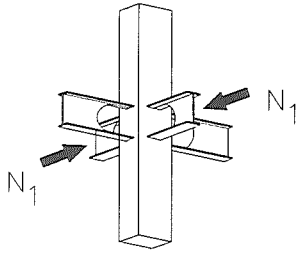
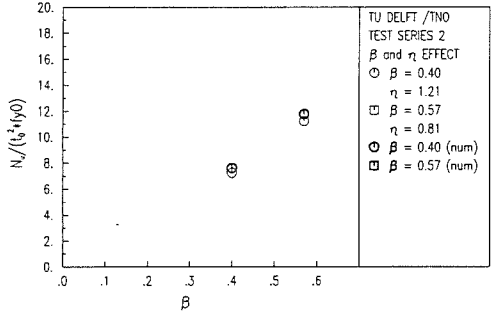
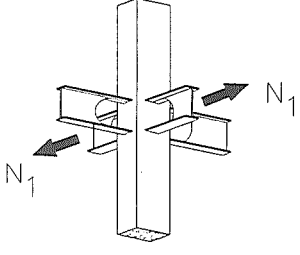

		Conclusions
 <p>- concrete infill</p>	 <p>TU DELFT /TNO TEST SERIES 2 beta and eta EFFECT ○ beta = 0.40 □ beta = 0.57 ○ eta = 1.21 □ eta = 0.81 ○ beta = 0.40 (num) □ beta = 0.57 (num)</p>	<ul style="list-style-type: none"> - Failure mode: Chord face yielding - An increase of β gives a larger N_U and initial stiffness
 <p>+ concrete infill</p>	 <p>TU DELFT /TNO TEST SERIES 2 beta and eta EFFECT ○ beta = 0.40 □ beta = 0.57 ○ beta = 0.40 (num) □ beta = 0.57 (num)</p>	<p>N_1 in tension:</p> <ul style="list-style-type: none"> - Failure mode: Punching shear at chord face - The location of the cracks are different from those for unfilled columns. The failure mode is similar to the "tearing" mode as used in fracture mechanics. Therefore the existing formula for punching shear cannot be used for concrete filled column connections - The concrete infill increases the N_U and initial stiffness

Table 8-6 Main results and conclusions for axial loading interaction effects (RHS)

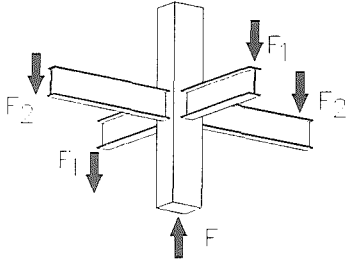
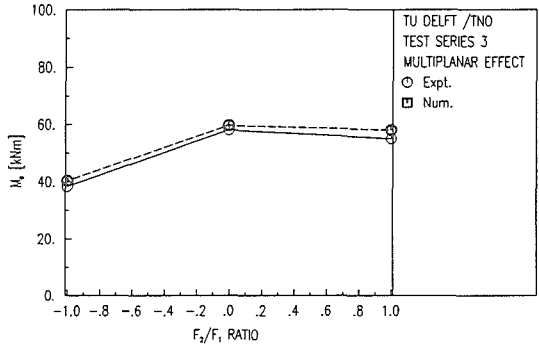
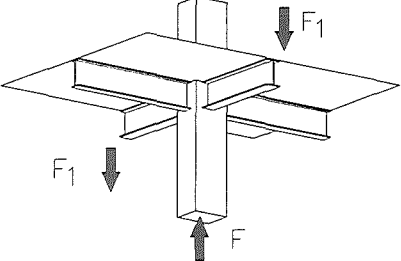
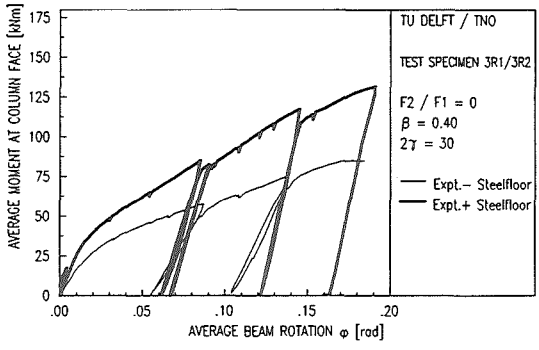
		Conclusions
	 <p>TU DELFT / TNO TEST SERIES 3 MULTIPLANAR EFFECT ○ Expt. □ Num.</p>	<ul style="list-style-type: none"> - Failure mode: Chord face yielding - For $F_2/F_1 = +1$ the initial stiffness is larger than for load case $F_2/F_1 = 0$ - For $F_2/F_1 = +1$ is $M_u \approx M_u(F_2/F_1 = 0)$ - For $F_2/F_1 = -1$ the M_u and initial stiffness is smaller than for $F_2/F_1 = 0$
	 <p>TU DELFT / TNO TEST SPECIMEN 3R1/3R2 $F_2 / F_1 = 0$ $\beta = 0.40$ $2T = 30$ — Expt. - Steel floor — Expt. + Steel floor</p>	<ul style="list-style-type: none"> - Failure mode: Chord face yielding - The steel plate increases the M_u and the initial stiffness

Table 8-7 Main results and conclusions for I-beam to RHS column connections under in-plane bending

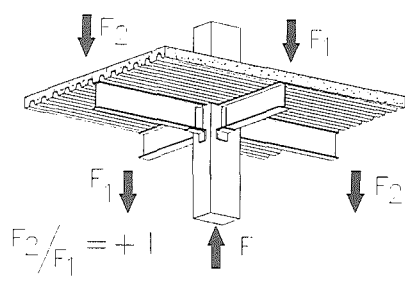
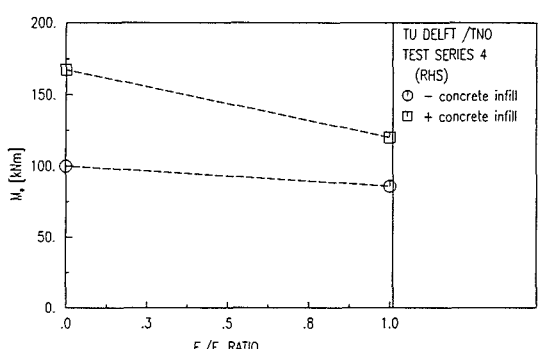
 <p>$F_2/F_1 = +1$</p>	 <p>TU DELFT /TNO TEST SERIES 4 (RHS) ○ - concrete infill □ + concrete infill</p> <table border="1"> <caption>Data points from the graph</caption> <thead> <tr> <th>F_2/F_1 RATIO</th> <th>M_u (kNm) - concrete infill</th> <th>M_u (kNm) + concrete infill</th> </tr> </thead> <tbody> <tr> <td>0.0</td> <td>100</td> <td>170</td> </tr> <tr> <td>1.0</td> <td>85</td> <td>125</td> </tr> </tbody> </table>	F_2/F_1 RATIO	M_u (kNm) - concrete infill	M_u (kNm) + concrete infill	0.0	100	170	1.0	85	125	<p>Conclusions</p> <ul style="list-style-type: none"> - Failure mode: progressive failure of the reinforcement bars - The concrete filled column gives a considerable increase of the connection strength, especially for $F_2/F_1 = 0$. - The multiplanar load ratio $F_2/F_1 = +1$ gives a decrease of the connection strength compared with $F_2/F_1 = 0$ <p>Design strength: On basis of nominal yield stress reinforcement bars: $M_u = 67$ kNm, if only $8\Phi 8$ are taken into account</p> <p>Theoretical strength: On basis of actual ultimate stress reinforcement bars: $M_u = 182$ kNm, if $8\Phi 8$ and $16\Phi 6$ are taken into account</p>
F_2/F_1 RATIO	M_u (kNm) - concrete infill	M_u (kNm) + concrete infill									
0.0	100	170									
1.0	85	125									

Table 8-8 Main results and conclusions for the bolted connections with a composite floor (RHS column)

FIGURES

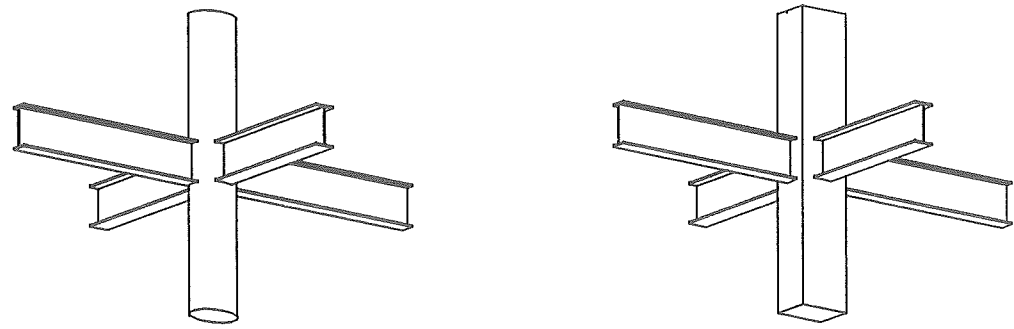


Fig. 1-1: Semi-rigid welded beam-to-column connections

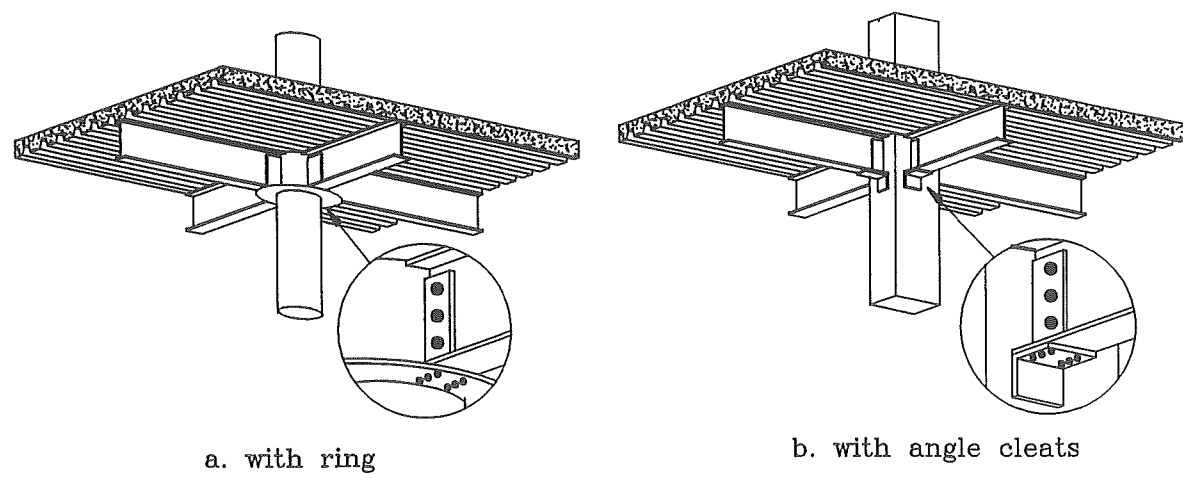


Fig. 1-2: Semi-rigid bolted beam-to-column connections

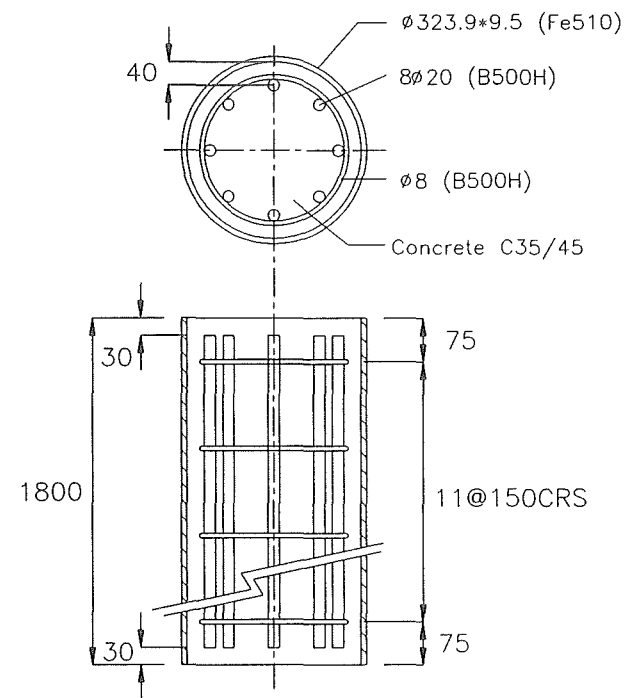


Fig. 4-1 : CHS columns with reinforced concrete filling

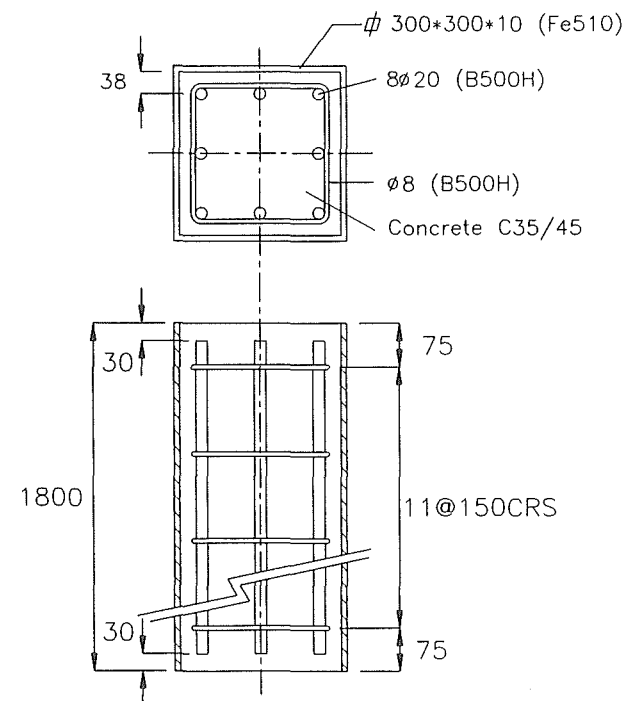


Fig. 4-2 : RHS columns with reinforced concrete filling

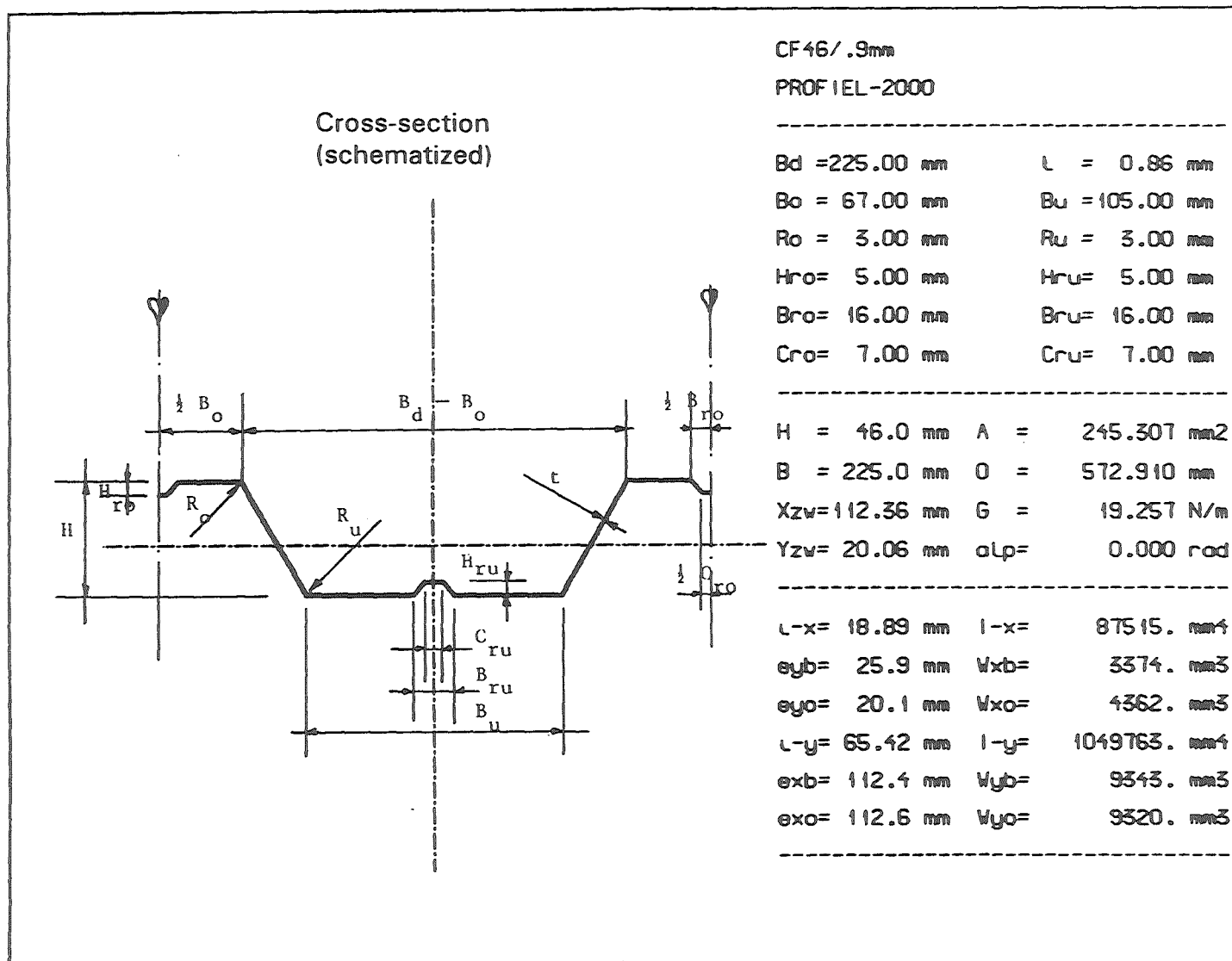


Fig. 4-3: Sheeting profile for deep steel deck PMF 46/0.9

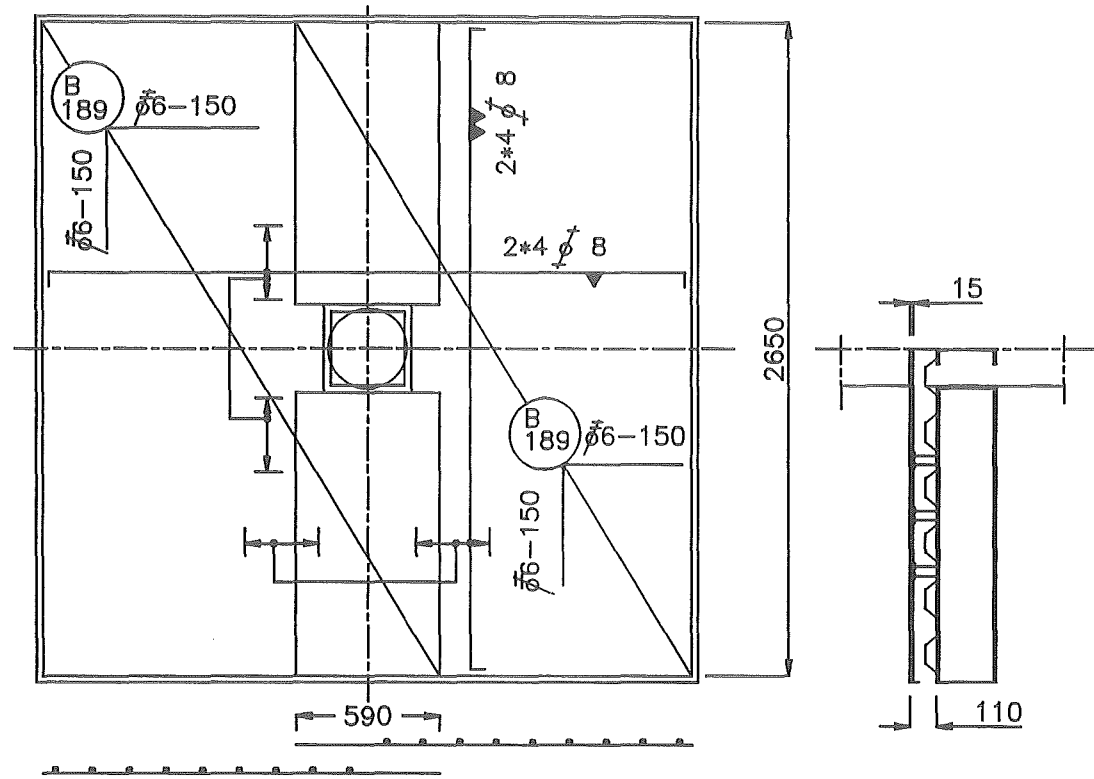


Fig. 4-4 : Reinforcement details for series 4 test specimens with CHS/RHS columns

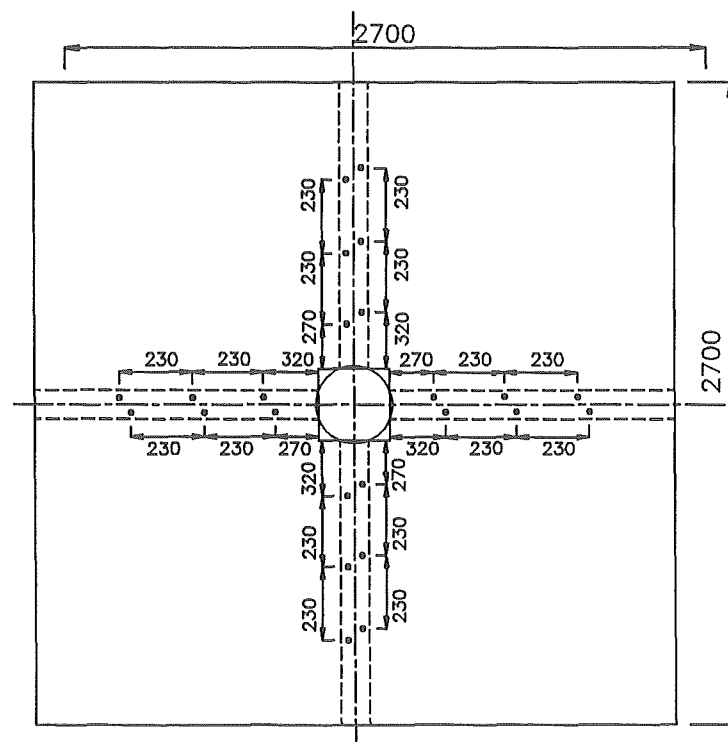


Fig. 4-5 : Standard arrangement of shear studs for series 4 tests (CHS/RHS)

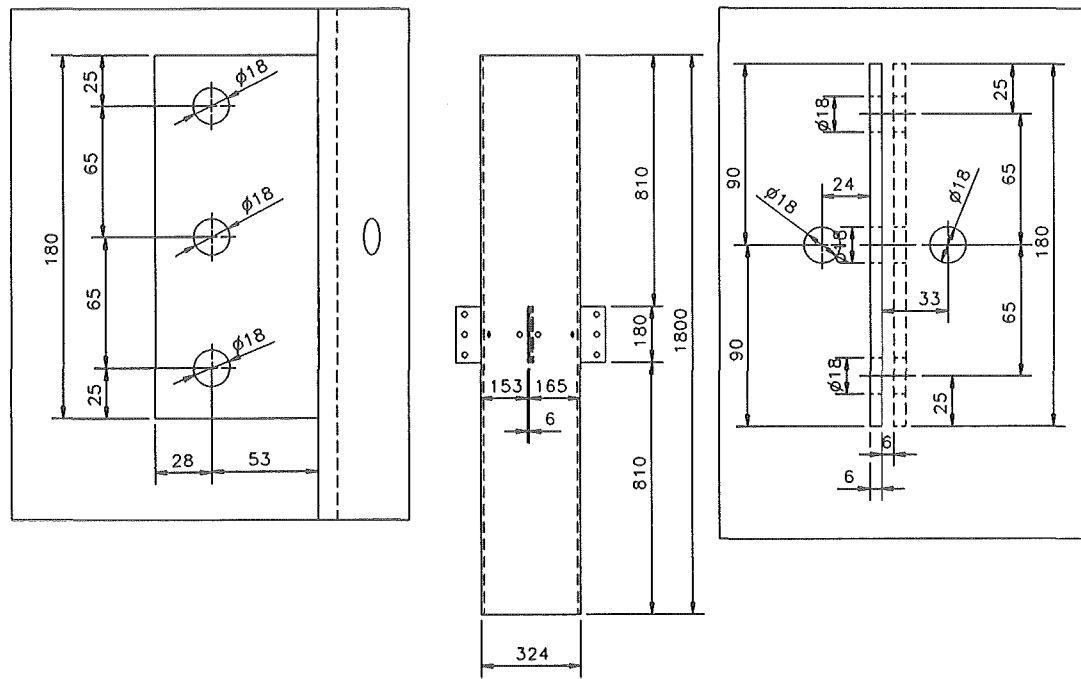


Fig. 4-6 : Web plate welded to columns (typical) for specimens 4C1 to 4C4

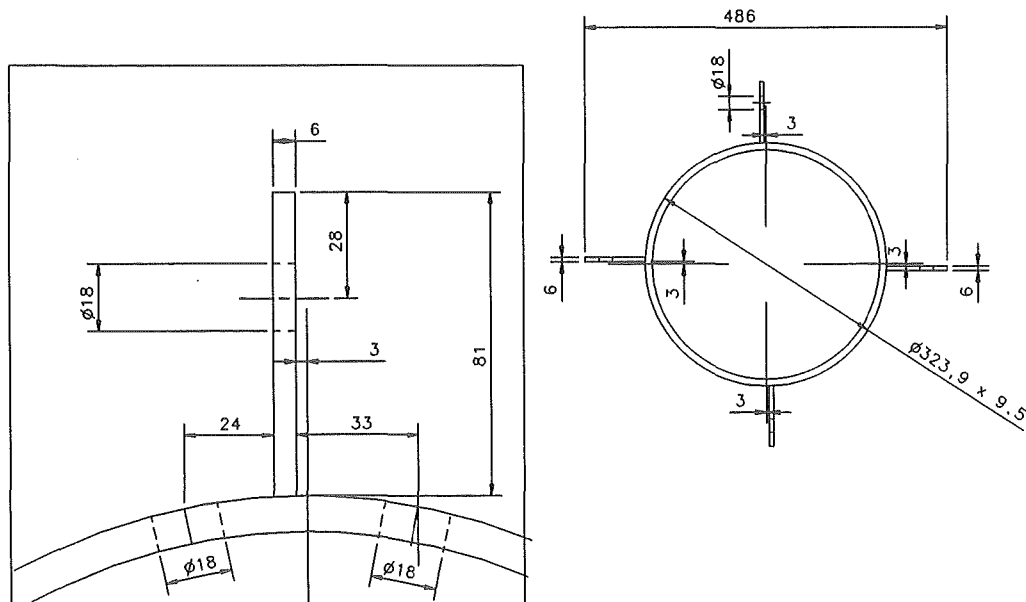


Fig. 4-7 : Specific details of web plate welded to columns (typical) for specimens 4C1 to 4C4

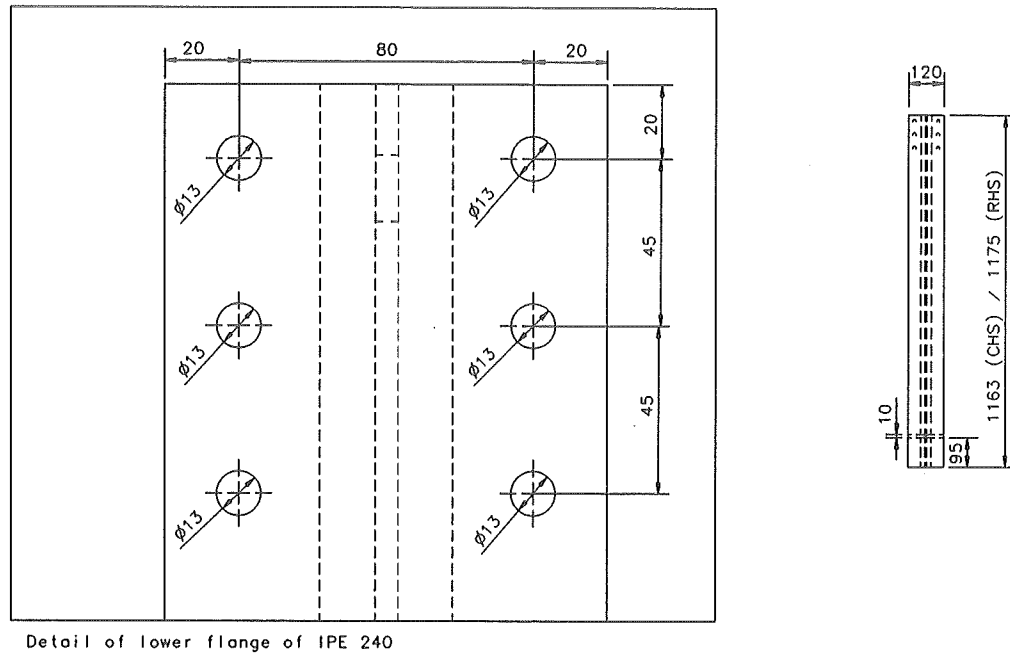


Fig. 4-12 : Details of bolt holes in I-beams for specimens 4C1 to 4C4 and 4R1 to 4R4 in plane

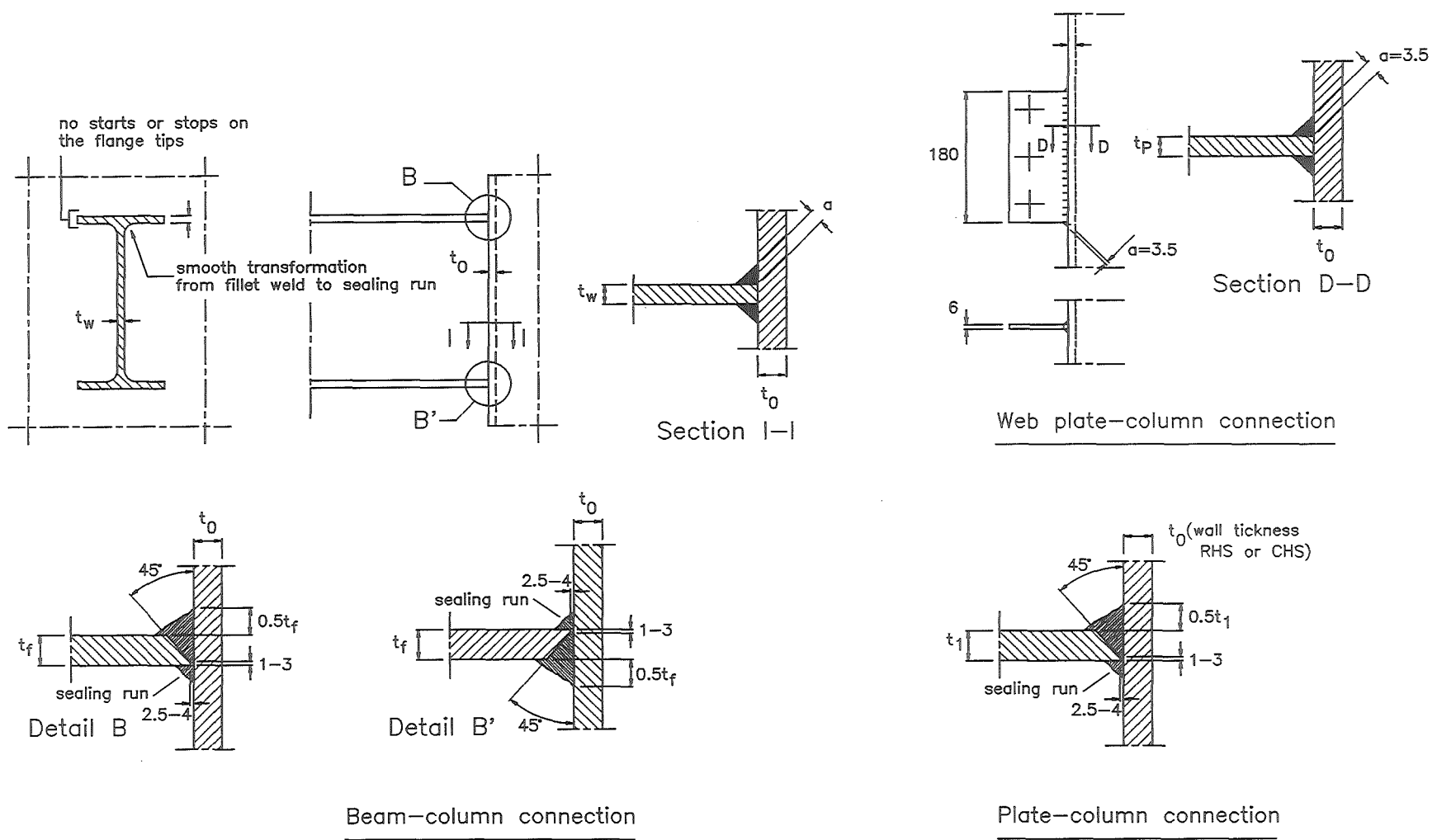


Fig. 4-13 : Welding details (welding process for all the welds : SMAW)

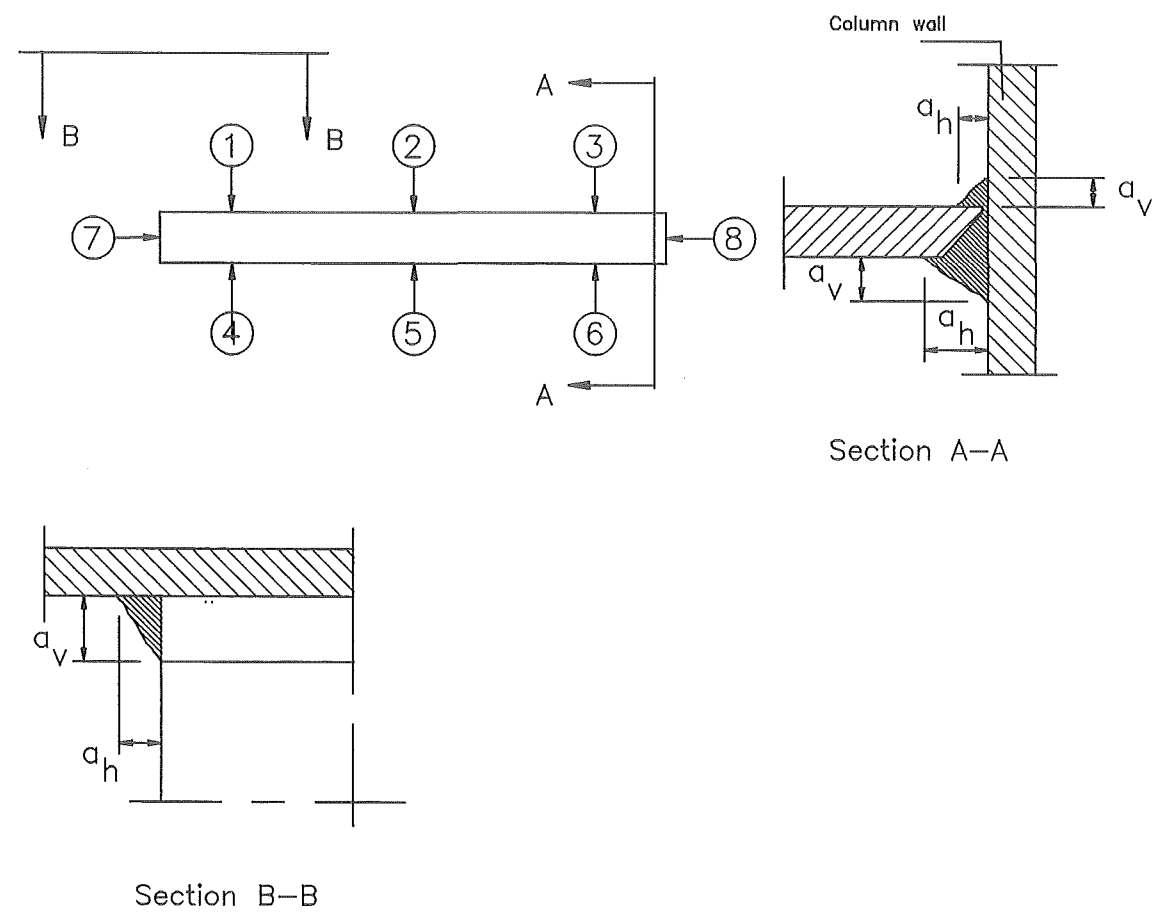
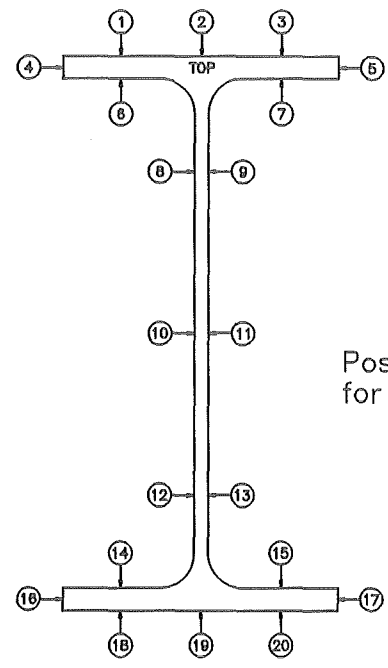


Fig. 4-14 : Weld measurements for series 1 and 2 with CHS and RHS columns



Position of weld measurements
for a_h and a_v

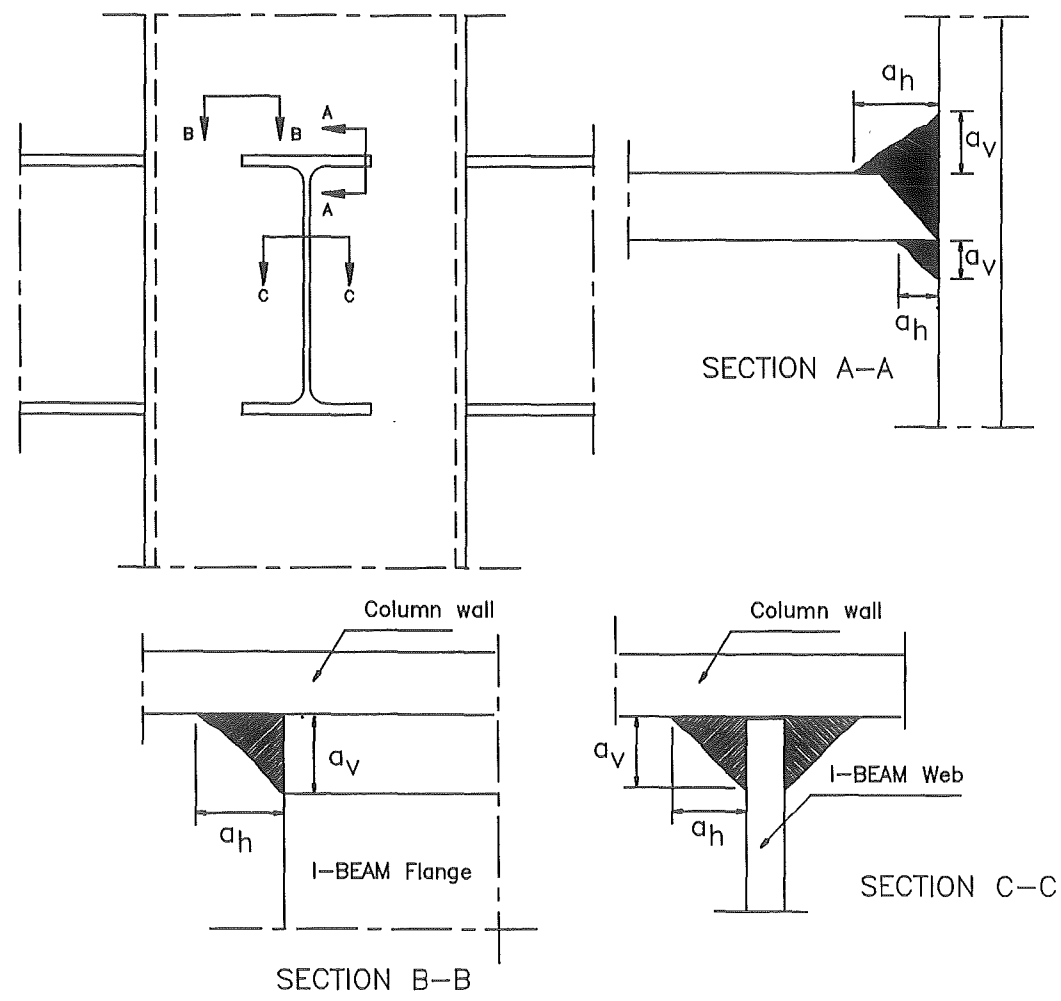
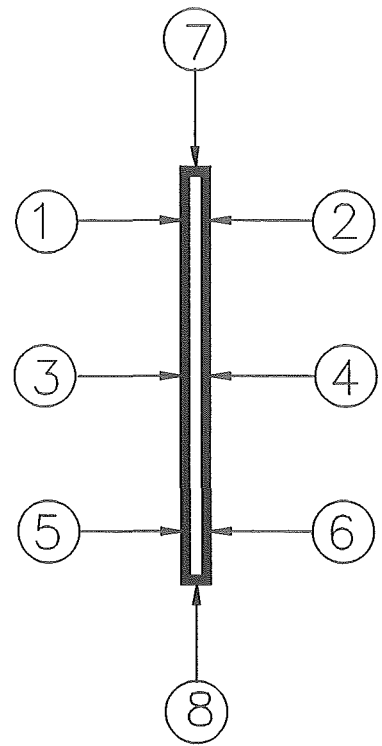
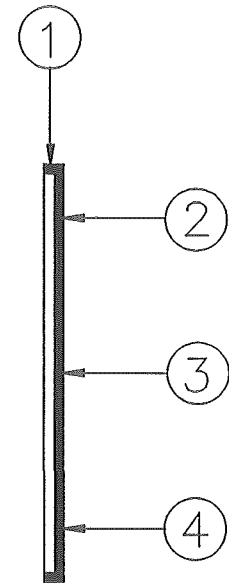


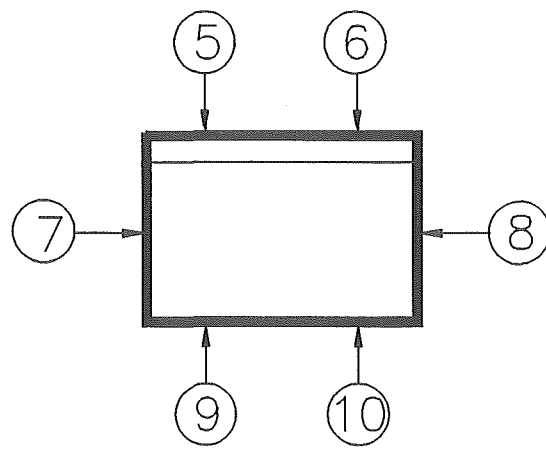
Fig. 4-15 : Weld measurements for series 3 with CHS and RHS columns



Web plate to CHS



Web plate to RHS



Cleat to RHS

Fig. 4-16 : Position of weld measurements for web plates and angle cleats of series 4 with CHS and RHS columns

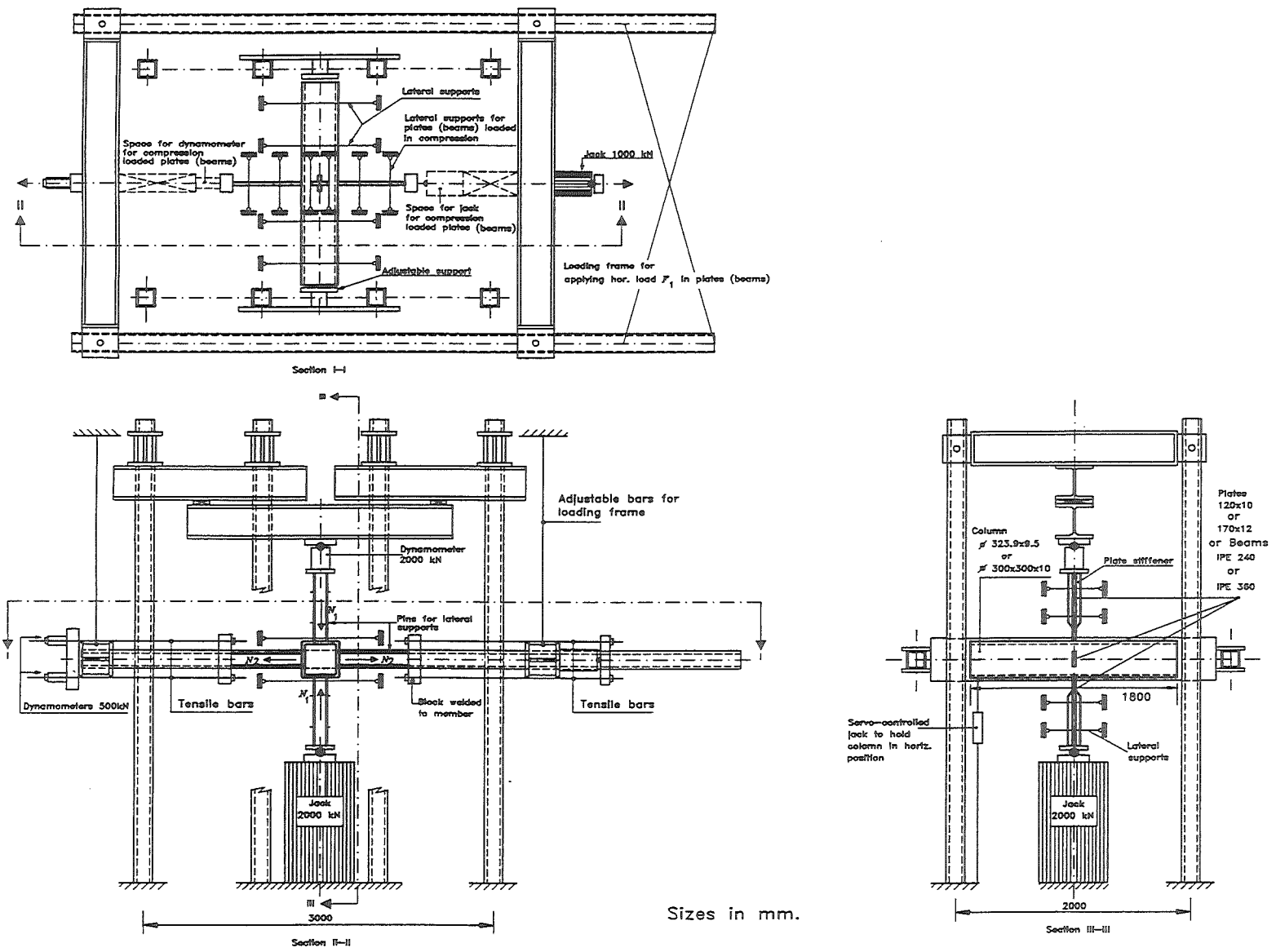


Figure 4-17 Test rig for connections with CHS/RHS columns and axially loaded plates and beams (series 1 and 2)

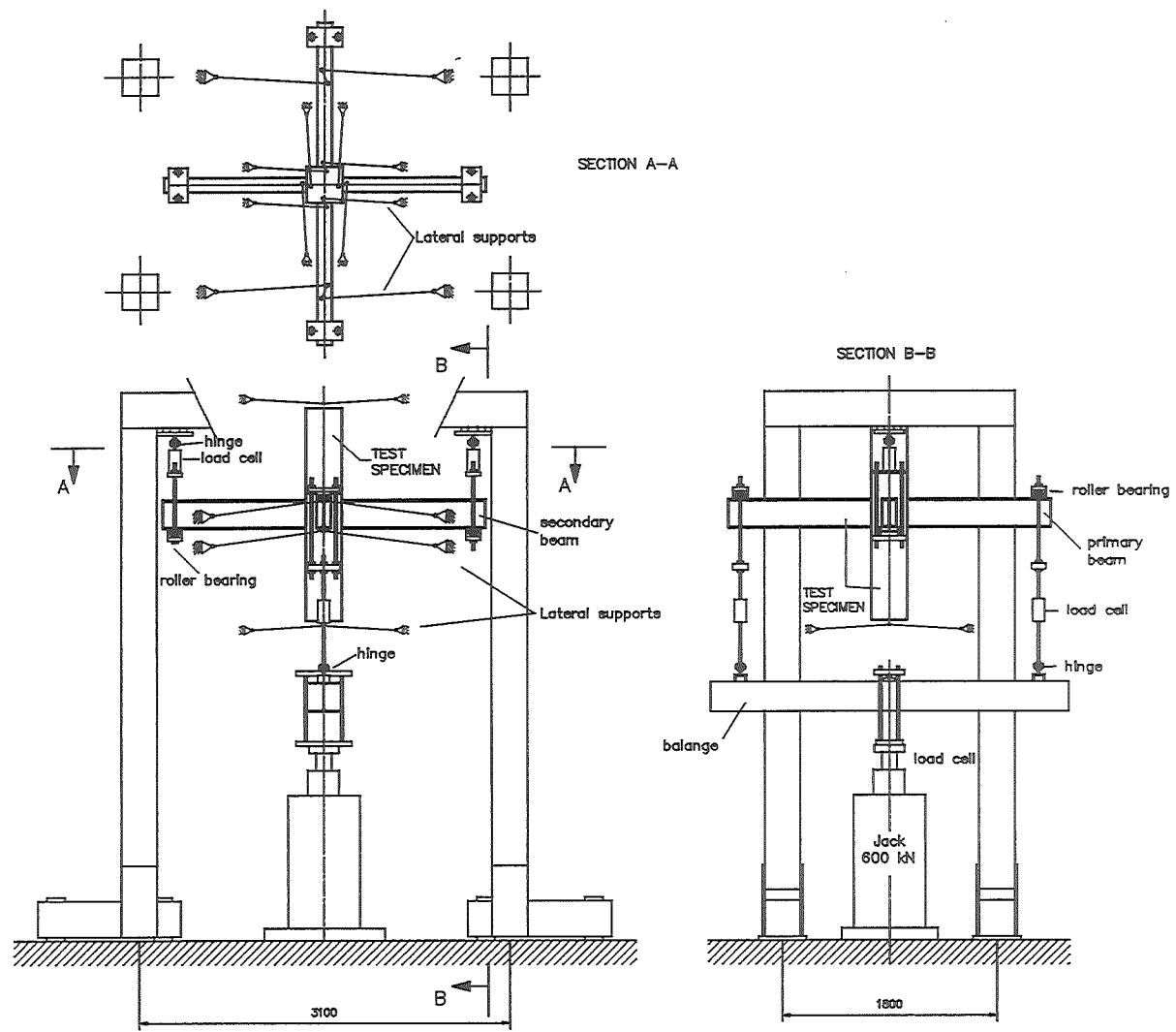


Fig 4-18 : Test rig for specimens 3C3 and 3R3 having CHS or RHS columns with primary beams under hogging moments and secondary beams under sagging moments

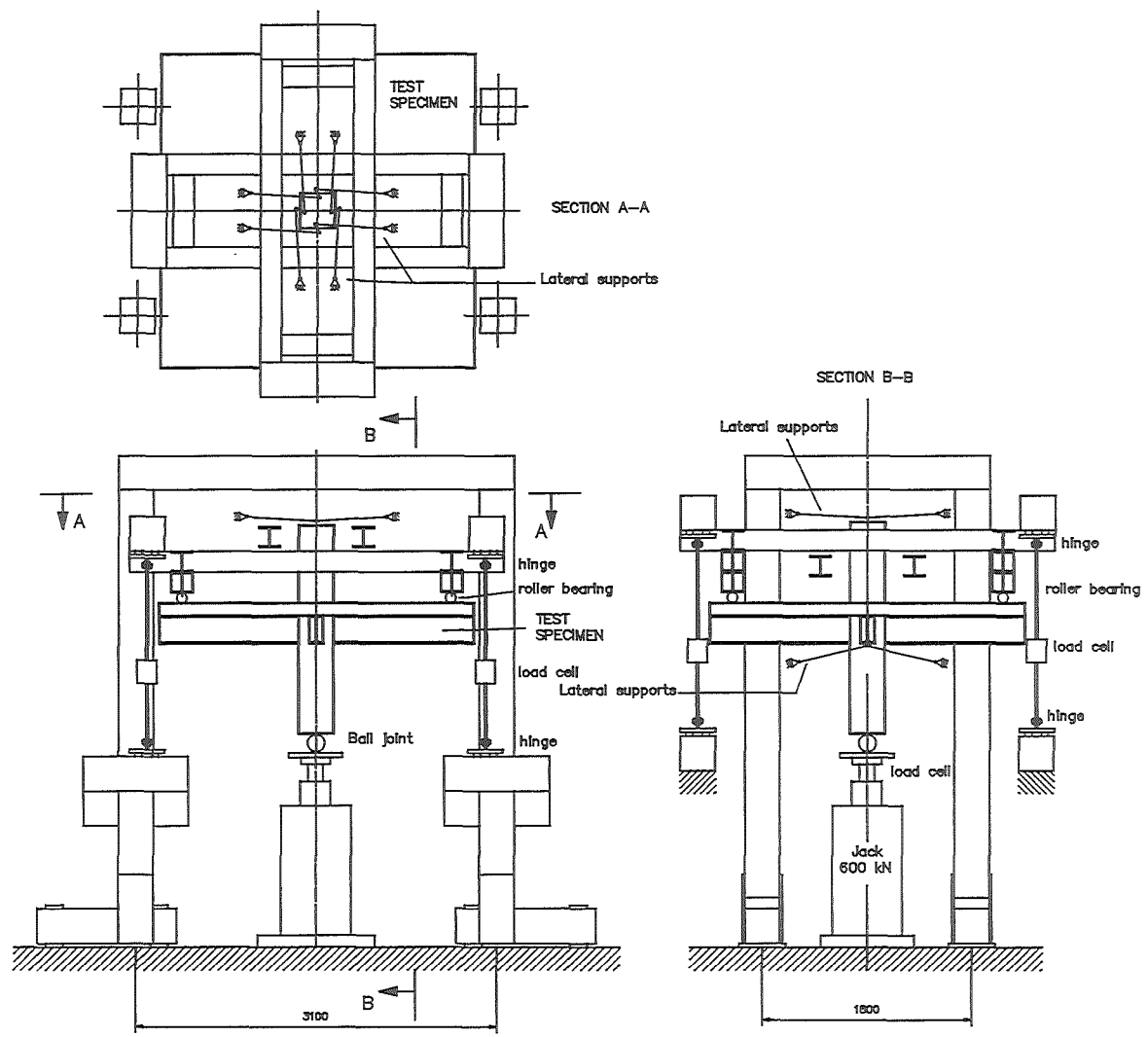
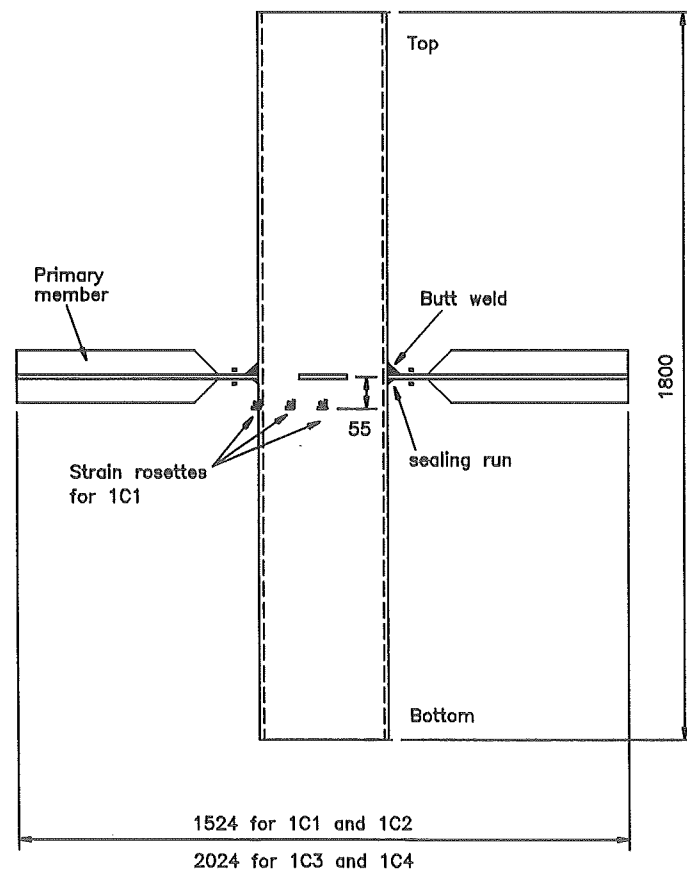
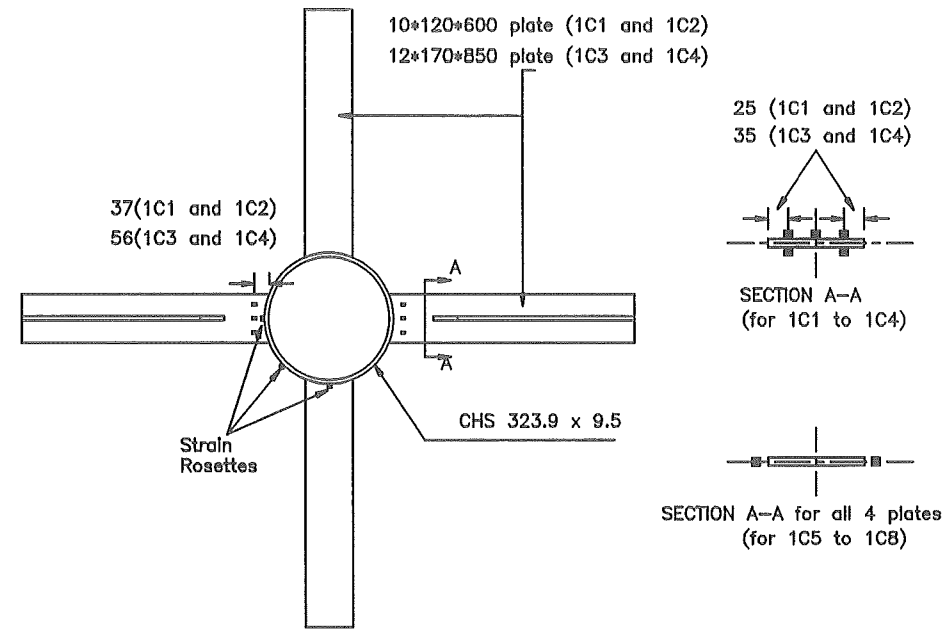
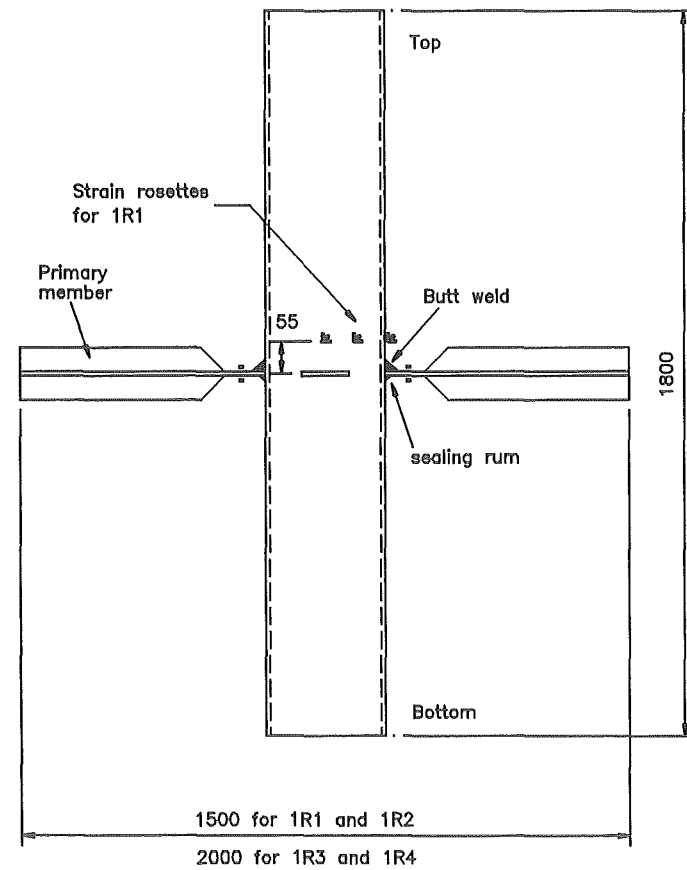
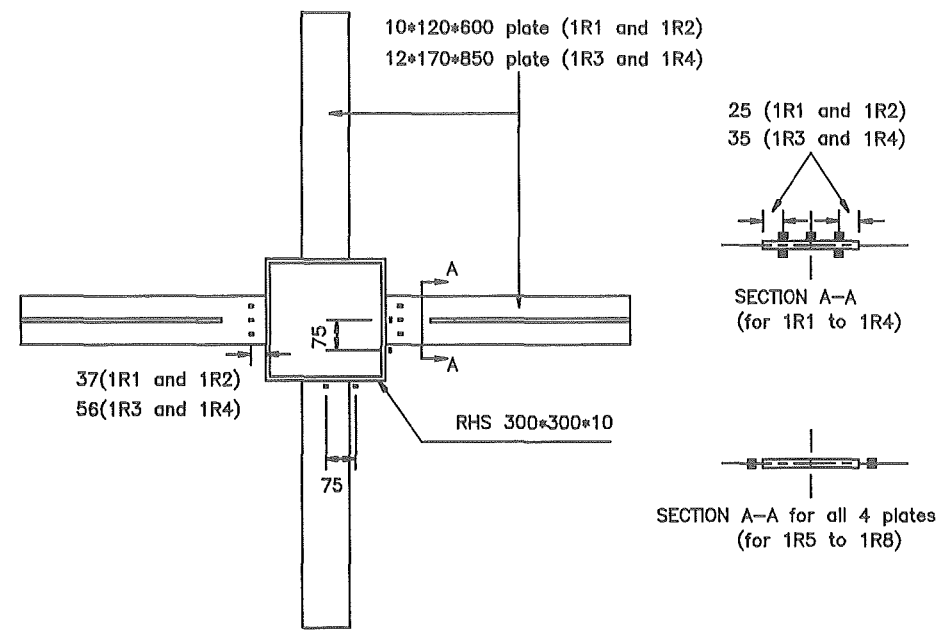


Fig 4-19 : Test rig for specimens 4C3, 4C4, 4R3 and 4R4 having CHS or RHS columns with all beams only under hogging moments



- Notes:
- 1) 5 strain gauges on each of the two loaded (primary) plate members (total = 10)
 - 2) 3 strain rosettes only for 1C1
 - 3) For 1C5 to 1C8 with loaded primary and secondary members, there are only 2 strain gauges per member (total =8) at the brace edges, at the same distance from the column as for 1C1 to 1C4

Fig. 4-20 : Typical strain gauge details for series 1 (CHS)



Notes:

- 1) 5 strain gauges on each of the two loaded (primary) plate members (total = 10)
- 2) 3 strain rosettes only for 1R1
- 3) For 1R5 to 1R8 with loaded primary and secondary members, there are only 2 strain gauges per member (total =8) at the brace edges, at the same distance from the column as for 1R1 to 1R4

Fig. 4-21 : Typical strain gauge details for series 1 (RHS)

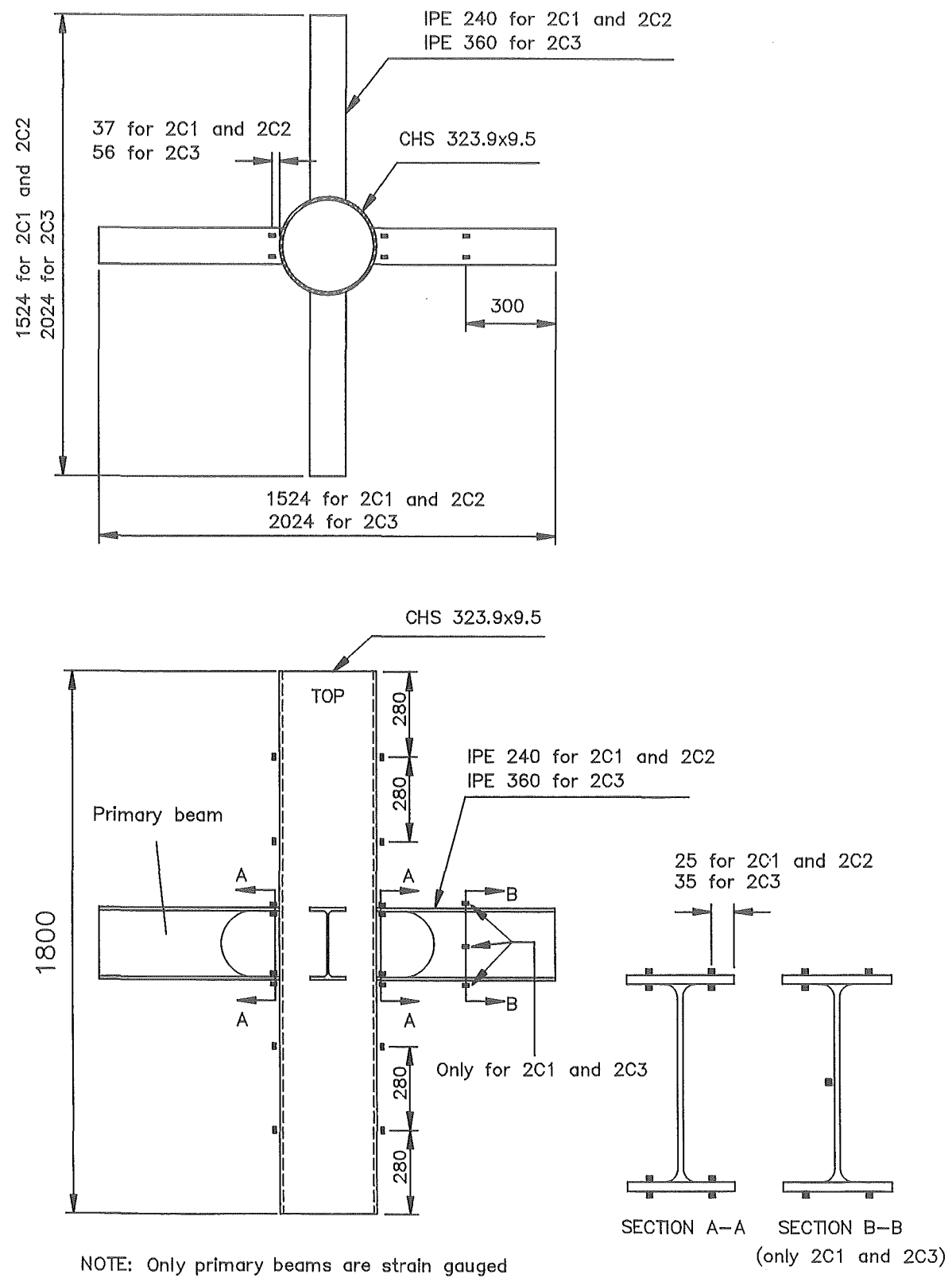


Fig. 4-22 : Strain gauges on beams for series 2 in CHS
(22 for 2C1 and 2C3, 16 for 2C2)

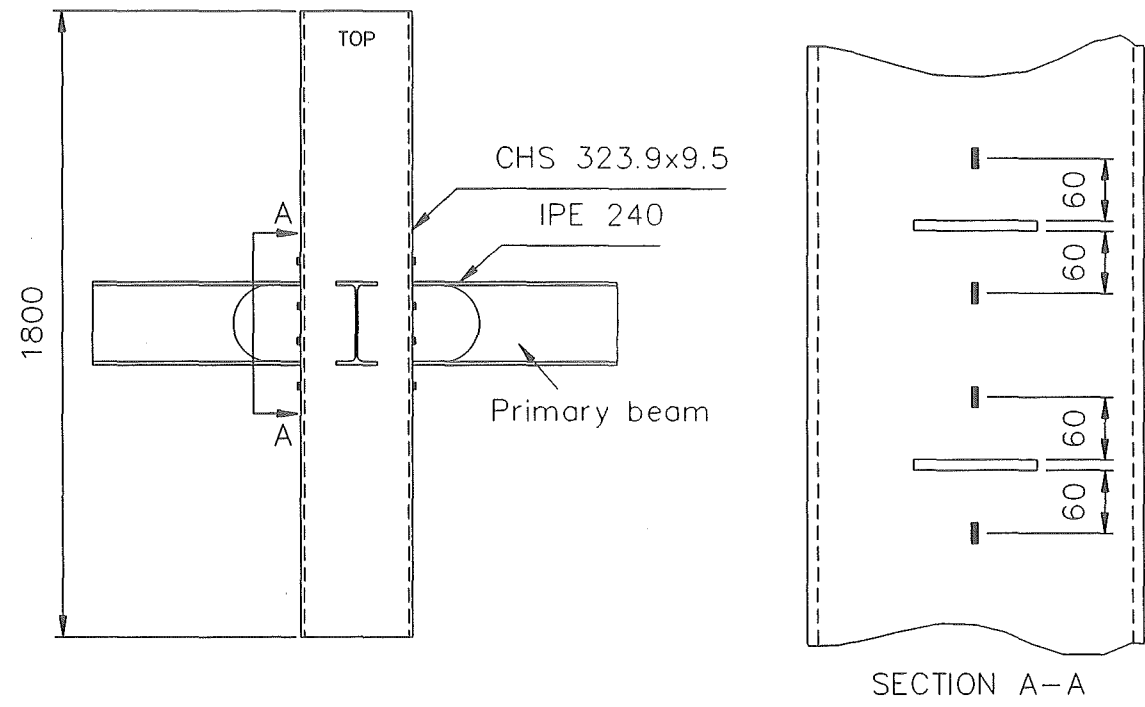


Fig. 4-23 : Strain gauges provided on column only for 2C1
(8 locations)

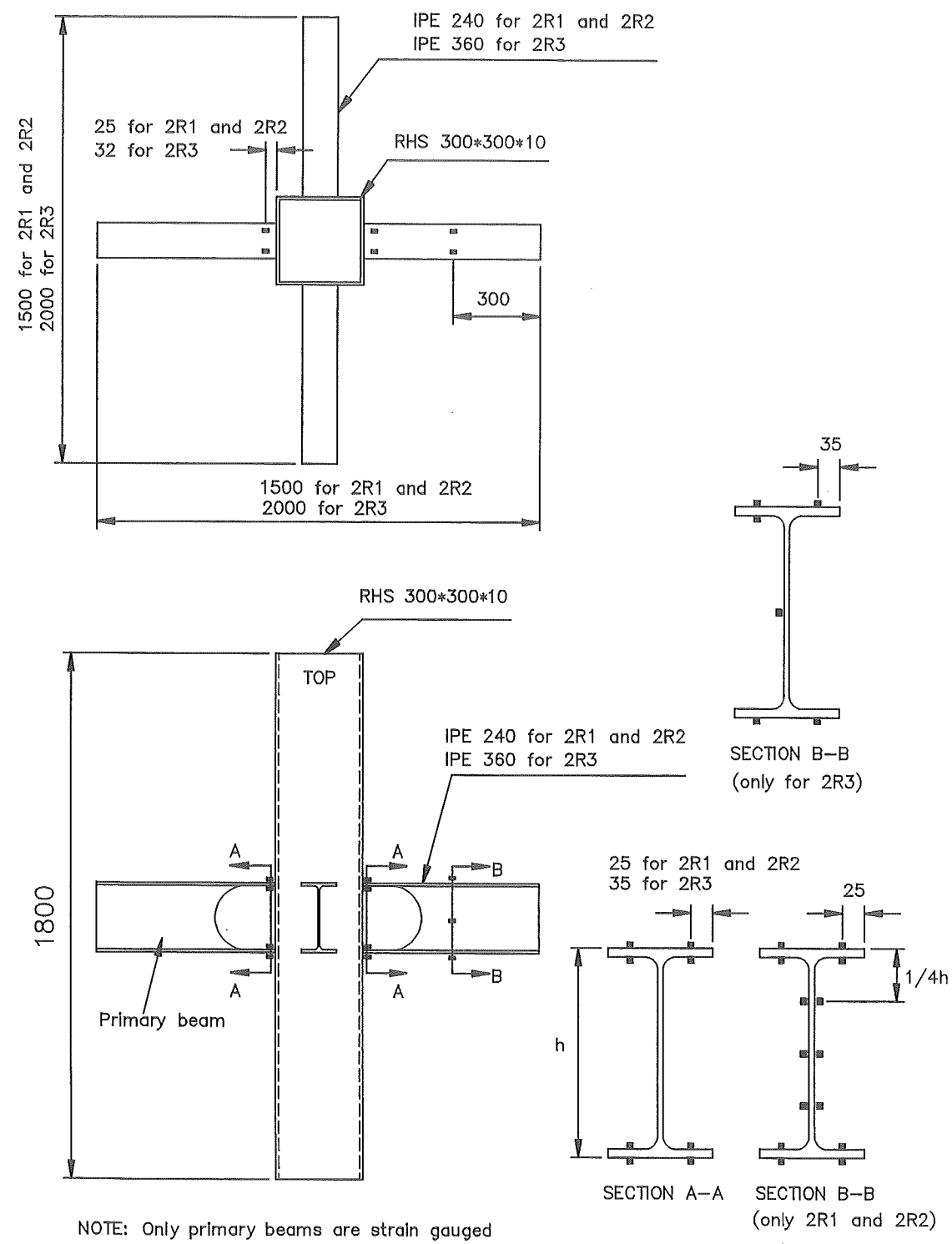


Fig. 4-24 : Strain gauges on beams for series 2 in RHS
 (30 for 2R1 and 2R2, 22 for 2R3)

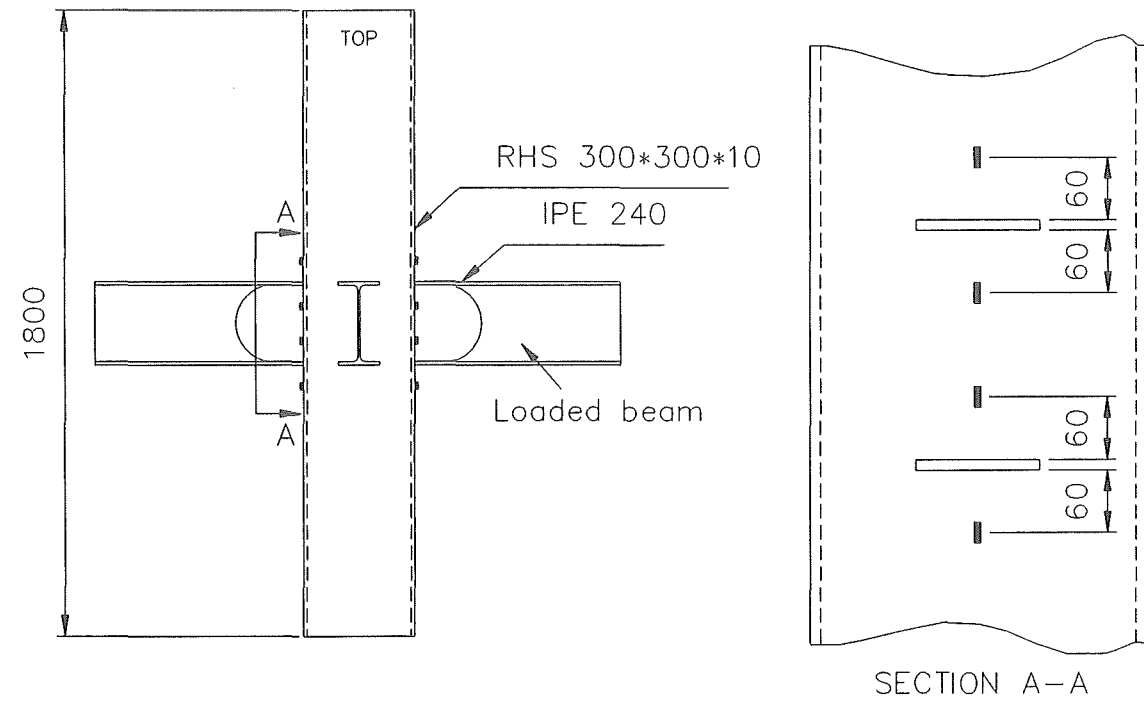


Fig. 4-25 : Strain gauges provided on column only for 2R1
(8 locations)

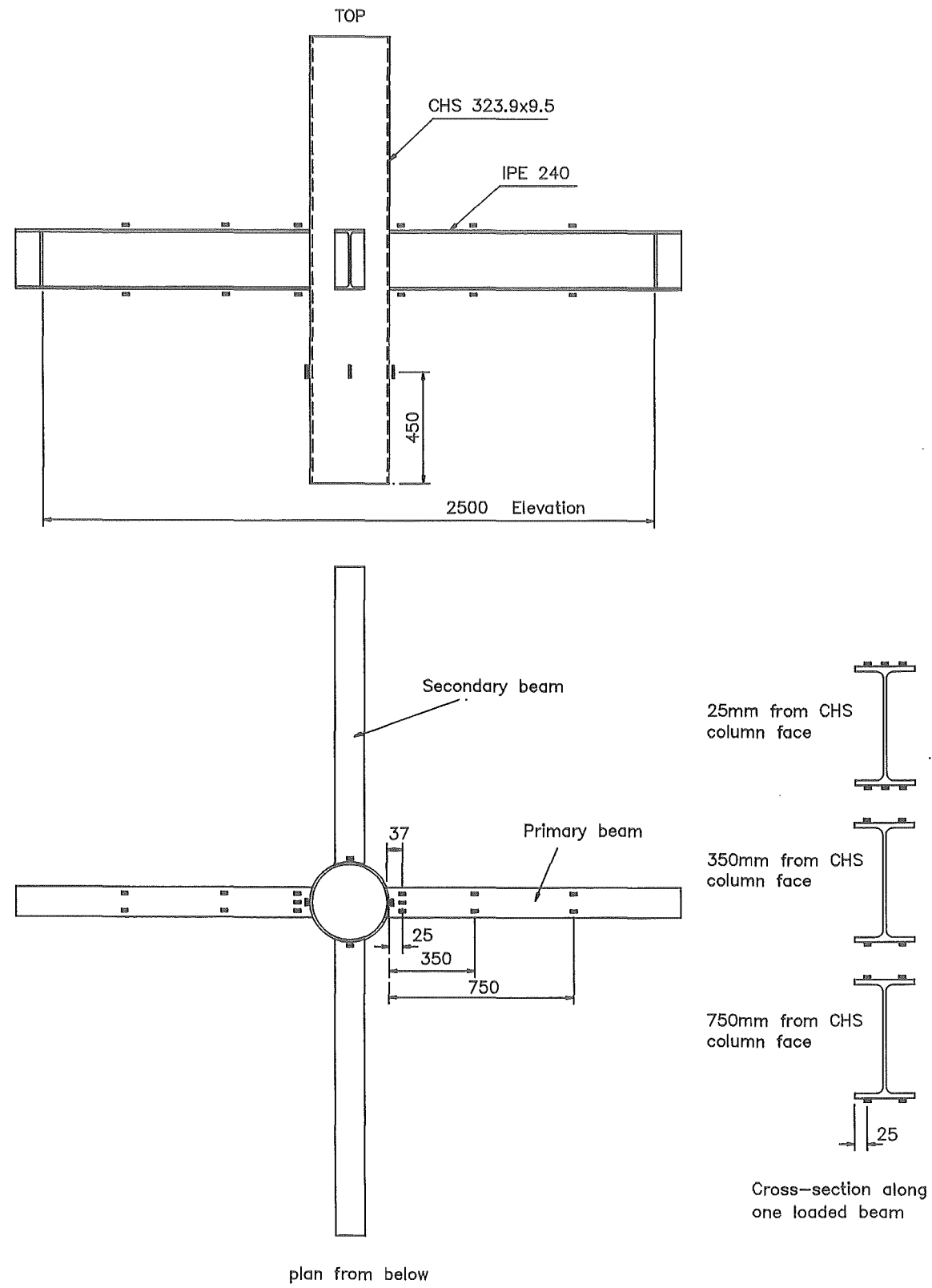


Fig. 4-26 : Strain gauging for 3C1 (28 on primary beams and 4 on column)

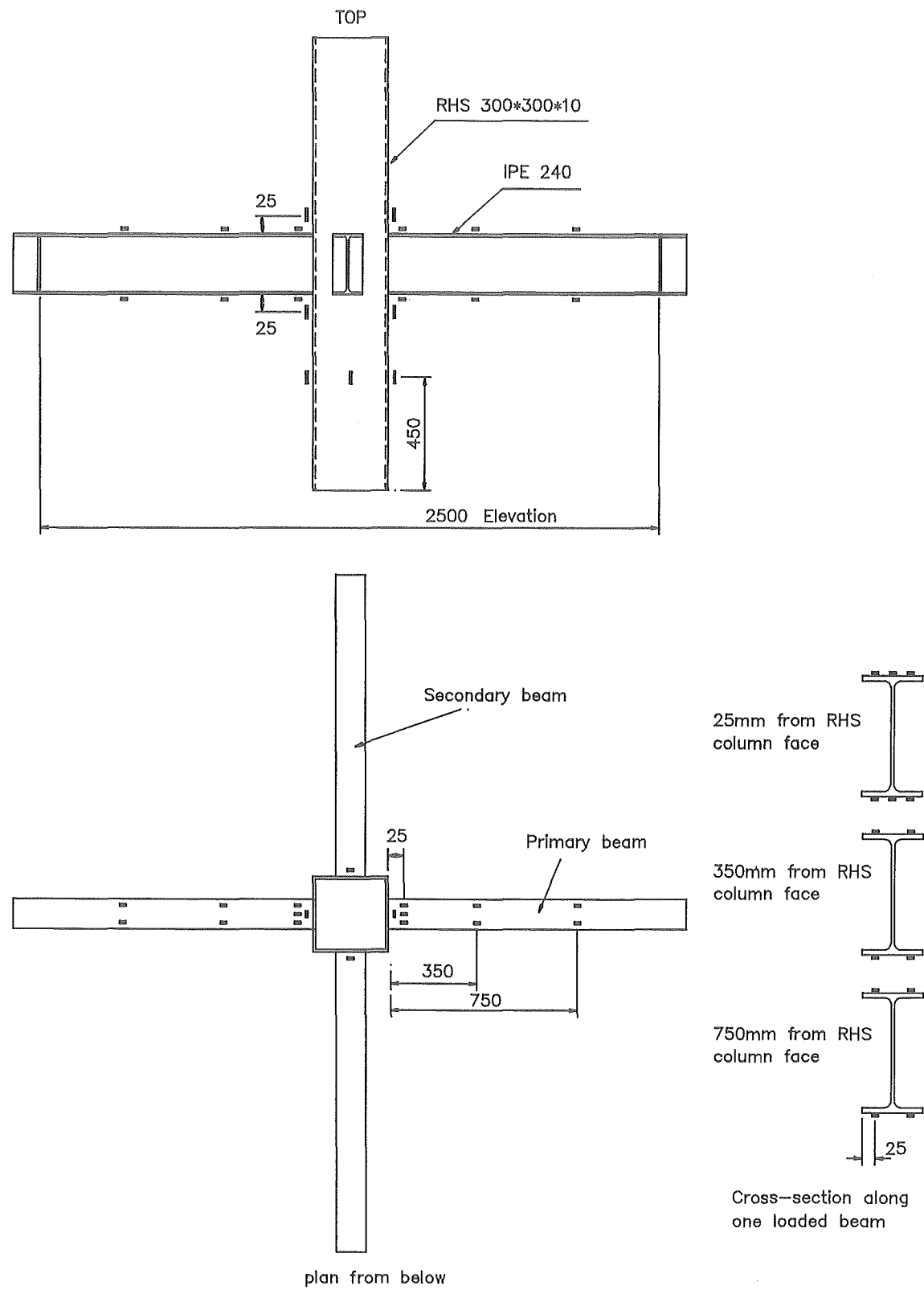


Fig. 4-27 : Strain gauging for 3R1 (28 on primary beams and 8 on column)

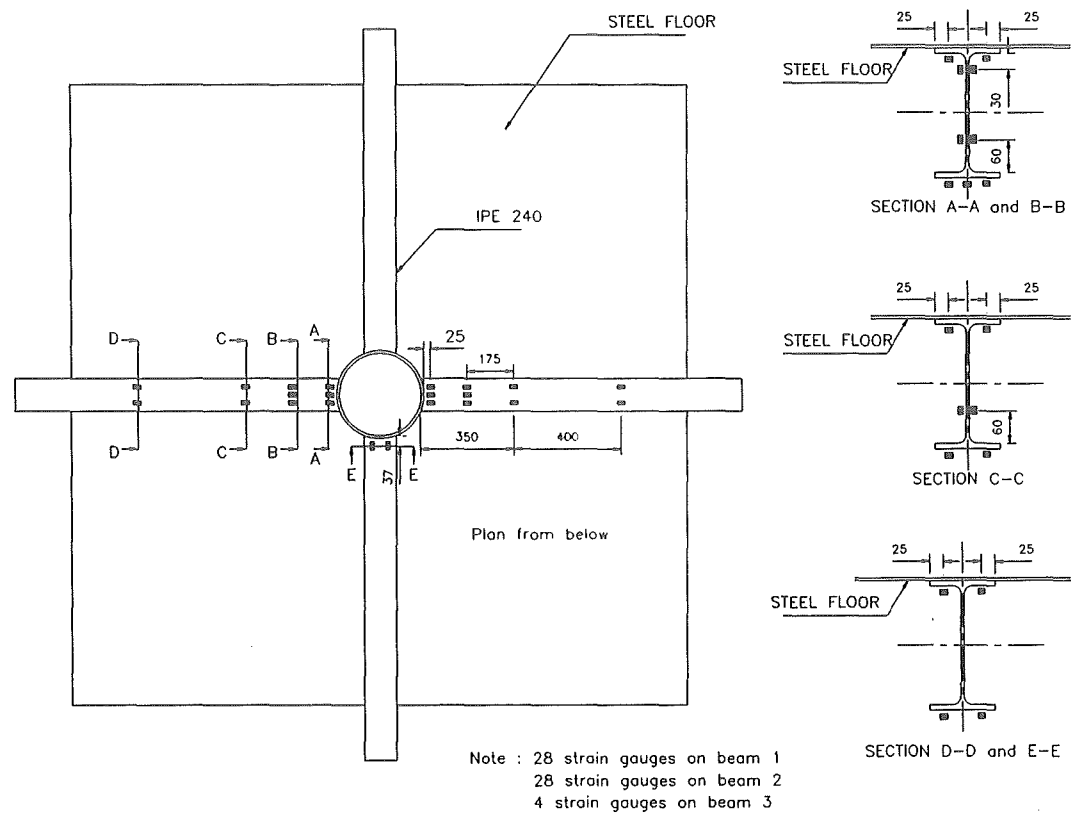


Fig. 4-28 : Strain gauges on beam for 3C2 (60 No.)

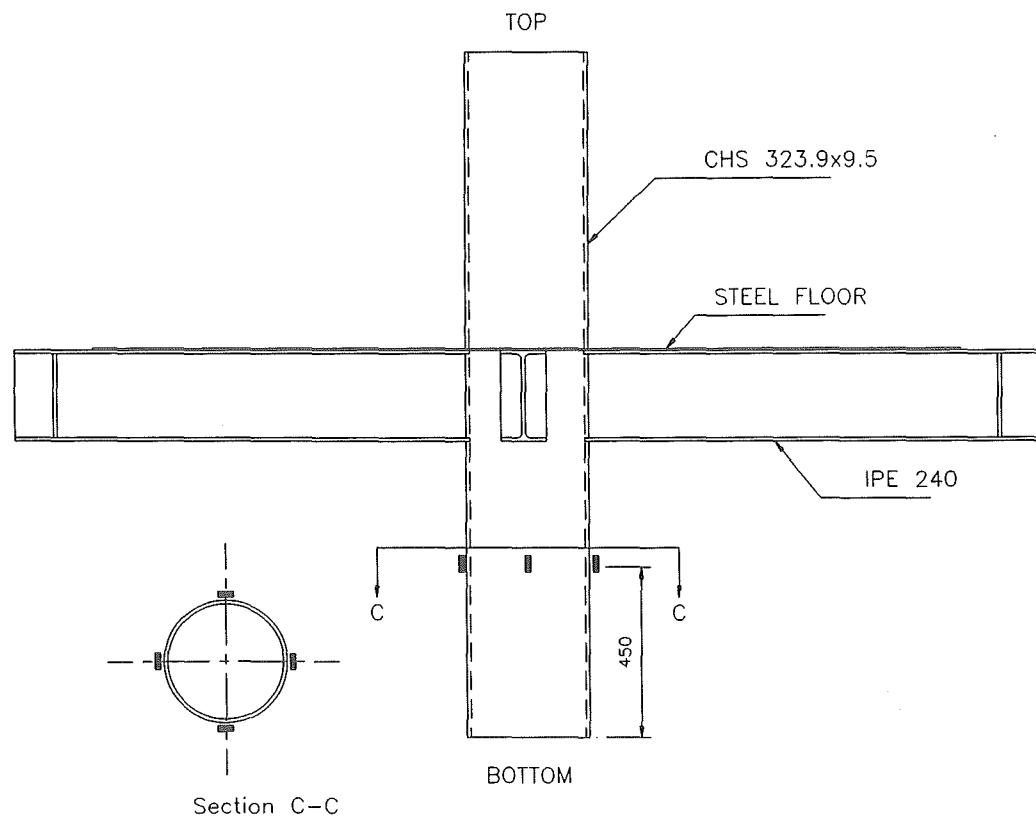
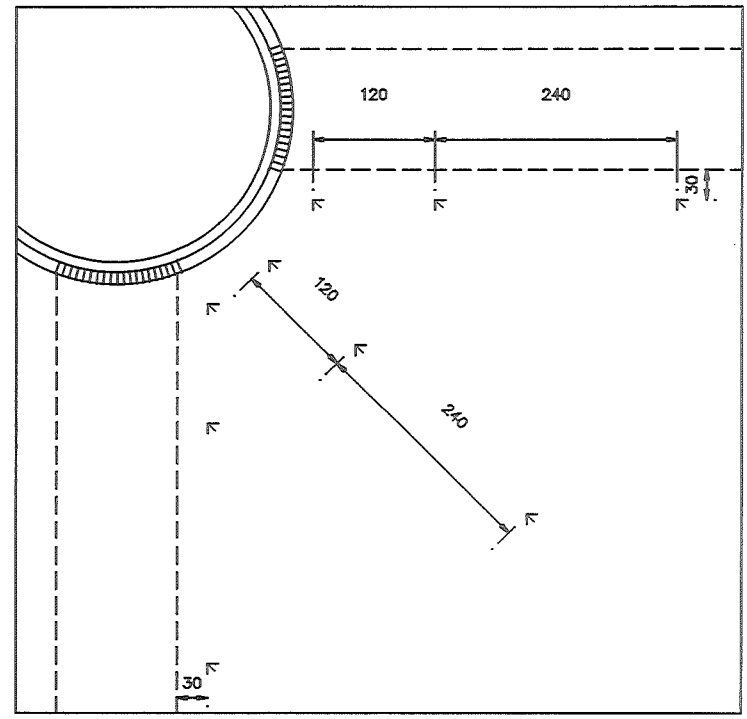
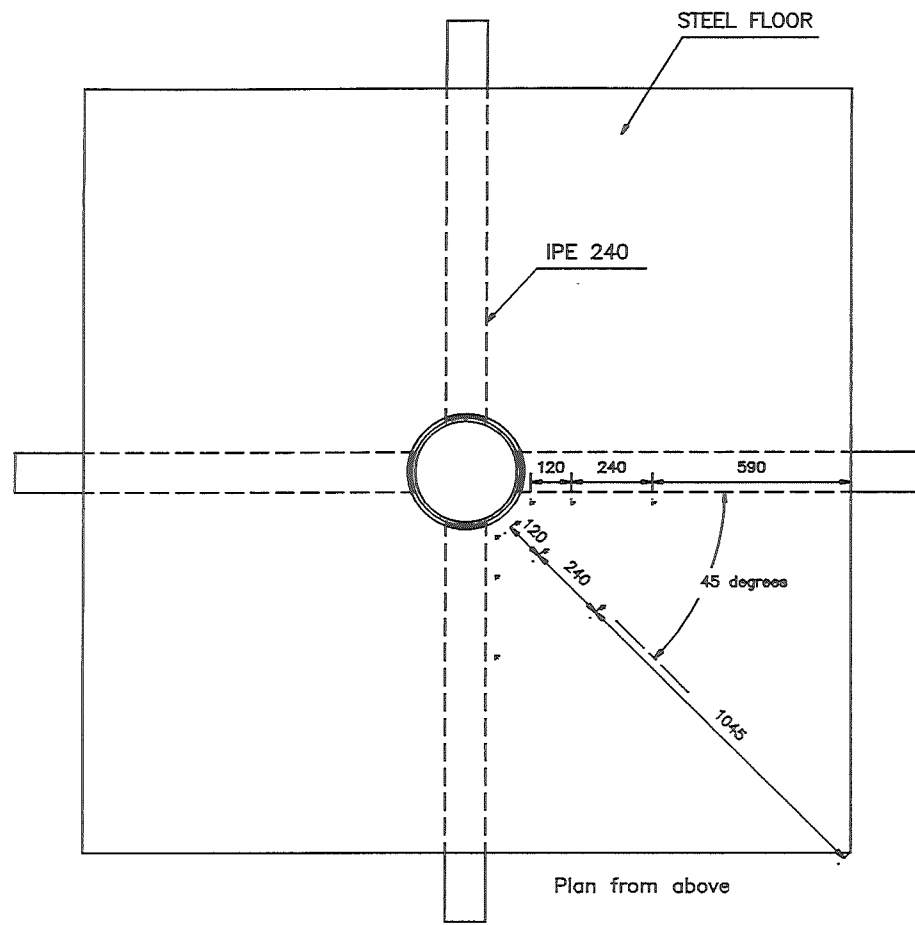


Fig. 4-29 : Strain gauges on column for 3C2 (4 No.)



Note : Arrangement of rosettes for 3R2 is similar to 3C2

Fig. 4-30 : Strain rosettes for steel floor of 3C2 (9 locations)

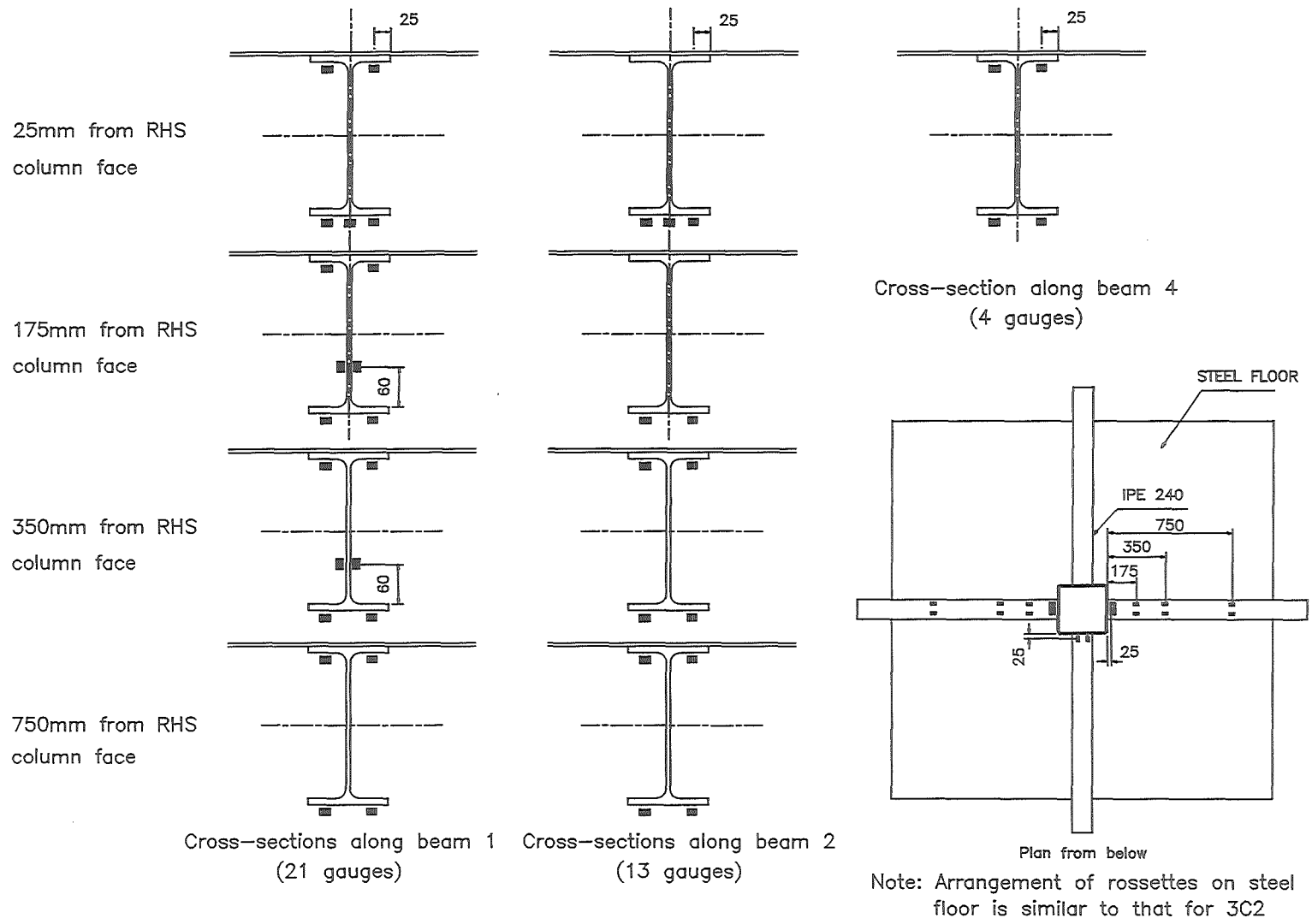


Fig. 4-31 : Strain gauges on beams for 3R2 (38 No.)

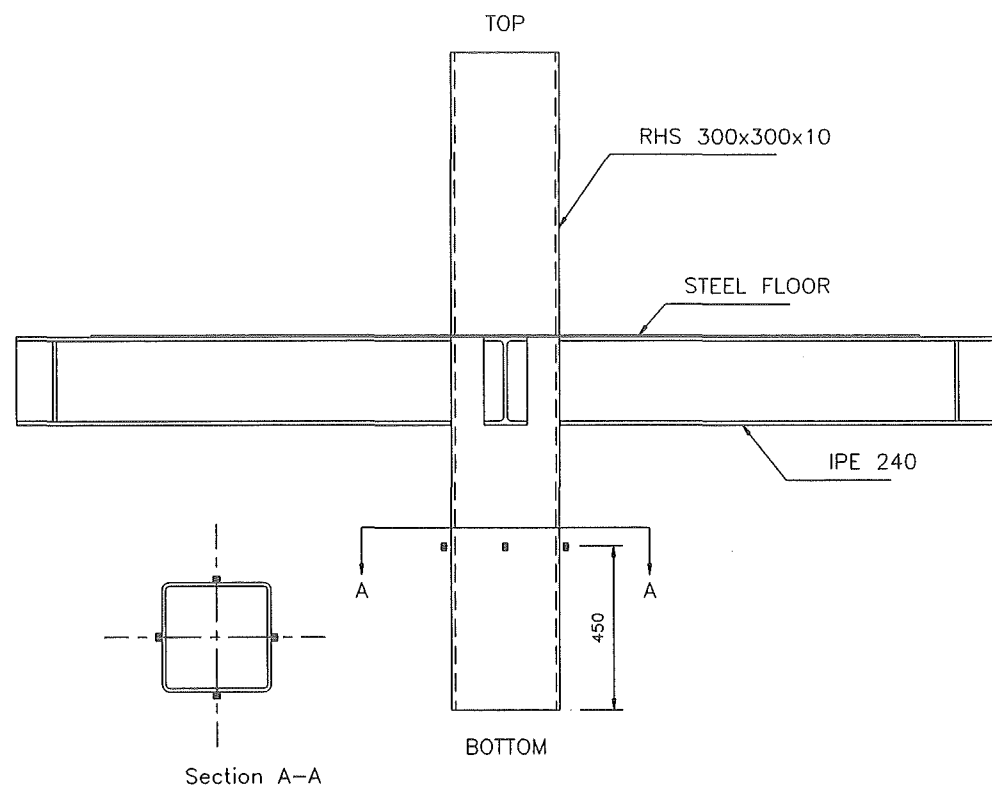


Fig. 4-32 : Strain gauges on column for 3R2

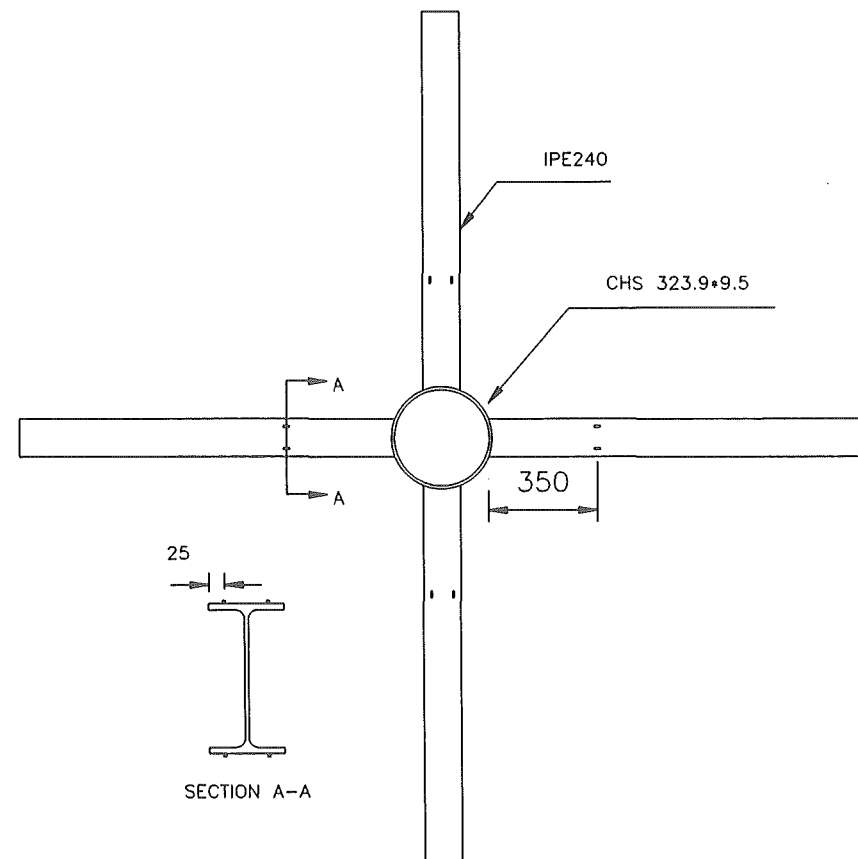
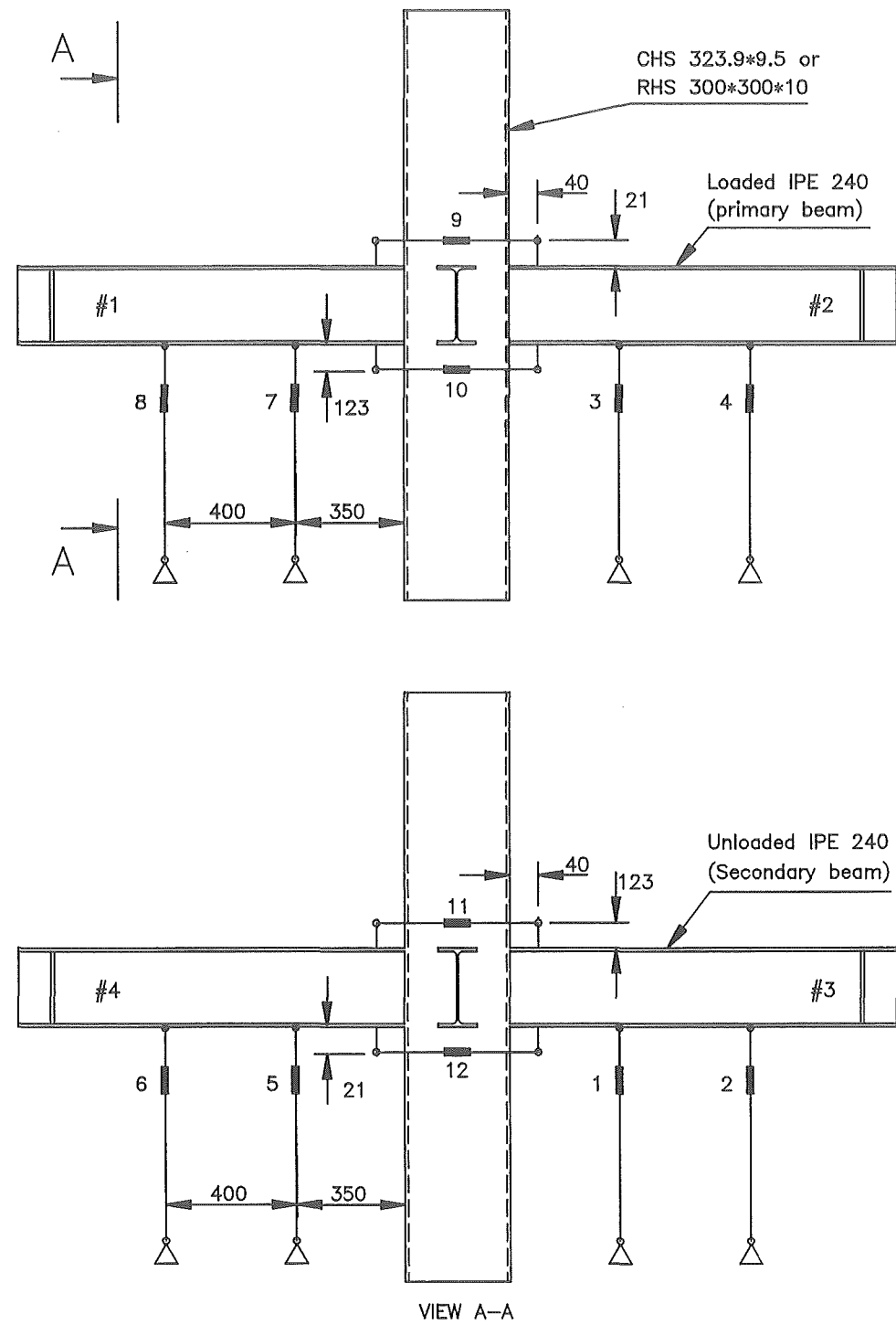


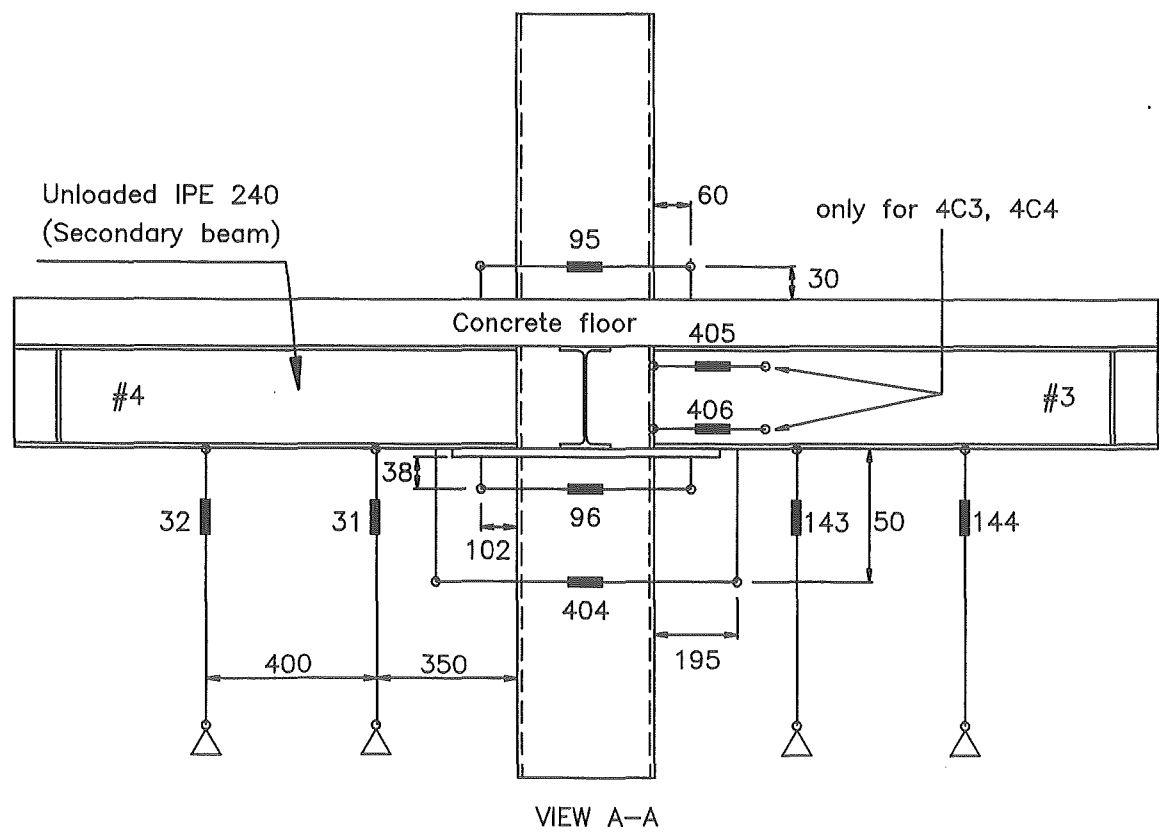
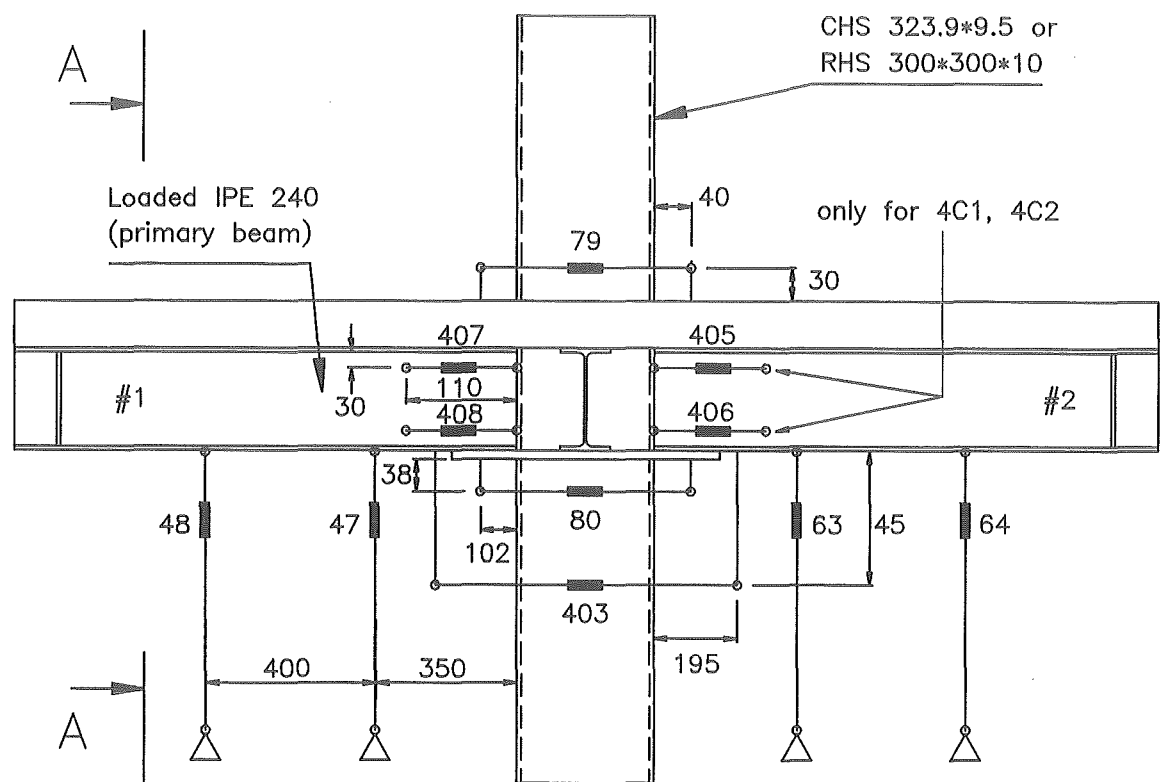
Fig. 4-33 : Strain gauges on beams for 3C3 and 3C4 (16 No. each)



Notes:

- 1) All transducer measurements are along beam centre-lines
- 2) Deflection of loaded beams at locations 3, 4, 7 and 8
- 2) Deflection of unloaded beams at locations 1, 2, 5 and 6
- 3) Deformation of column at locations 9, 10, 11 and 12

Fig. 4-42 : Typical schematic details of transducers for series 3 (3C1-3C4, 3R1-3R4)



VIEW A-A

Fig. 4-43 : Typical schematic details of transducers for series 4 (4C1, 4C2, 4C3 and 4C4)

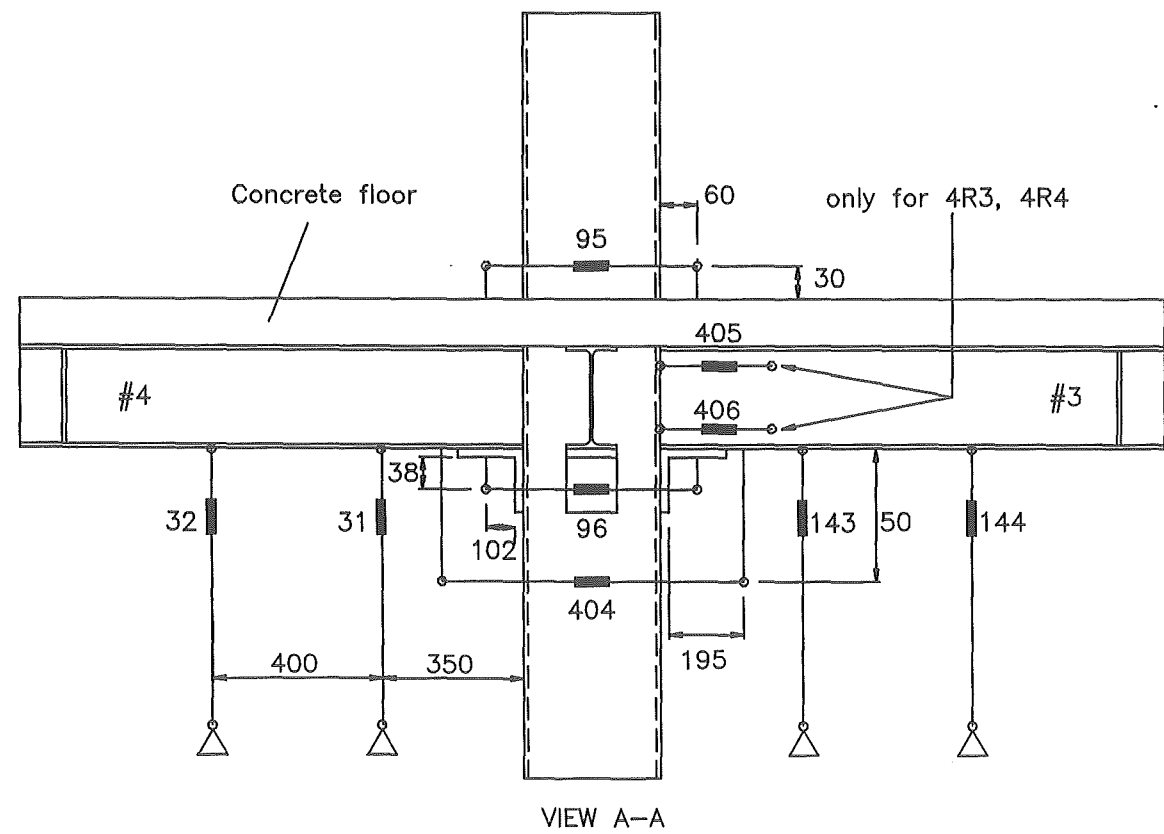
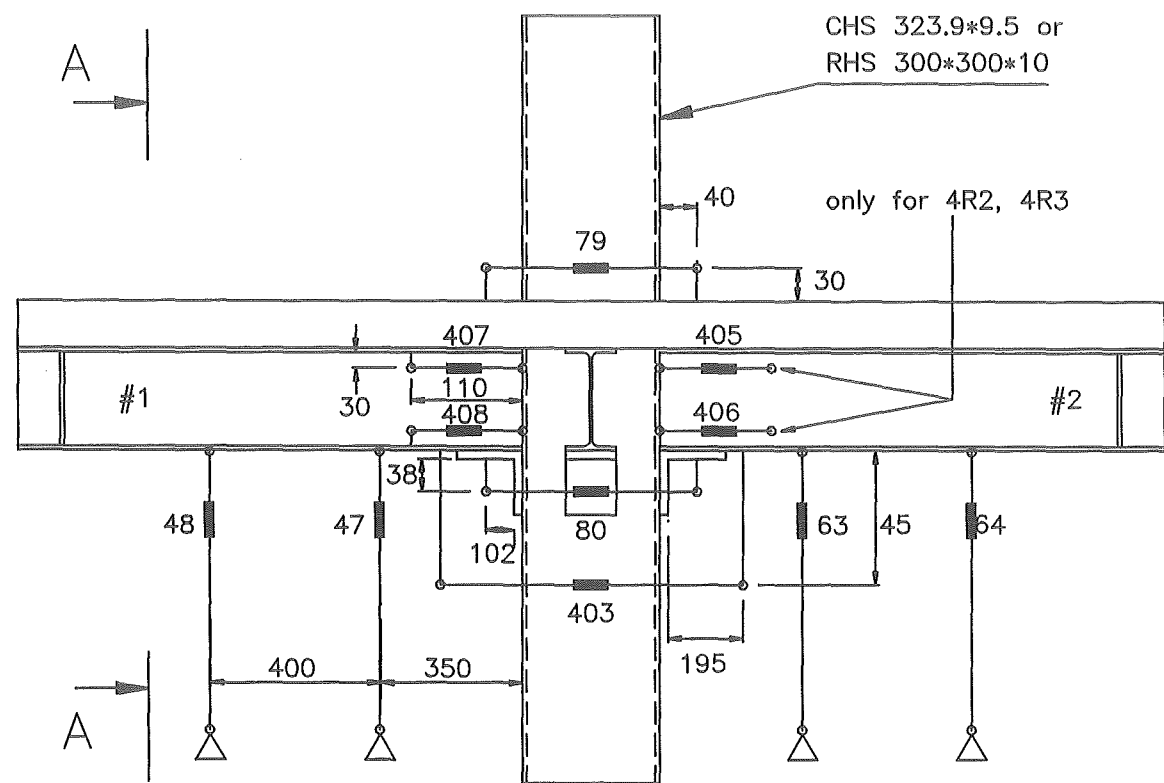


Fig. 4-44 : Typical schematic details of transducers for series 4 (4R1, 4R2, 4R3 and 4R4)

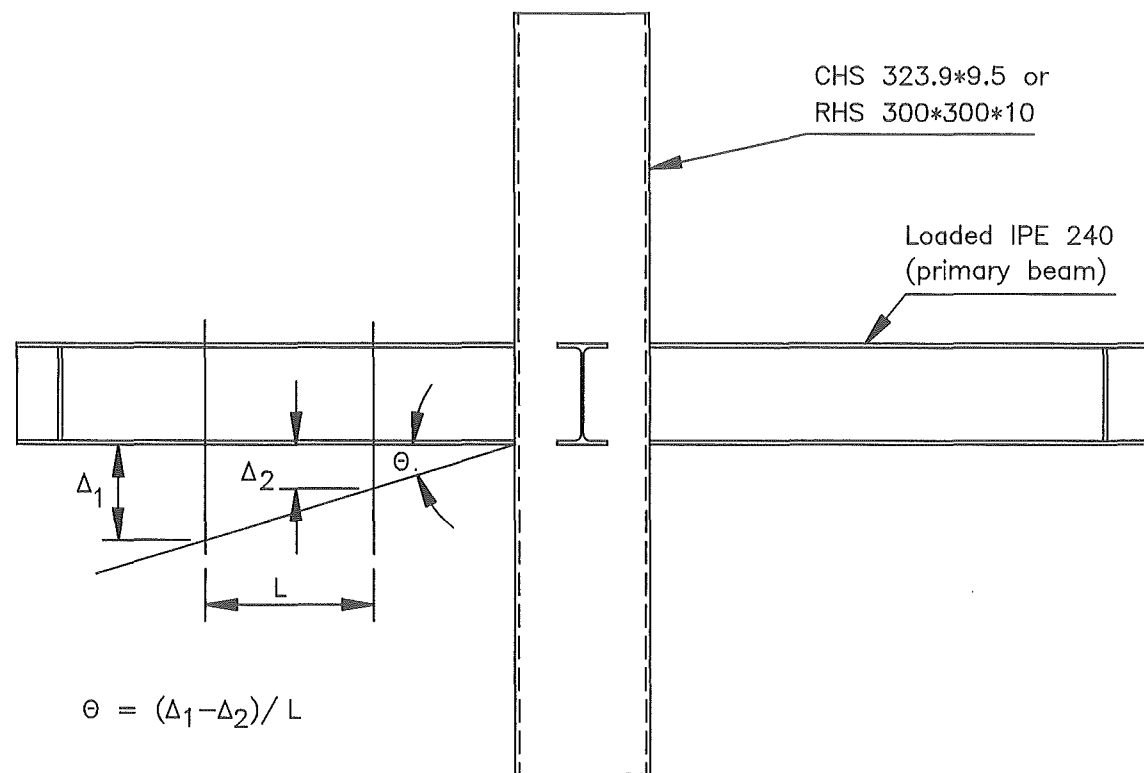


Fig. 4-45 : Definition of connection rotation

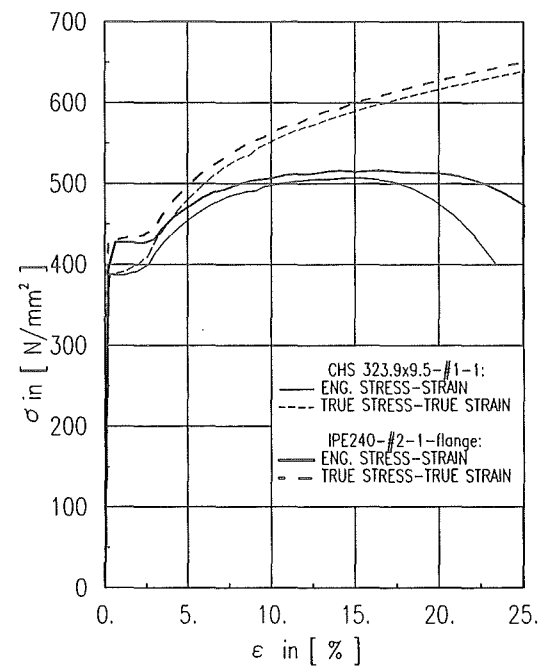


Fig.: 5-1 Typical stress-strain relationships

WELD SIZES FOR FE MESHES OF 3C3

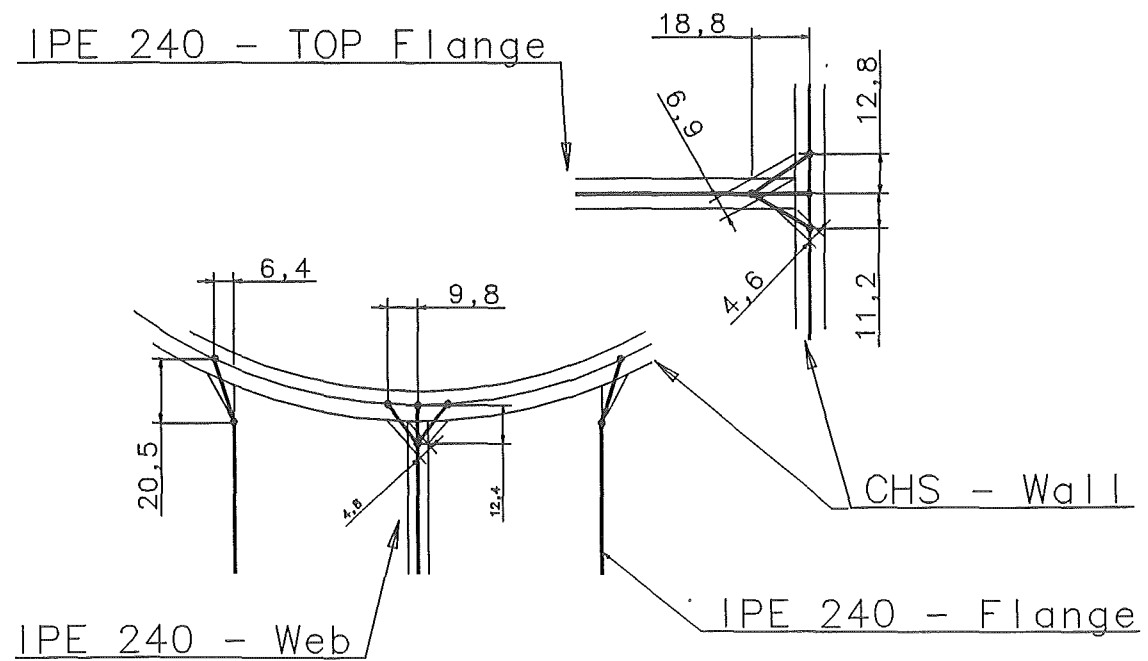


Fig: 5-2 Weld simulations with shell elements

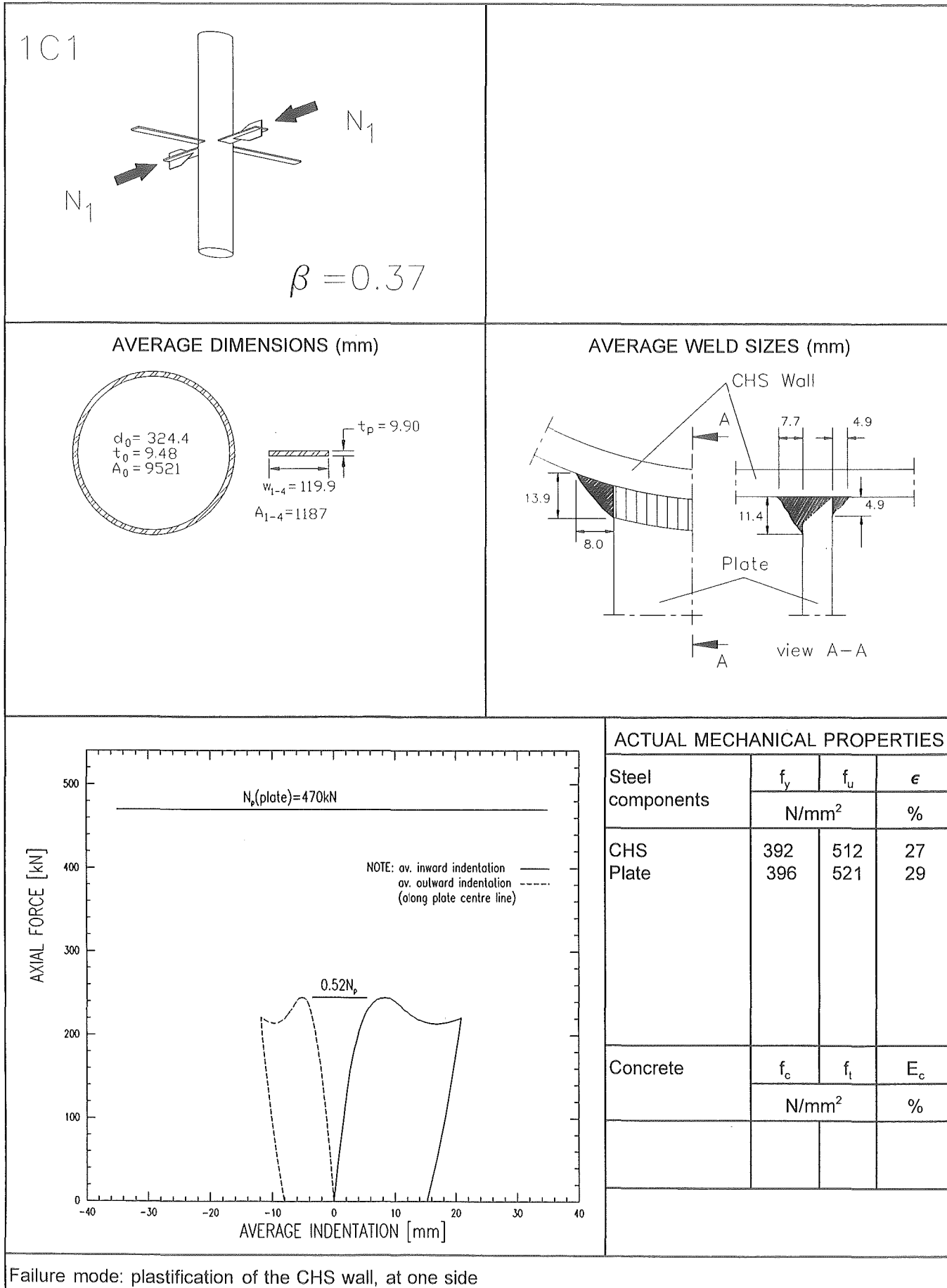


Fig. 6-1 : Data sheet for test 1C1

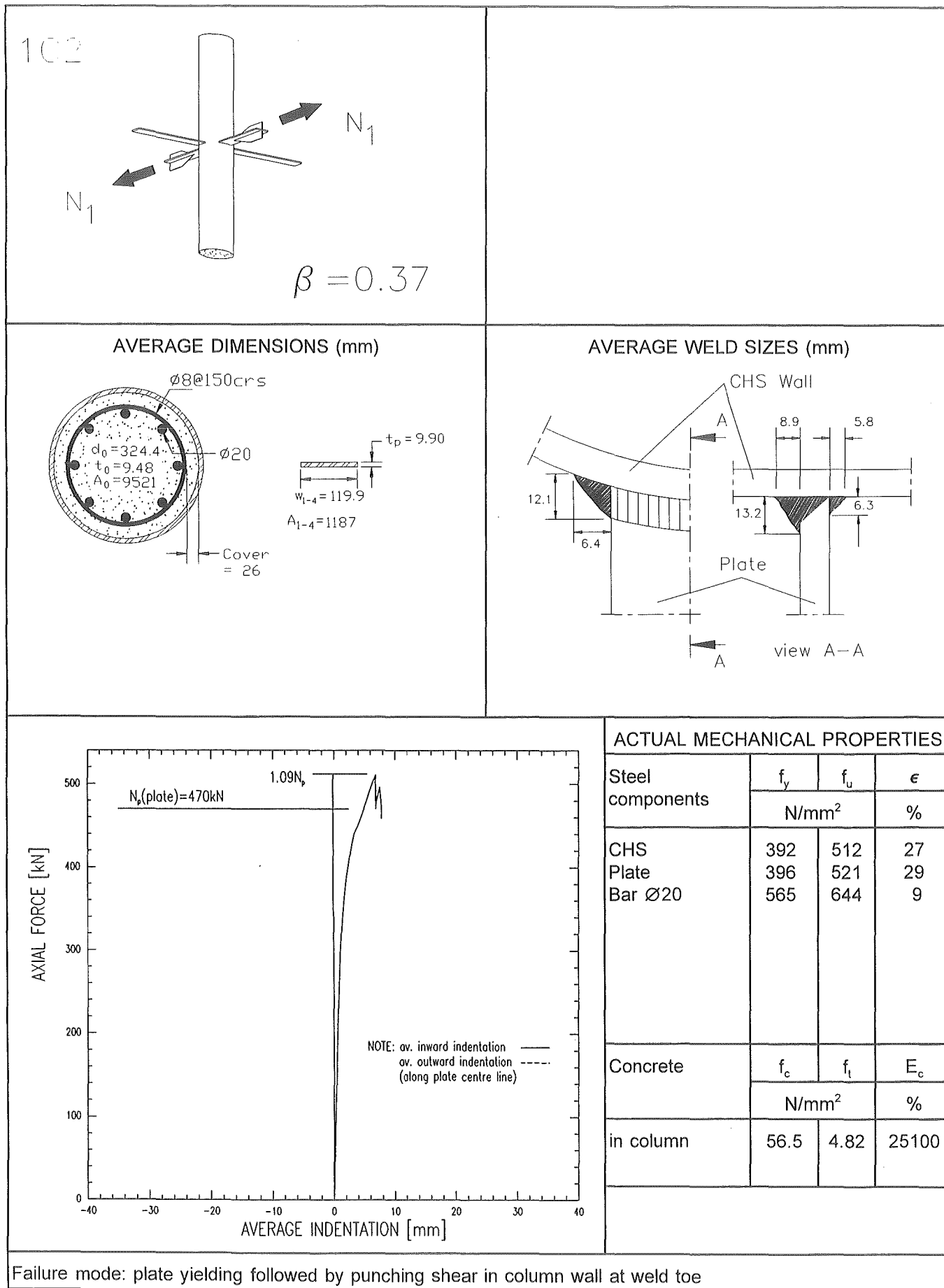
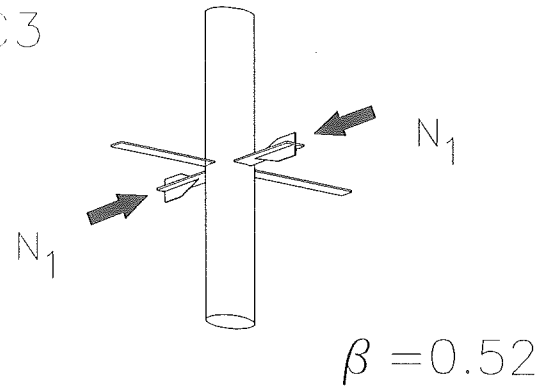
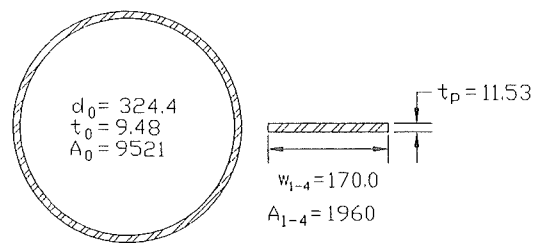


Fig. 6-2 : Data sheet for test 1C2

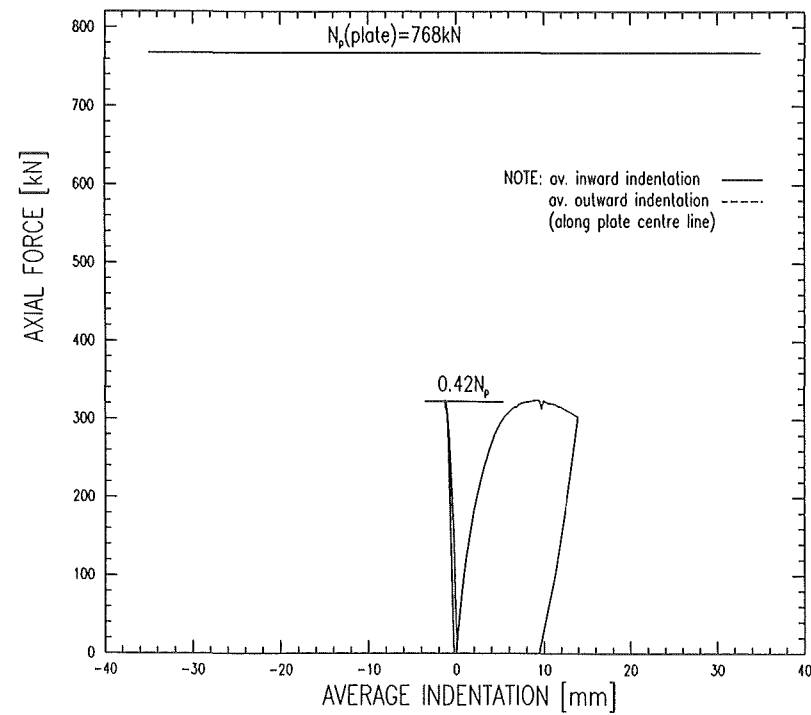
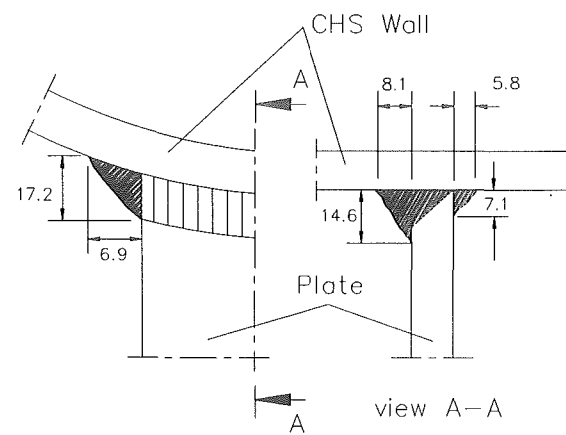
1C3



AVERAGE DIMENSIONS (mm)



AVERAGE WELD SIZES (mm)



ACTUAL MECHANICAL PROPERTIES

Steel components	f_y	f_u	ϵ
	N/mm ²		%
CHS Plate	392	512	27
	392	516	31
Concrete	f_c	f_t	E_c
	N/mm ²		%

Failure mode: plastification of the CHS wall

Fig. 6-3 : Data sheet for test 1C3

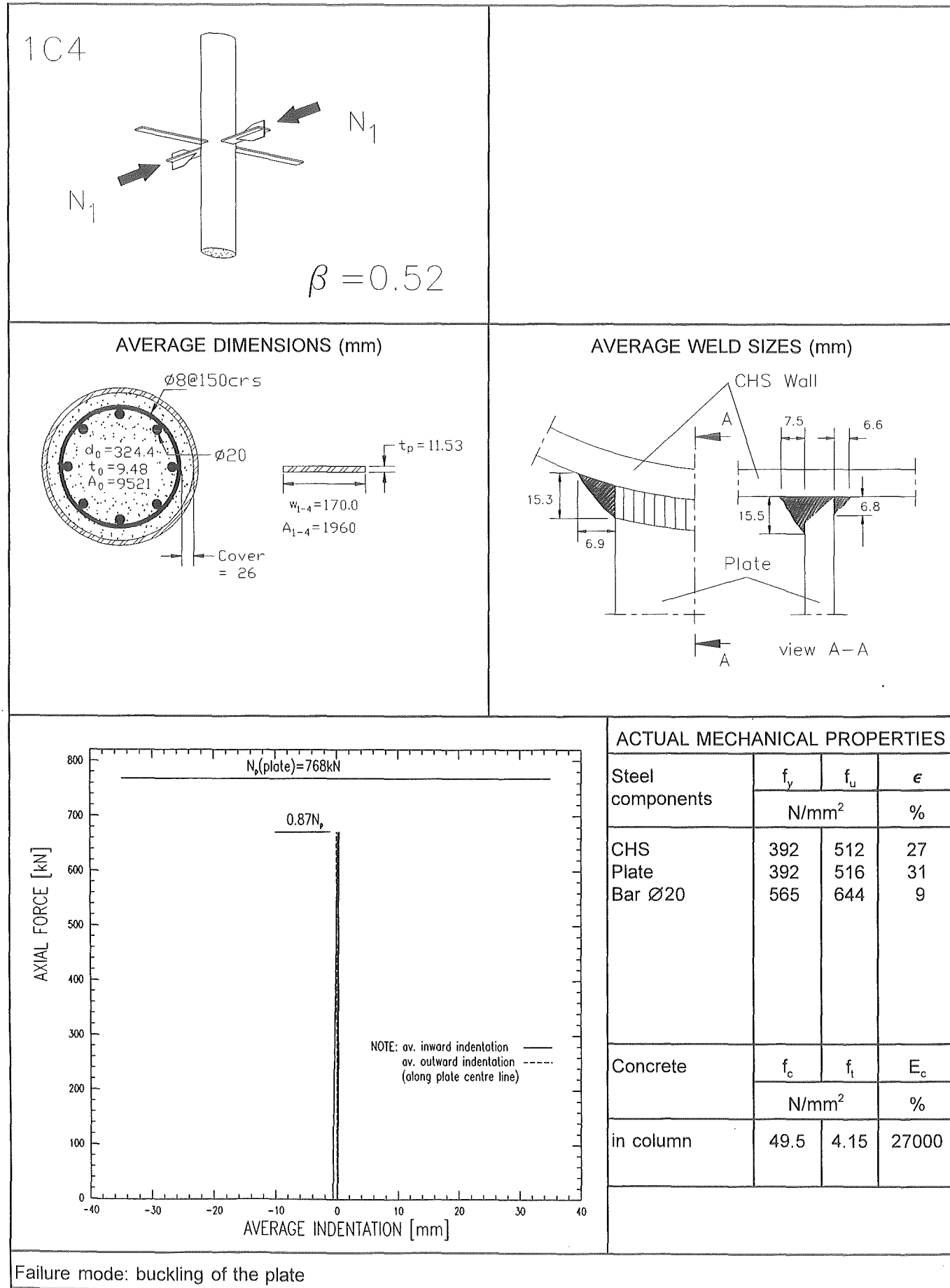


Fig. 6-4 : Data sheet for test 1C4

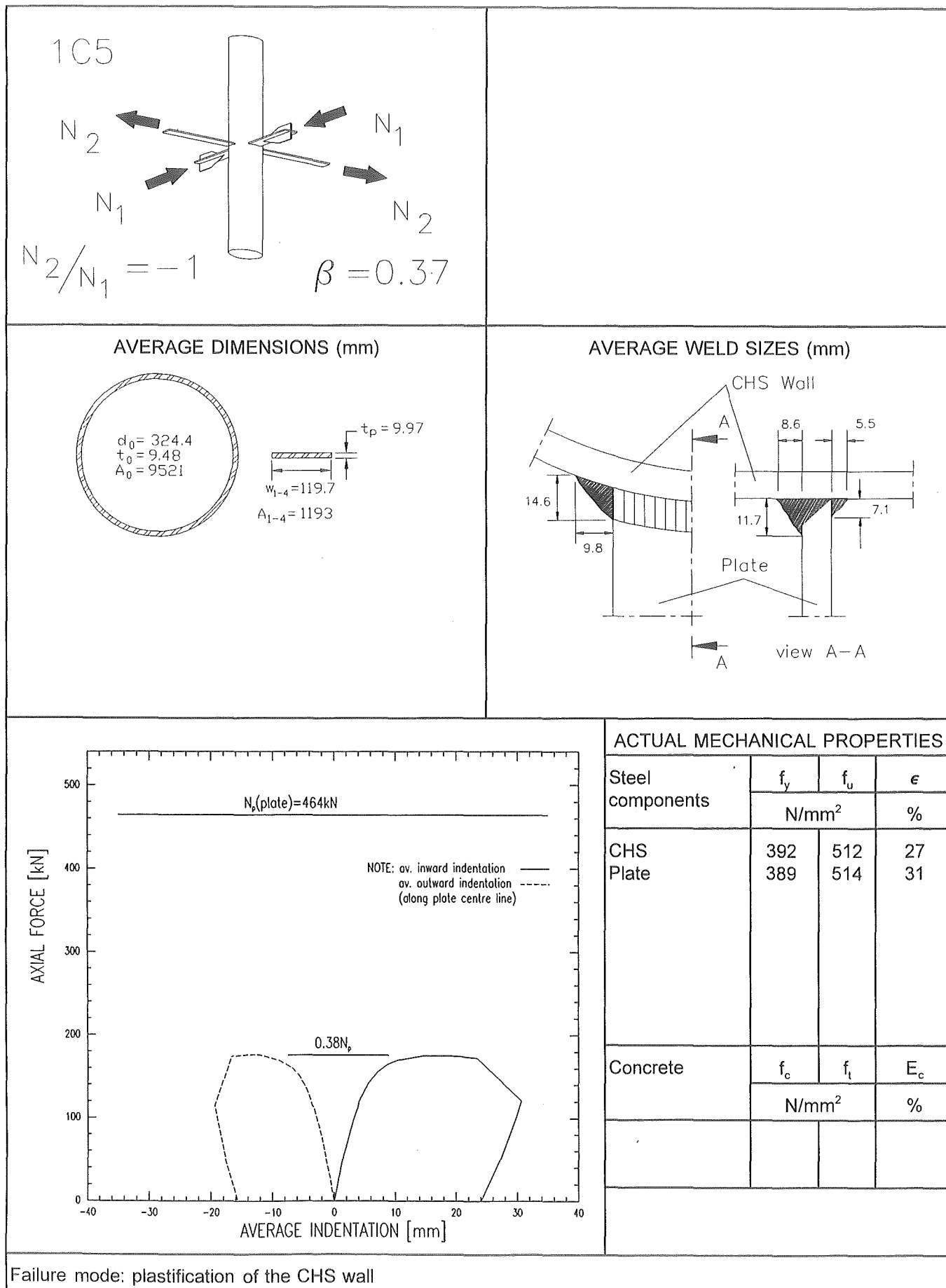
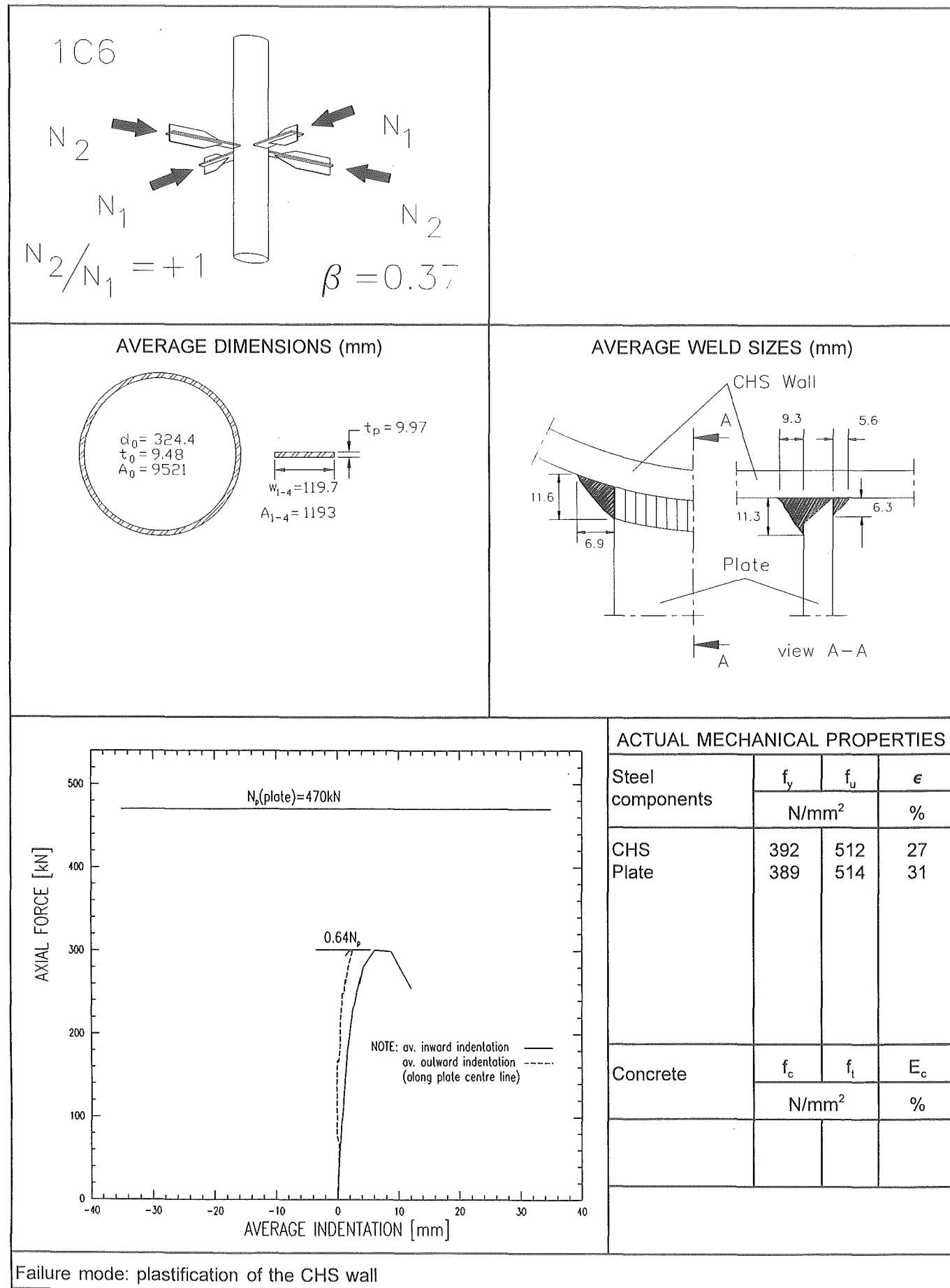


Fig. 6-5 : Data sheet for test 1C5



Failure mode: plastification of the CHS wall

Fig. 6-6 : Data sheet for test 1C6

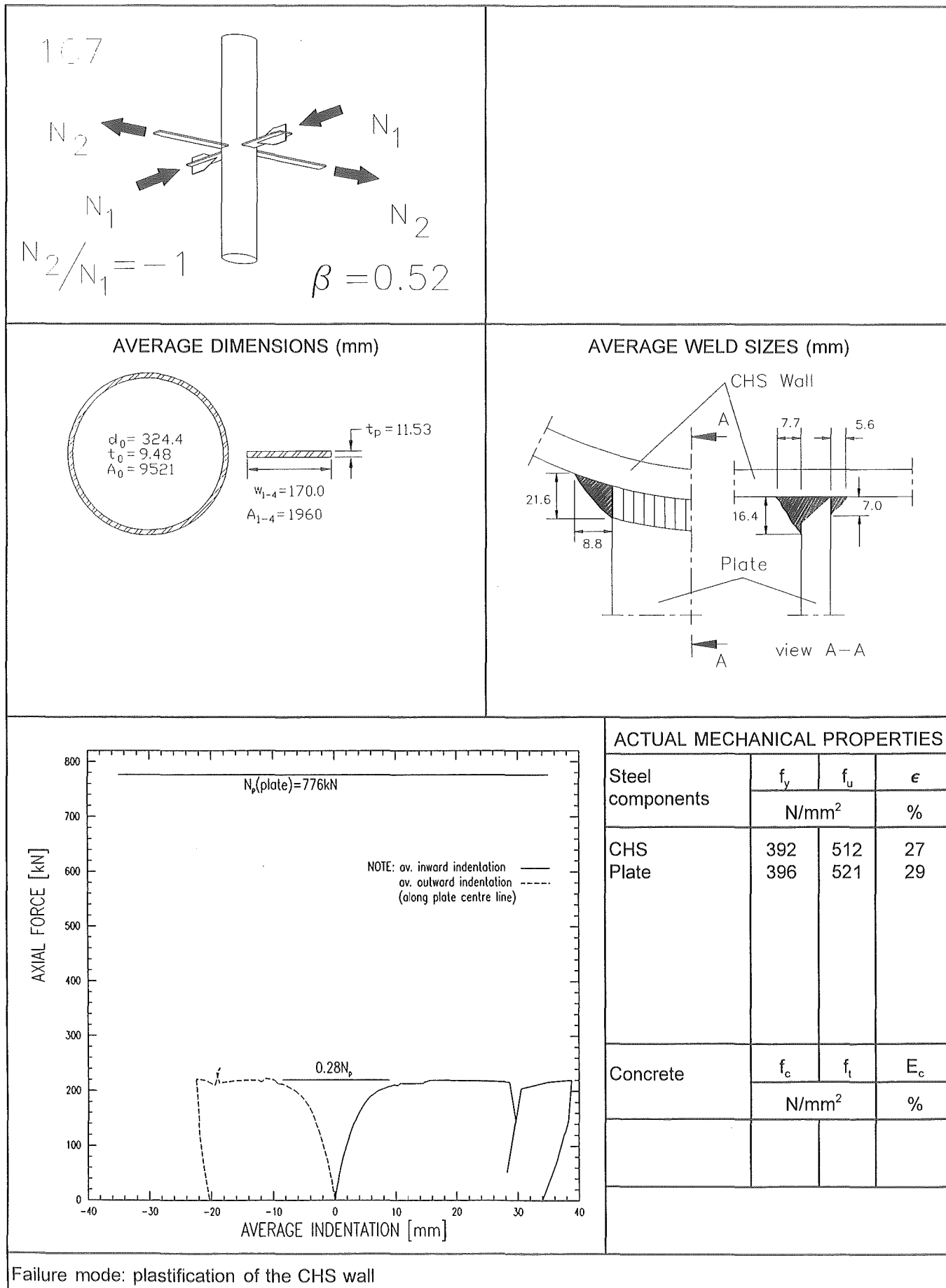


Fig. 6-7 : Data sheet for test 1C7

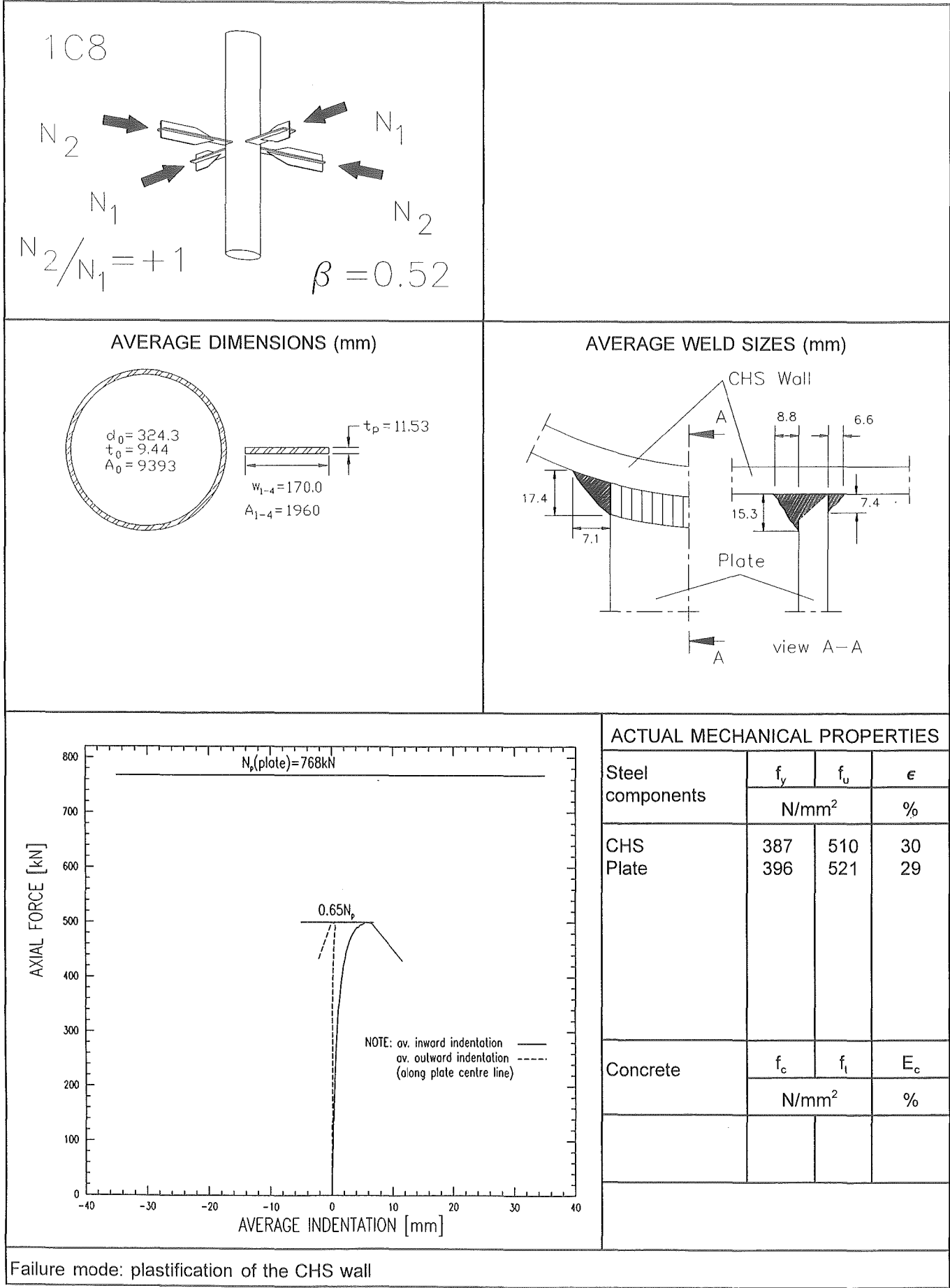
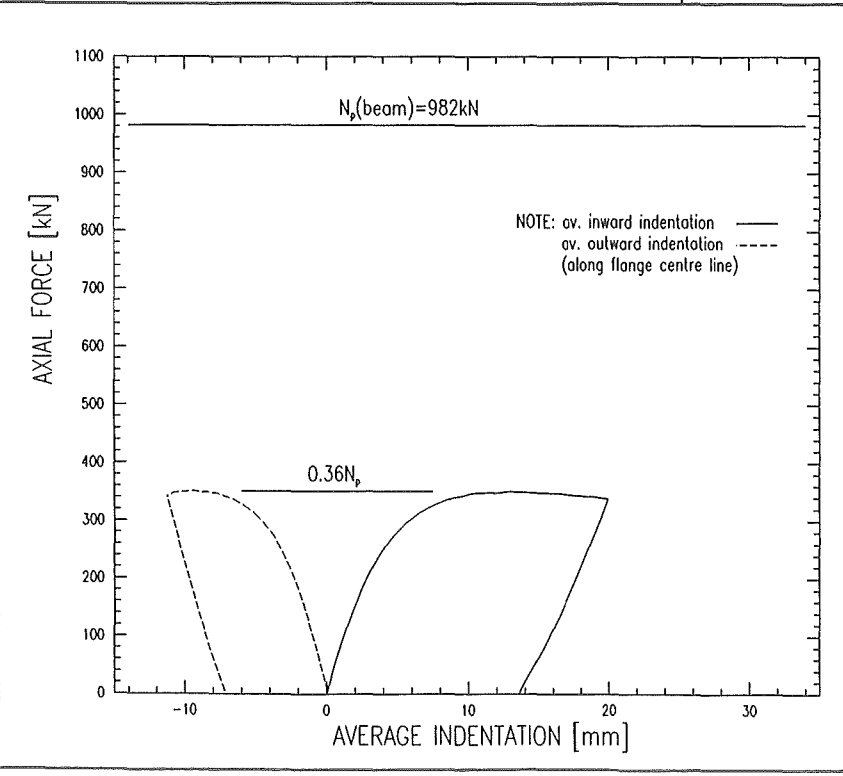
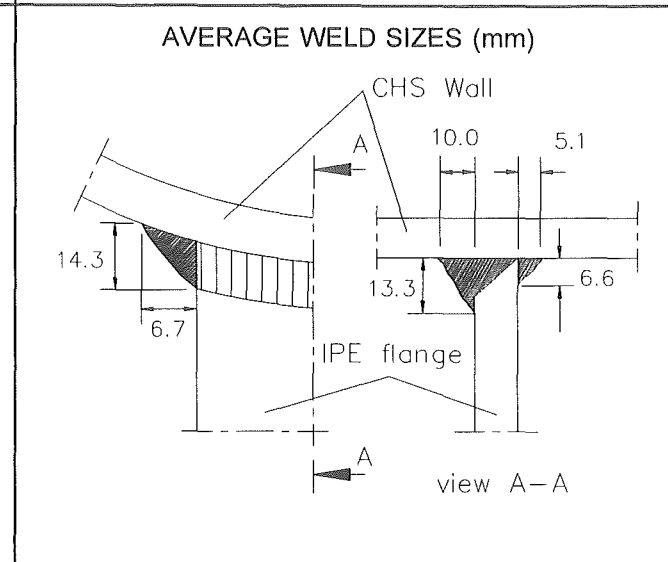
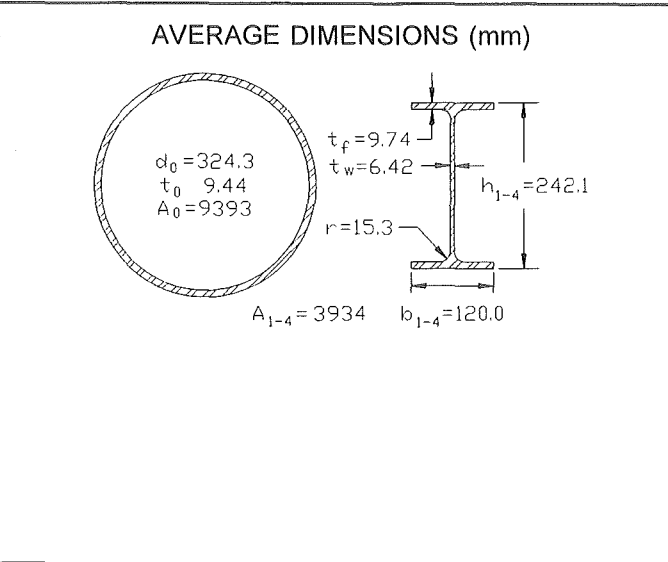
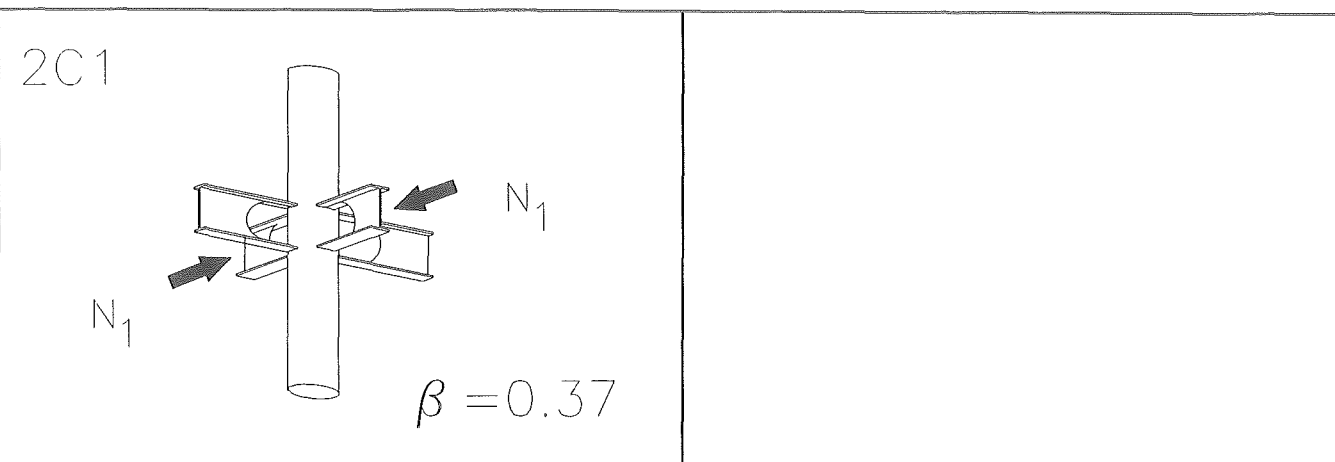


Fig. 6-8 : Data sheet for test 1C8



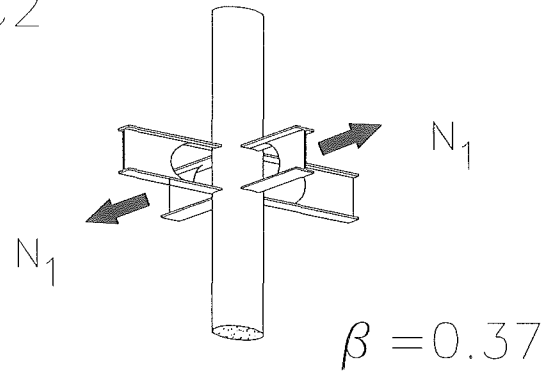
ACTUAL MECHANICAL PROPERTIES

Steel components	f_y	f_u	ϵ
	N/mm ²		%
CHS	387	510	30
IPE(flange)	420	520	32
IPE(web)	480	633	26
Concrete	f_c	f_t	E_c
	N/mm ²		%

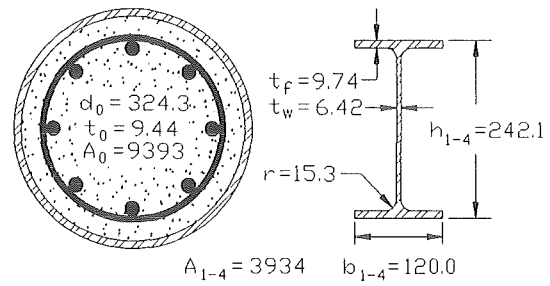
Failure mode: plastification of the CHS wall

Fig. 6-9 : Data sheet for test 2C1

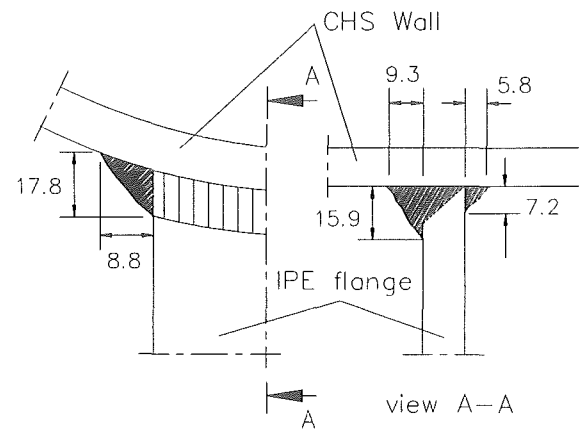
2C2



AVERAGE DIMENSIONS (mm)

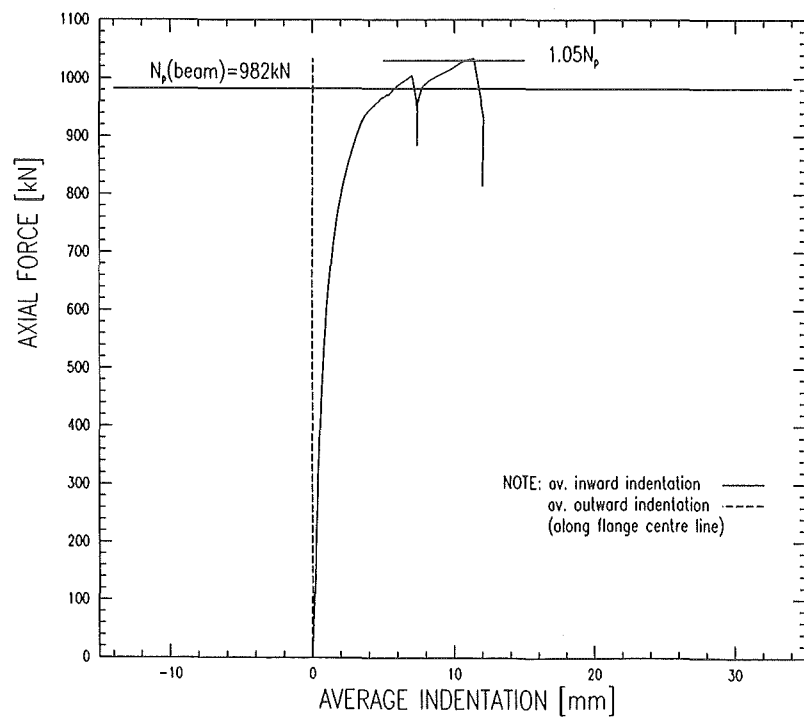


AVERAGE WELD SIZES (mm)



ACTUAL MECHANICAL PROPERTIES

Steel components	f_y	f_u	ϵ
	N/mm ²		%
CHS	387	510	30
IPE(flange)	420	520	32
IPE(web)	480	633	26
Bar $\varnothing 20$	565	644	9
Concrete	f_c	f_t	E_c
	N/mm ²		%
column	54.7	3.88	27200



Failure mode: plate yielding followed by punching shear in column wall at weld toe

Fig. 6-10 : Data sheet for test 2C2

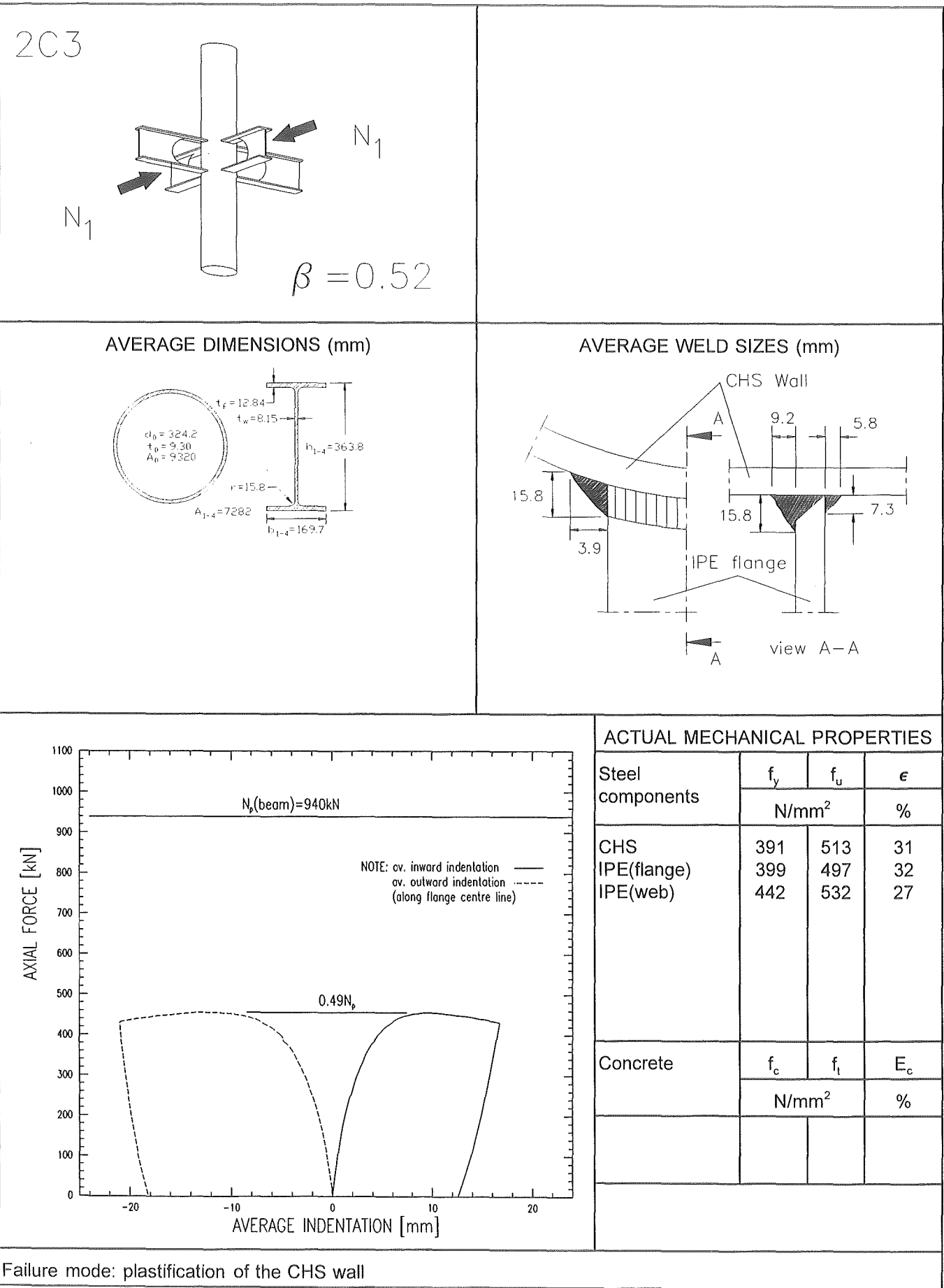
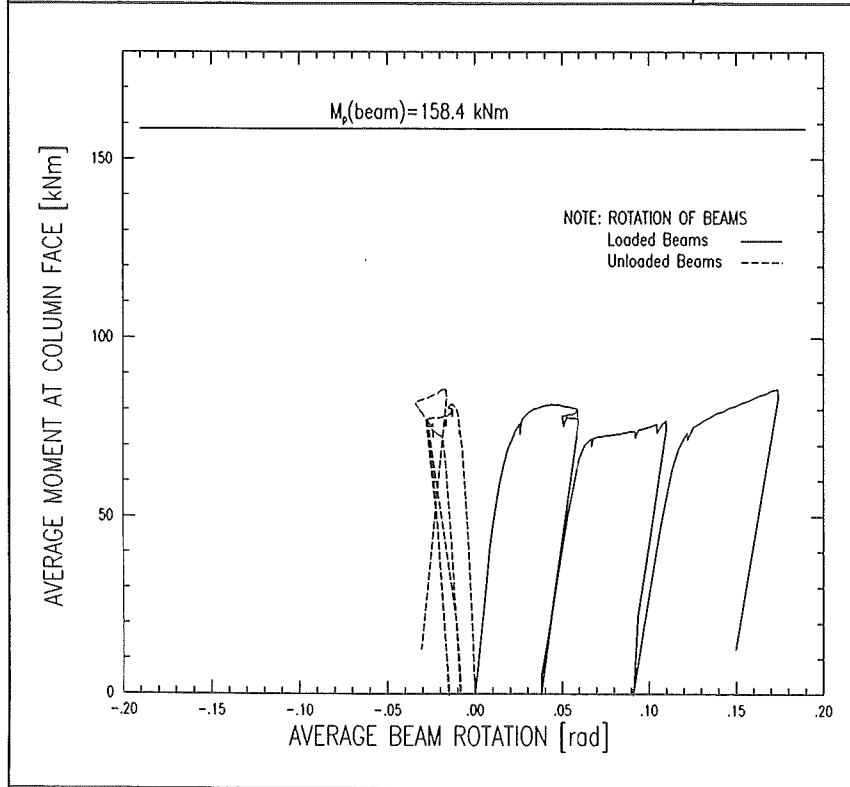
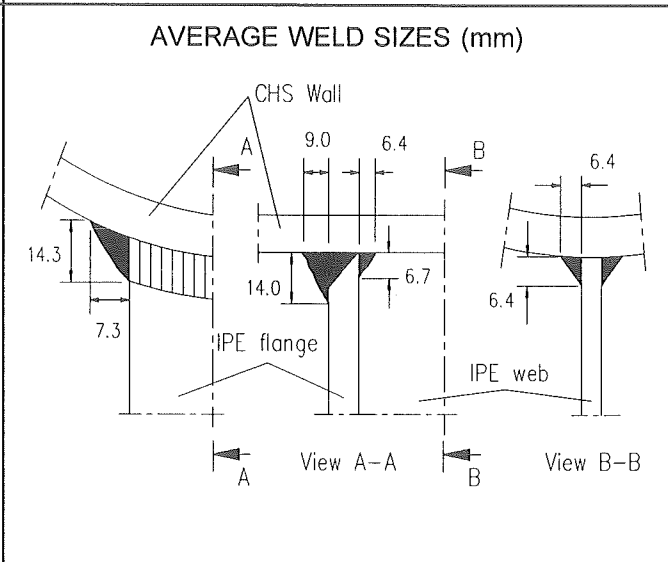
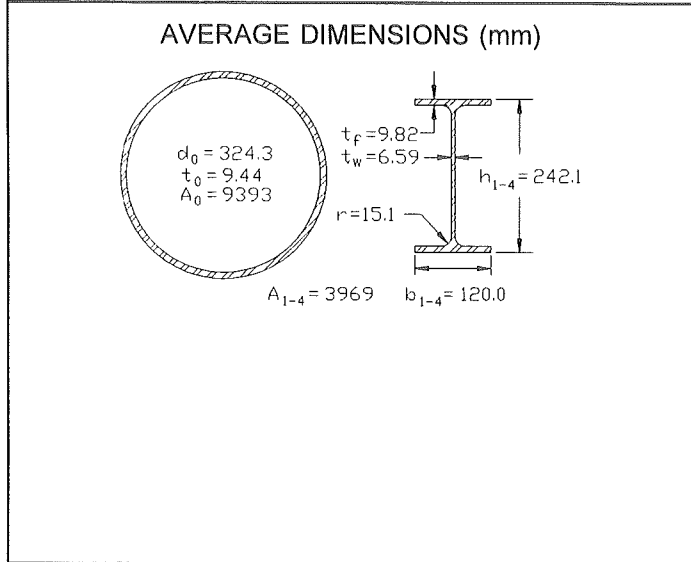
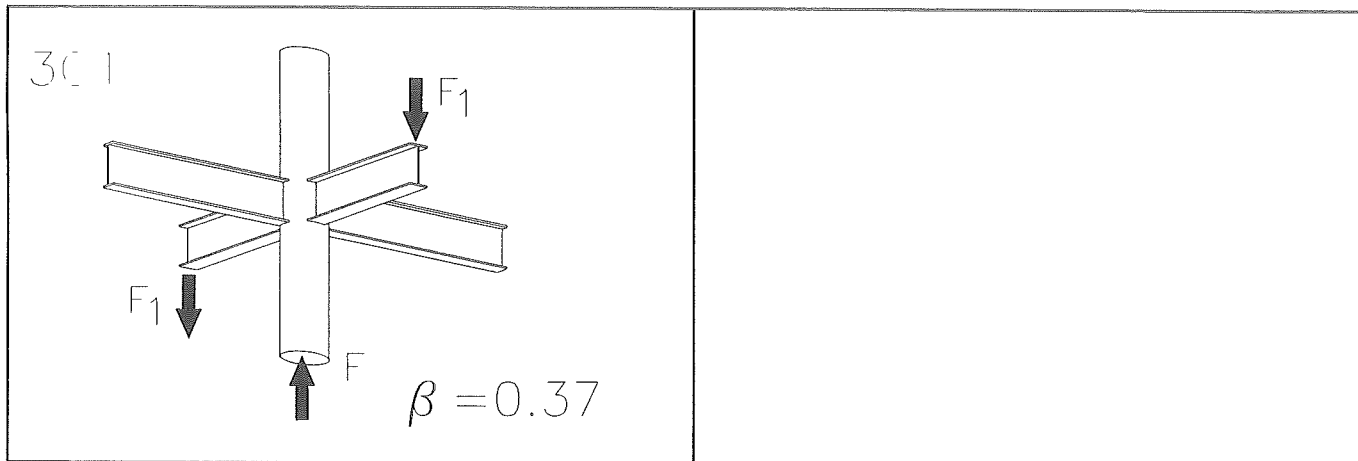


Fig. 6-11 : Data sheet for test 2C3

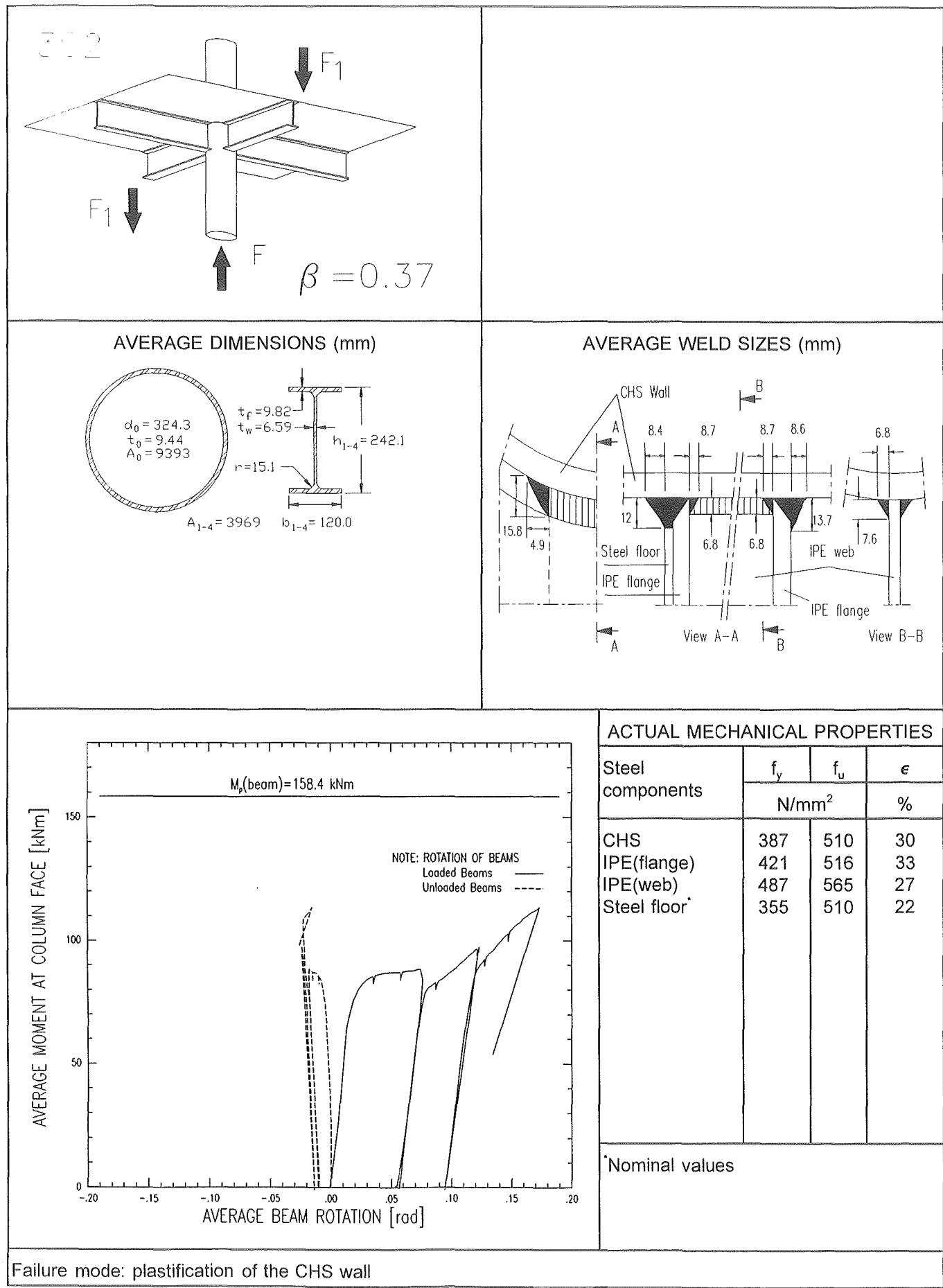


ACTUAL MECHANICAL PROPERTIES

Steel components	f_y	f_u	ϵ
	N/mm ²		%
CHS	387	510	30
IPE(flange)	421	516	33
IPE(web)	487	565	27

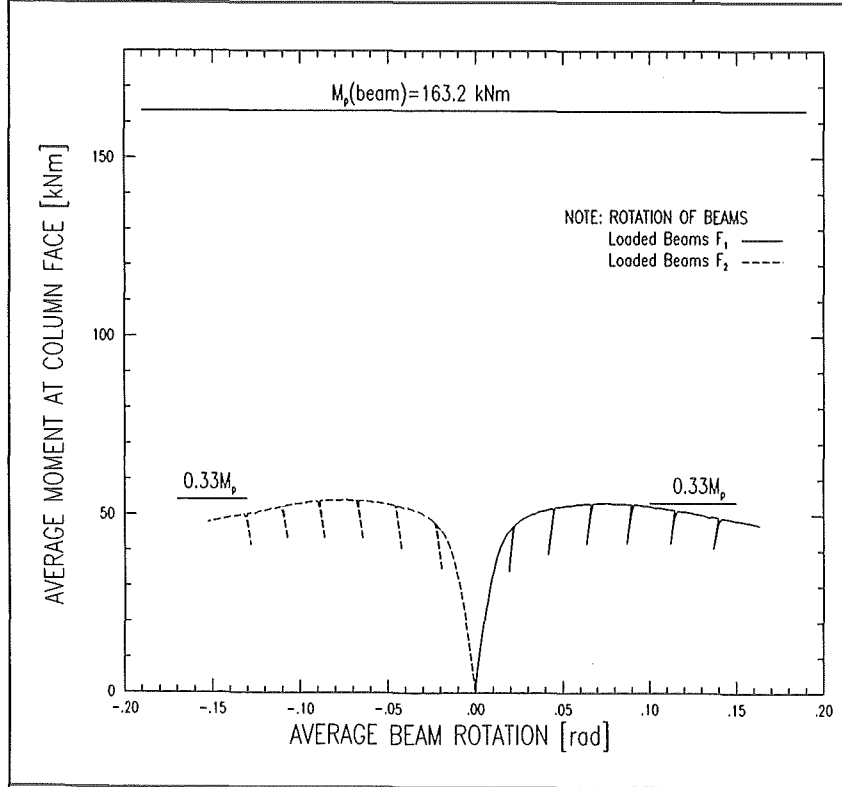
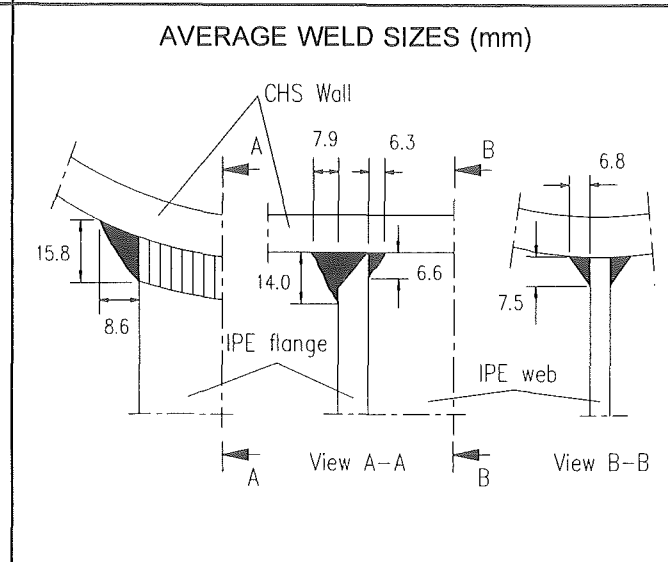
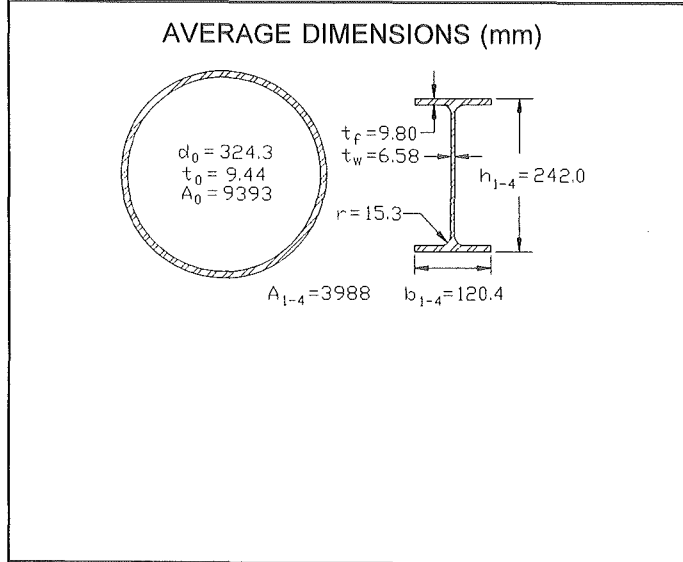
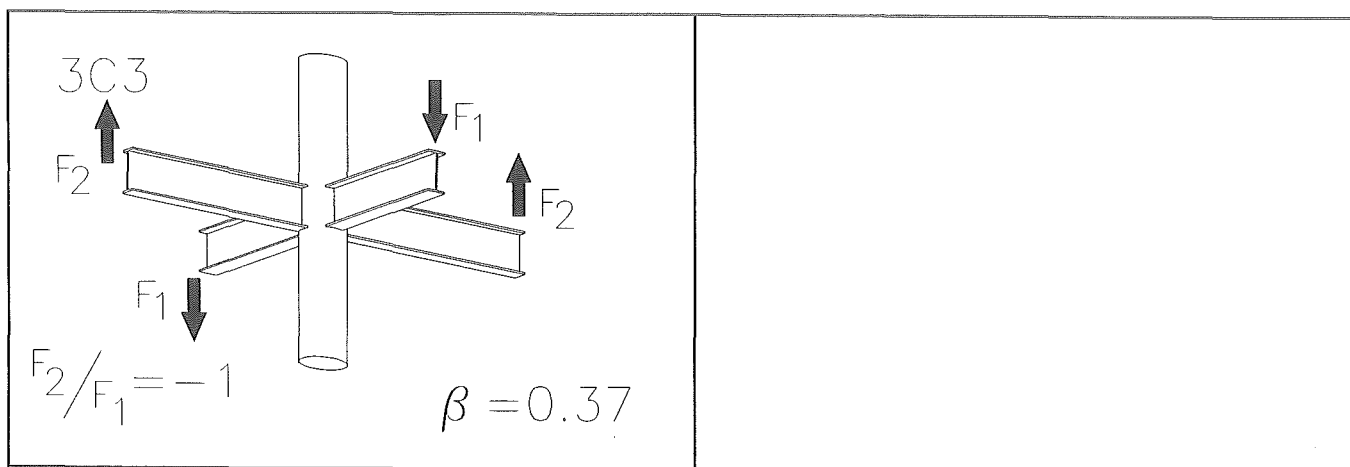
Failure mode: plastification of the CHS wall

Fig. 6-12 : Data sheet for test 3C1



Failure mode: plastification of the CHS wall

Fig. 6-13 : Data sheet for test 3C2



ACTUAL MECHANICAL PROPERTIES

Steel components	f_y	f_u	ϵ
	N/mm ²		%
CHS	387	510	30
IPE(flange)	433	526	33
IPE(web)	502	573	27

Failure mode: plastification of the CHS wall

Fig. 6-14 : Data sheet for test 3C3

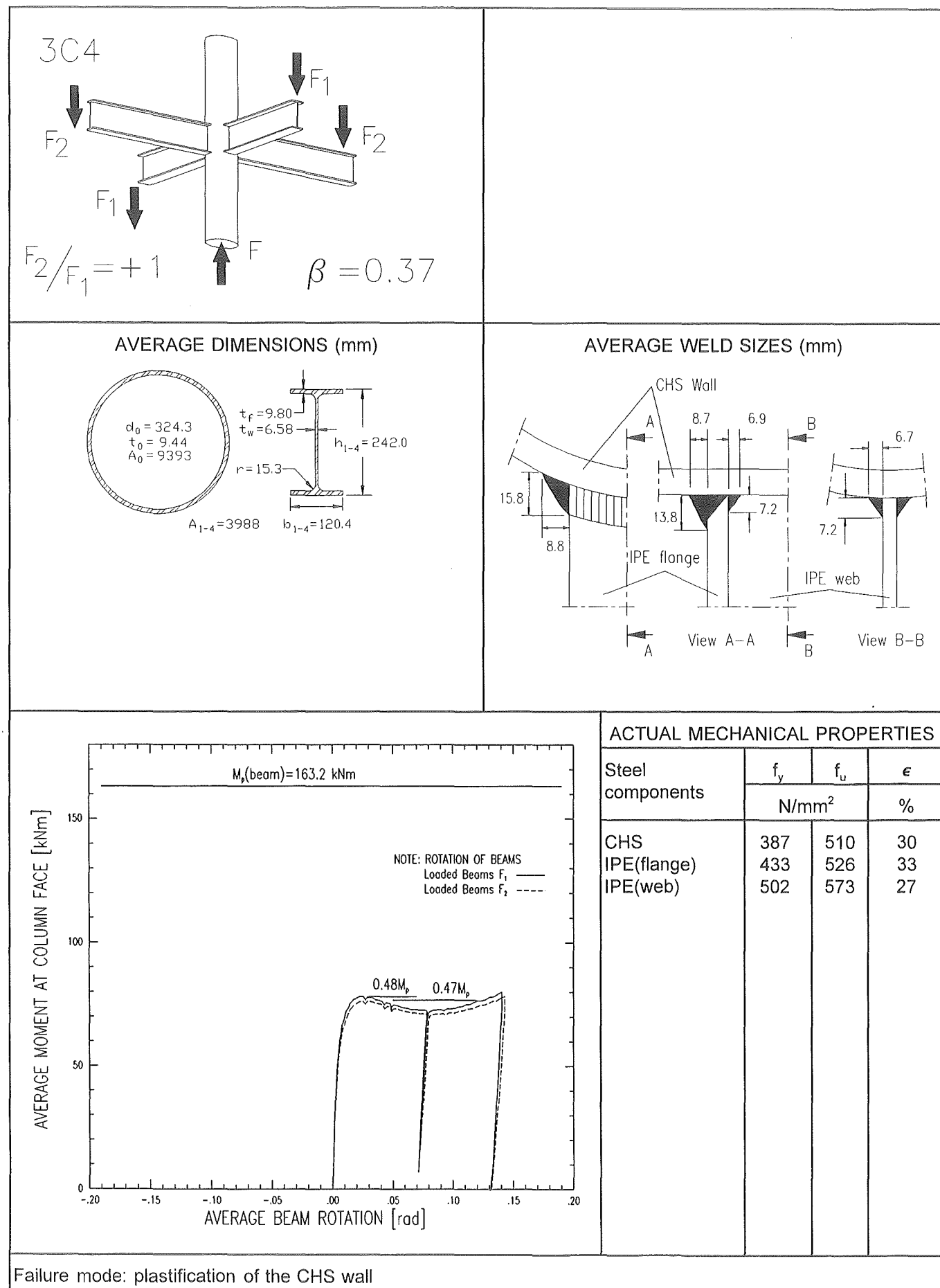
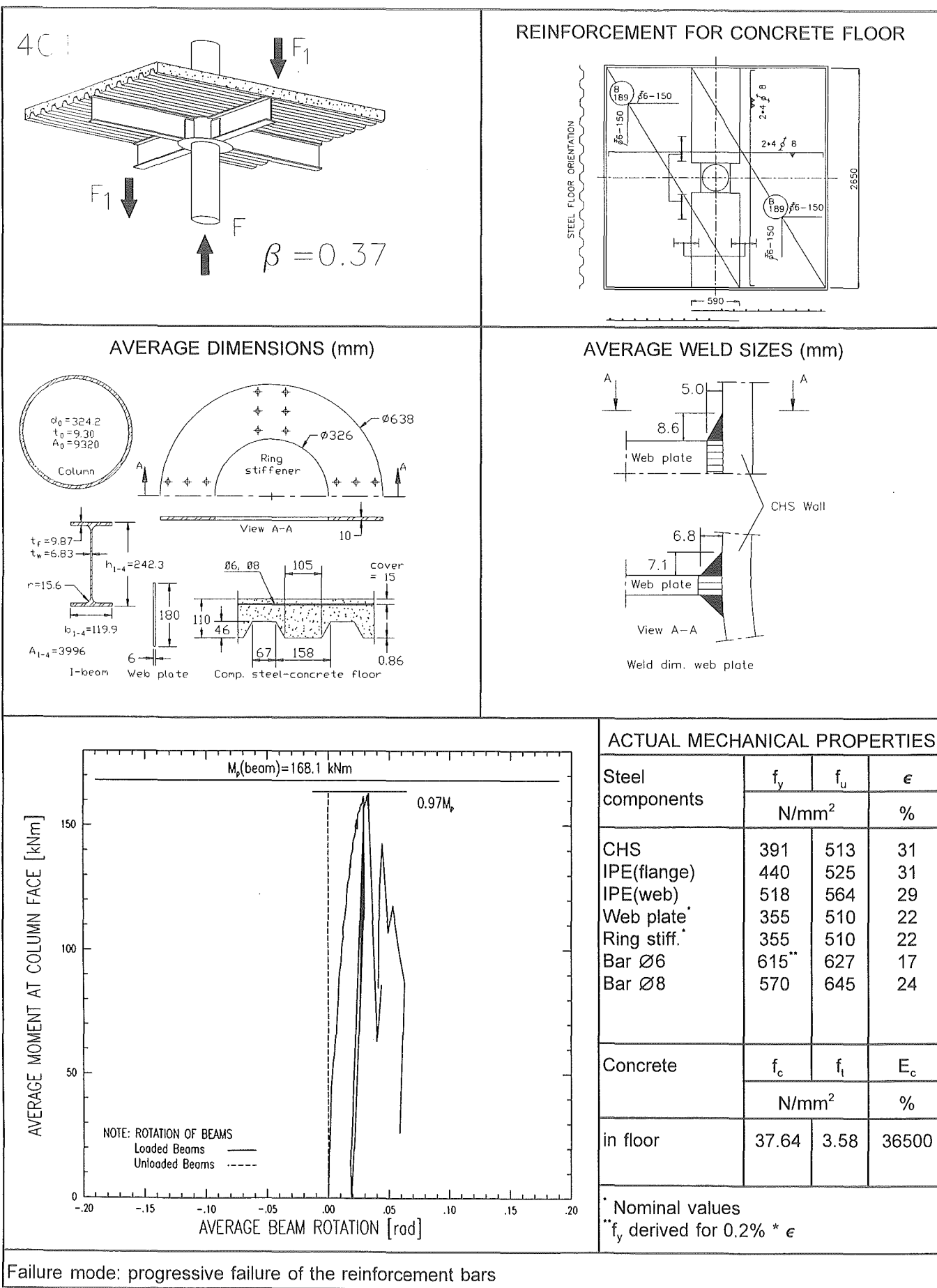
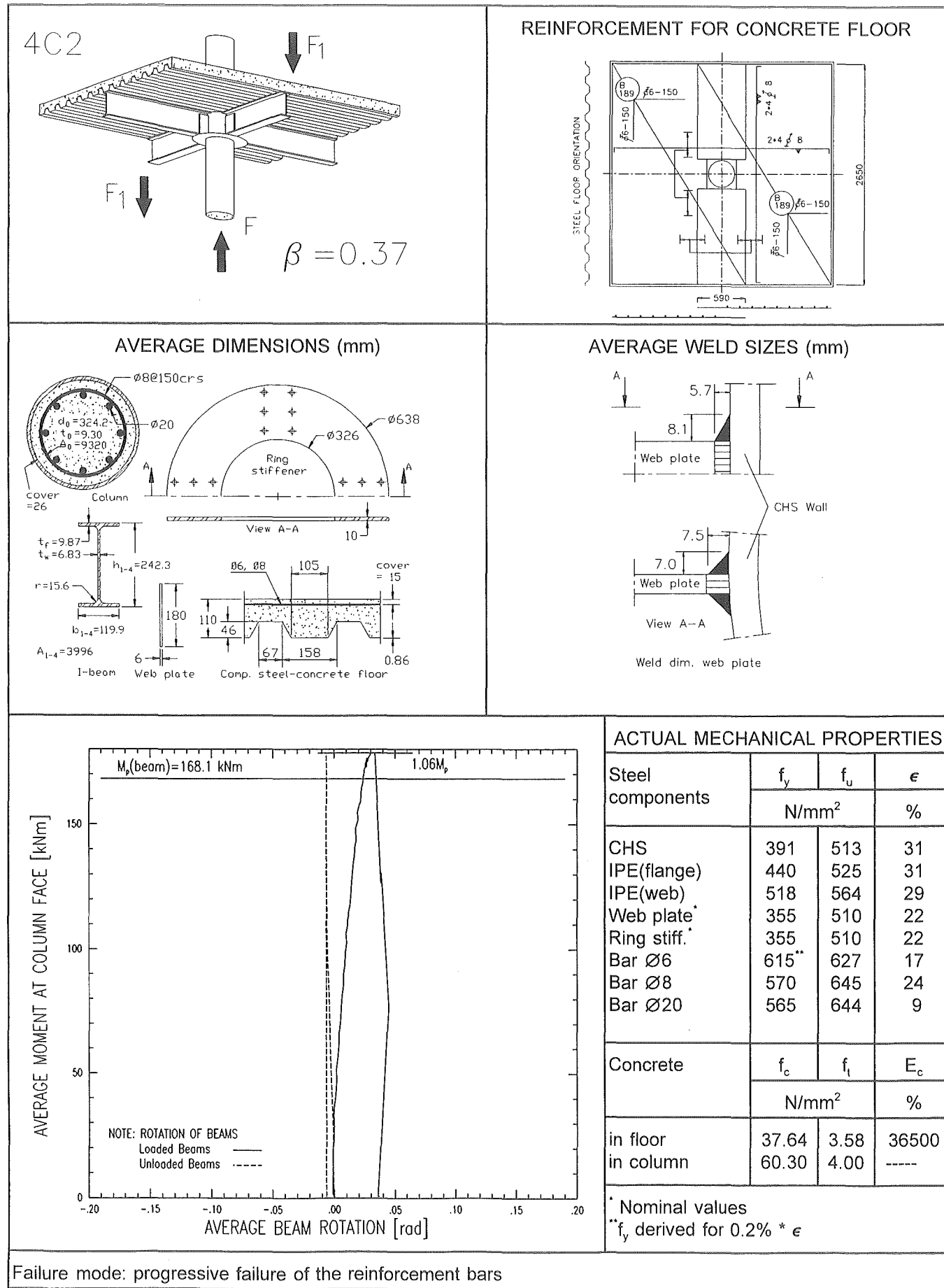


Fig. 6-15 : Data sheet for test 3C4



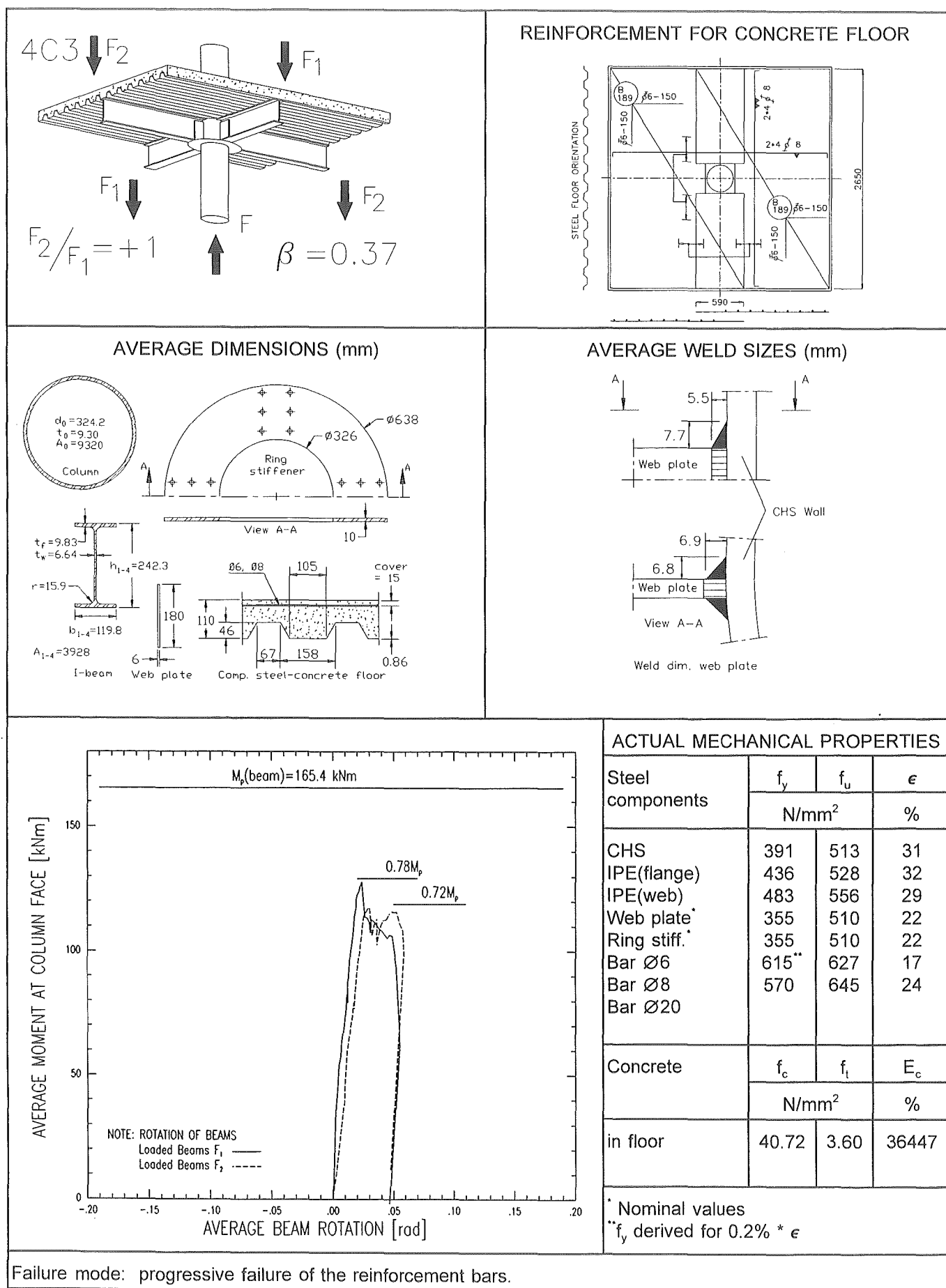
Failure mode: progressive failure of the reinforcement bars

Fig. 6-16 : Data sheet for test 4C1



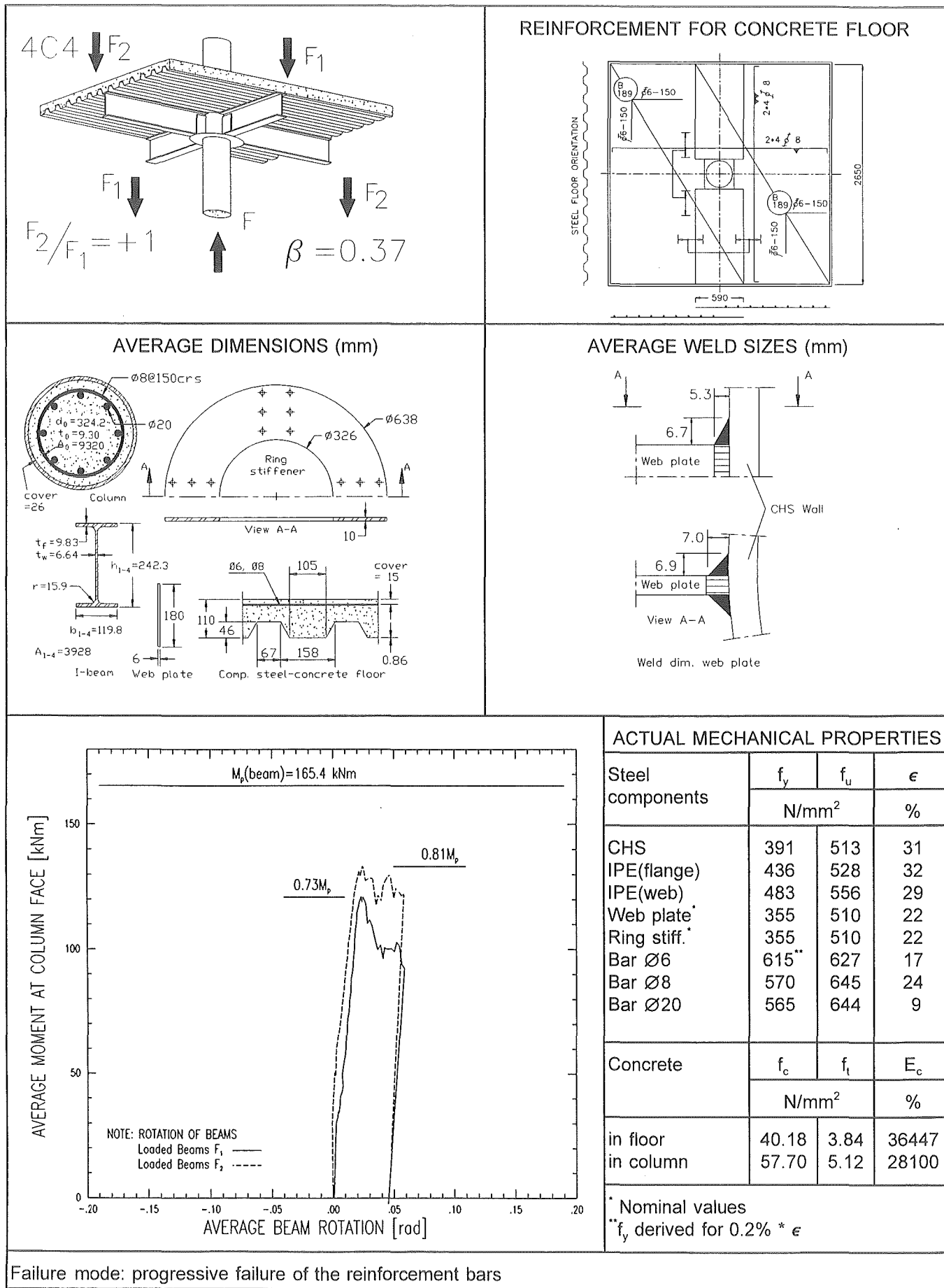
Failure mode: progressive failure of the reinforcement bars

Fig. 6-17 : Data sheet for test 4C2



Failure mode: progressive failure of the reinforcement bars.

Fig. 6-18 : Data sheet for test 4C3



Failure mode: progressive failure of the reinforcement bars

Fig. 6-19 : Data sheet for test 4C4

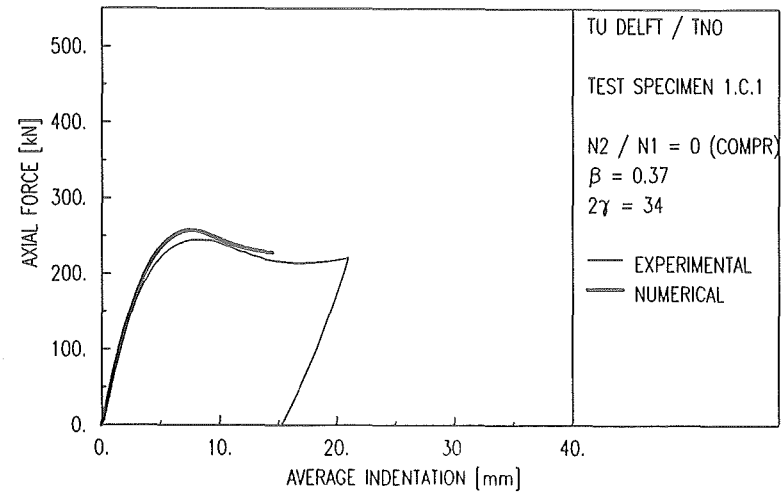


Fig: 6-20 Experimental and numerical load-deformation diagram for 1C1

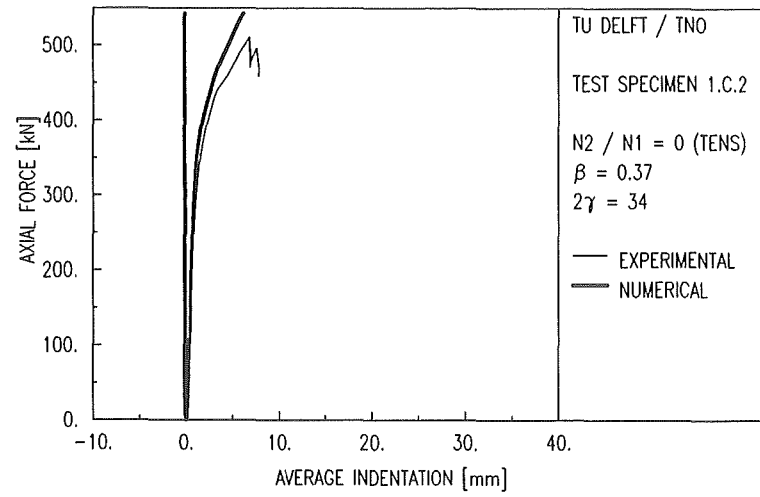


Fig: 6-21 Experimental and numerical load-deformation diagram for 1C2

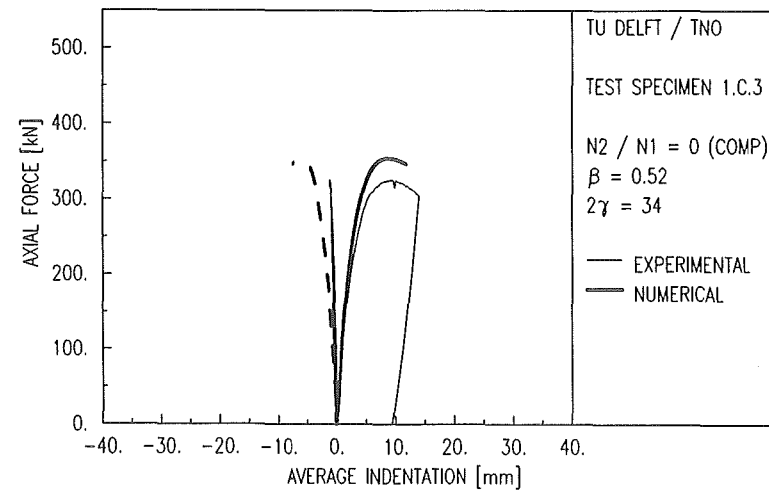


Fig: 6-22 Experimental and numerical load-deformation diagram for 1C3

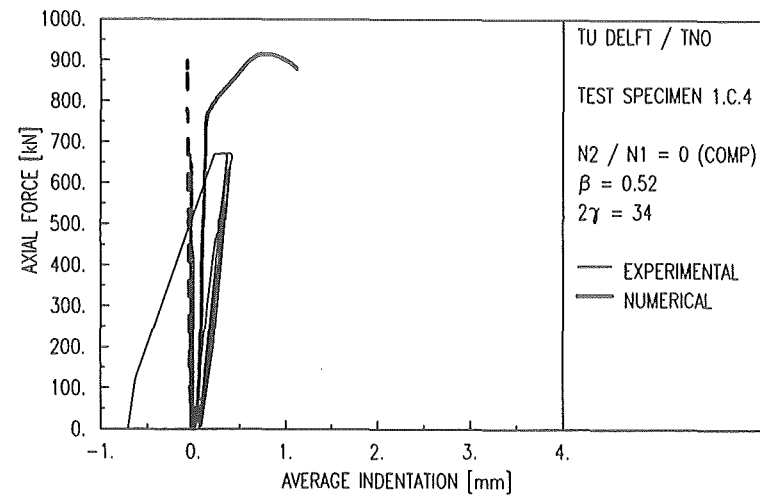


Fig: 6-23 Experimental and numerical load-deformation diagram for 1C4

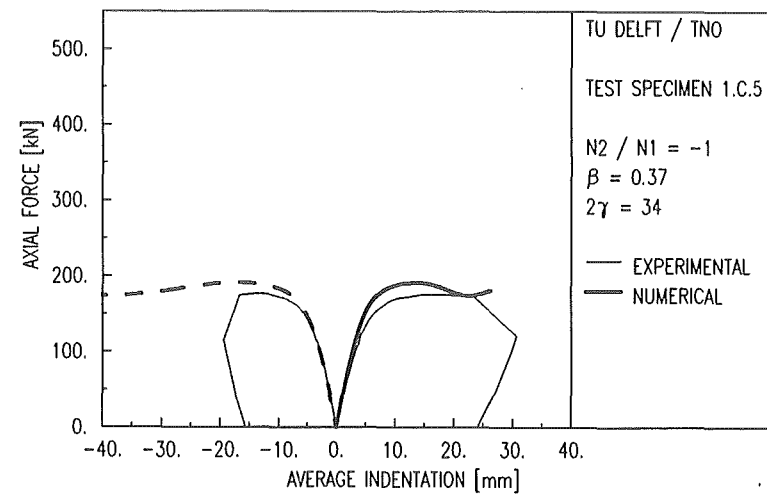


Fig: 6-24 Experimental and numerical load-deformation diagram for 1C5

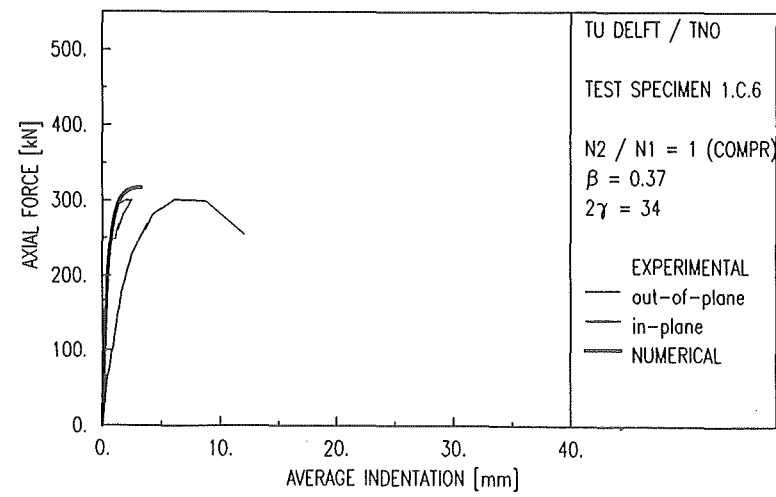


Fig: 6-25 Experimental and numerical load-deformation diagram for 1C6

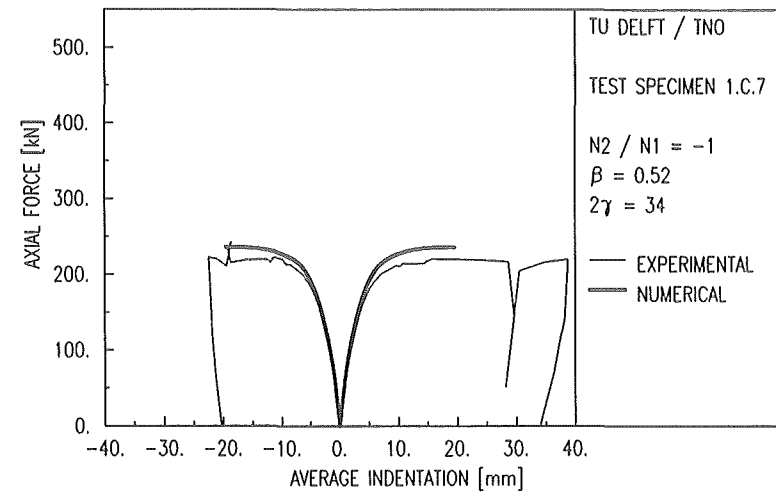


Fig: 6-26 Experimental and numerical load-deformation diagram for 1C7

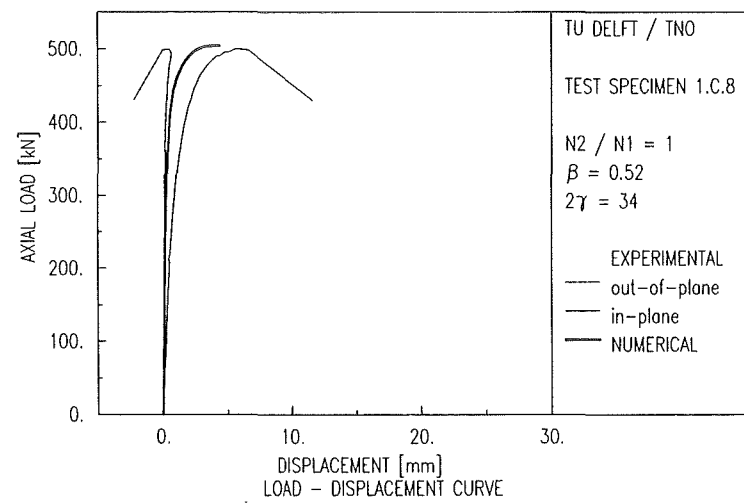


Fig: 6-27 Experimental and numerical load-deformation diagram for 1C8

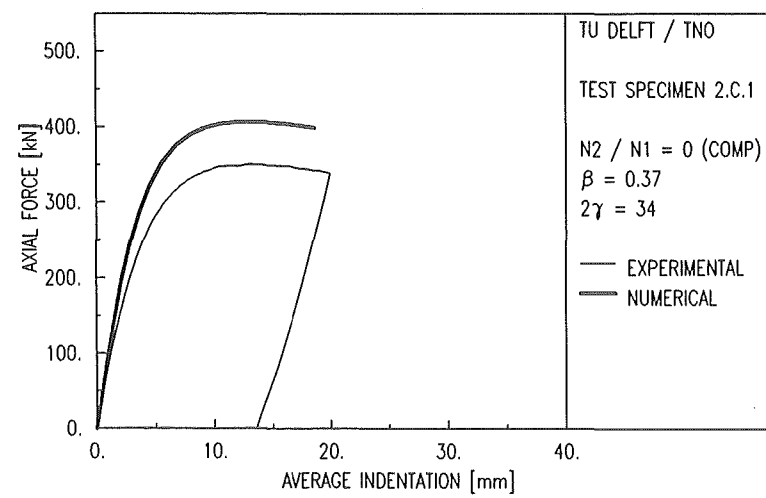


Fig: 6-28 Experimental and numerical load-deformation diagram for 2C1

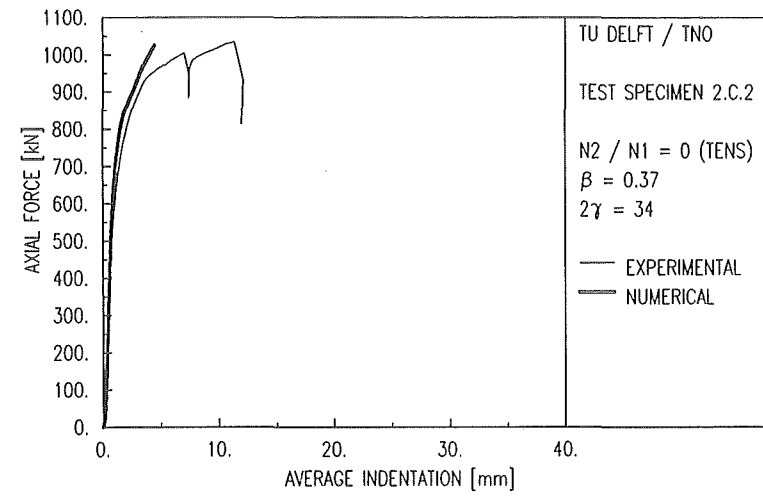


Fig: 6-29 Experimental and numerical load-deformation diagram for 2C2

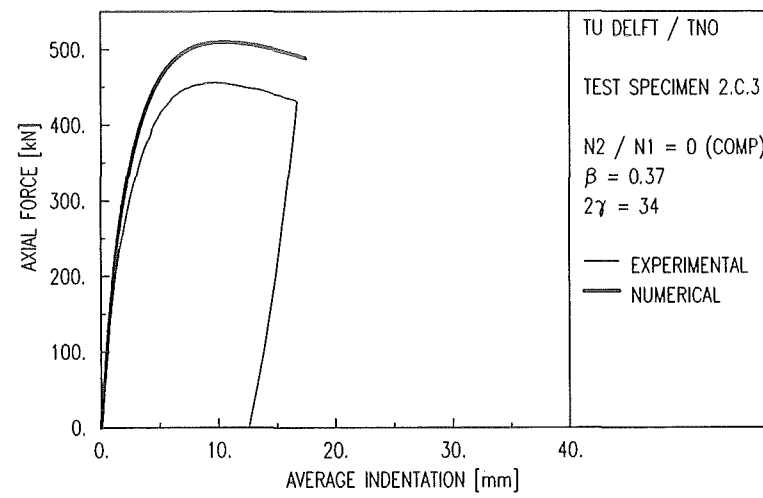


Fig: 6-30 Experimental and numerical load-deformation diagram for 2C3

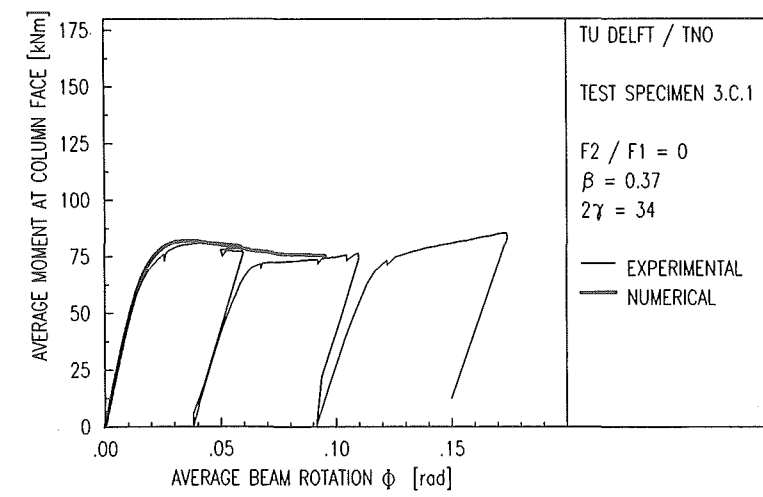


Fig: 6-31 Experimental and numerical moment-rotation diagram for 3C1

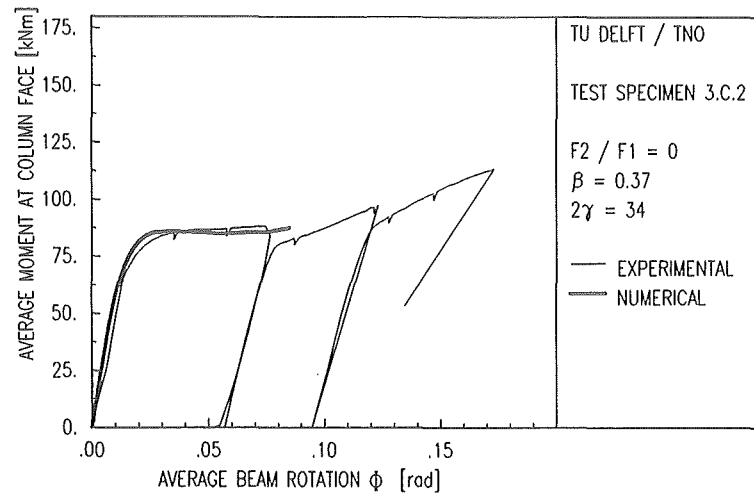


Fig: 6-32 Experimental and numerical moment-rotation diagram for 3C2

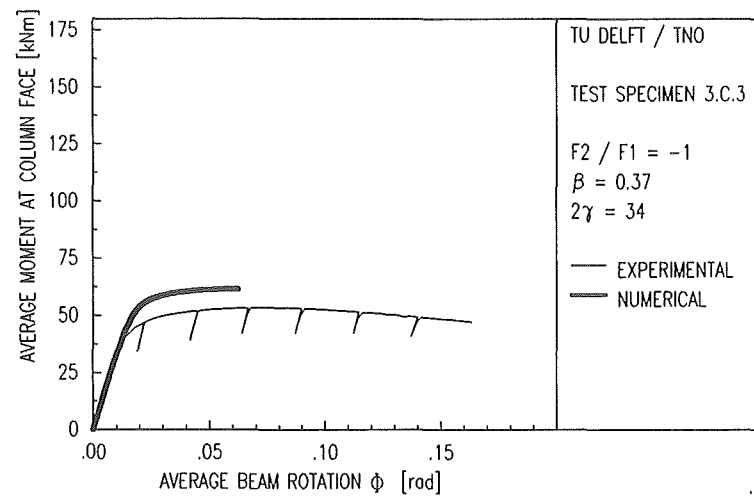


Fig: 6-33 Experimental and numerical moment-rotation diagram for 3C3

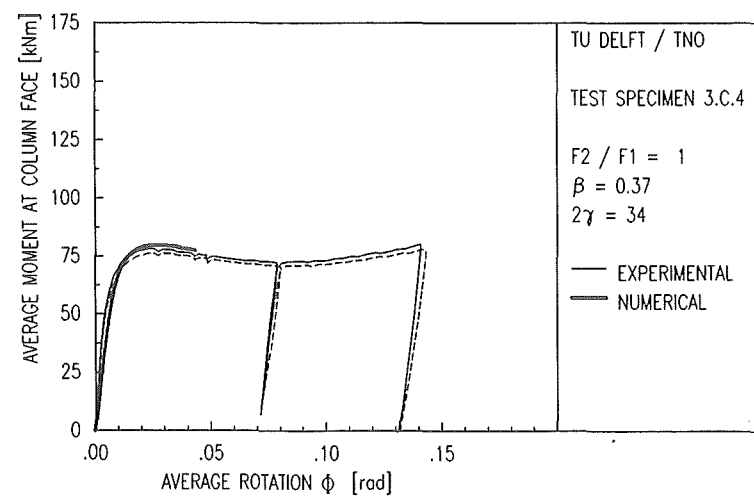


Fig: 6-34 Experimental and numerical moment-rotation diagram for 3C4

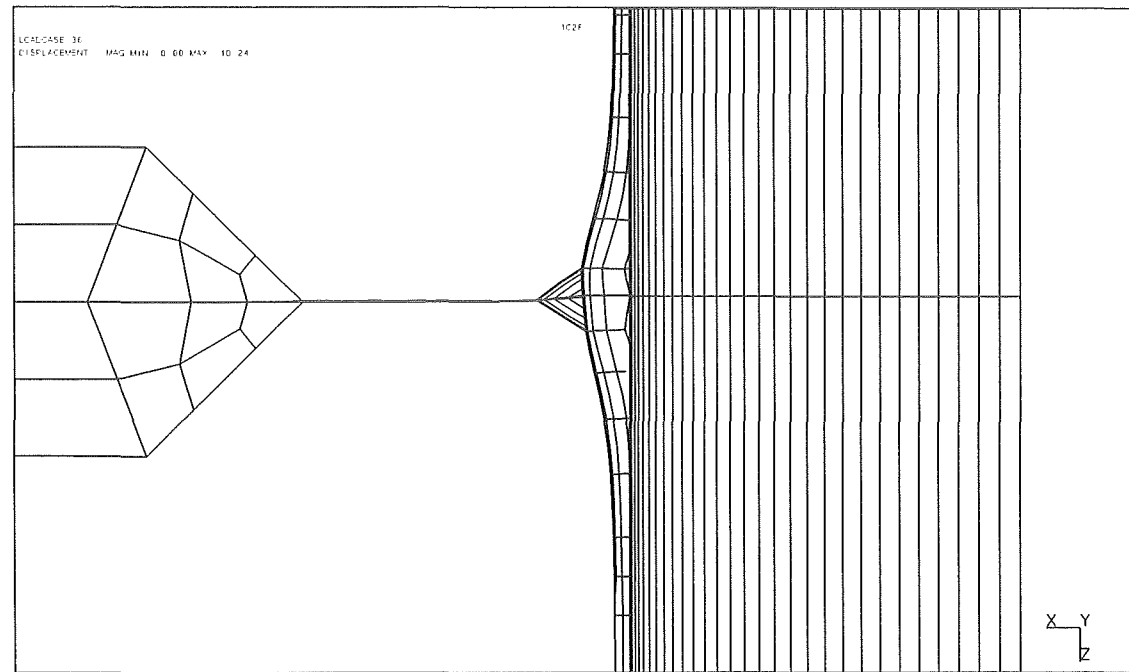


Fig: 6-35 Deformed finite element mesh of model 1C2

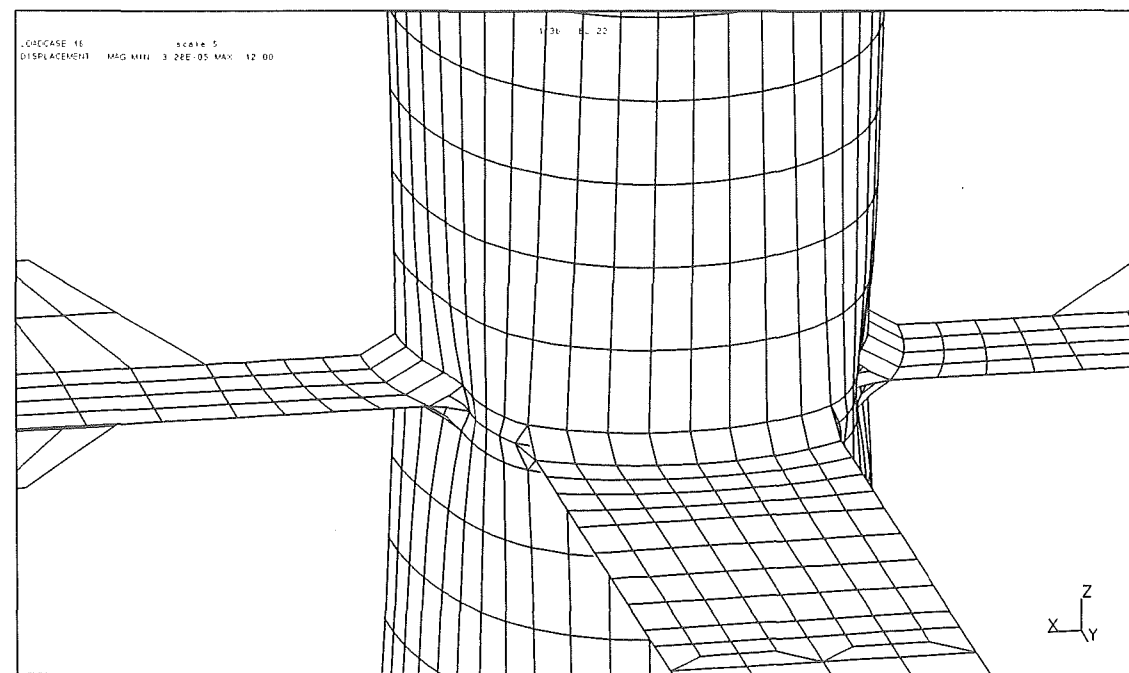


Fig: 6-36 Deformed finite element mesh of model 1C3

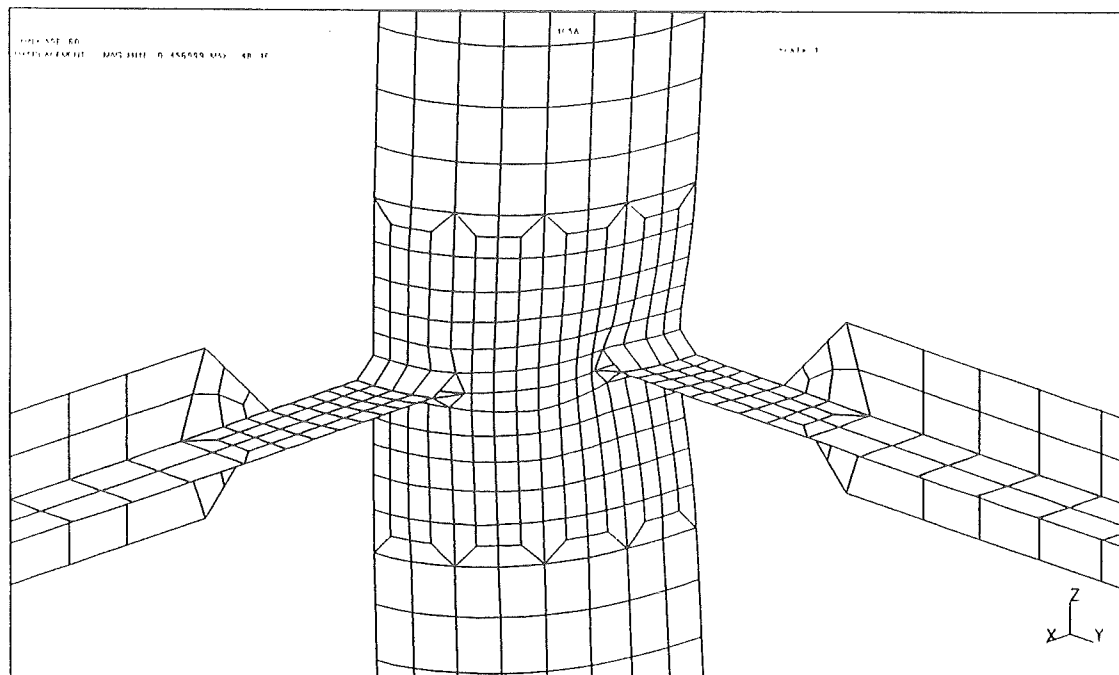


Fig: 6-37 Deformed finite element mesh of model 1C5

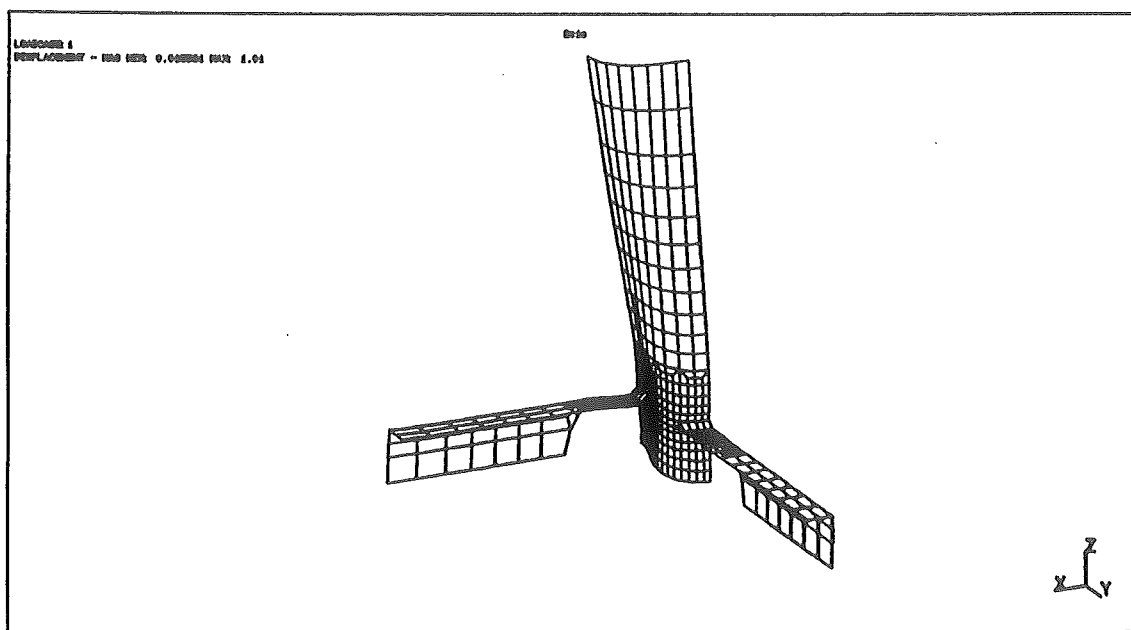


Fig: 6-38 Deformed finite element mesh of model 2C1

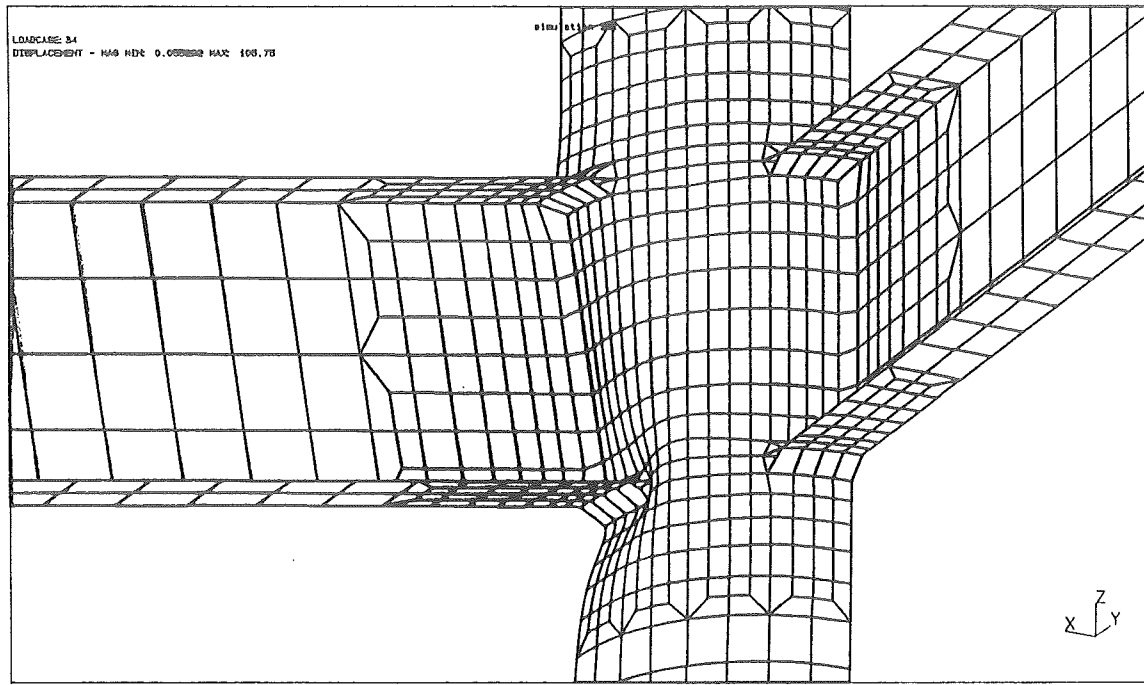


Fig: 6-39 Deformed finite element mesh of model 3C1

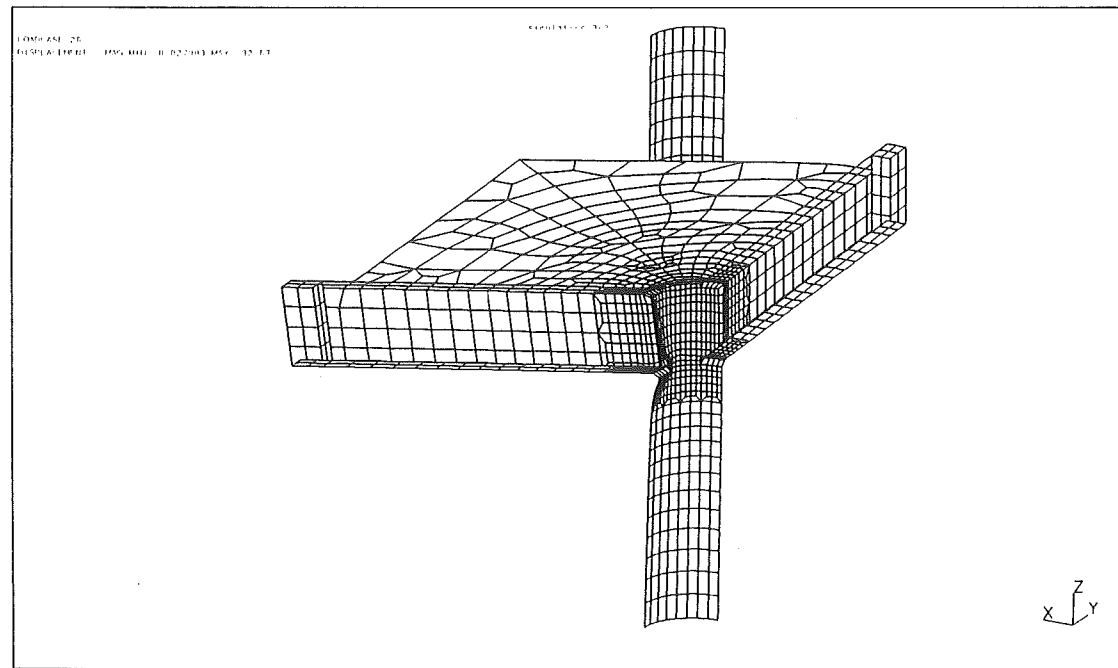


Fig: 6-40 Deformed finite element mesh of model 3C2

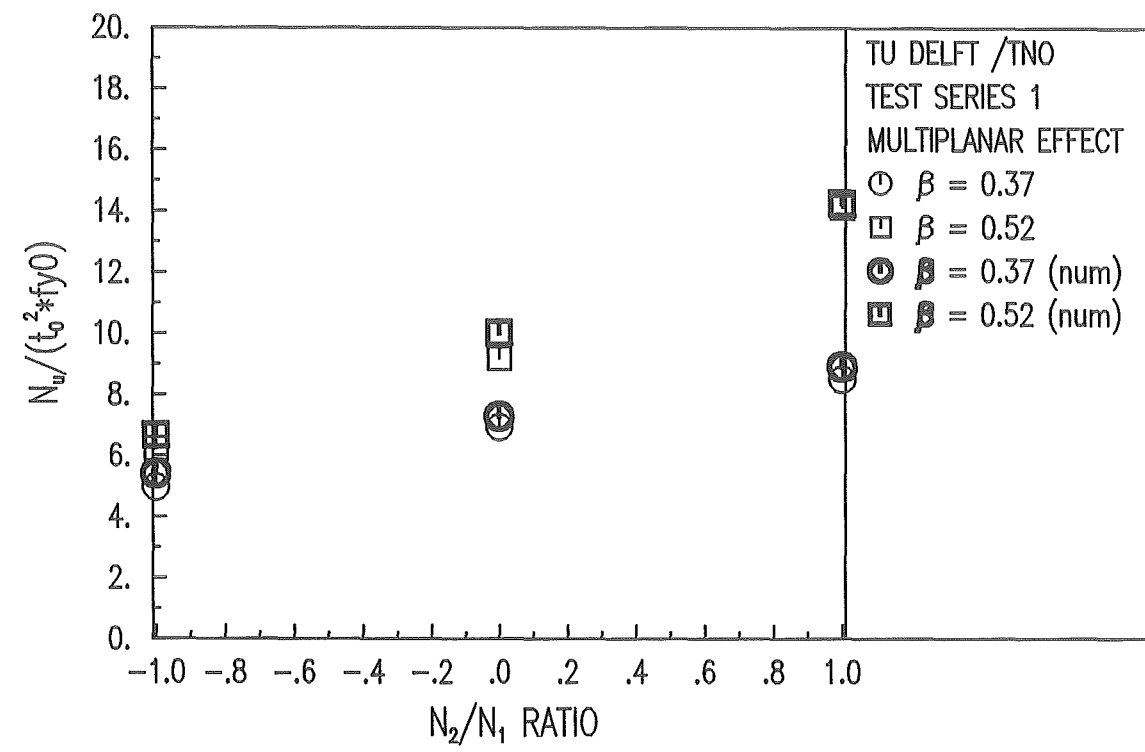


Fig: 6-41 Multiplanar effect axial loading tests series 1

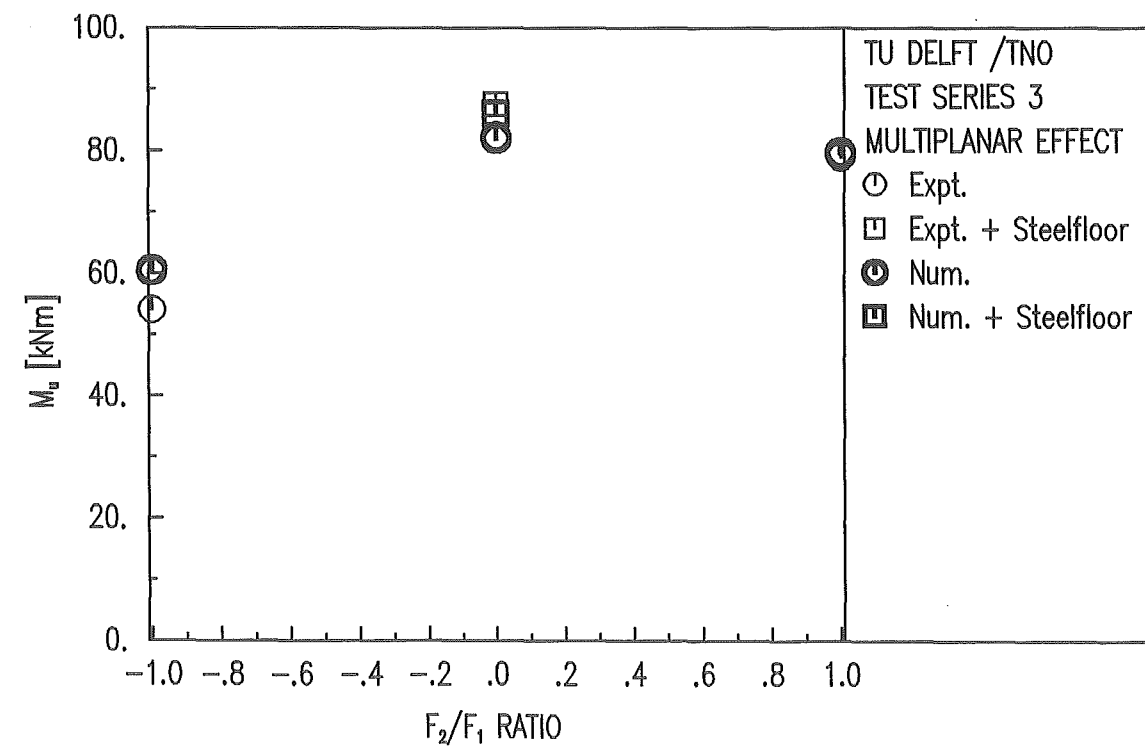
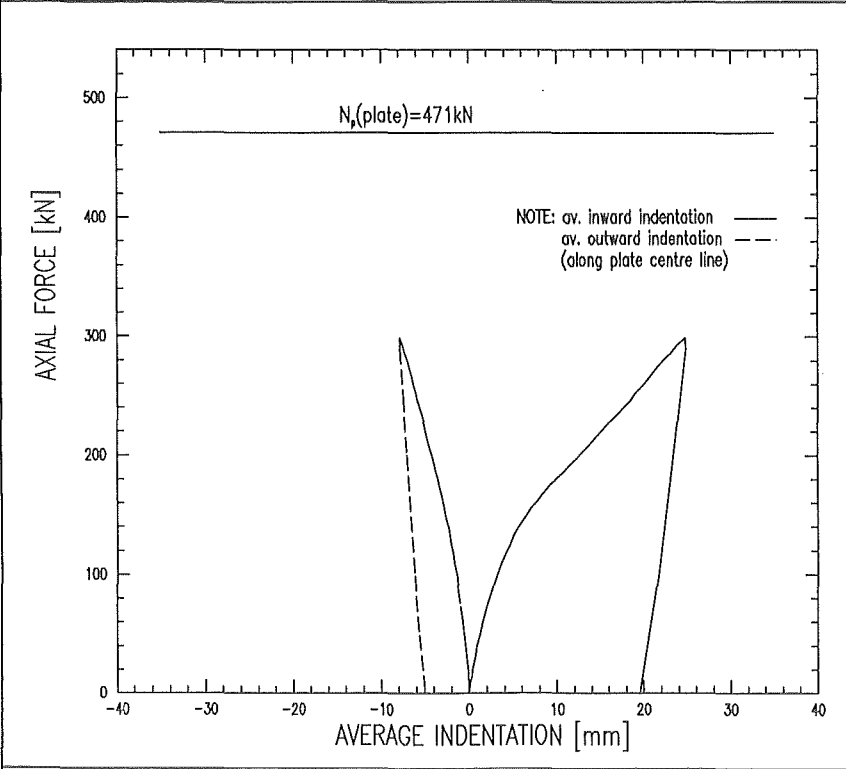
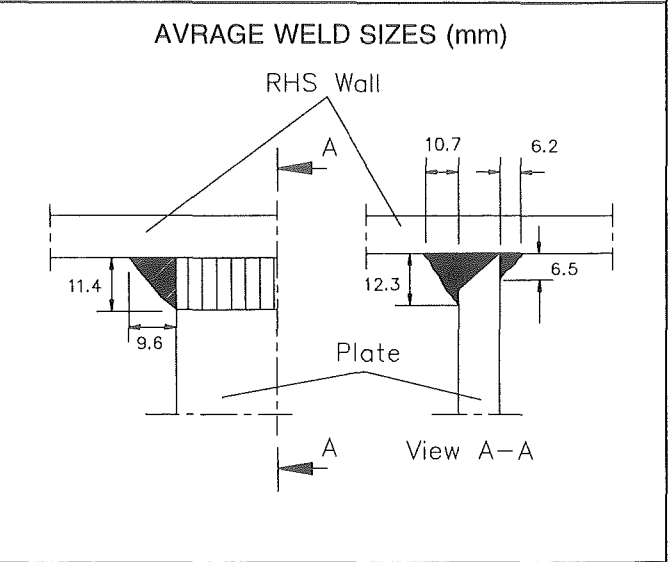
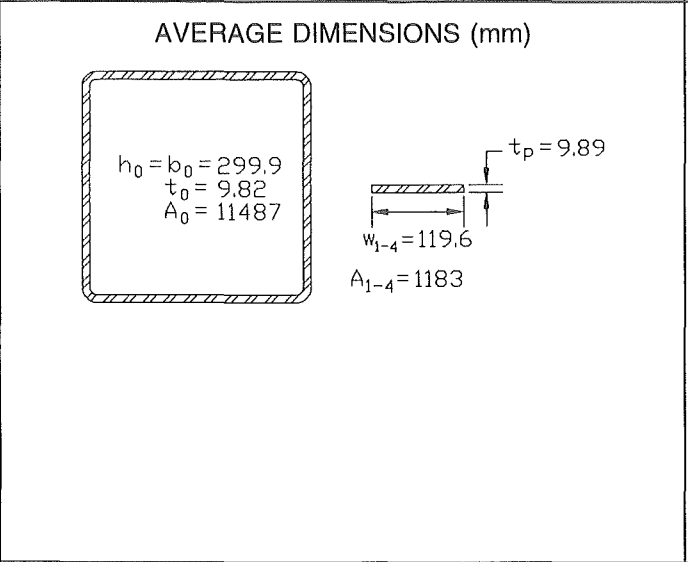
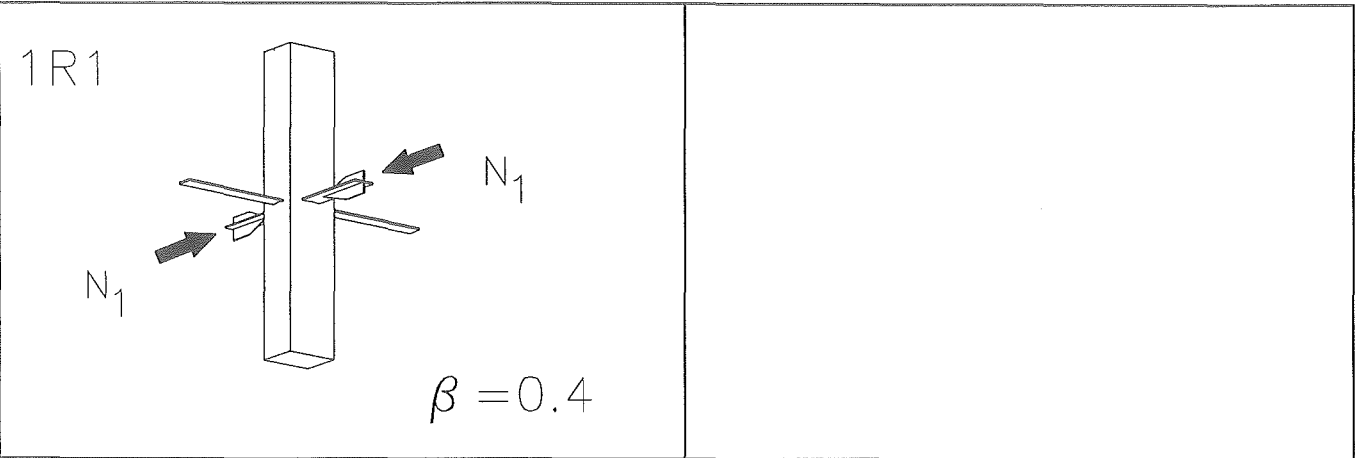


Fig: 6-42 Multiplanar effect in-plane bending tests series 3

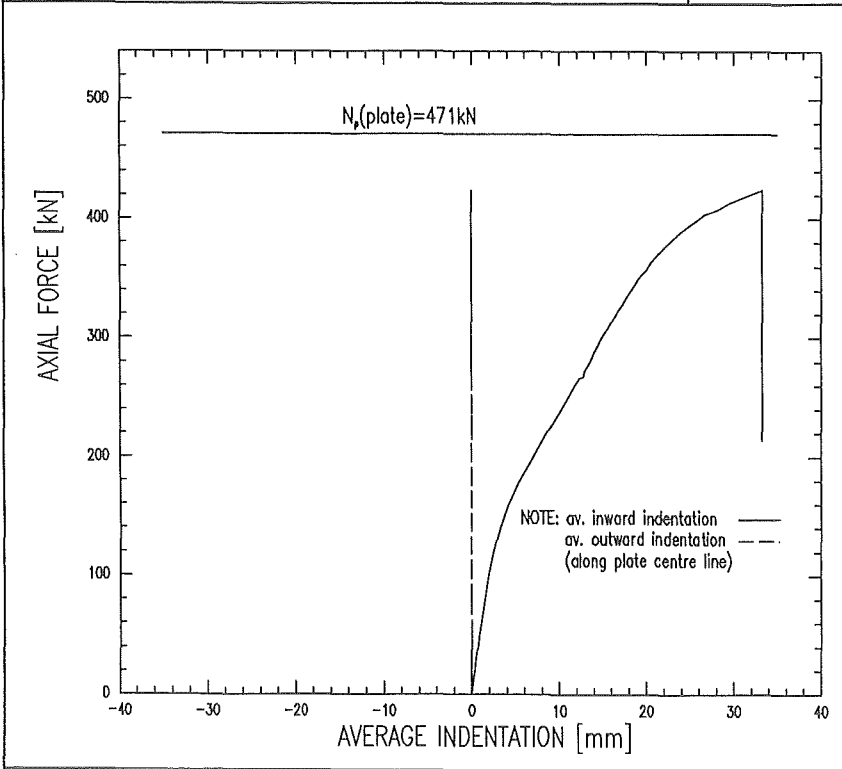
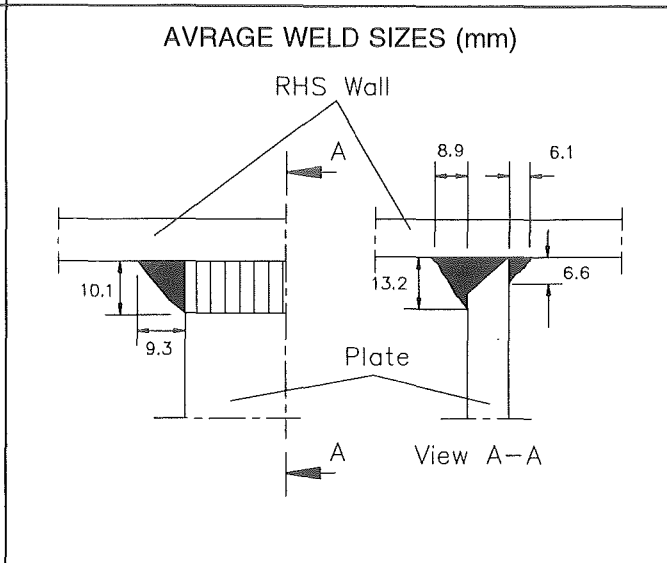
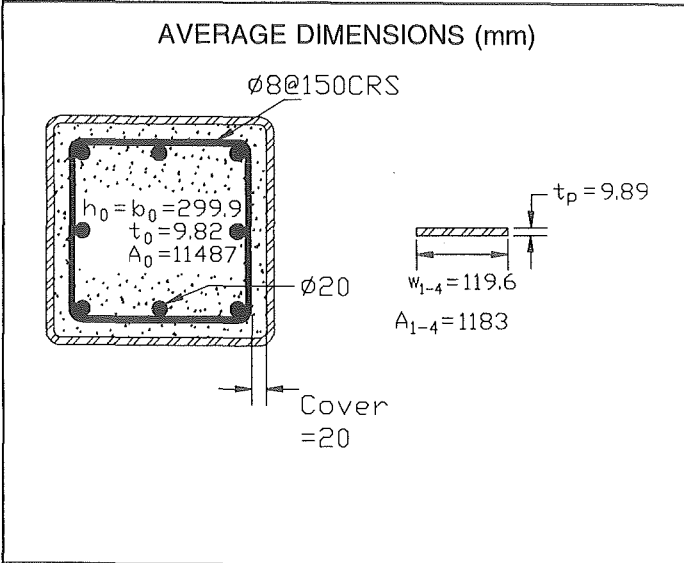
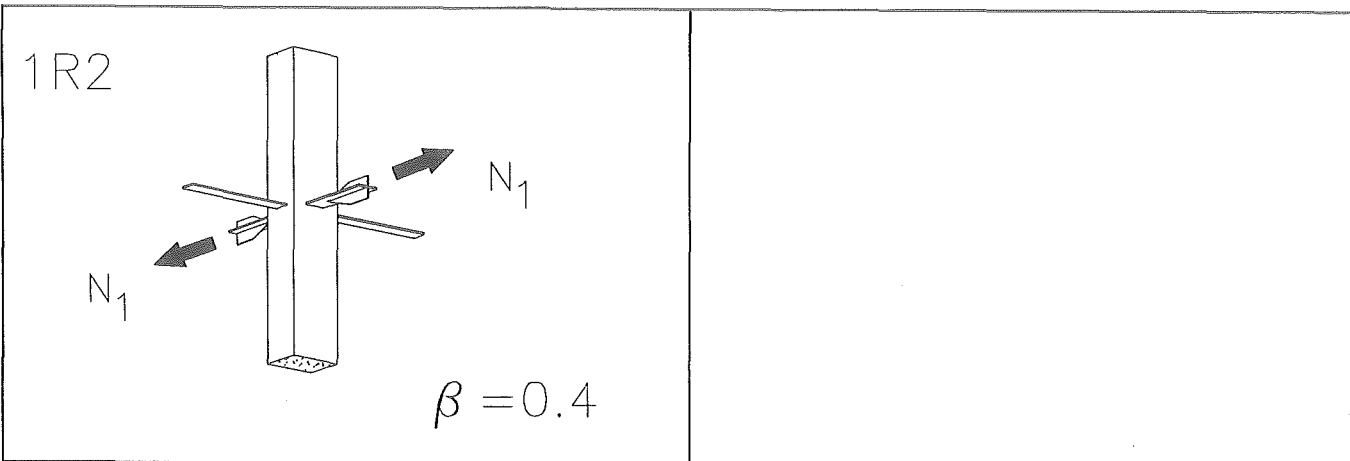


ACTUAL MECHANICAL PROPERTIES

Steel components	f_y	f_u	ϵ
	N/mm ²		%
RHS Plate	434	560	30
	398	529	29
Concrete	f_c	f_t	E_c
	N/mm ²		%

Failure mode: no failure mode. Test stopped after sufficient deformation reached

Fig. 7-1 : Data sheet for test 1R1

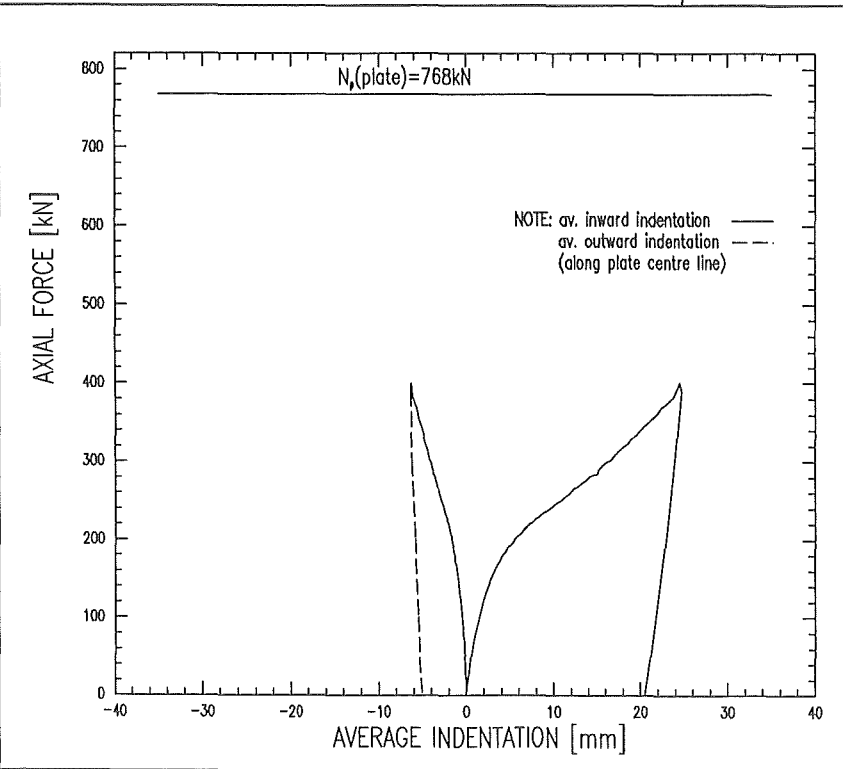
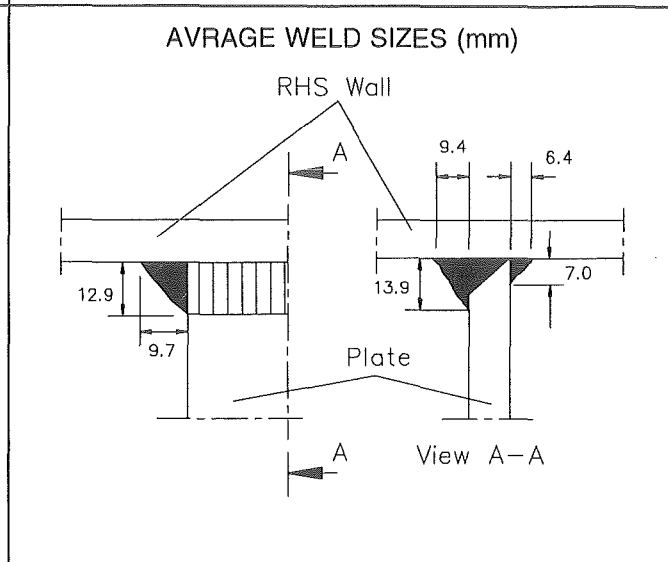
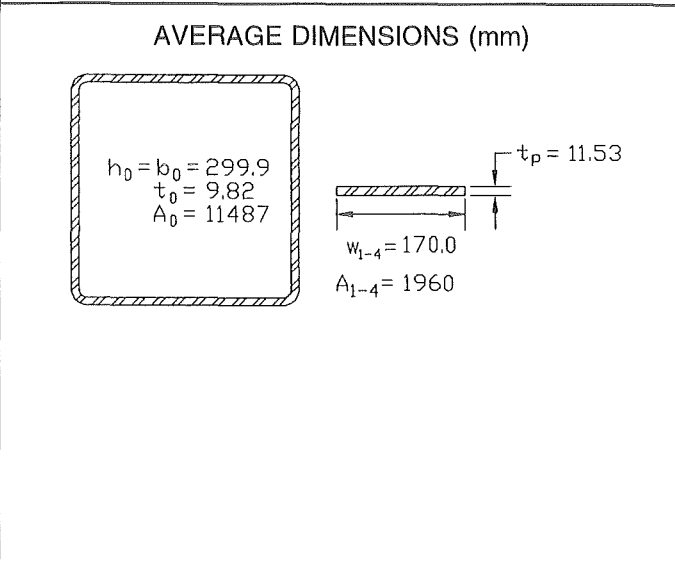
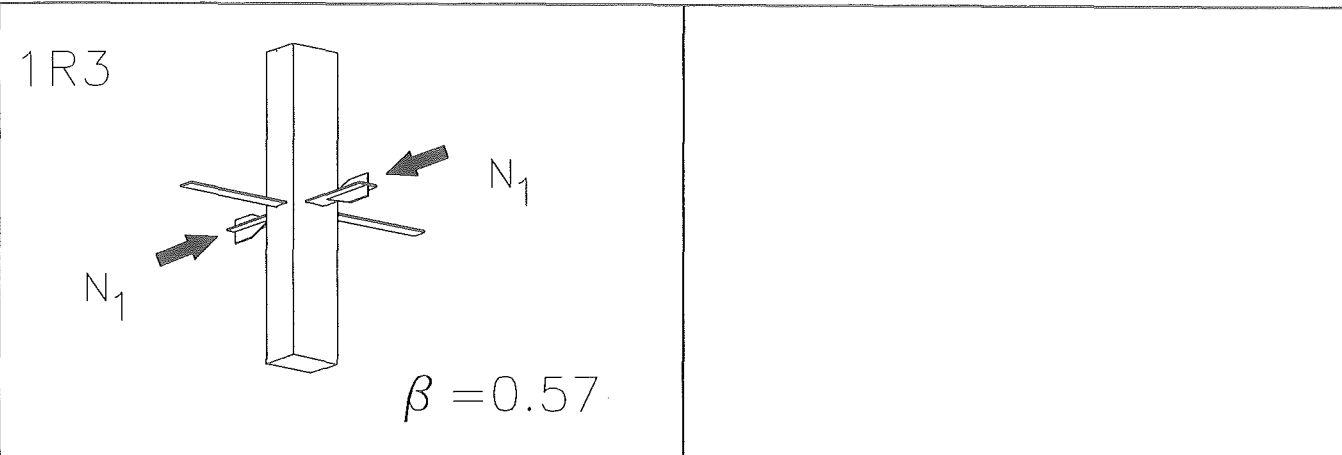


ACTUAL MECHANICAL PROPERTIES

Steel components	f_y	f_u	ϵ
	N/mm ²		%
RHS	434	560	30
Plate	398	529	29
Bar $\phi 20$	565	644	9
Concrete	f_c	f_t	E_c
	N/mm ²		%
in column	56.5	4.82	25100

Failure mode: plastification of RHS wall followed by punching shear

Fig. 7-2 : Data sheet for test 1R2



ACTUAL MECHANICAL PROPERTIES

Steel components	f_y	f_u	ϵ
	N/mm ²		%
RHS Plate	434	560	30
	392	516	31
Concrete	f_c	f_t	E_c
	N/mm ²		%

Failure mode: no failure mode. Test was stopped after sufficient deformation reached

Fig. 7-3 : Data sheet for test 1R3

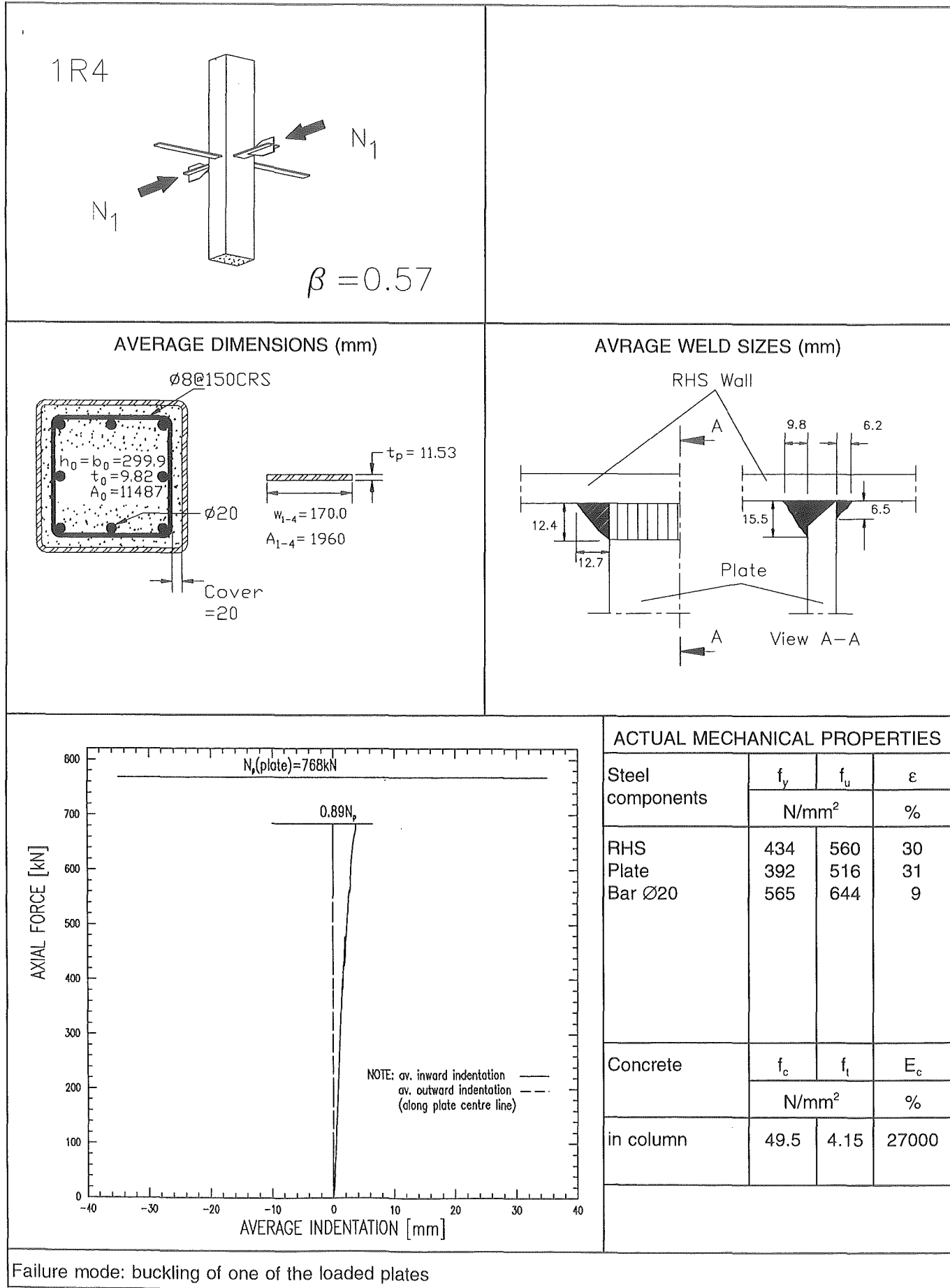


Fig. 7-4 : Data sheet for test 1R4

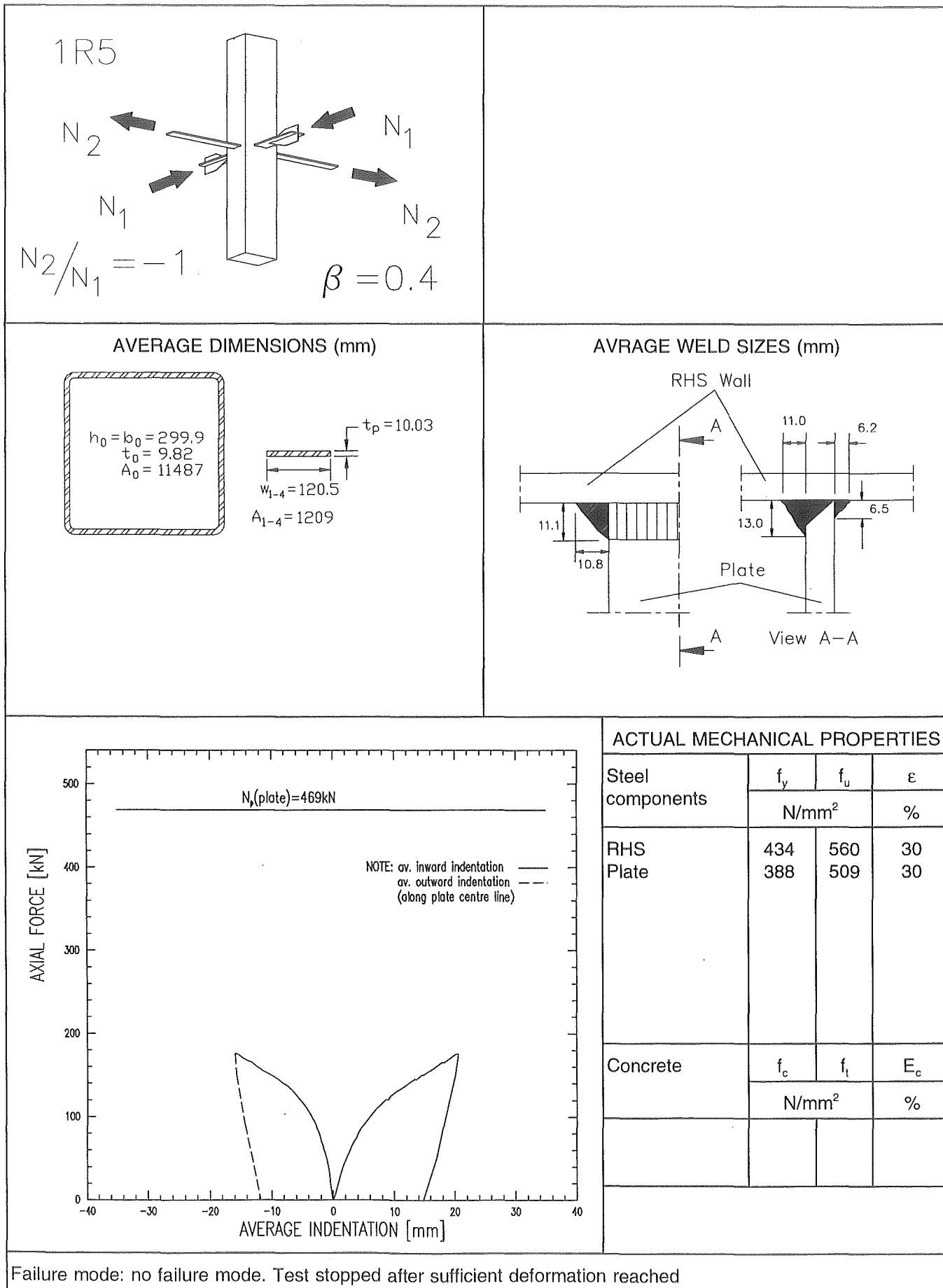


Fig. 7-5 : Data sheet for test 1R5

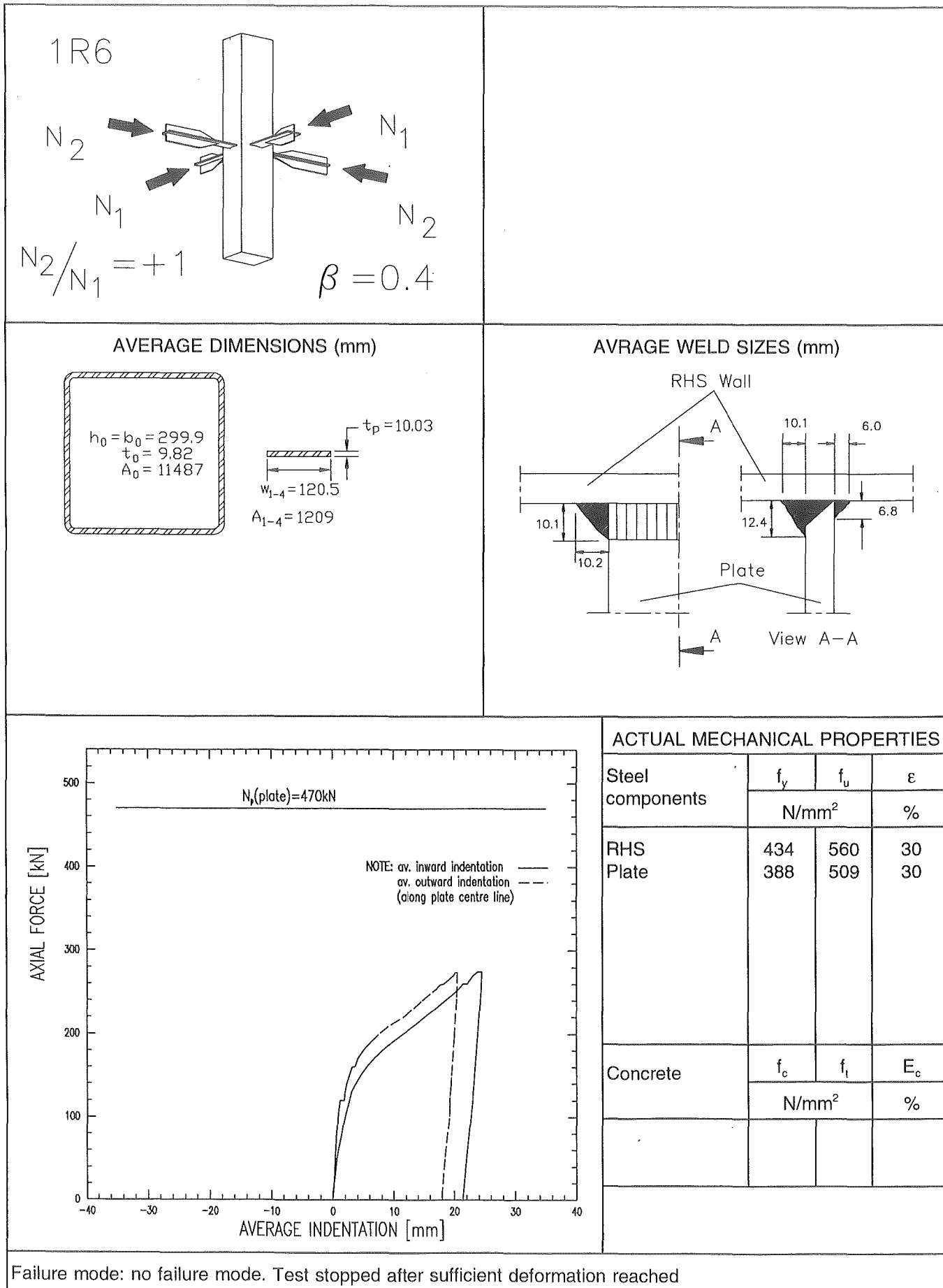
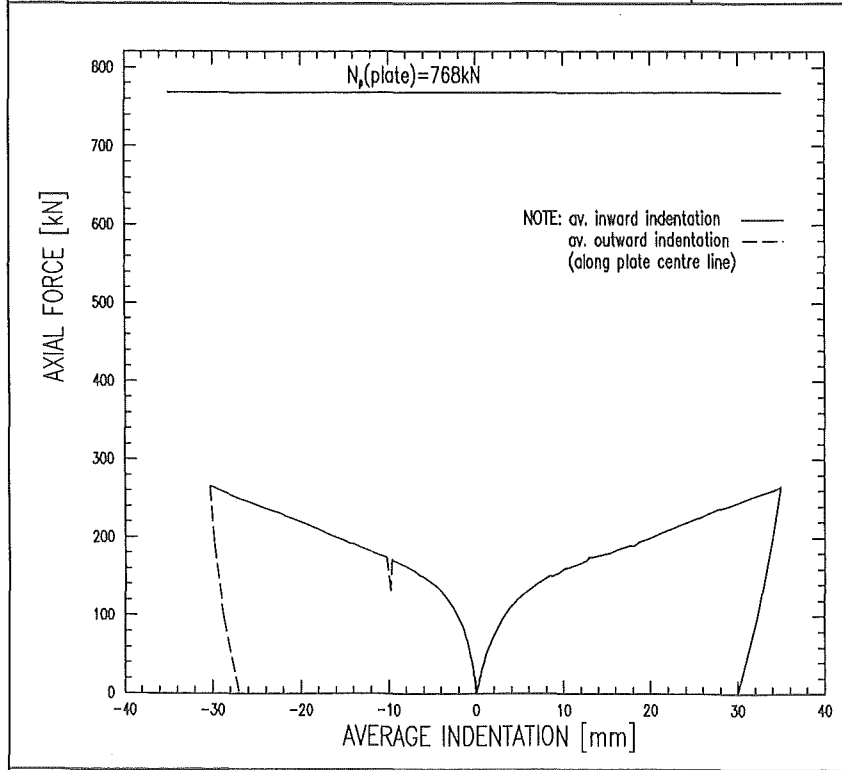
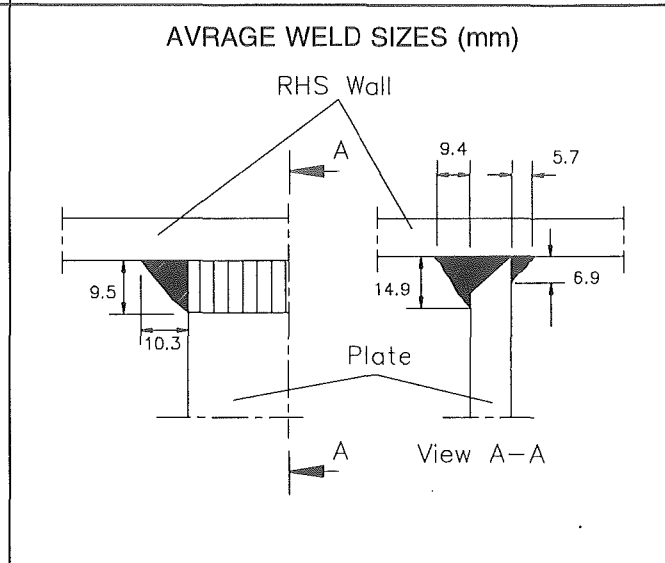
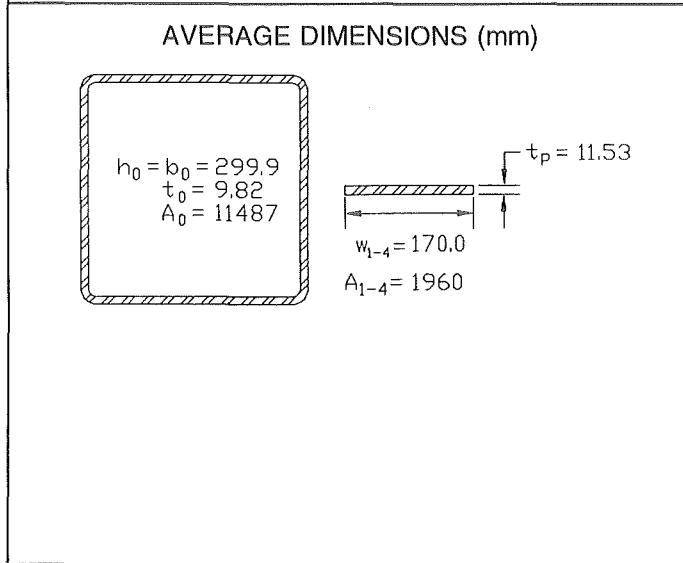
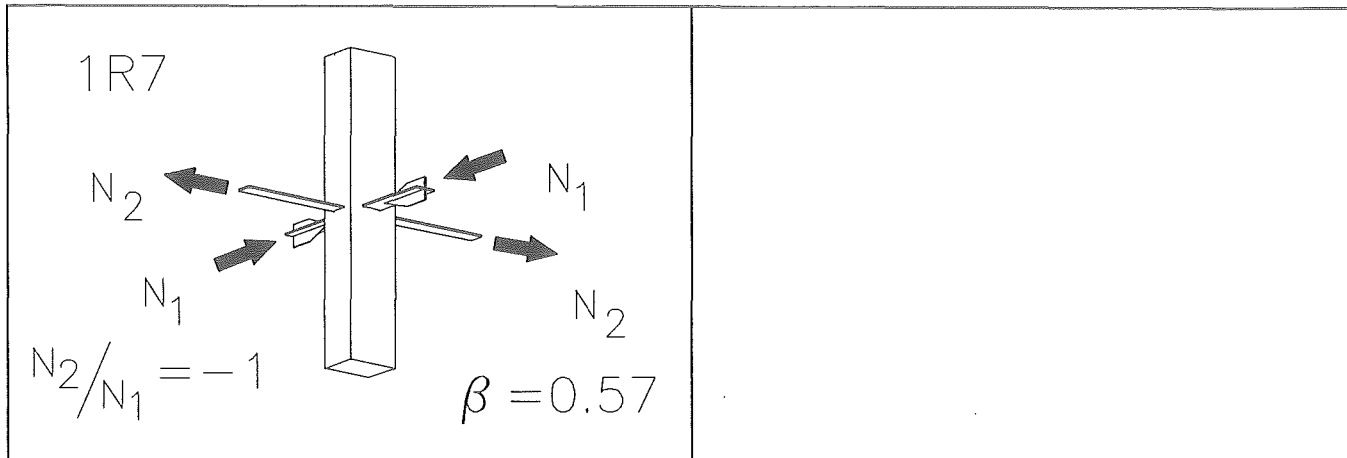


Fig. 7-6 : Data sheet for test 1R6



ACTUAL MECHANICAL PROPERTIES

Steel components	f_y	f_u	ϵ
	N/mm ²		%
RHS Plate	434	560	30
	392	516	31
Concrete	f_c	f_t	E_c
	N/mm ²		%

Failure mode: no failure mode. Test stopped after sufficient deformation reached

Fig. 7-7 : Data sheet for test 1R7

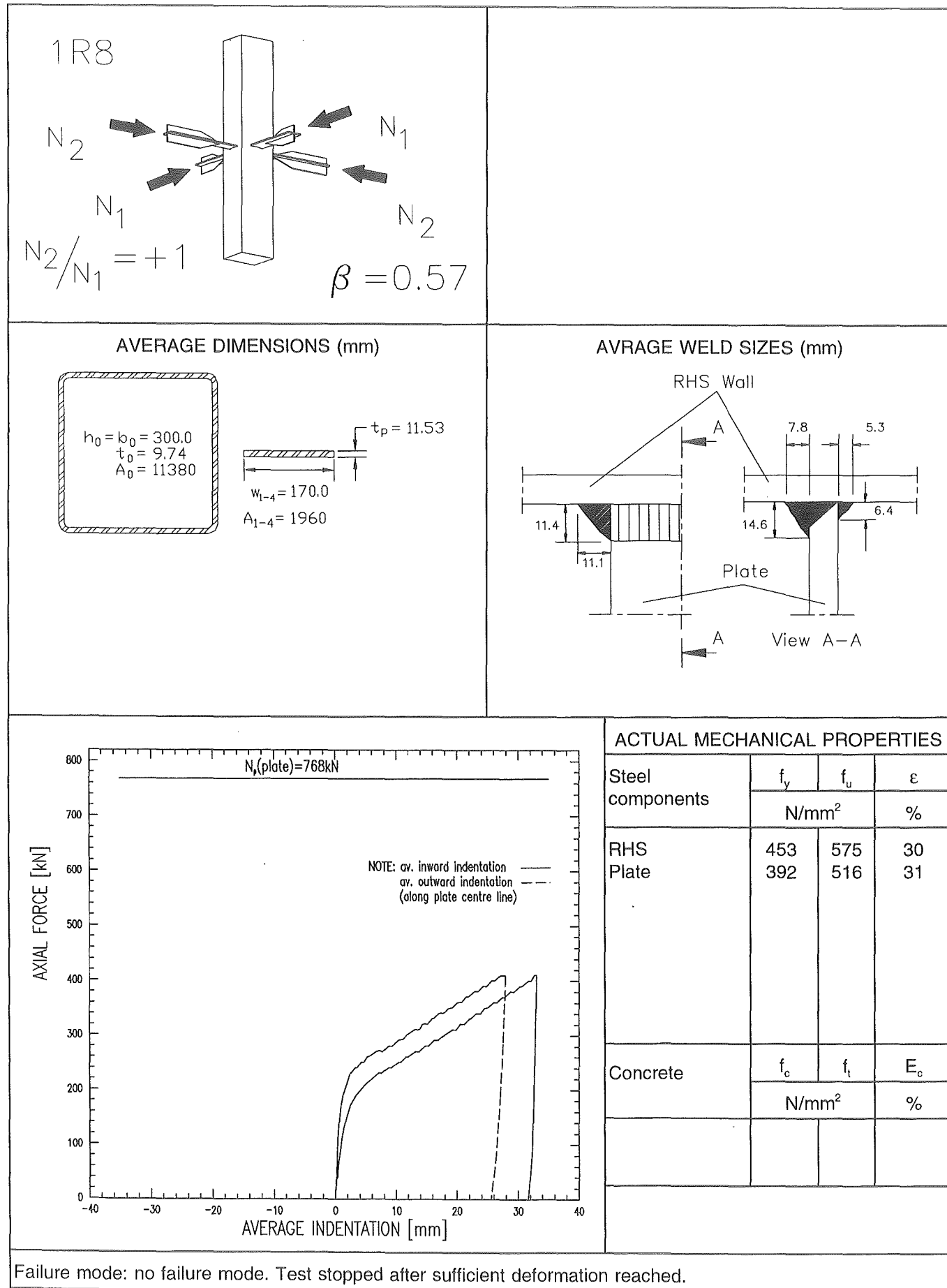
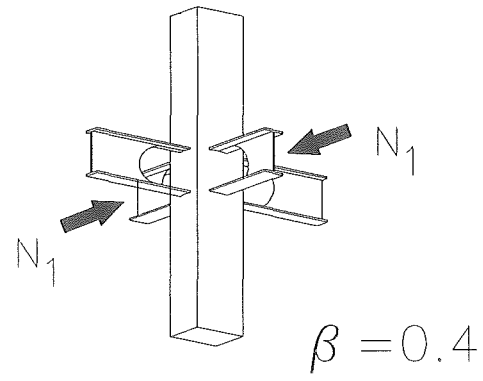
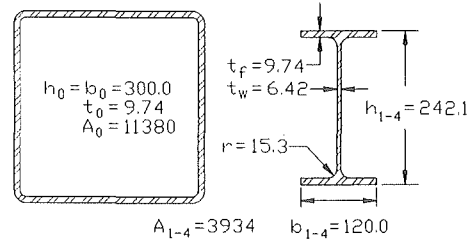


Fig. 7-8 : Data sheet for test 1R8

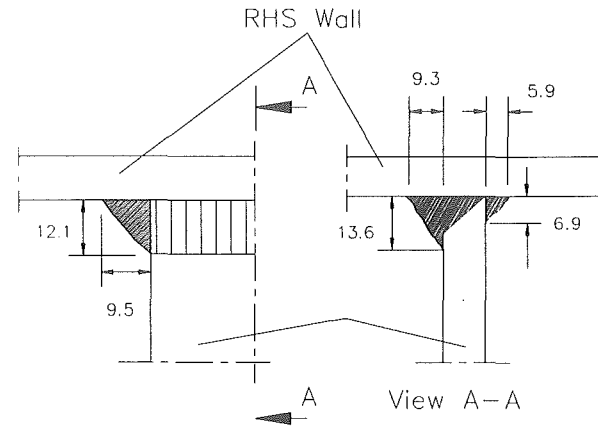
2R1



AVERAGE DIMENSIONS (mm)

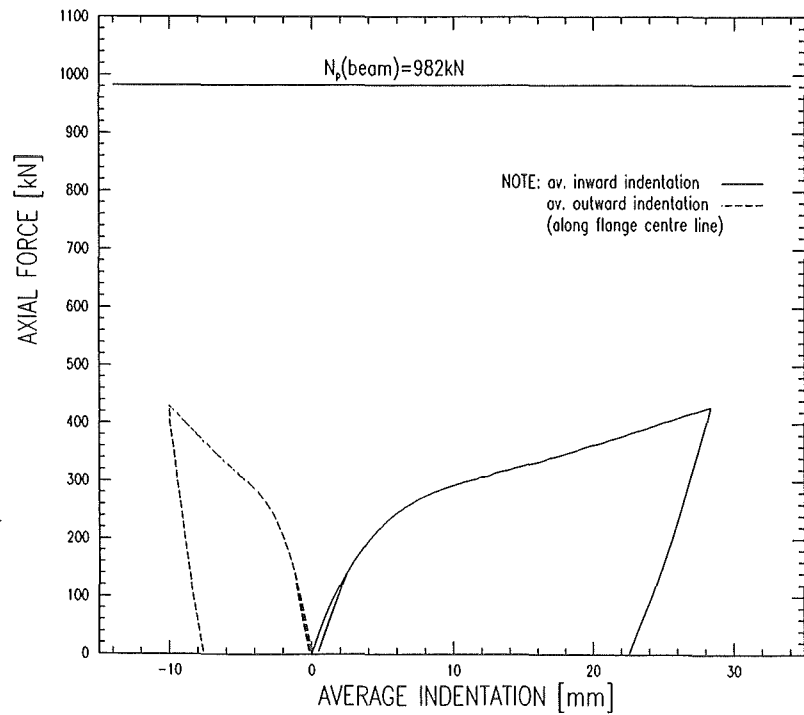


AVERAGE WELD SIZES (mm)



ACTUAL MECHANICAL PROPERTIES

Steel components	f_y	f_u	ϵ
	N/mm ²		%
RHS	453	575	30
IPE(flange)	420	520	32
IPE(web)	480	633	26
Concrete	f_c	f_t	E_c
	N/mm ²		%



Failure mode: no failure mode. Test stopped after sufficient deformation reached.

Fig. 7-9 : Data sheet for test 2R1

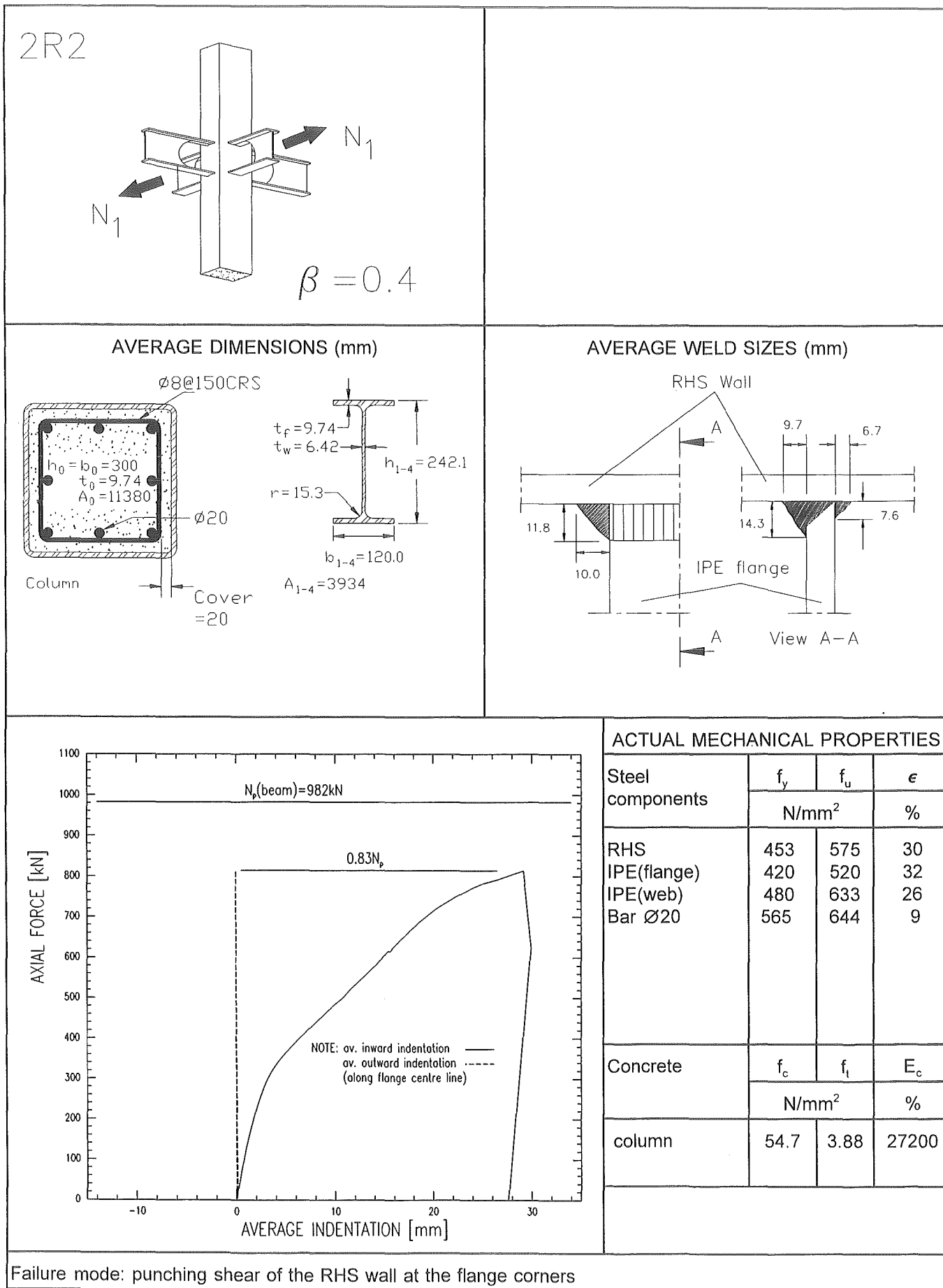
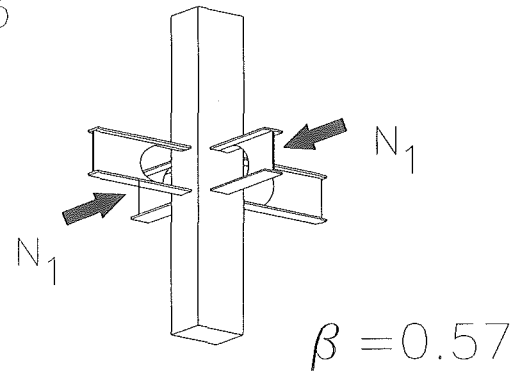
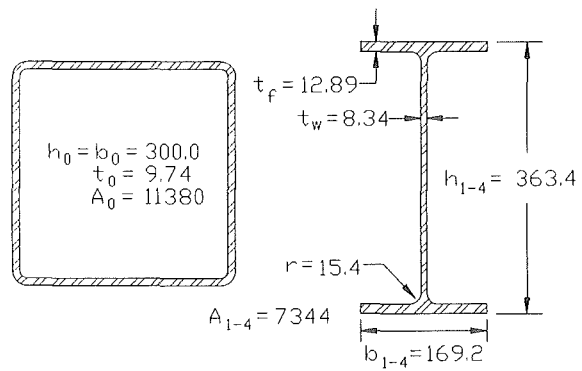


Fig. 7-10 : Data sheet for test 2R2

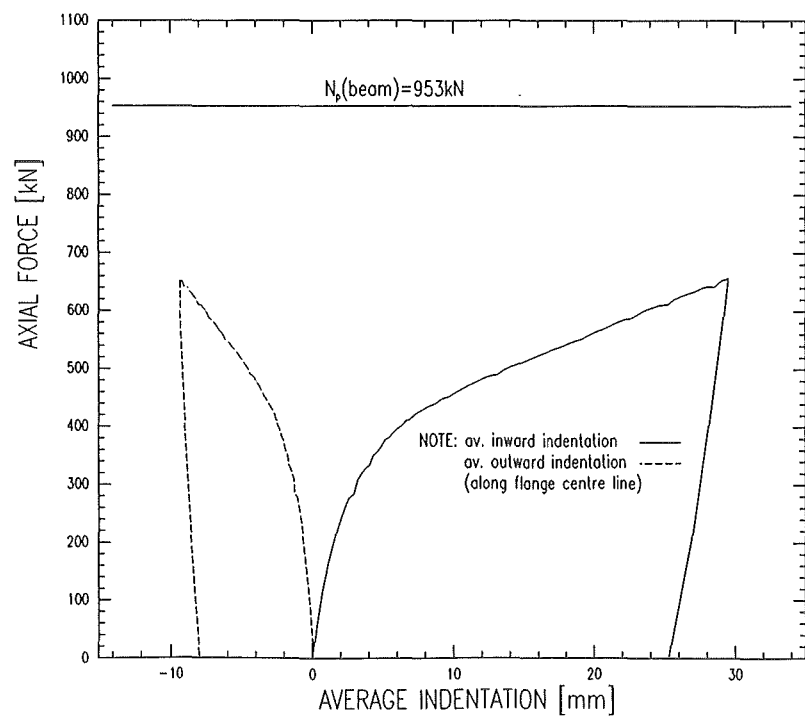
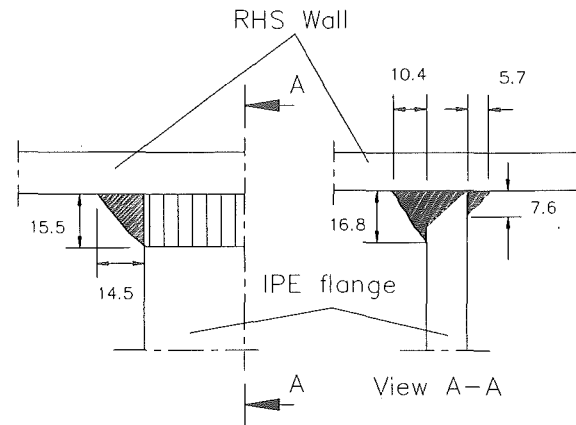
2R3



AVERAGE DIMENSIONS (mm)



AVERAGE WELD SIZES (mm)



ACTUAL MECHANICAL PROPERTIES

Steel components	f_y	f_u	ϵ
	N/mm ²		%
RHS	453	575	30
IPE(flange)	404	469	34
IPE(web)	442	540	28
Concrete	f_c	f_t	E_c
	N/mm ²		%

Failure mode: no failure mode. Test stopped after sufficient deformation

Fig. 7-11 : Data sheet for test 2R3

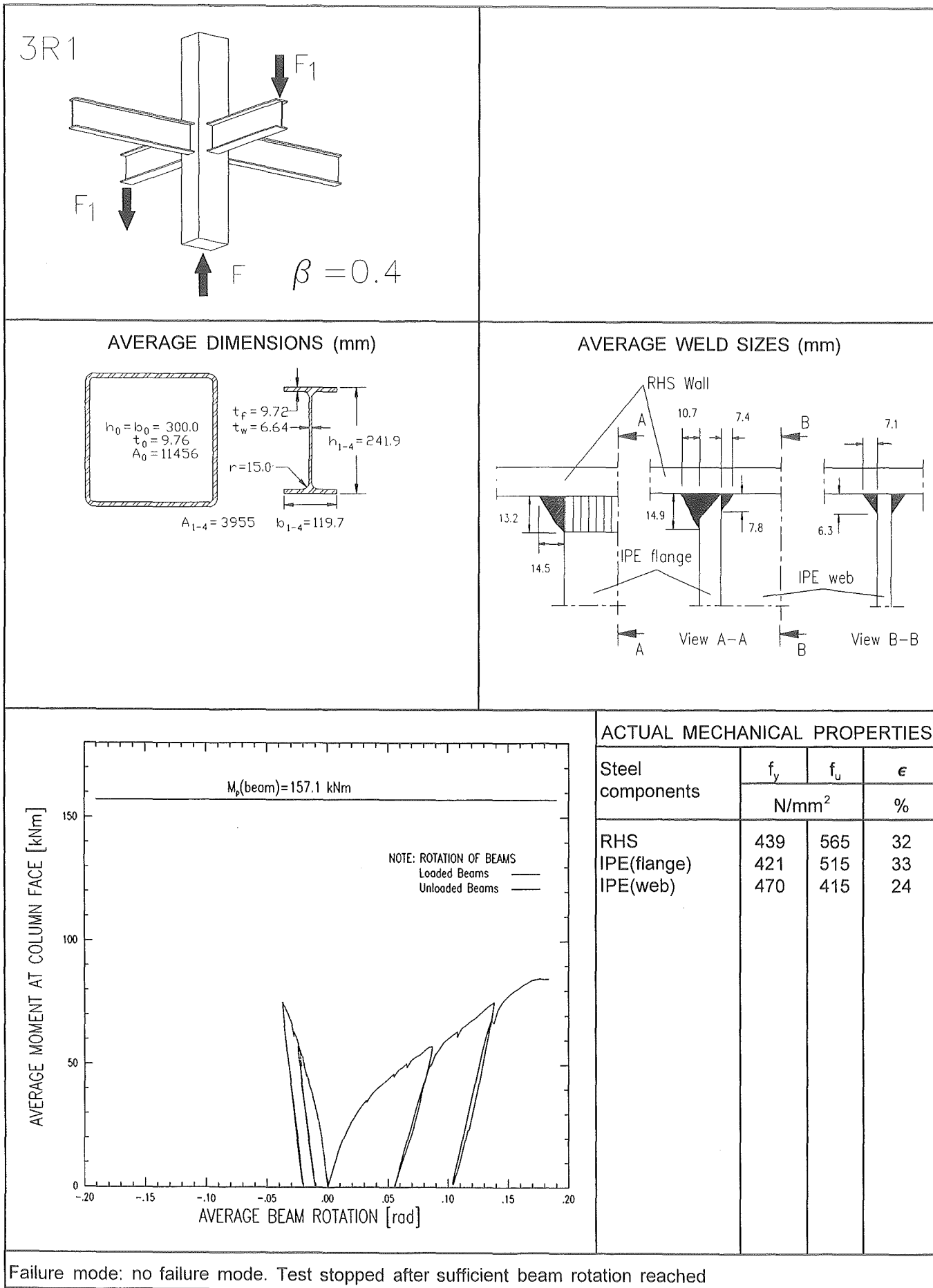
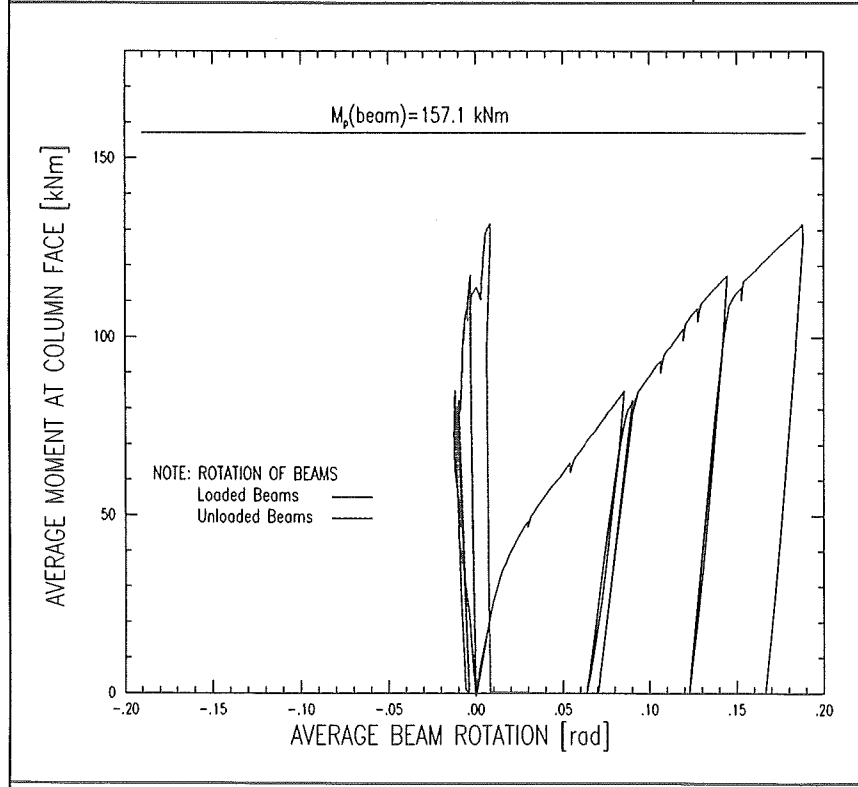
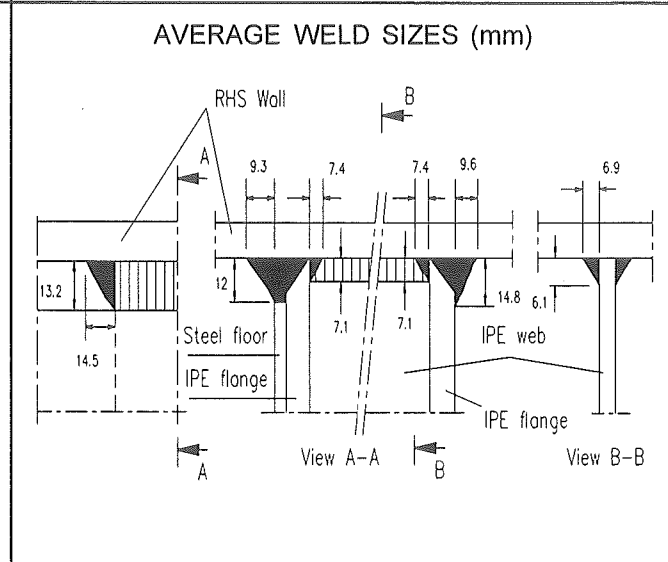
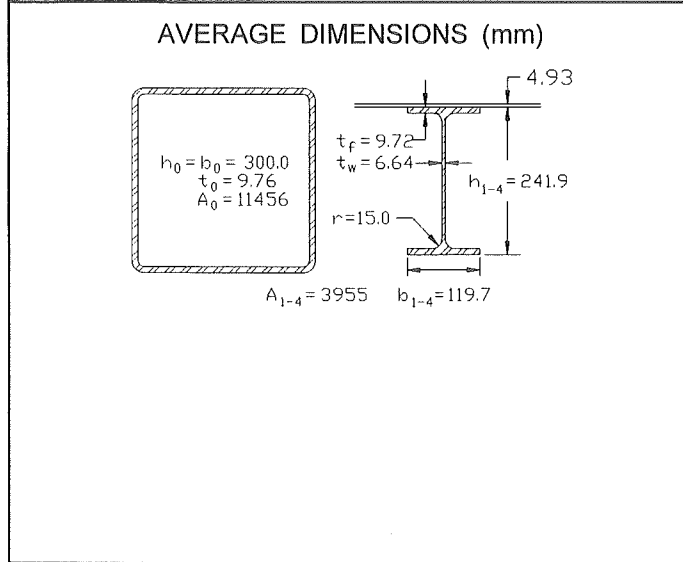
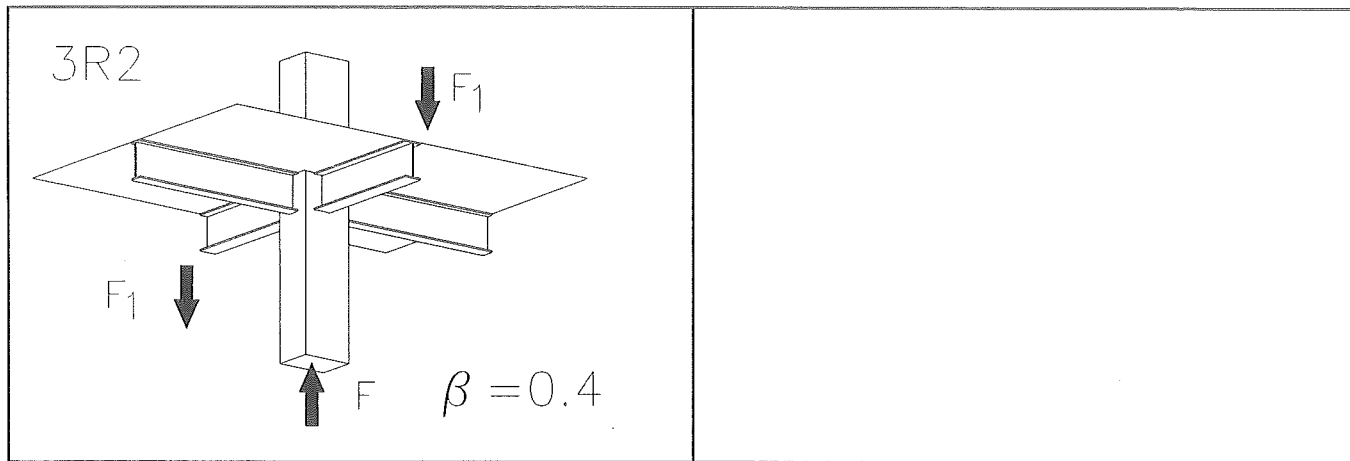


Fig. 7-12 : Data sheet for test 3R1



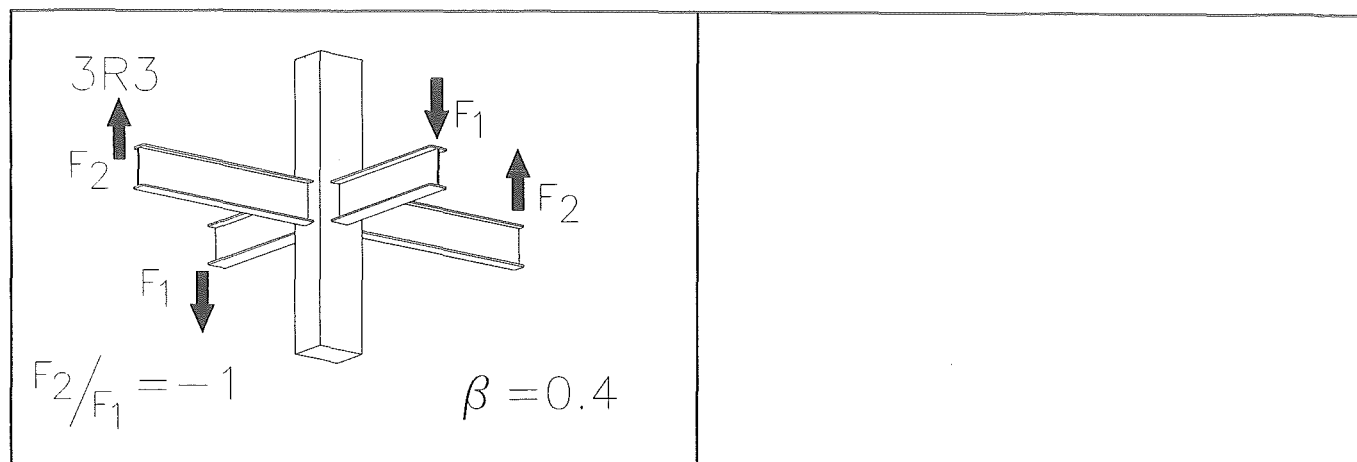
ACTUAL MECHANICAL PROPERTIES

Steel components	f_y	f_u	ϵ
	N/mm ²		%
RHS	439	565	32
IPE(flange)	421	515	33
IPE(web)	470	541	24
Steel floor	355	510	22

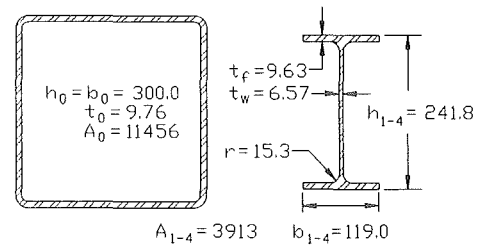
*Nominal values

Failure mode: no failure mode. Test stopped after sufficient beam rotation reached.

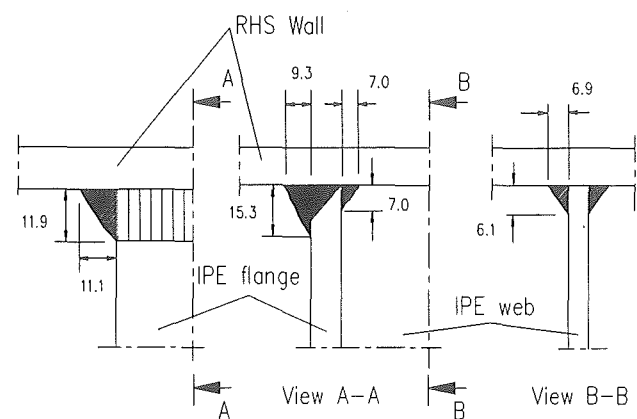
Fig. 7-13 : Data sheet for test 3R2



AVERAGE DIMENSIONS (mm)

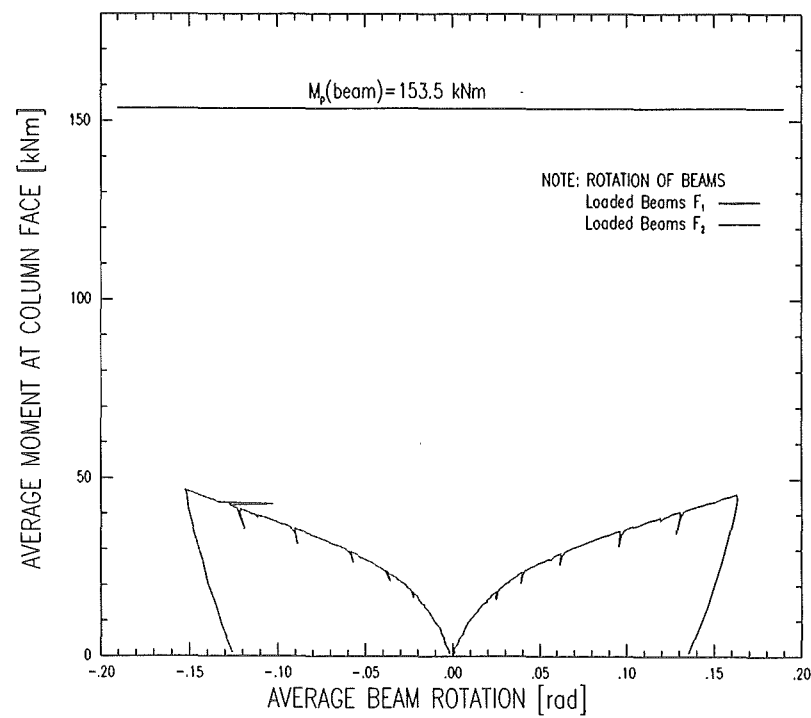


AVERAGE WELD SIZES (mm)



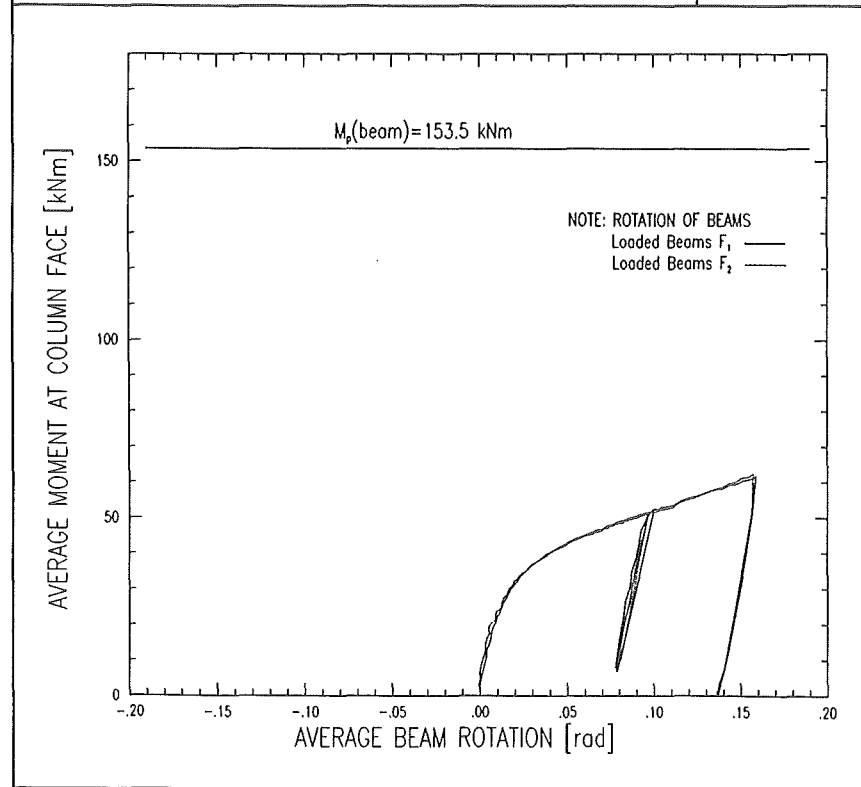
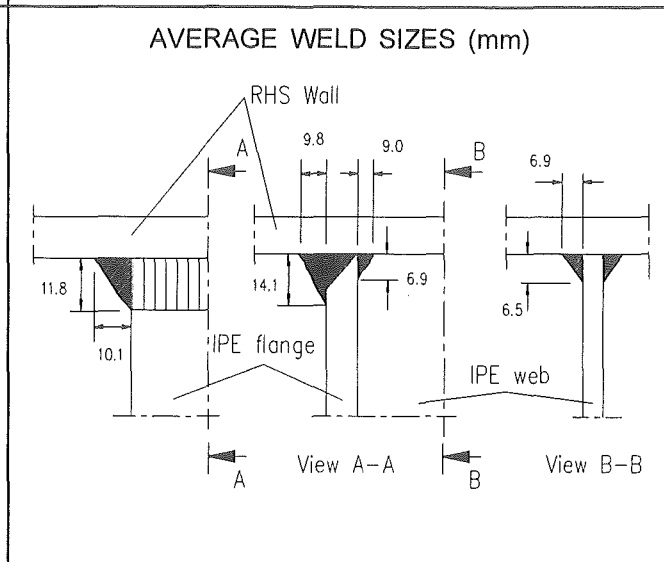
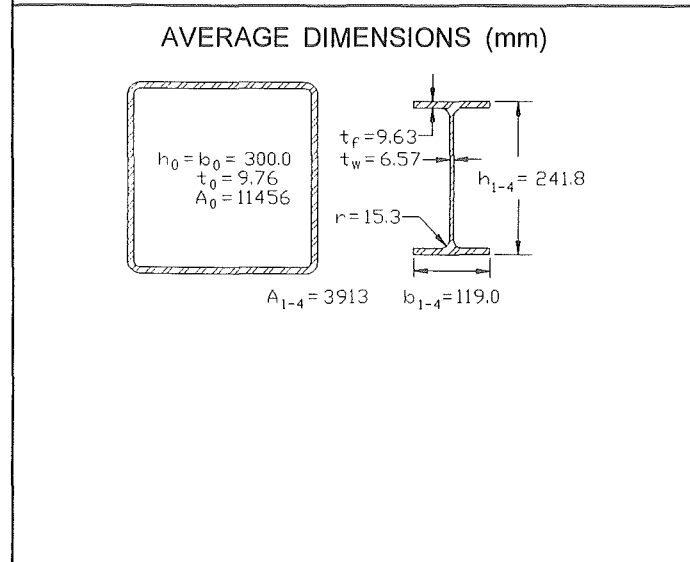
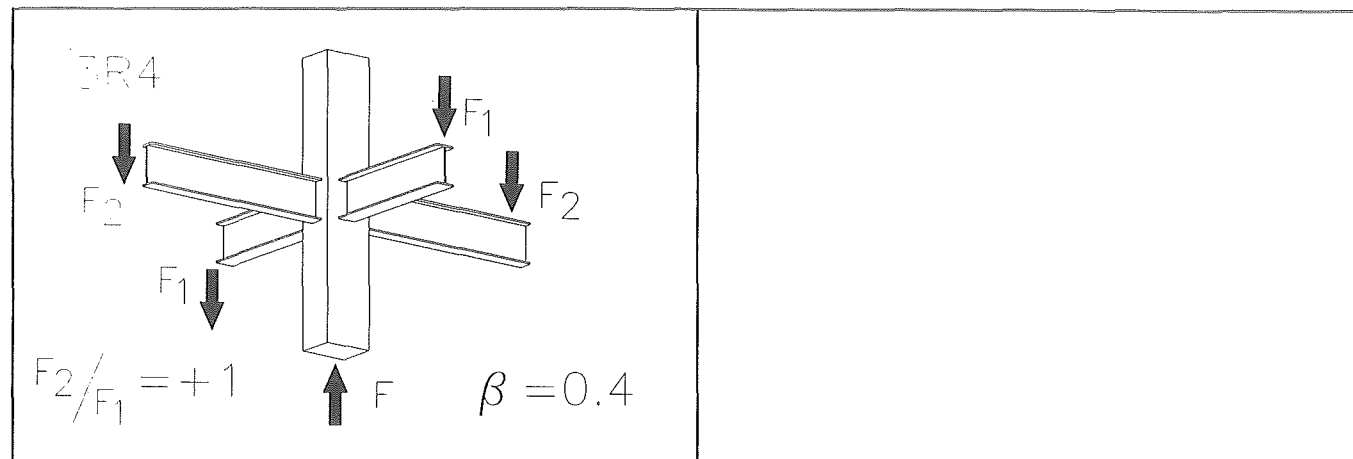
ACTUAL MECHANICAL PROPERTIES

Steel components	f_y	f_u	ϵ
	N/mm ²		%
RHS	439	565	32
IPE(flange)	419	519	32
IPE(web)	473	553	27



Failure mode: no failure mode. Test stopped after sufficient beam rotation reached

Fig. 7-14 : Data sheet for test 3R3



ACTUAL MECHANICAL PROPERTIES

Steel components	f_y	f_u	ϵ
	N/mm ²		%
RHS	387	565	32
IPE(flange)	419	519	32
IPE(web)	473	553	27

Failure mode: no failure mode. Test stopped after sufficient beam rotation reached

Fig. 7-15 : Data sheet for test 3R4

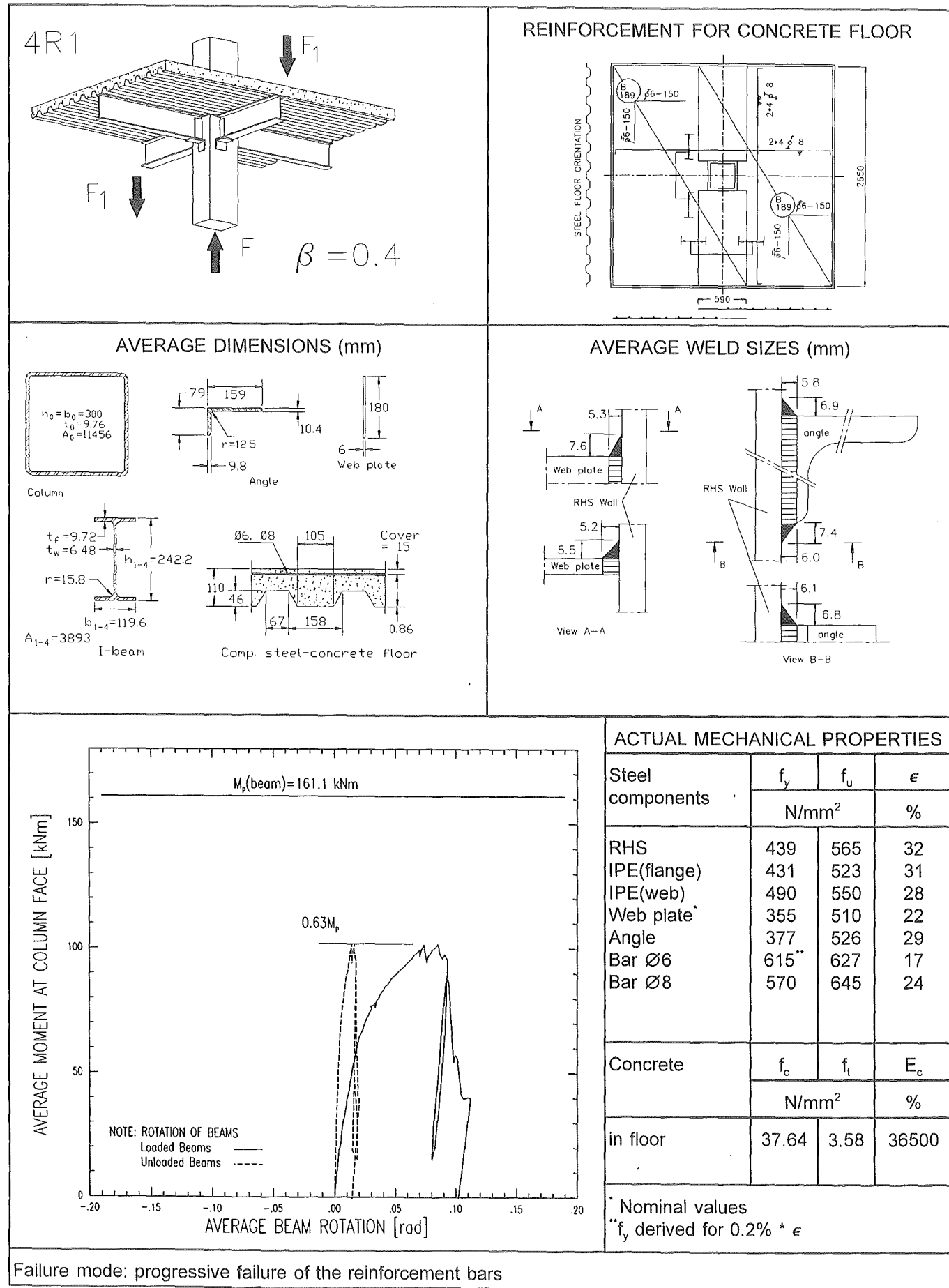


Fig. 7-16 : Data sheet for test 4R1

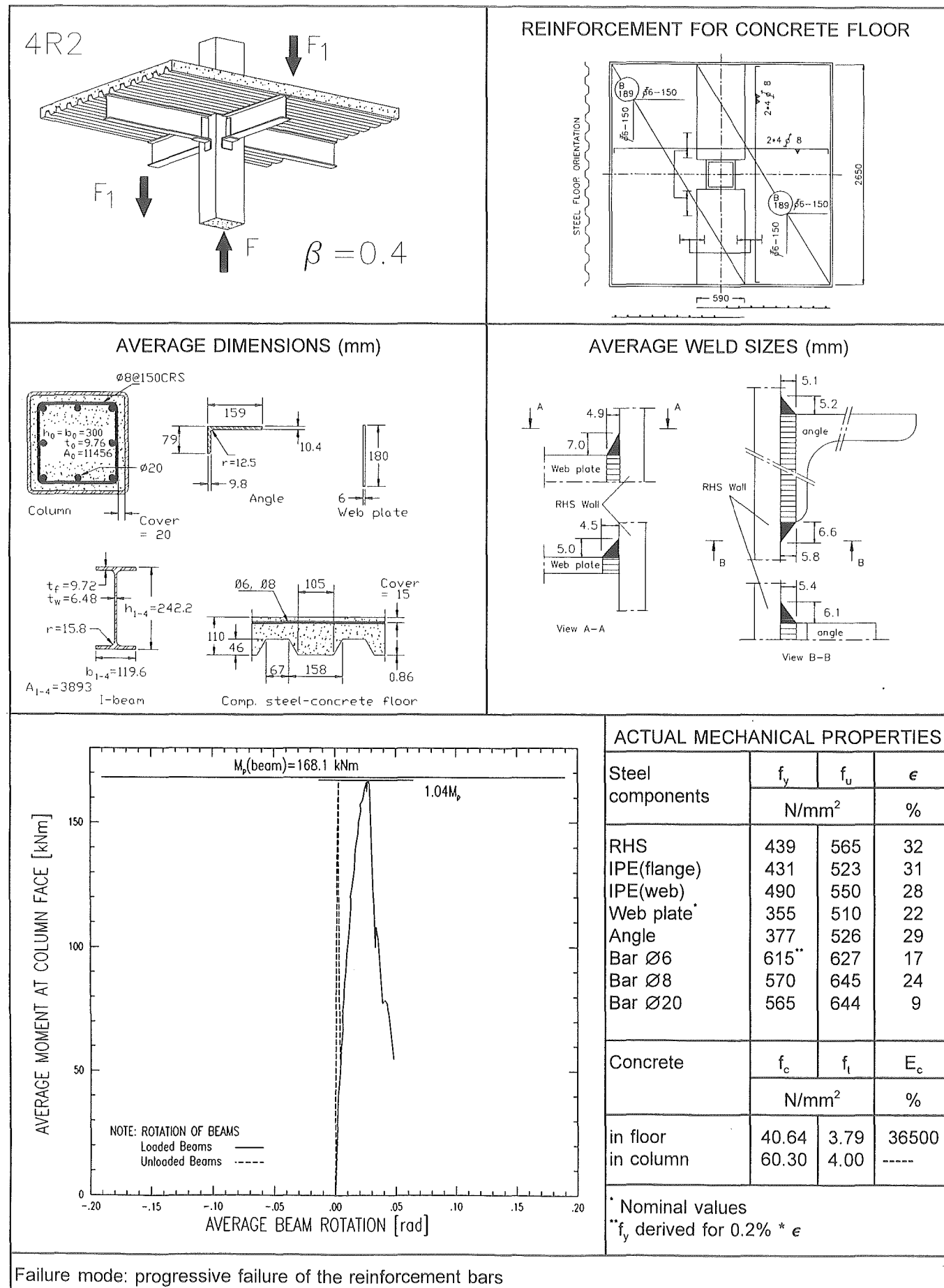


Fig. 7-17 : Data sheet for test 4R2

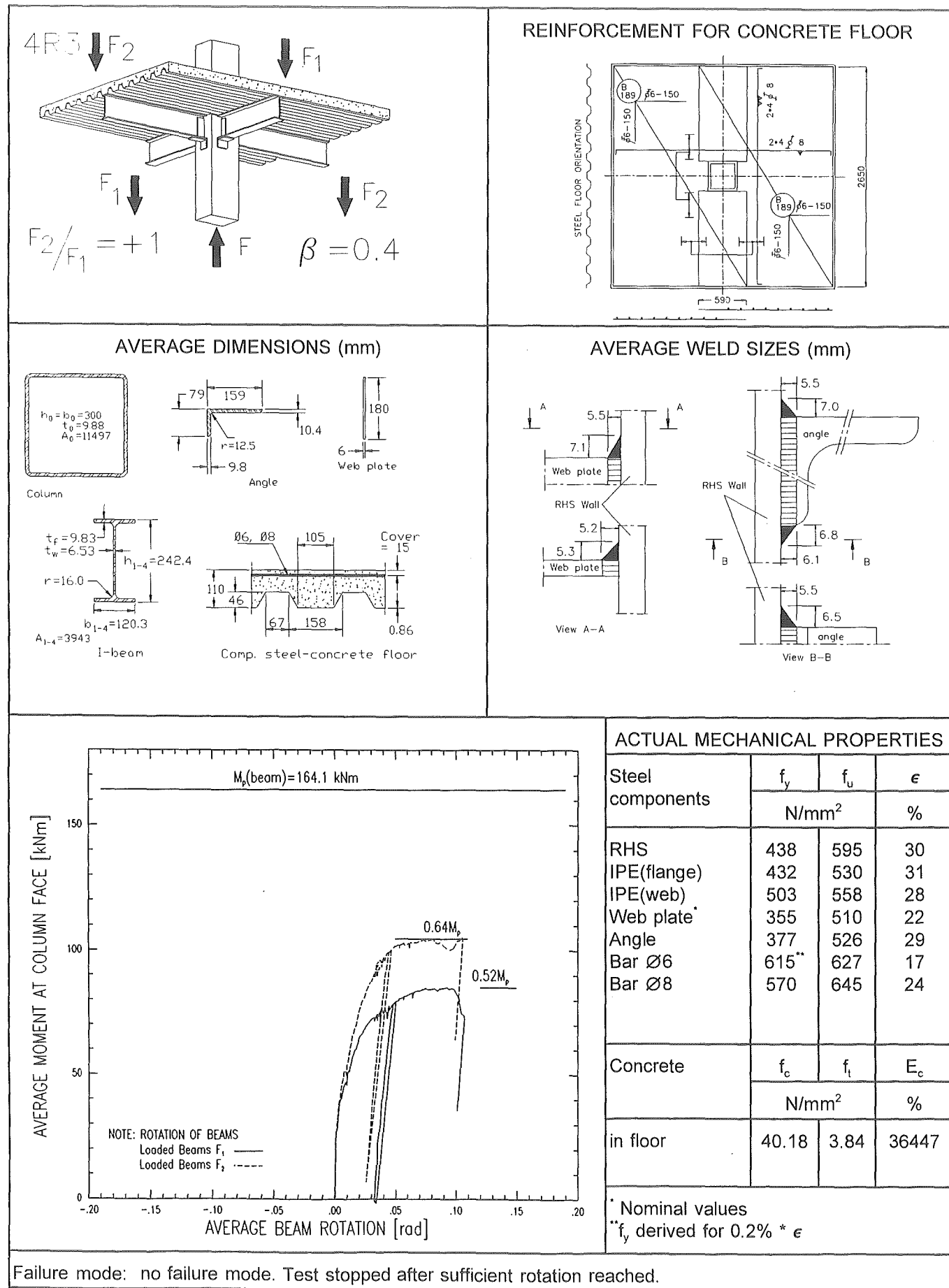
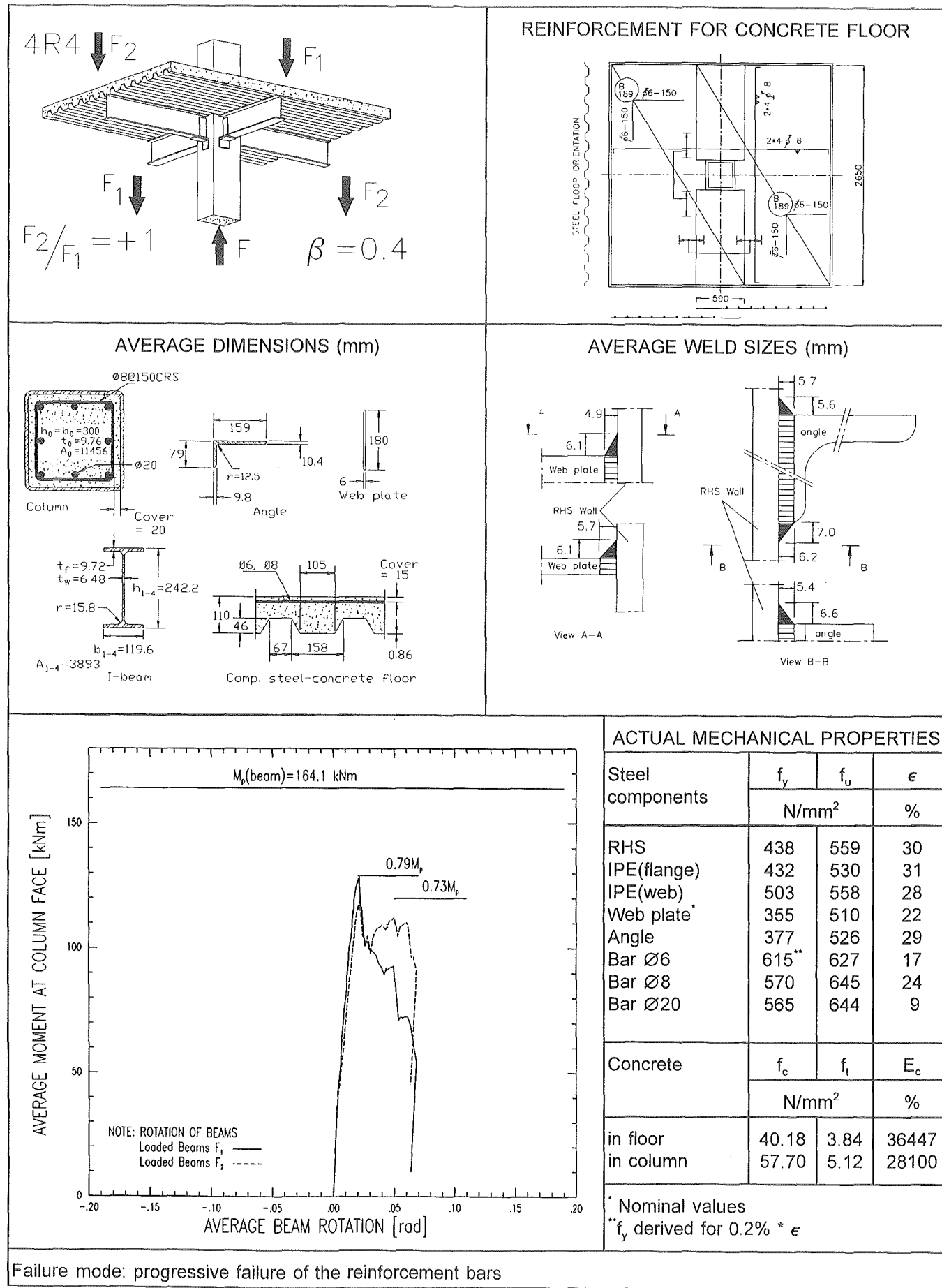


Fig. 7-18 : Data sheet for test 4R3



Failure mode: progressive failure of the reinforcement bars

Fig. 7-19 : Data sheet for test 4R4

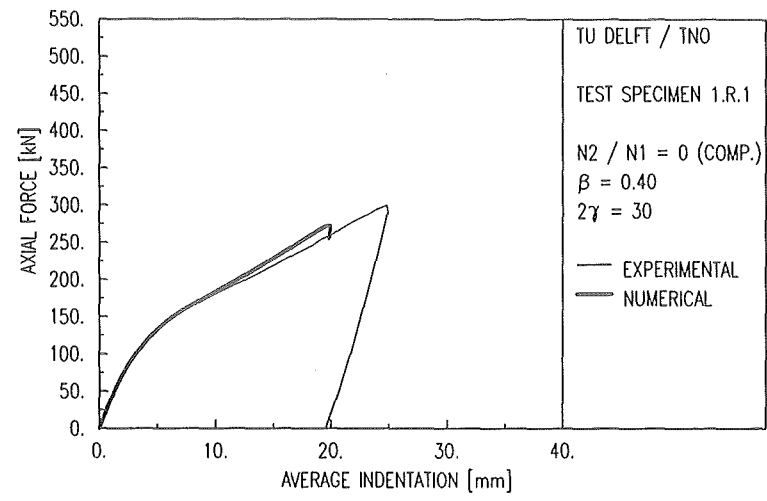


Fig: 7-20 Experimental and numerical load-deformation diagram for 1R1

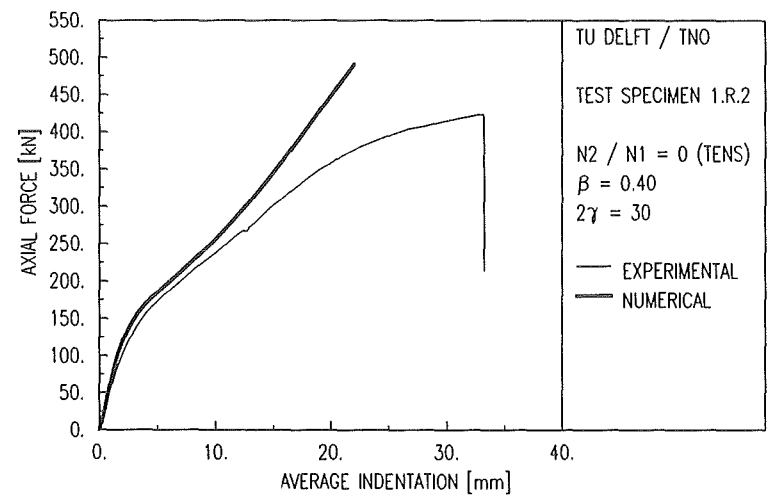


Fig: 7-21 Experimental and numerical load-deformation diagram for 1R2

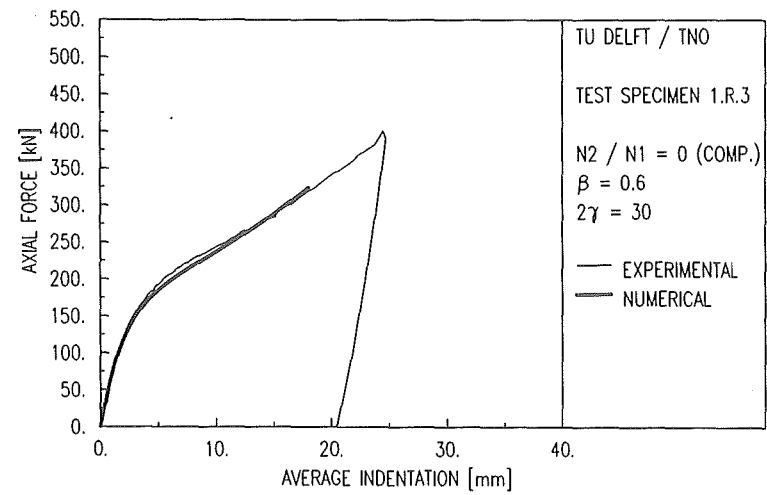


Fig: 7-22 Experimental and numerical load-deformation diagram for 1R3

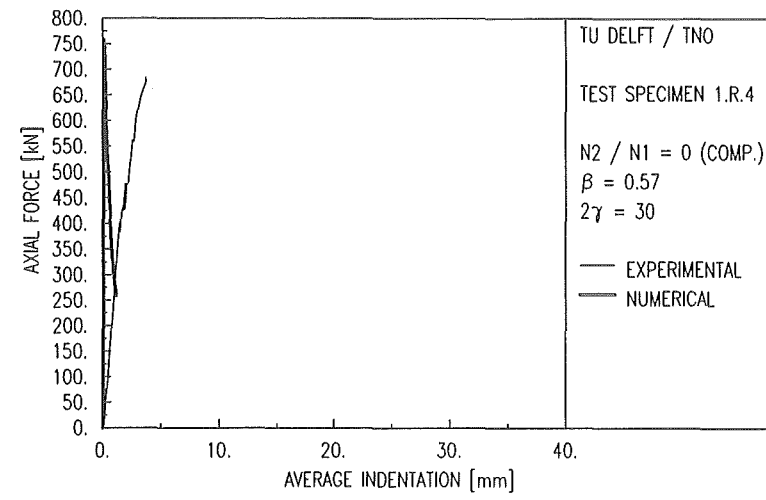


Fig: 7-23 Experimental and numerical load-deformation diagram for 1R4

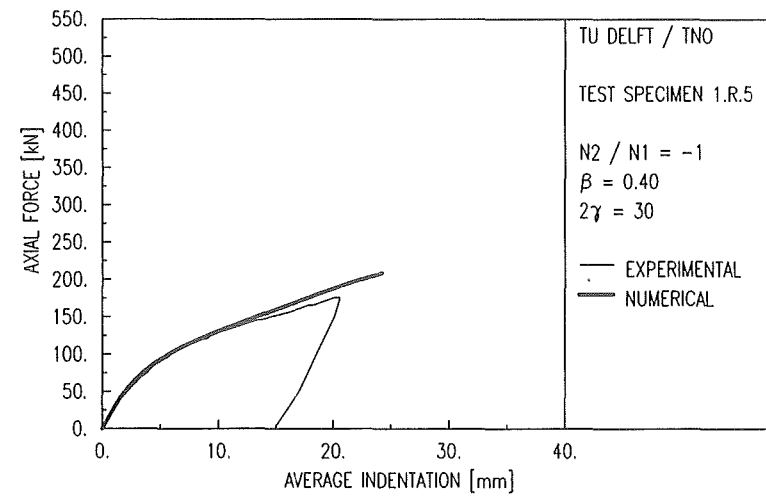


Fig: 7-24 Experimental and numerical load-deformation diagram for 1R5

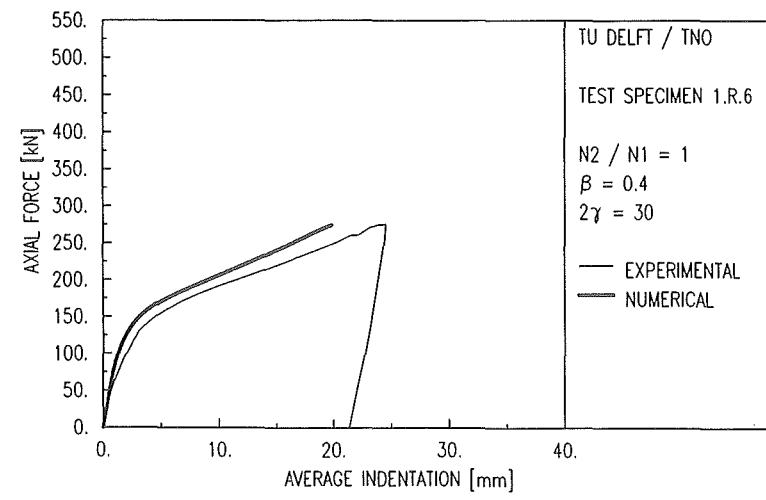


Fig: 7-25 Experimental and numerical load-deformation diagram for 1R6

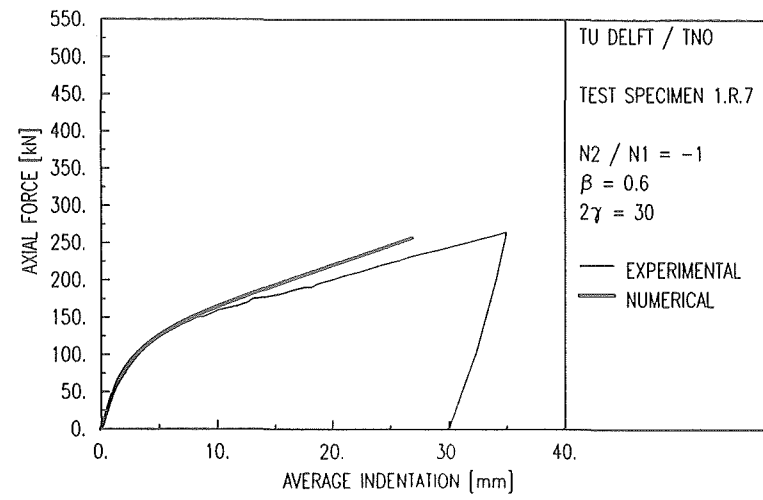


Fig: 7-26 Experimental and numerical load-deformation diagram for 1R7

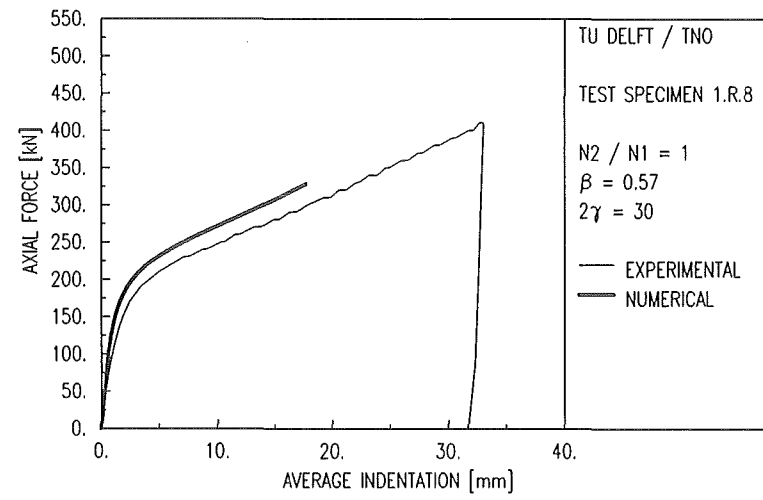


Fig: 7-27 Experimental and numerical load-deformation diagram for 1R8

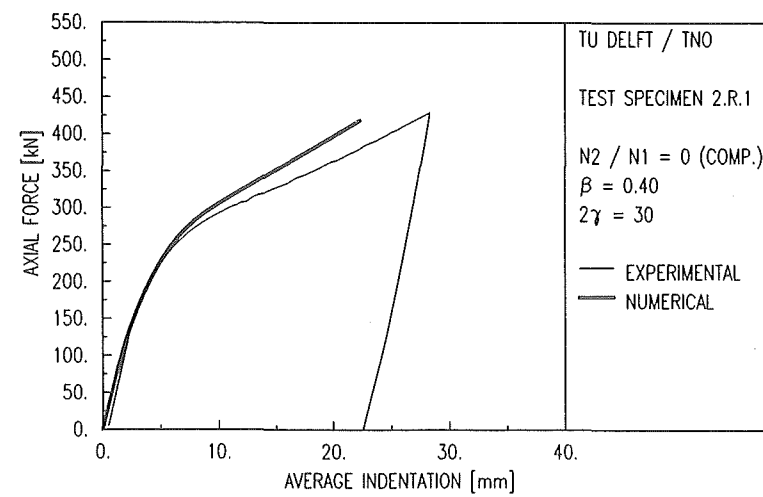


Fig: 7-28 Experimental and numerical load-deformation diagram for 2R1

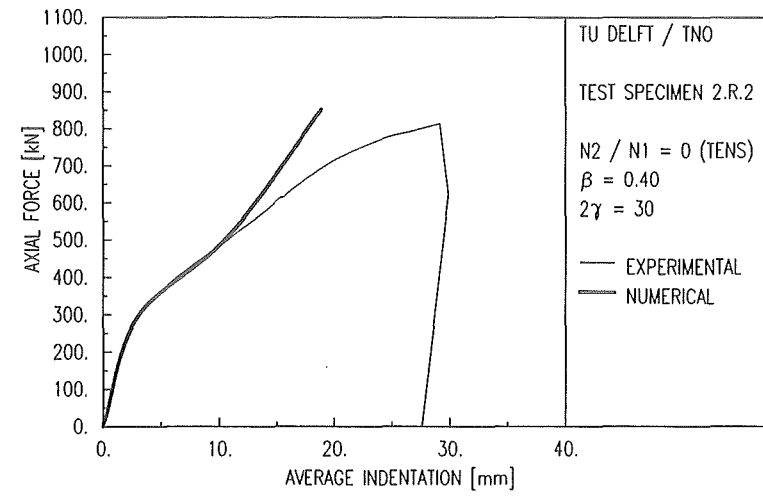


Fig: 7-29 Experimental and numerical load-deformation diagram for 2R2

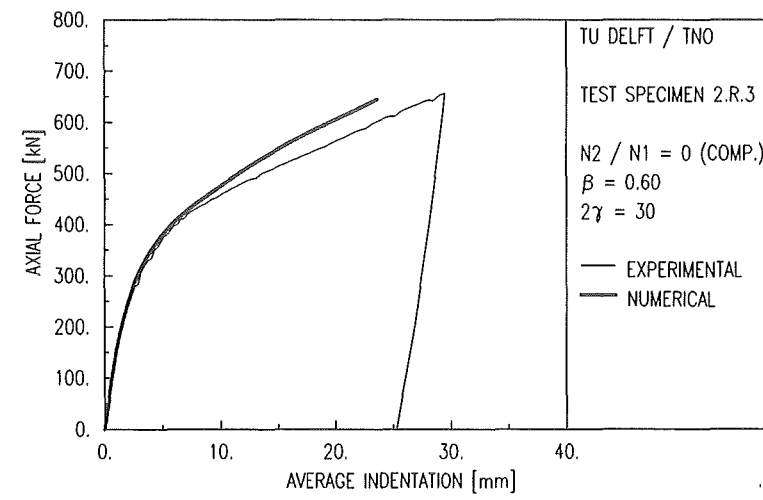


Fig: 7-30 Experimental and numerical load-deformation diagram for 2R3

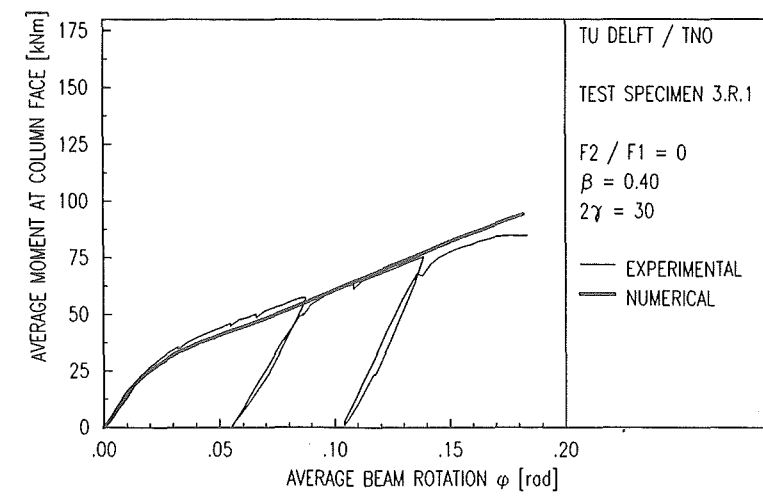


Fig: 7-31 Experimental and numerical moment-rotation diagram for 3R1

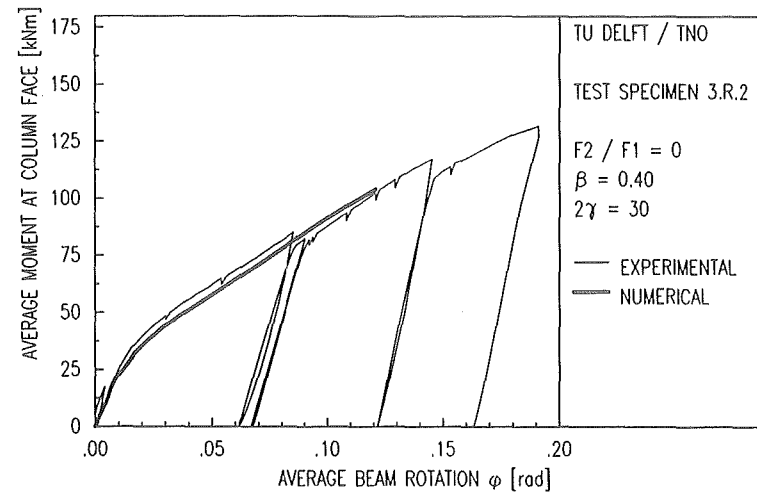


Fig: 7-32 Experimental and numerical moment-rotation diagram for 3R2

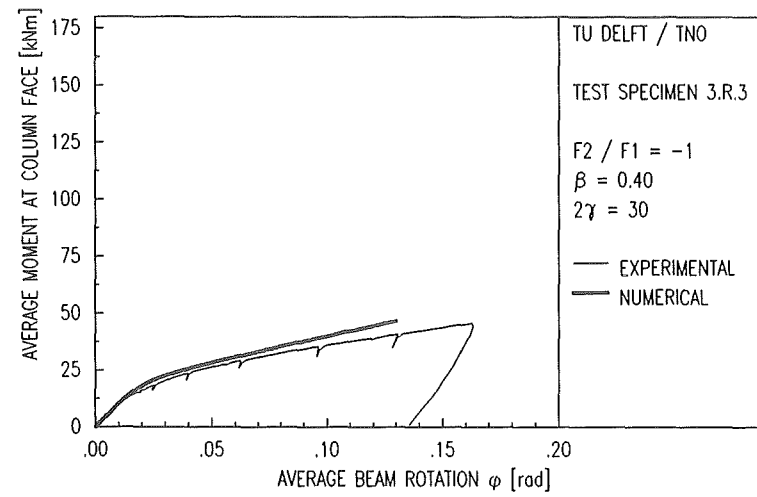


Fig: 7-33 Experimental and numerical moment-rotation diagram for 3R3

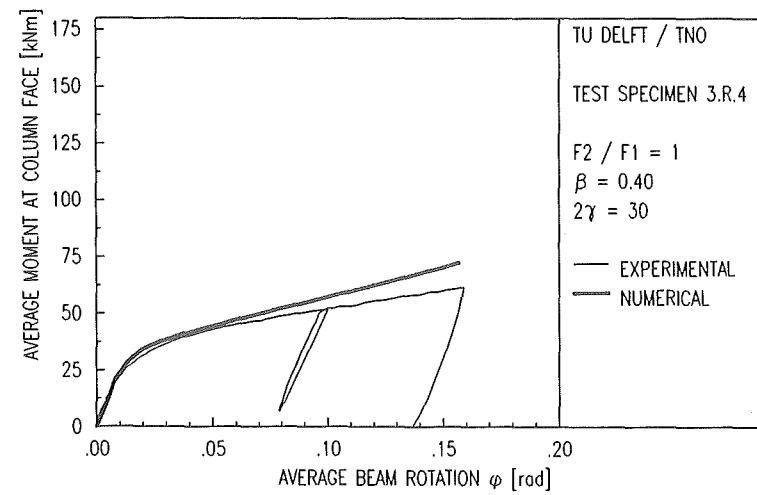


Fig: 7-34 Experimental and numerical moment-rotation diagram for 3R4

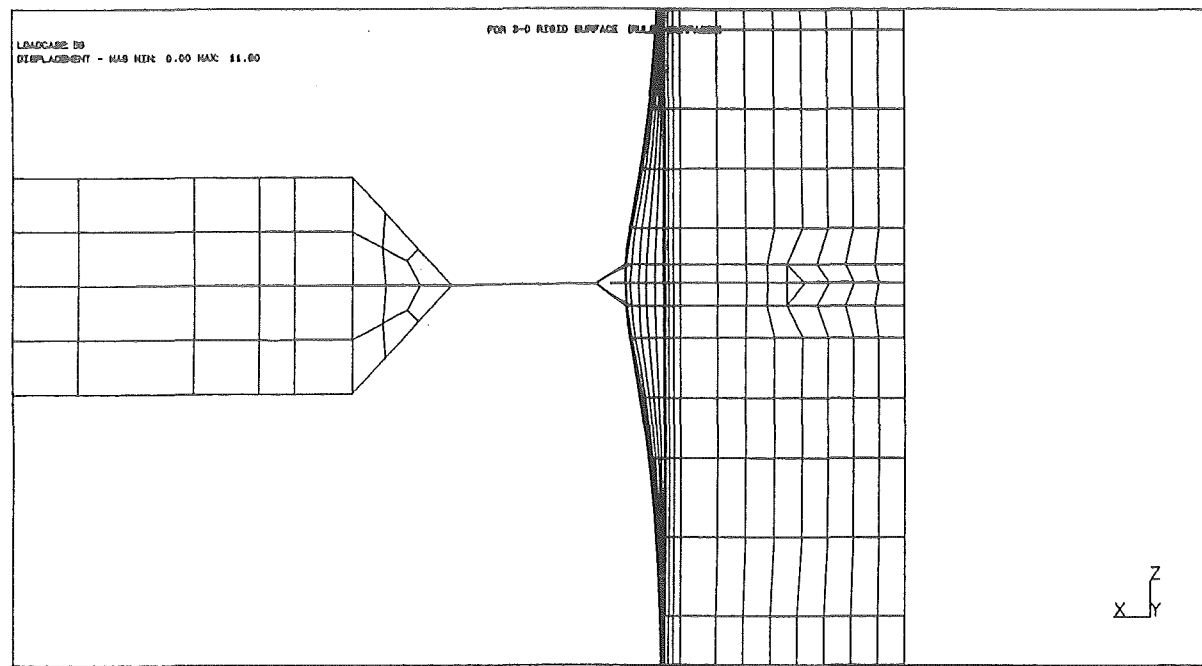


Fig: 7-35 Deformed finite element mesh of model 1R2

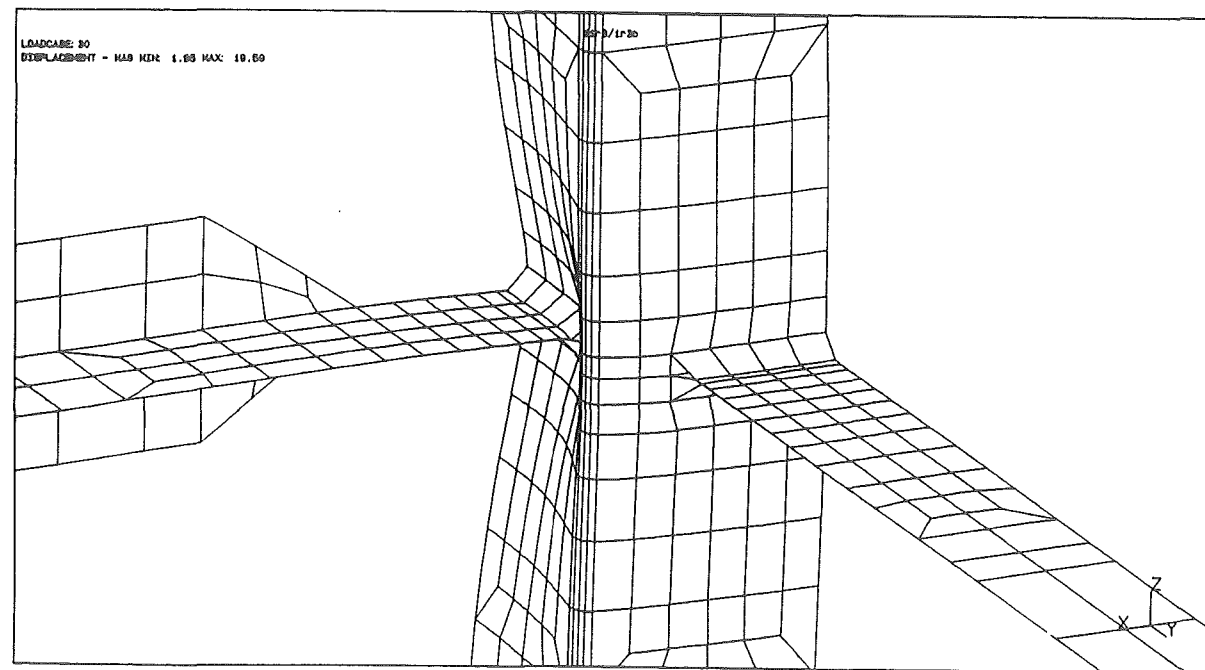


Fig: 7-36 Deformed finite element mesh of model 1R3

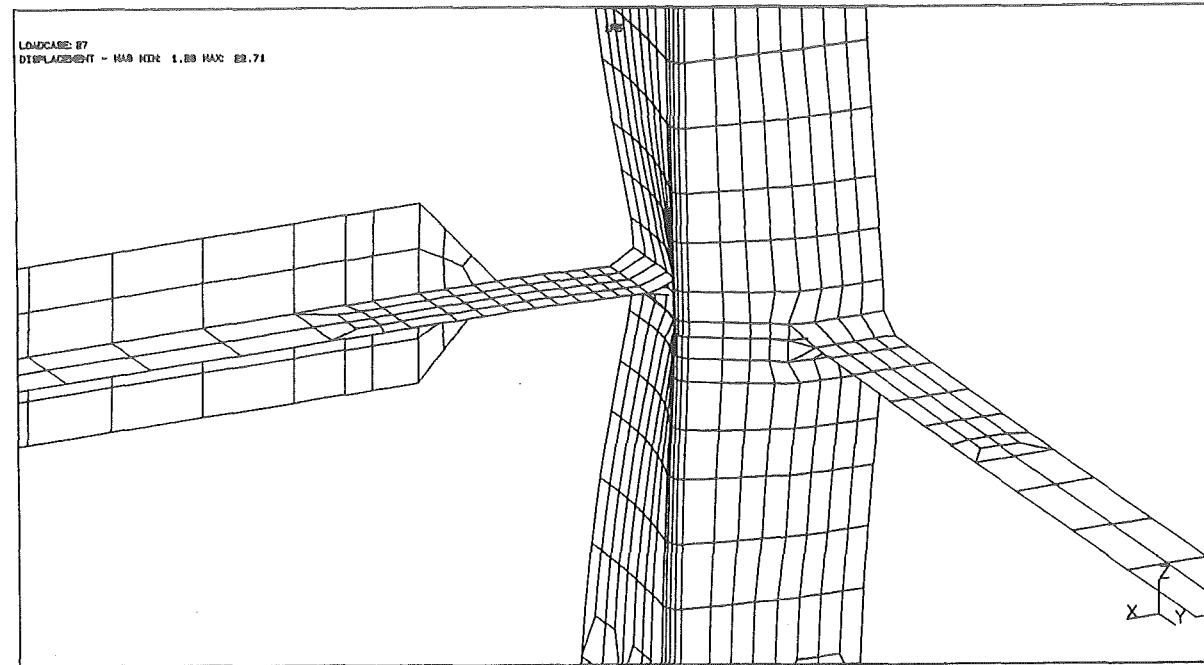


Fig: 7-37 Deformed finite element mesh of model 1R5

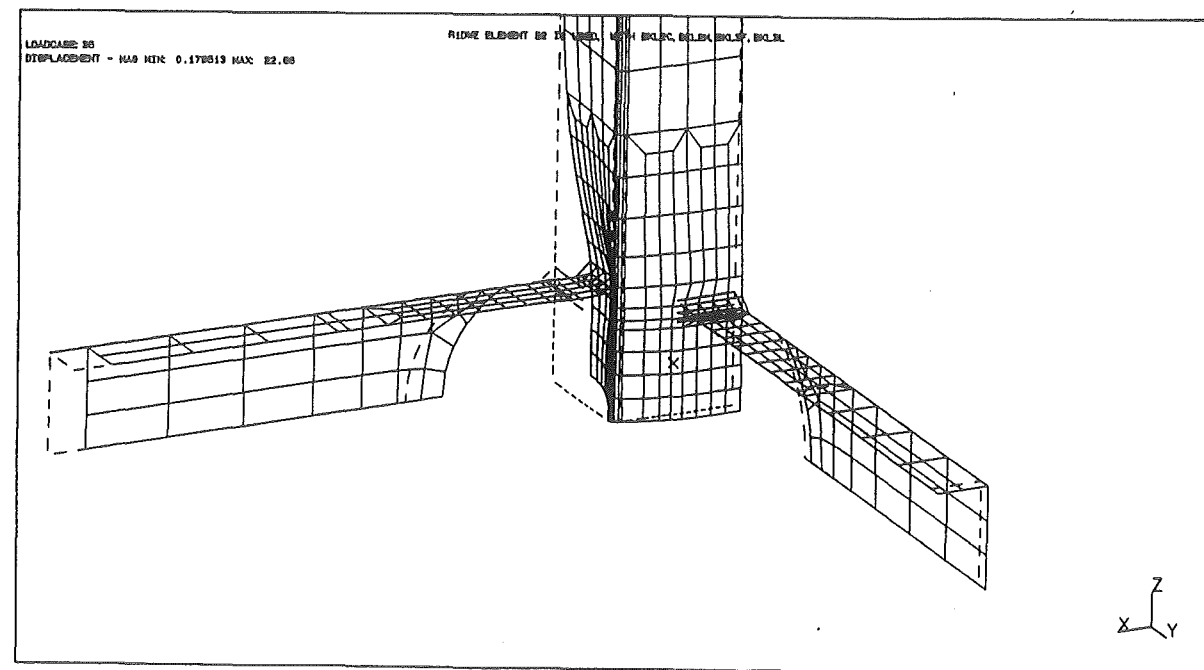


Fig: 7-38 Deformed finite element mesh of model 2R1

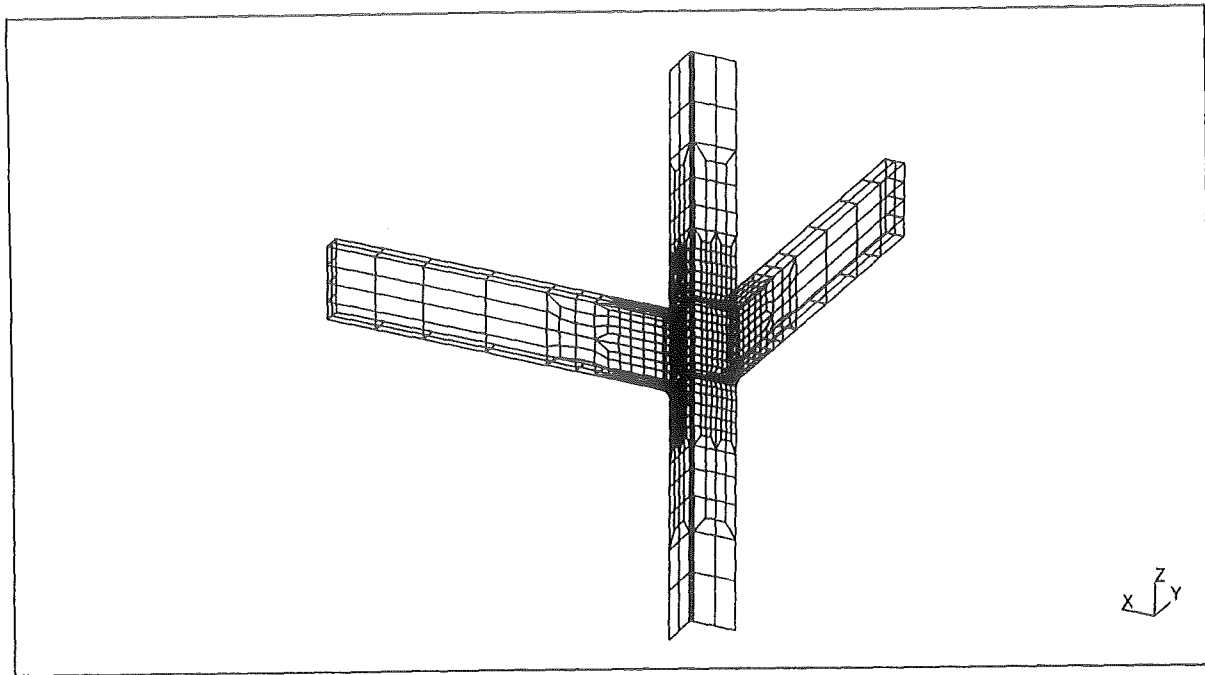


Fig: 7-39 Finite element mesh of model 3R1

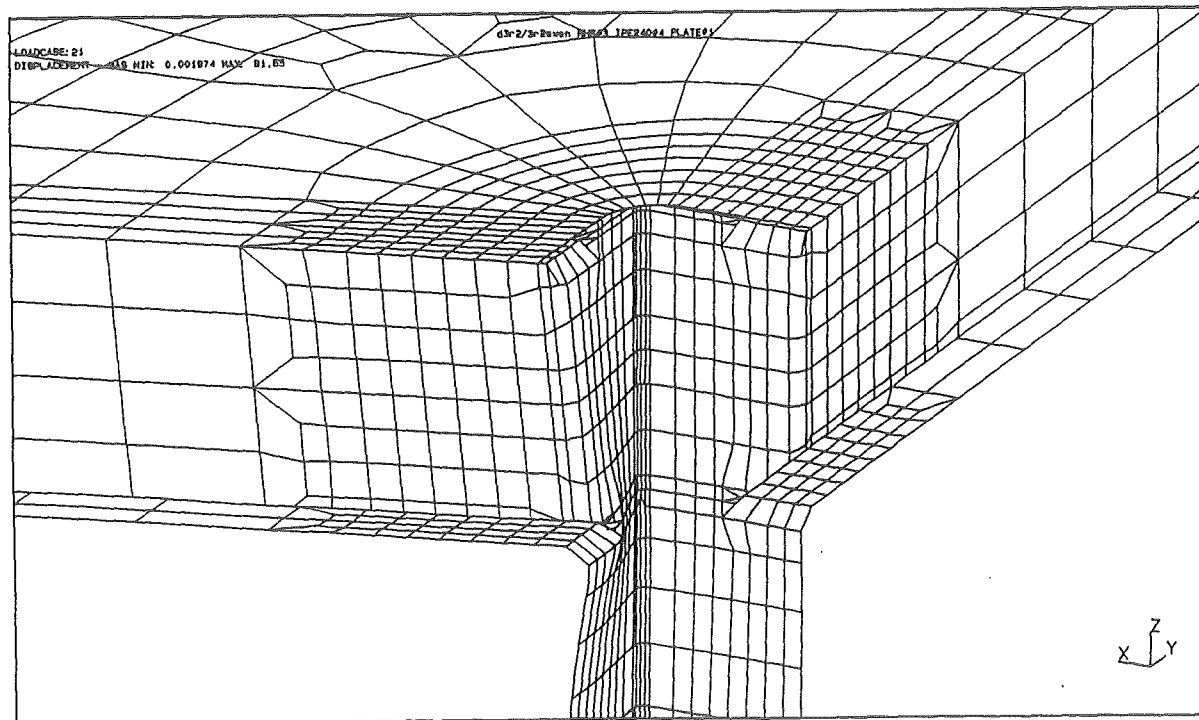


Fig: 7-40 Deformed finite element mesh of model 3R2

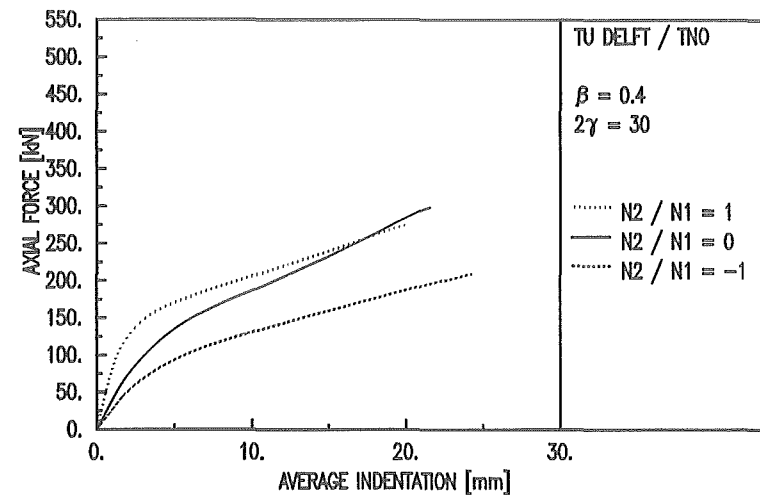


Fig: 7-41 Multiplanar effect axial loading tests series 1

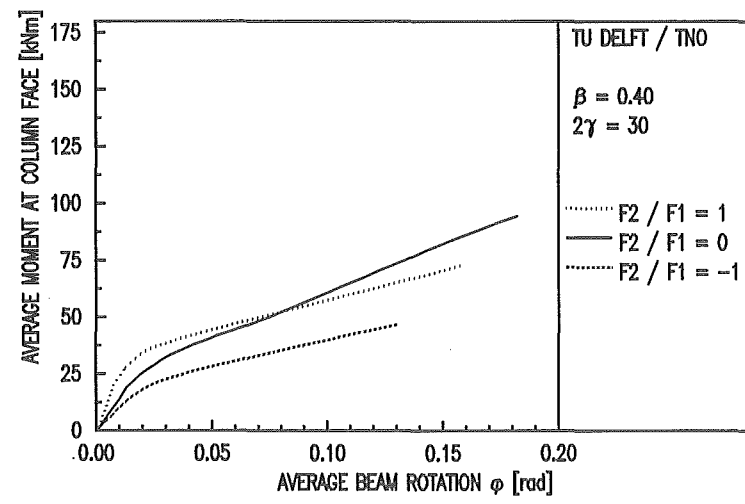


Fig: 7-42 Multiplanar effect in-plane bending tests series 3

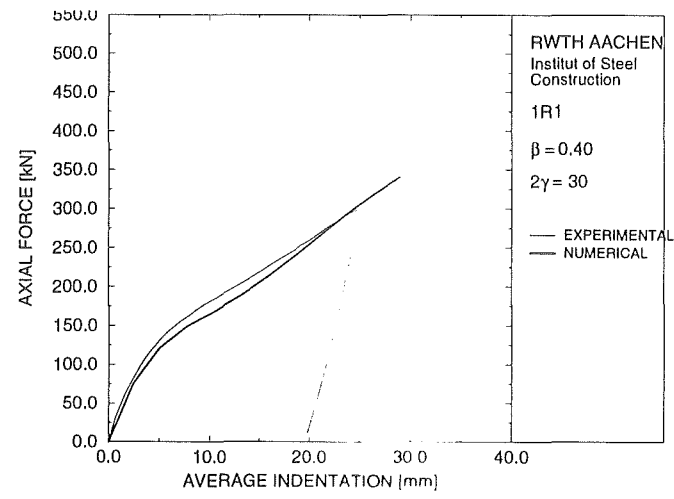


Fig: 7-43 Experimental and numerical load-deformation diagram for 1R1 (Aachen)

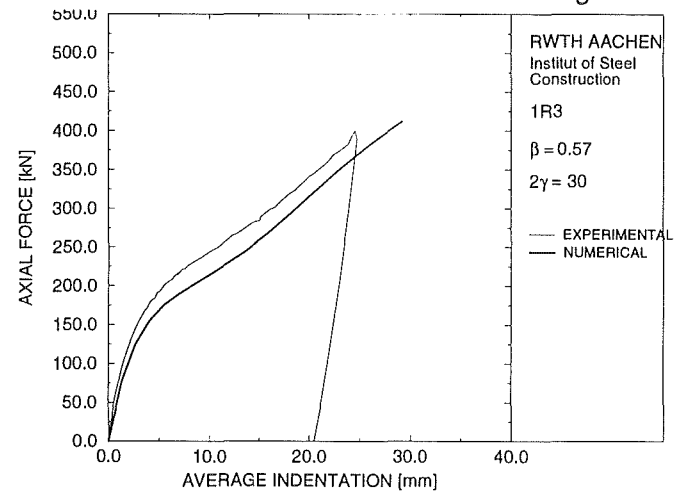


Fig: 7-44 Experimental and numerical load-deformation diagram for 1R3 (Aachen)

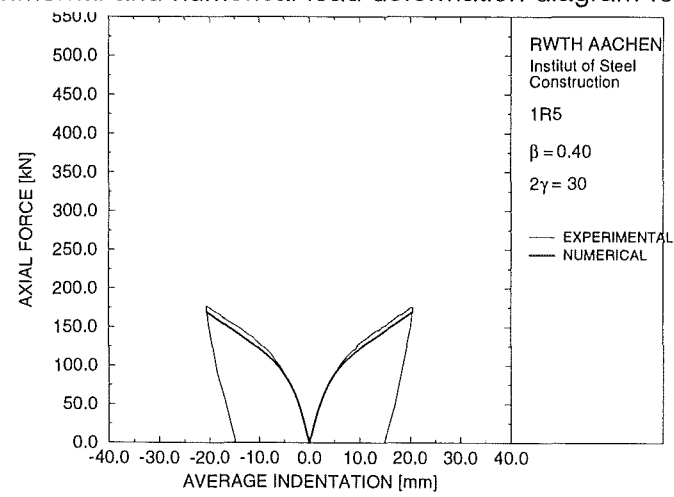


Fig: 7-45 Experimental and numerical load-deformation diagram for 1R5 (Aachen)

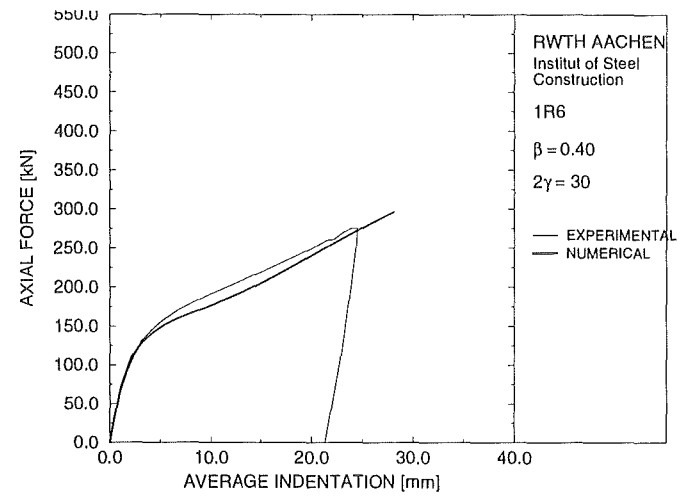


Fig: 7-46 Experimental and numerical load-deformation diagram for 1R6 (Aachen)

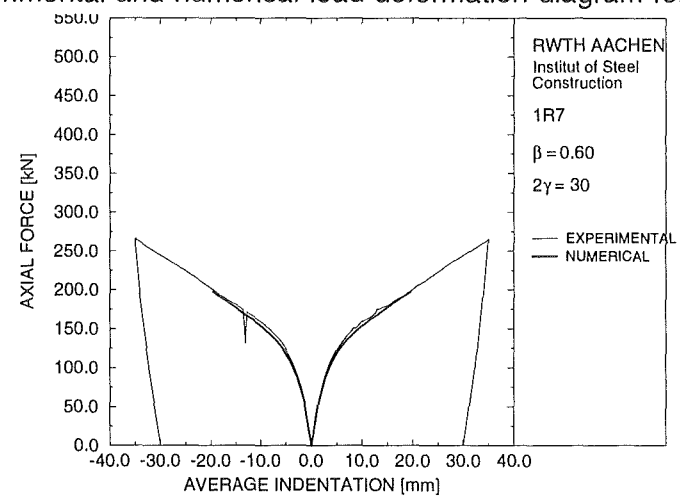


Fig: 7-47 Experimental and numerical load-deformation diagram for 1R7 (Aachen)

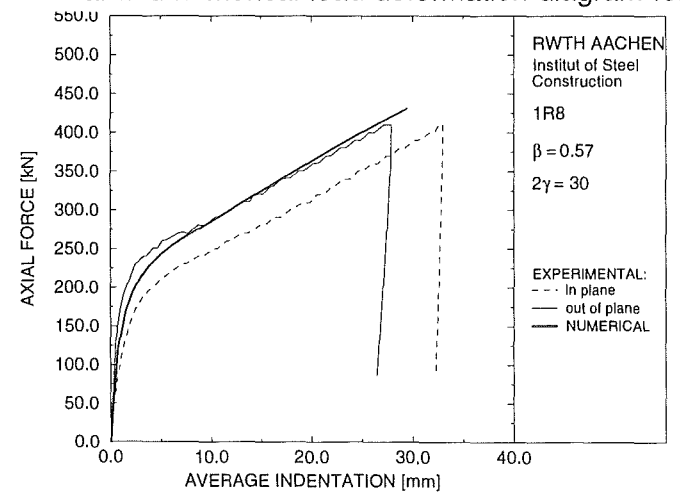


Fig: 7-48 Experimental and numerical load-deformation diagram for 1R8 (Aachen)

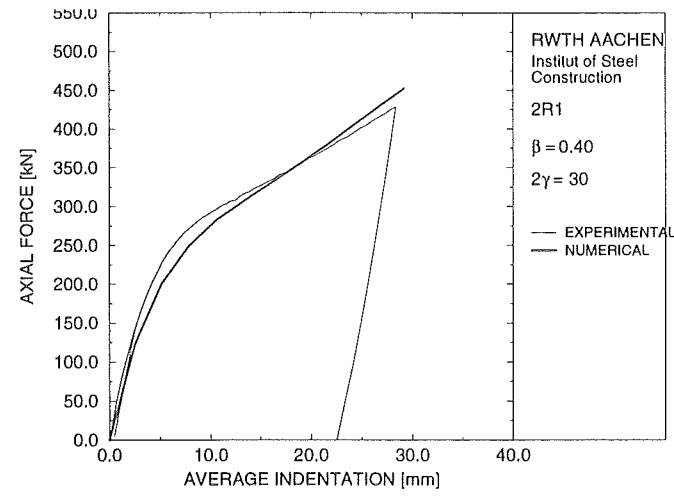


Fig: 7-49 Experimental and numerical load-deformation diagram for 2R1 (Aachen)

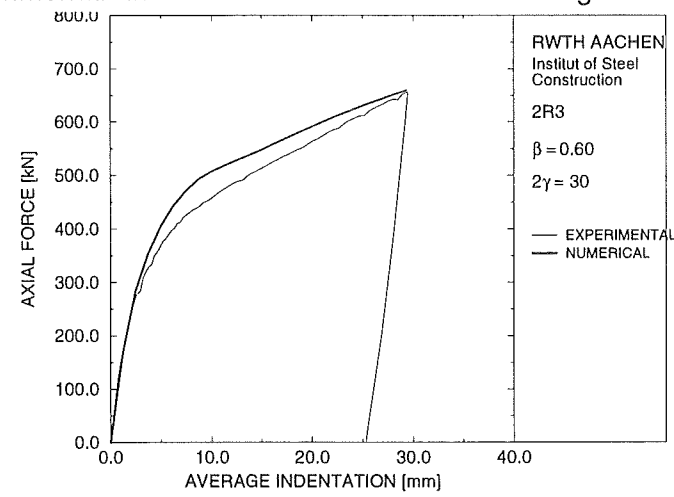


Fig: 7-50 Experimental and numerical load-deformation diagram for 2R3 (Aachen)

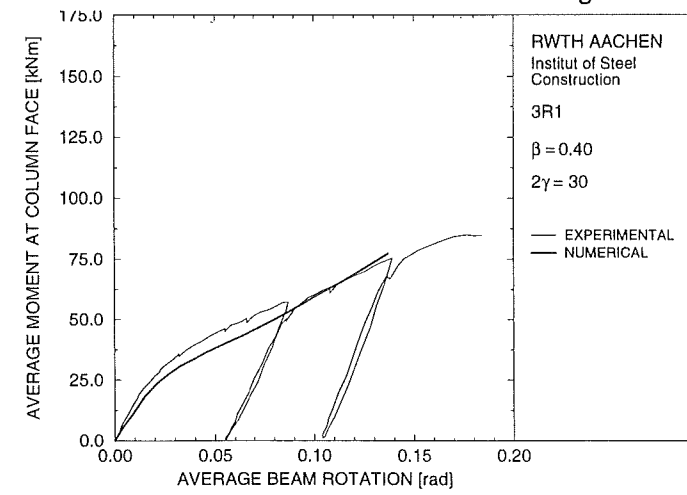


Fig: 7-51 Experimental and numerical moment-rotation diagram for 3R1

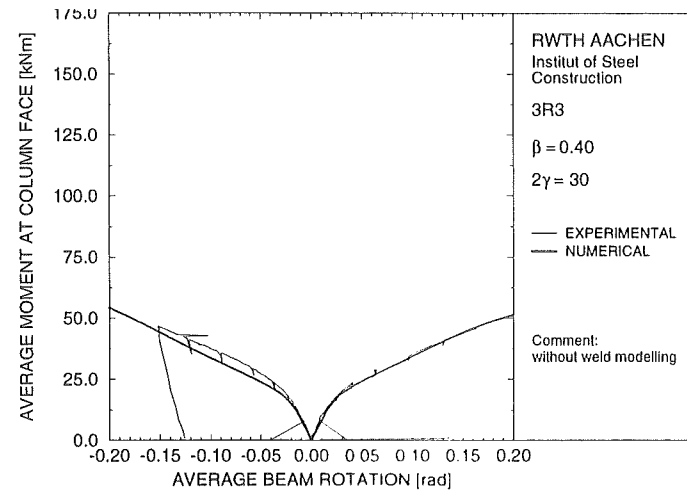


Fig: 7-52 Experimental and numerical moment-rotation diagram for 3R3

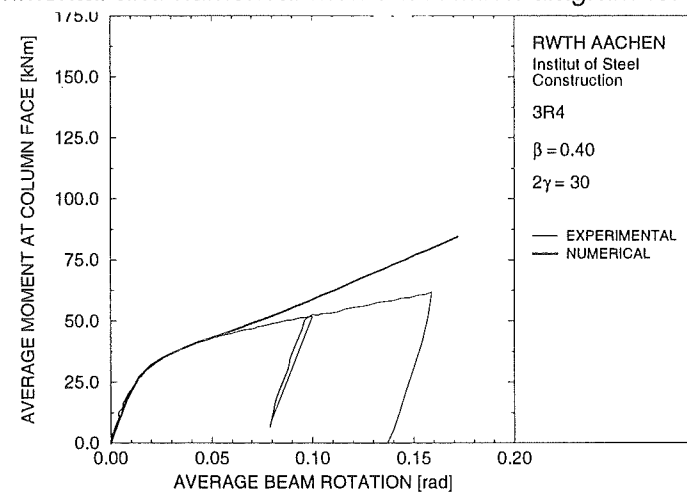


Fig: 7-53 Experimental and numerical moment-rotation diagram for 3R4

PHOTO'S

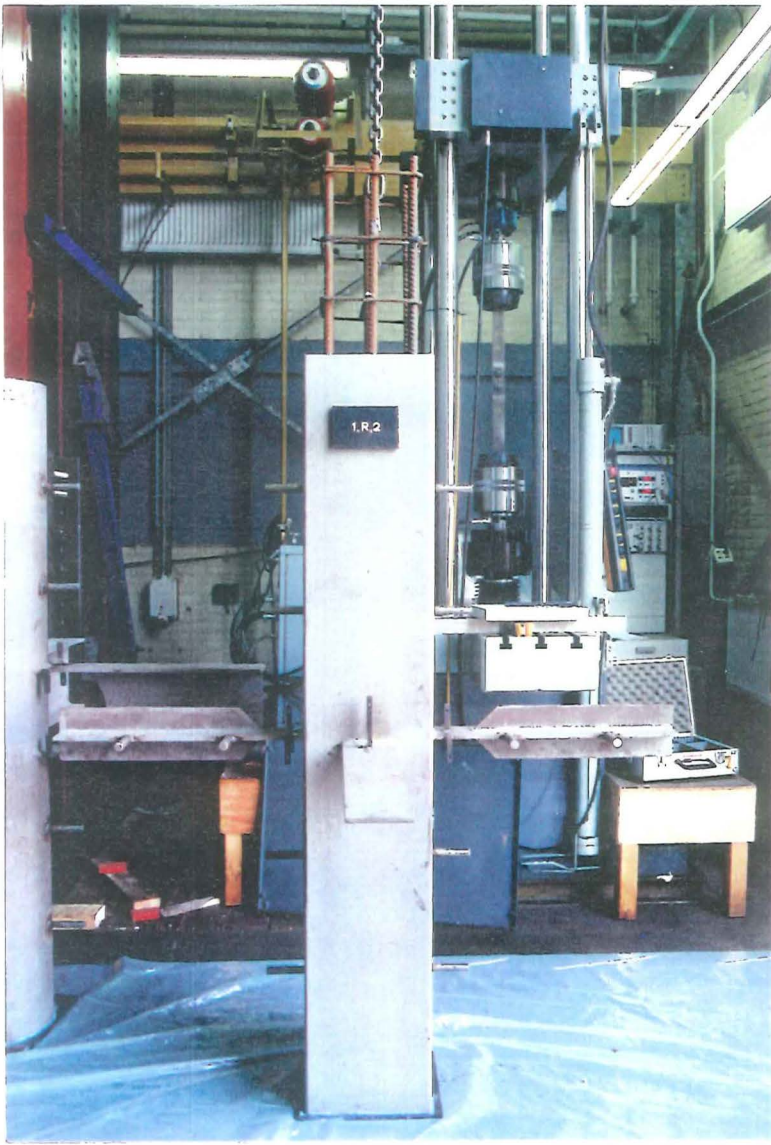


Photo 4-1 : Placement of reinforcement cages of typical RHS columns



Photo 4-2 : Placement of reinforcement cages of typical CHS columns



Photo 4-3 : Reinforcement arrangement inside CHS columns



Photo 4-4 : Reinforcement arrangement inside RHS columns

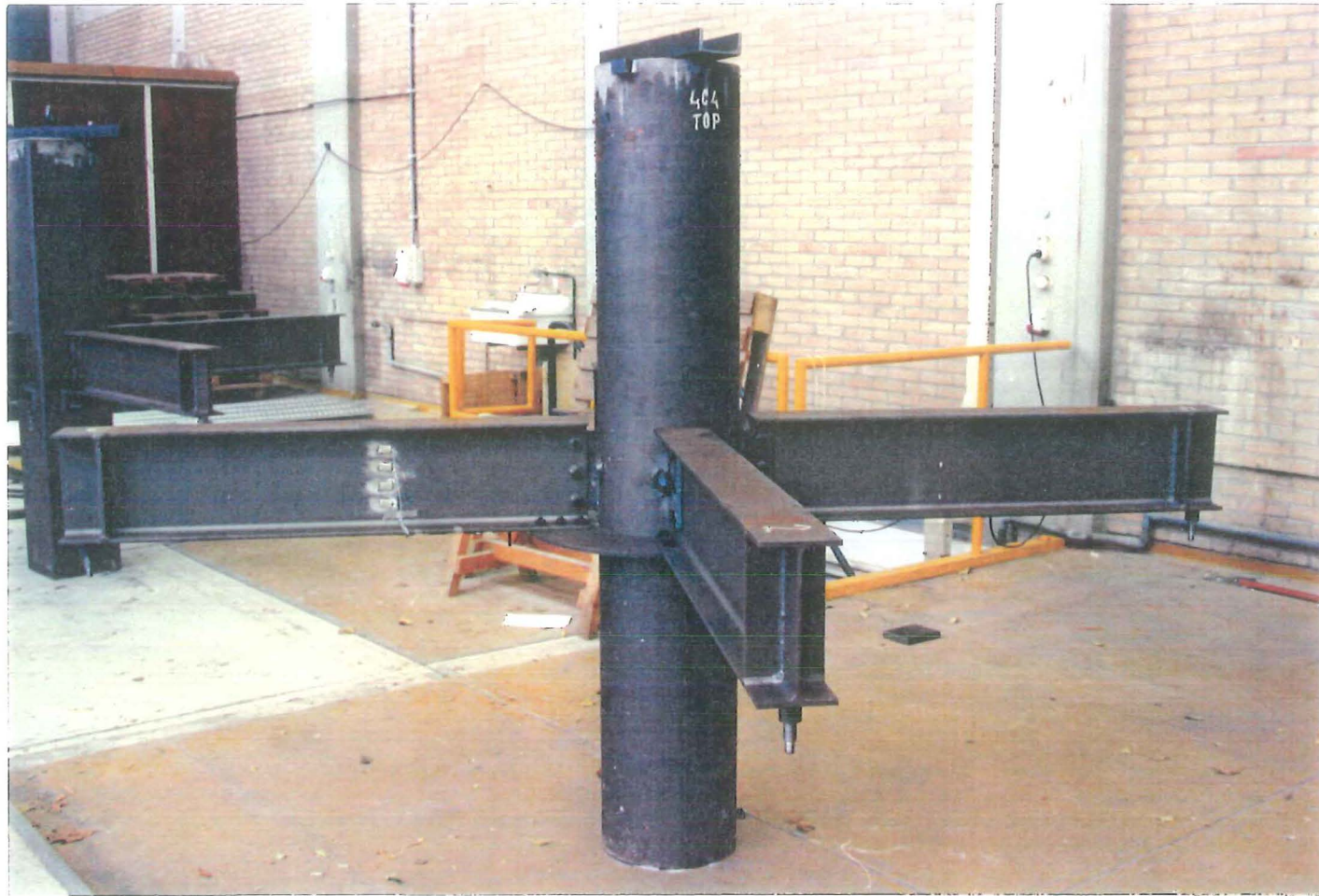


Photo 4-5 : Beams bolted to CHS columns



Photo 4-6 : Beams bolted to RHS columns



Photo 4-7 : Placement of steel decks on specimen in CHS

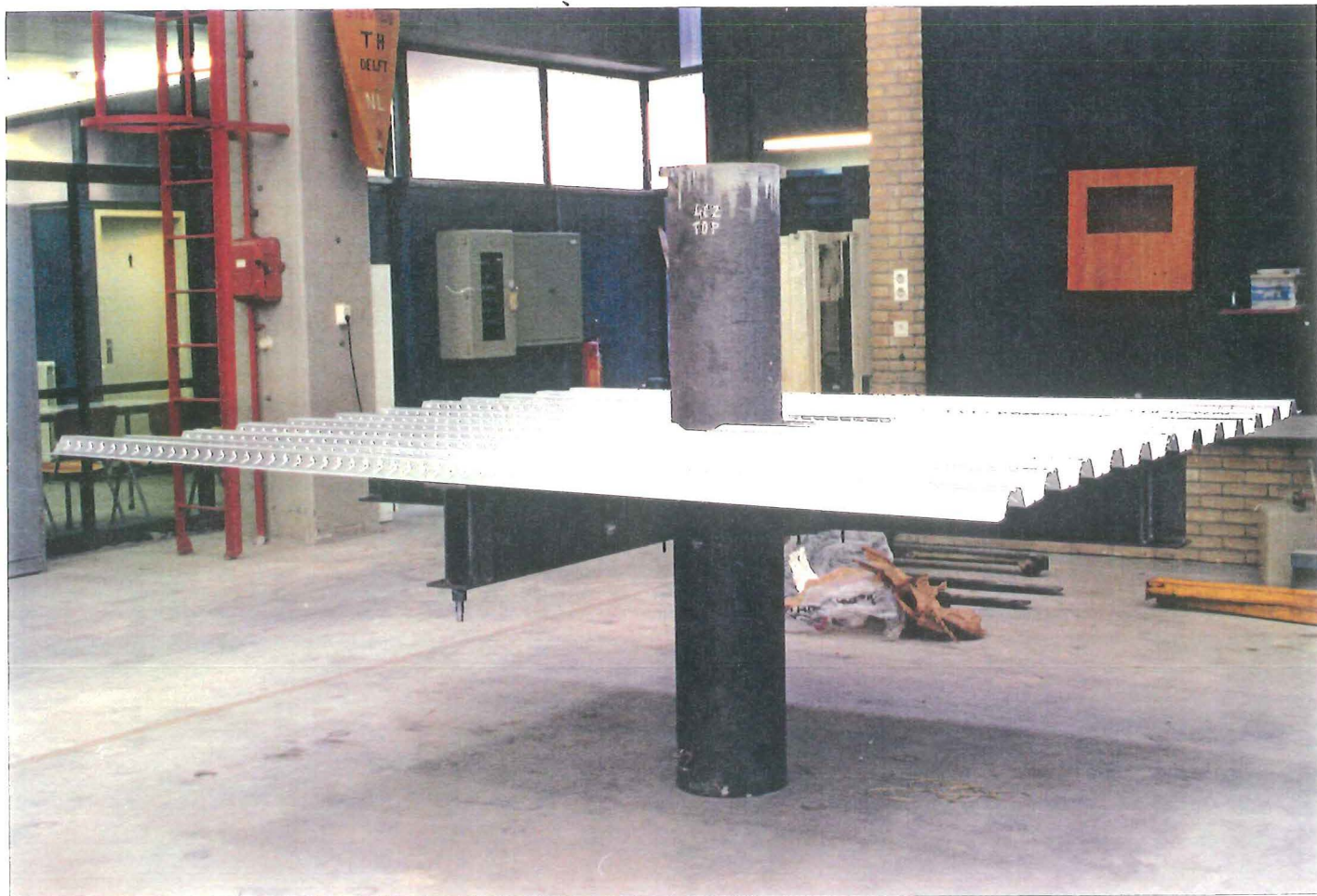


Photo 4-8 : Placement of steel decks on specimen in RHS

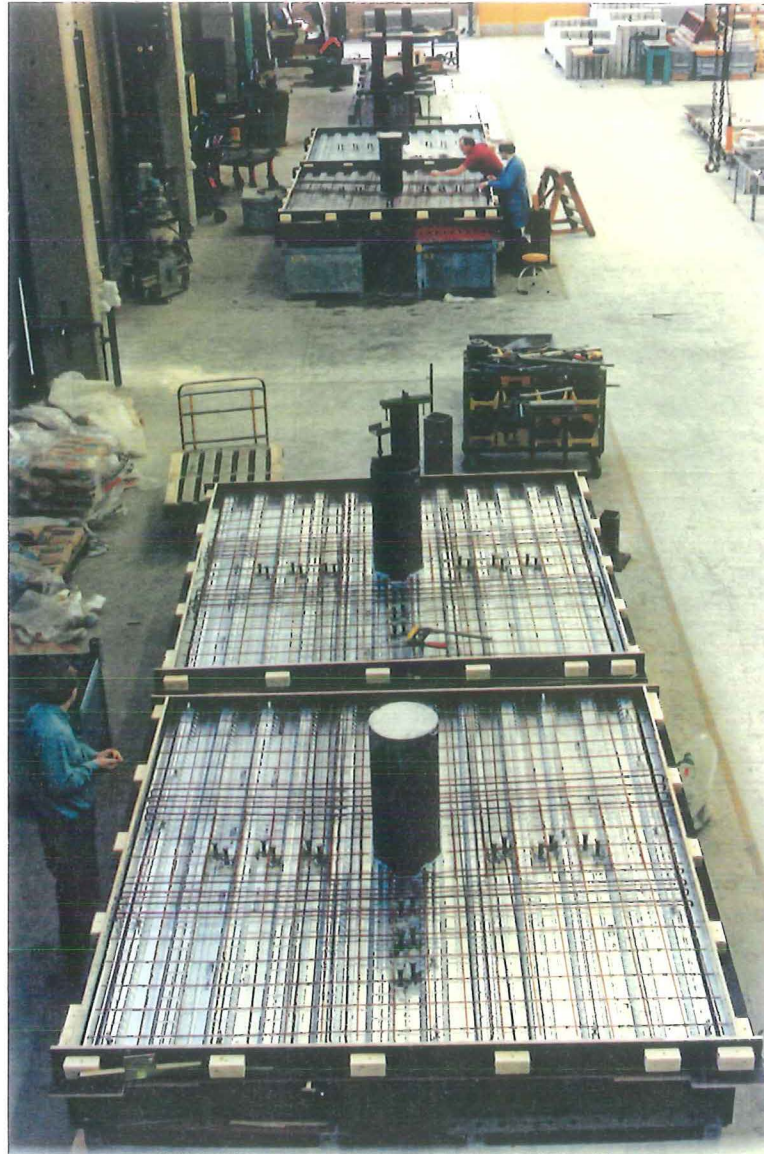


Photo 4-9 : Laying reinforcement



Photo 4-10 : Concreting

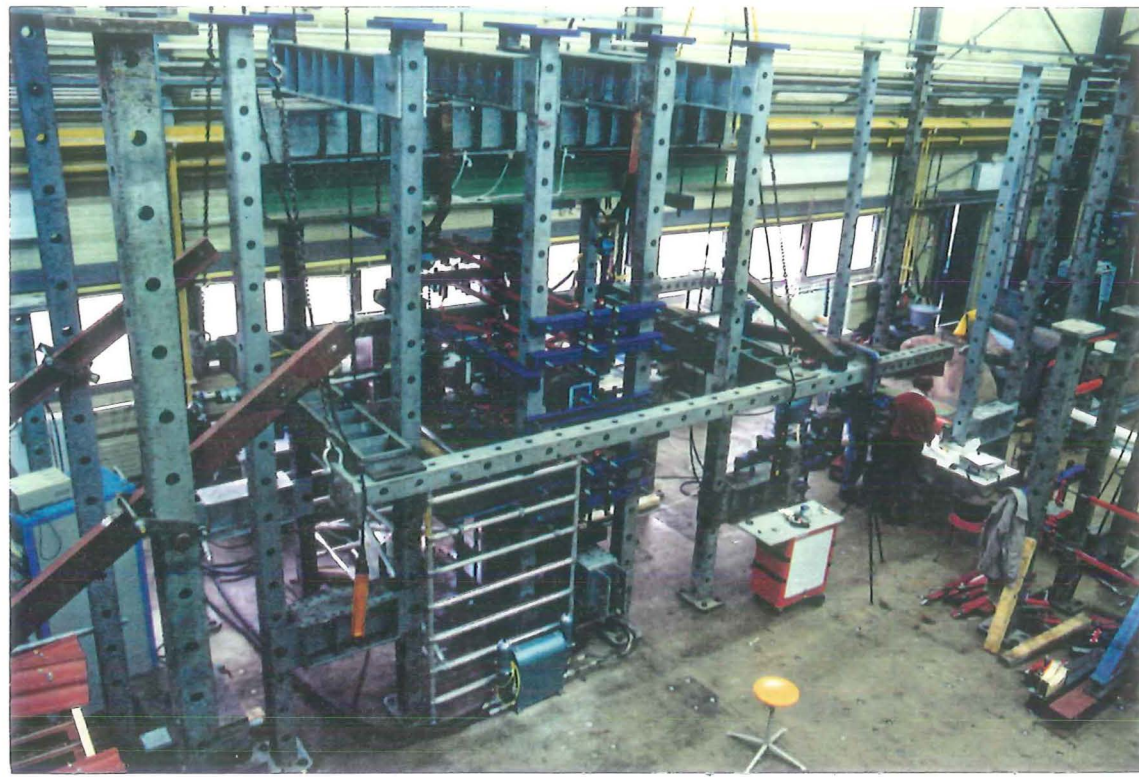


Photo 4-11 : Test rig for connections with axially loaded plates and beams in CHS and RHS columns (series 1 and 2)

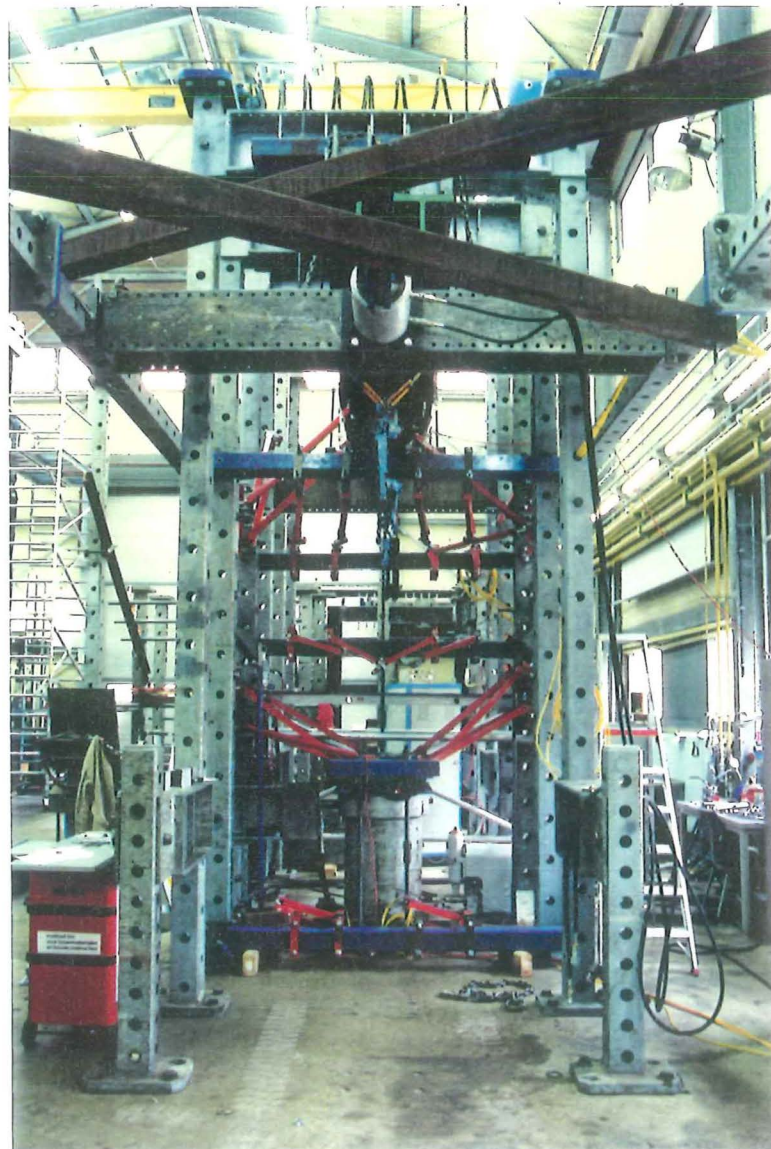


Photo 4-12 :
Test rig for connections with axially loaded plates and beams in CHS and RHS columns (series 1 and 2)



Photo 4-13 : Test rig for series 1 and 2, specimen 1C4, with composite CHS column and primary members (plates) in compression



Photo 4-14 :
Test rig for series 1 and 2,
specimen 1C4, with composite CHS
column and primary members
(plates) in compression

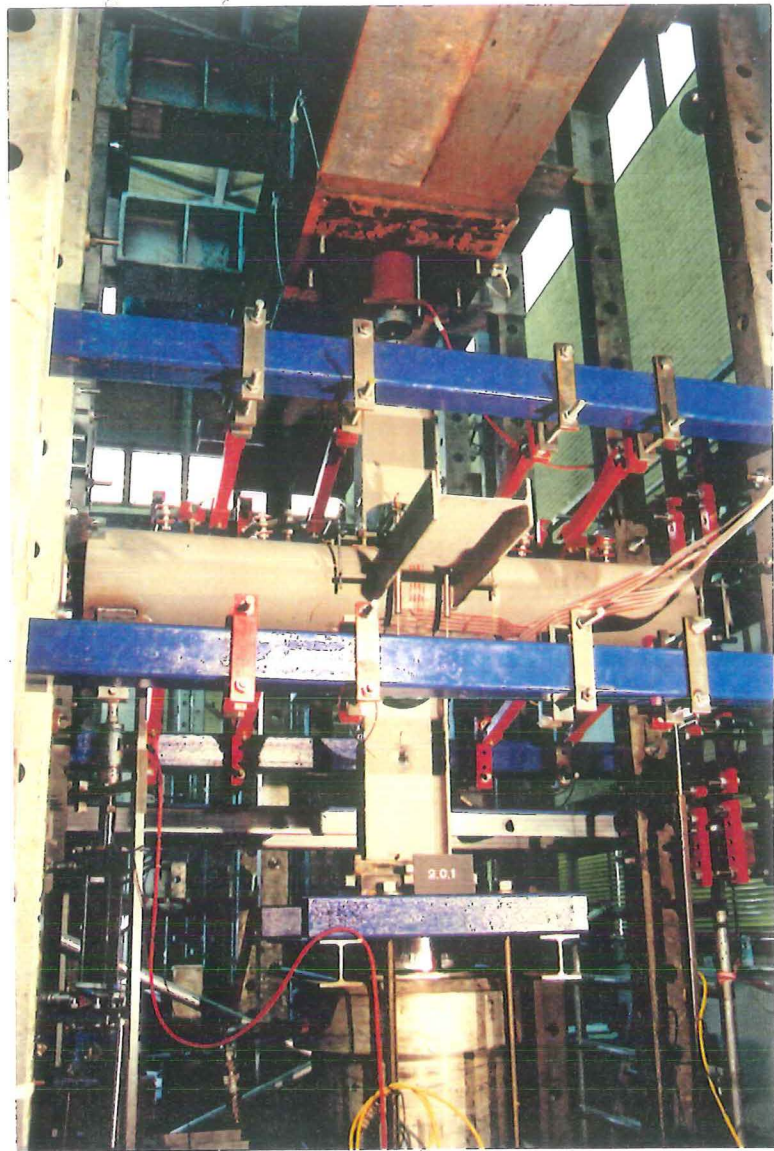


Photo 4-15 :
Test rig for series 1 and 2,
specimen 2C1, with CHS column
and primary beams in compression

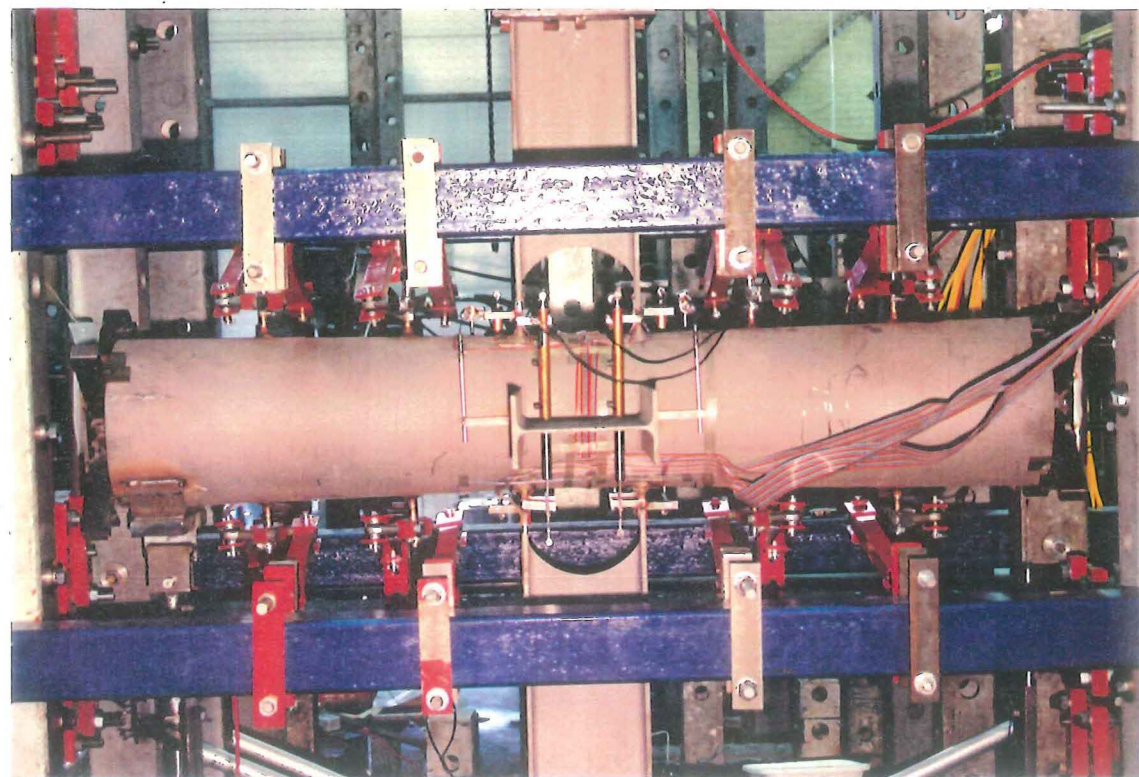


Photo 4-16 : Test rig for series 1 and 2, specimen 2C1, with
CHS column and primary beams in compression ;

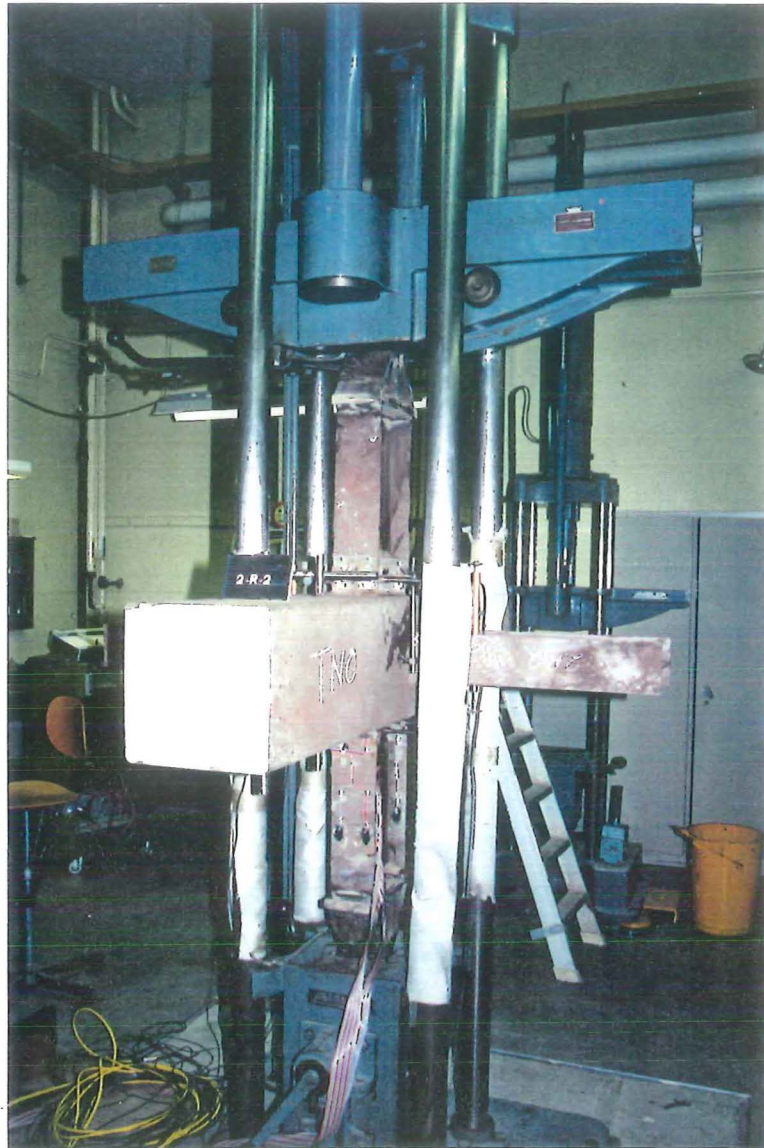


Photo 4-17 :
2R2 in tensile testing machine-
used for testing specimens 1C2,
2C2, 1R2 and 2R2

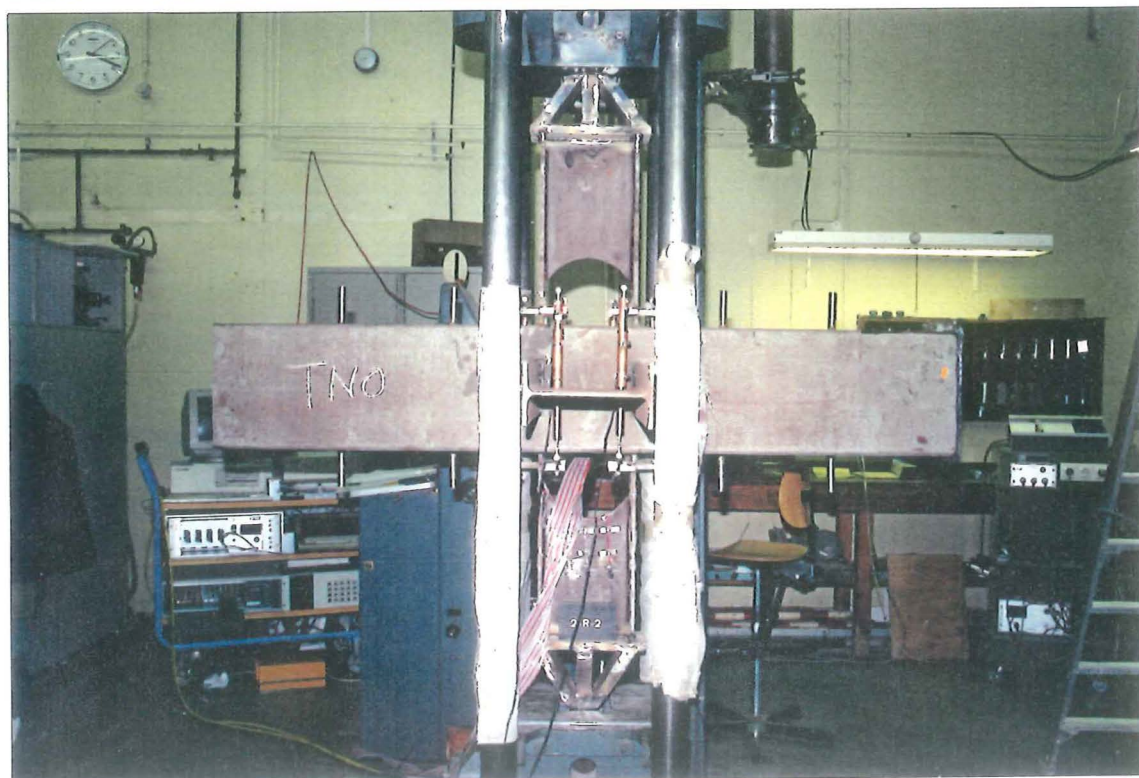


Photo 4-18 : 2R2 in tensile testing machine used for testing
specimens 1C2, 2C2, and 2R2

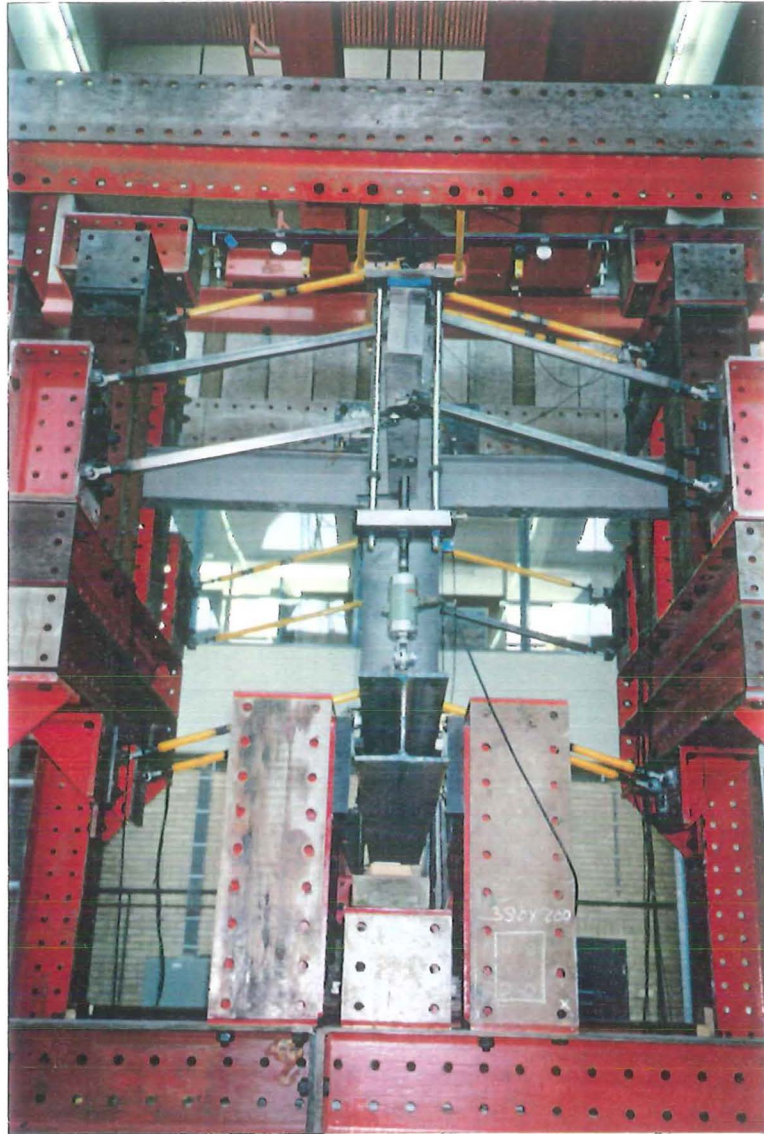


Photo 4-19 :
Test rig for series 3 and 4
with beams under hogging moment
only (all except 3C3 and 3R3) .



Photo 4-20 : Test rig for series 3 and 4 with 3R2 during testing



Photo 4-21 : Test rig for series 4 with 4C3

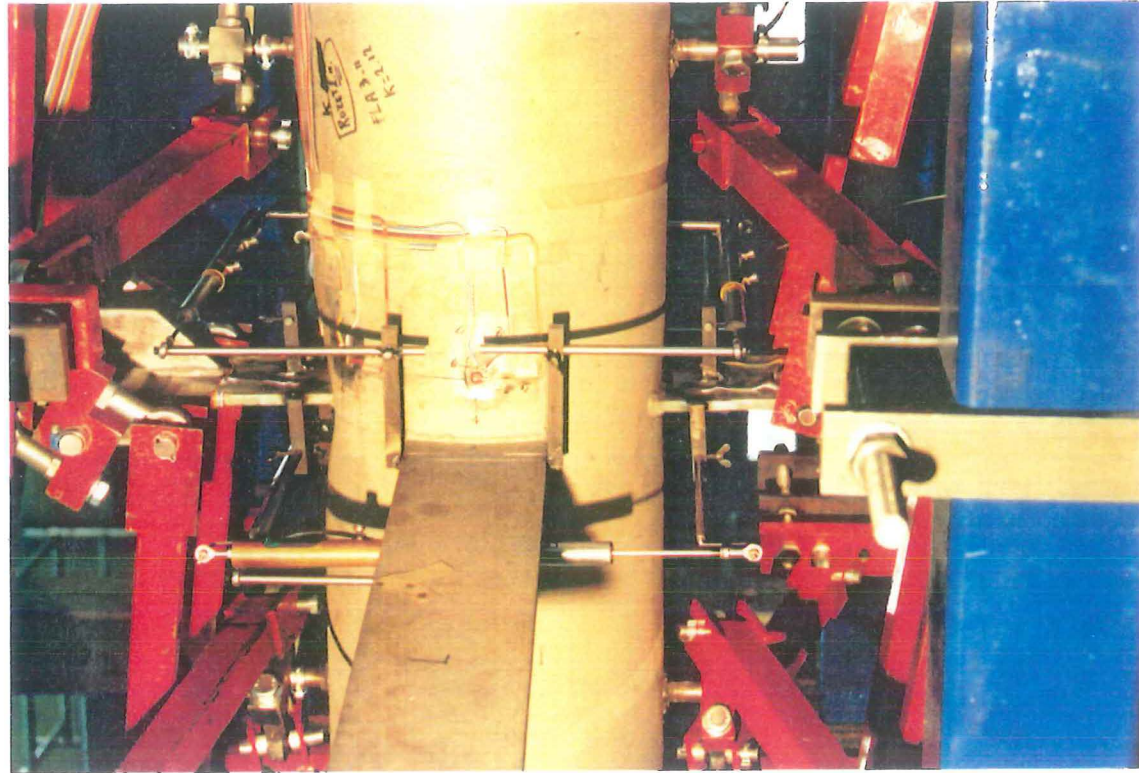


Photo 4-22 : Some transducers and column rosettes for 1C1

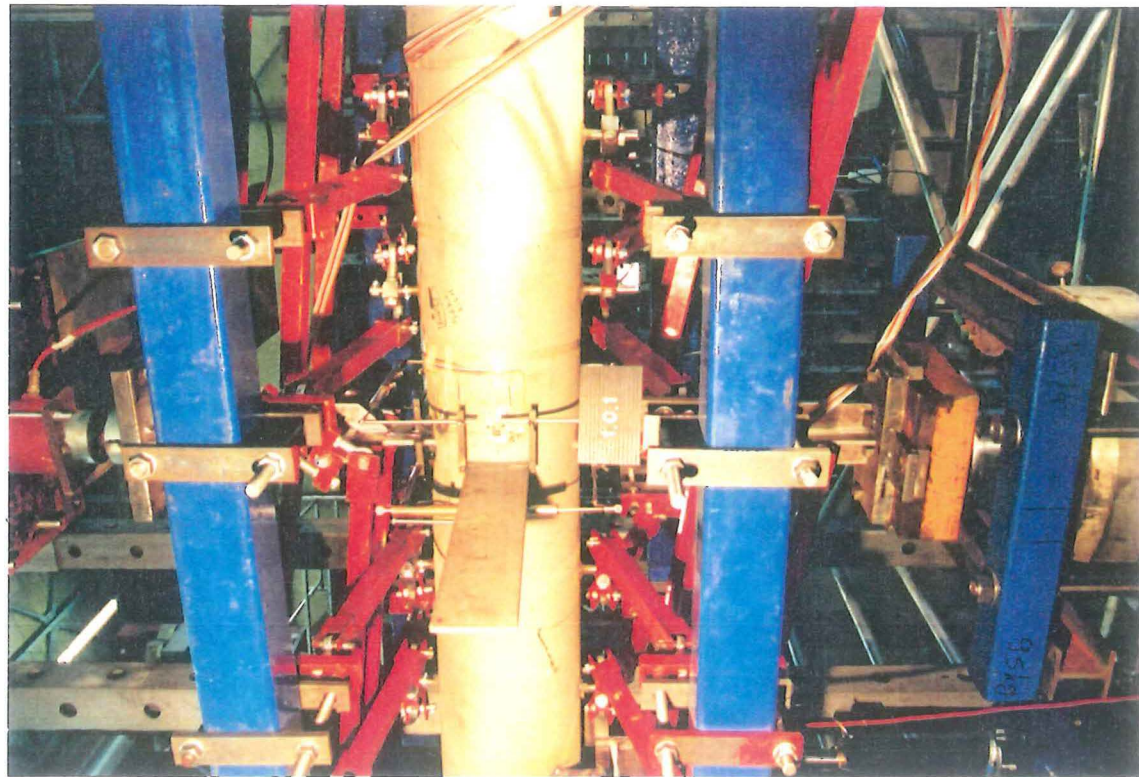


Photo 4-23 : Some transducers and column rosettes for 1C1

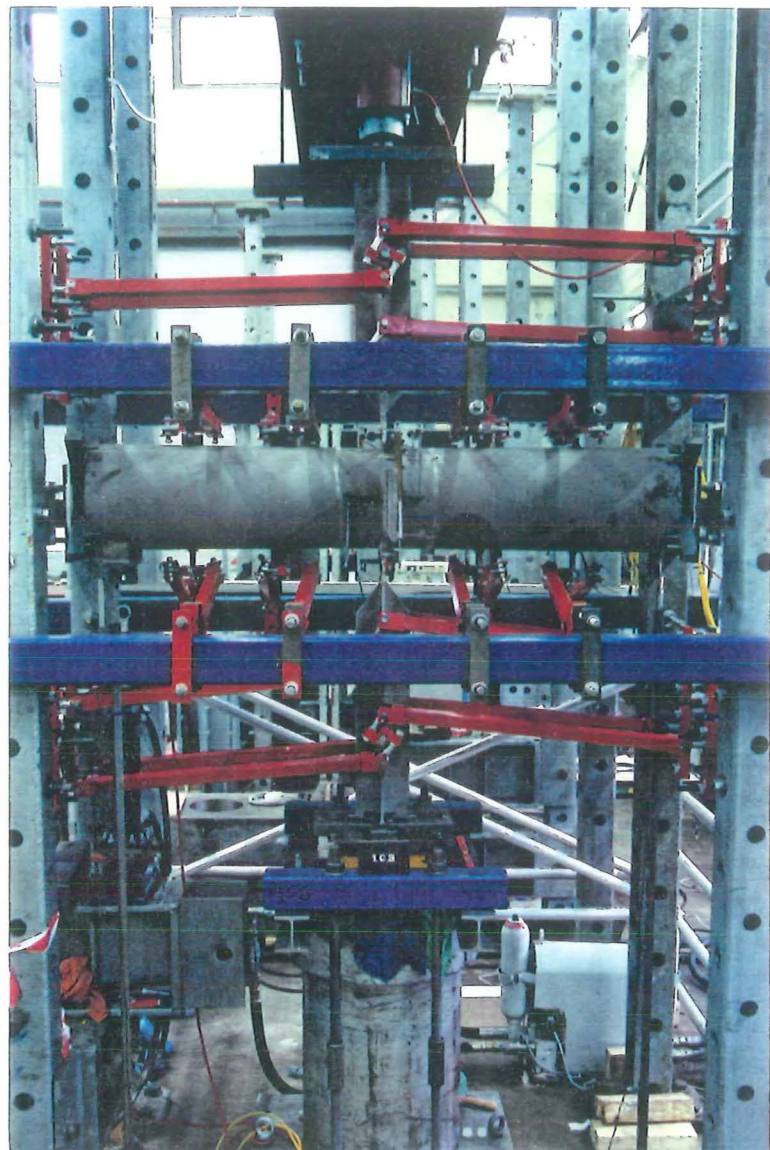


Photo 4-24 :
1C3 fully instrumented in test rig

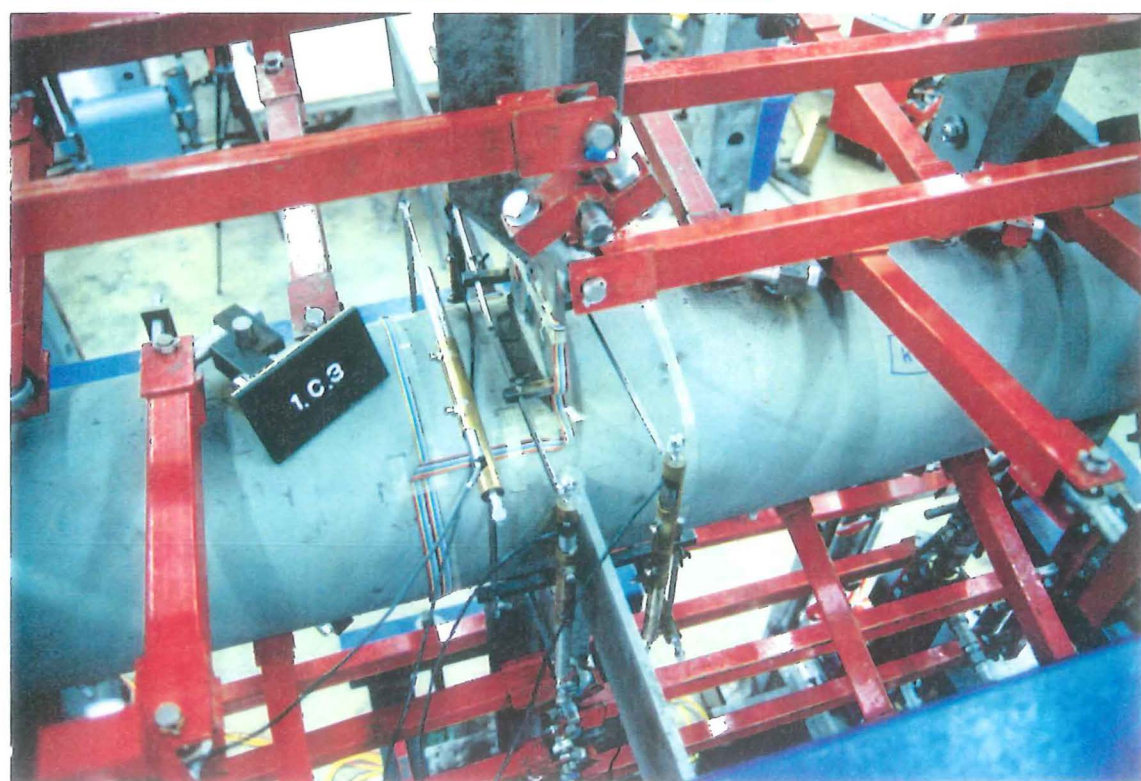


Photo 4-25 : 1C3 fully instrumented in test rig

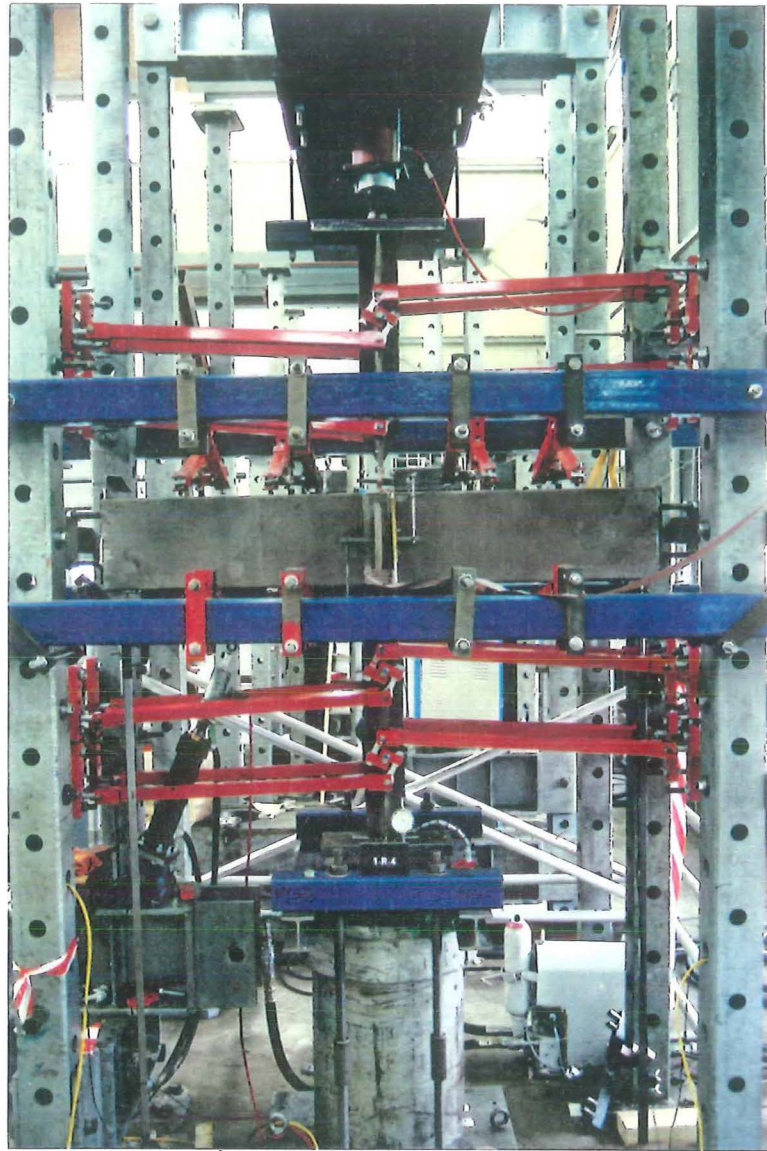


Photo 4-26 :
1R4 showing transducers

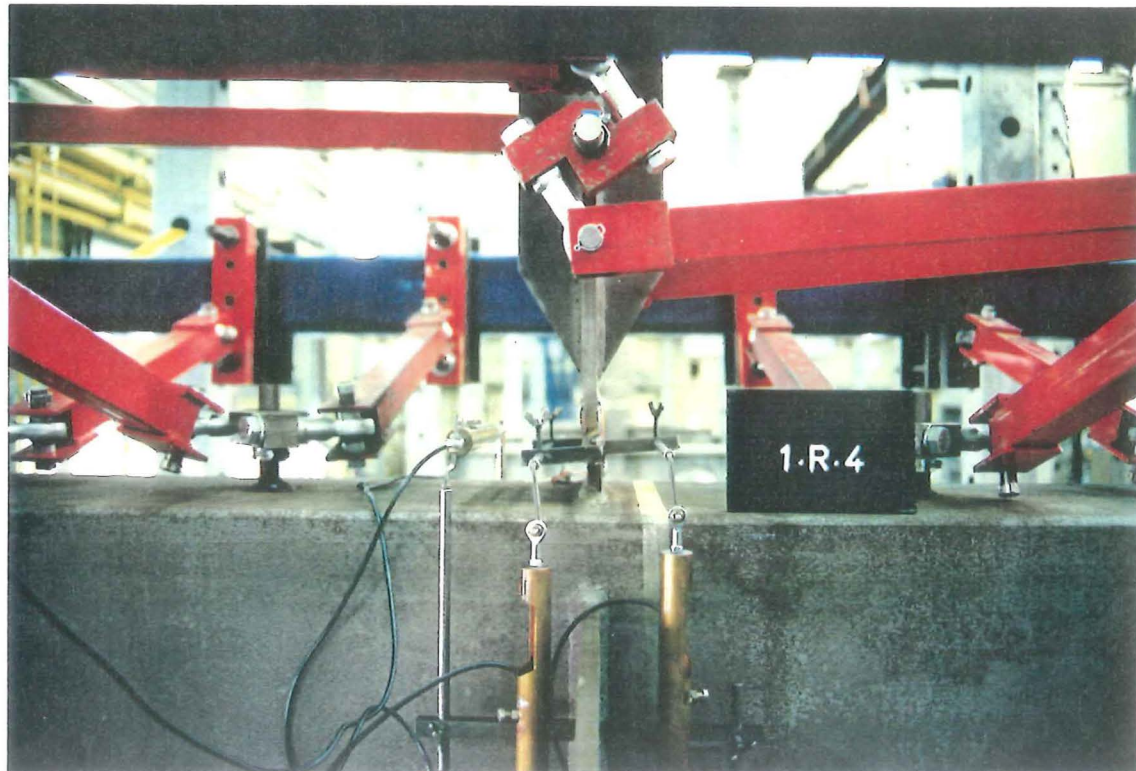


Photo 4-27 : 1R4 showing transducers

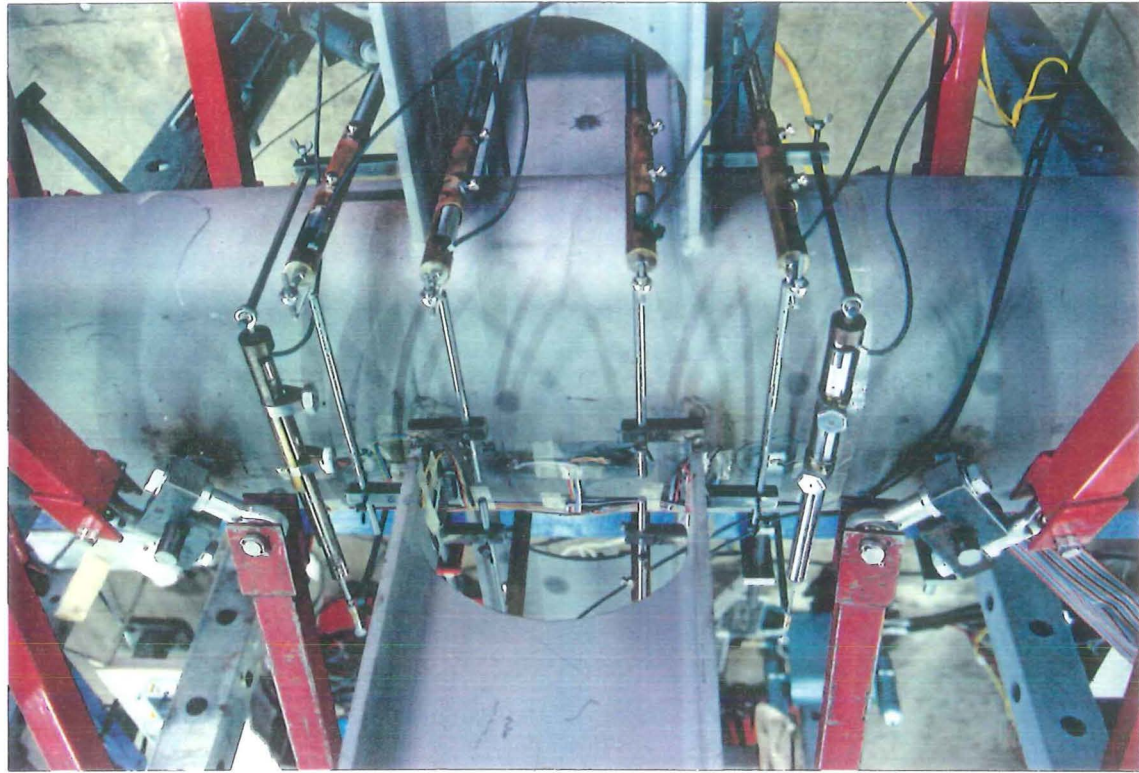


Photo 4-28 : 2C1 showing transducers

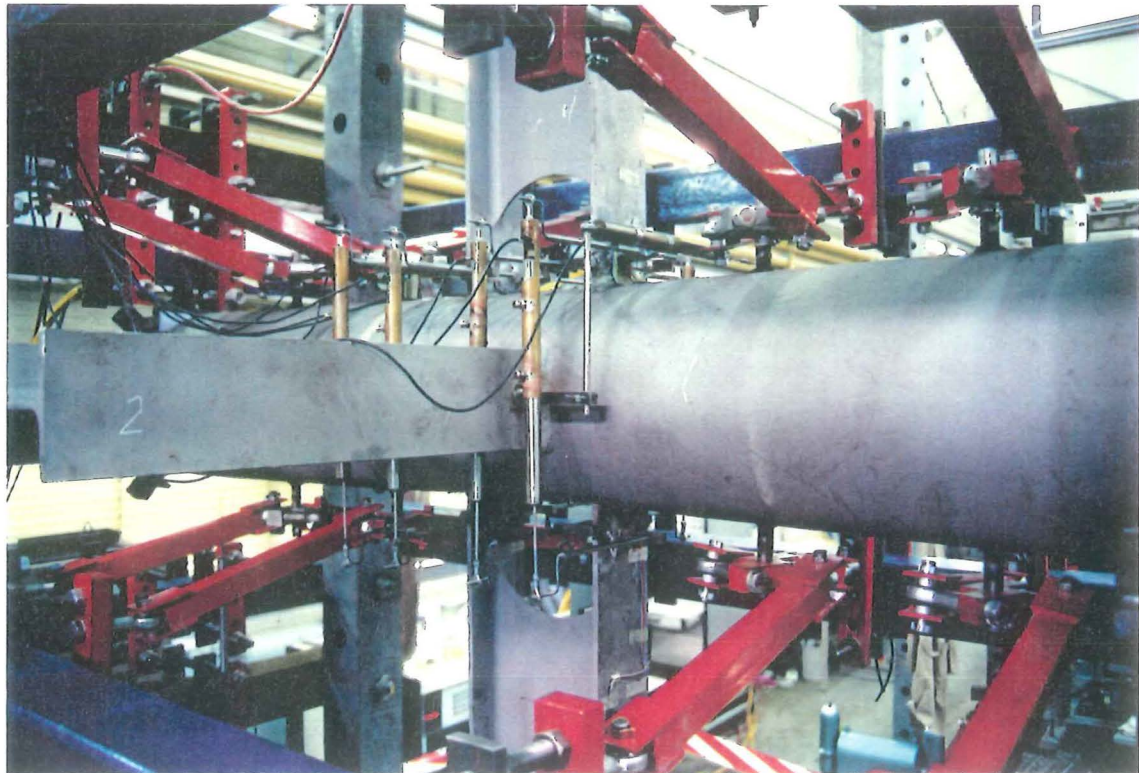


Photo 4-29 : 2C1 showing transducers

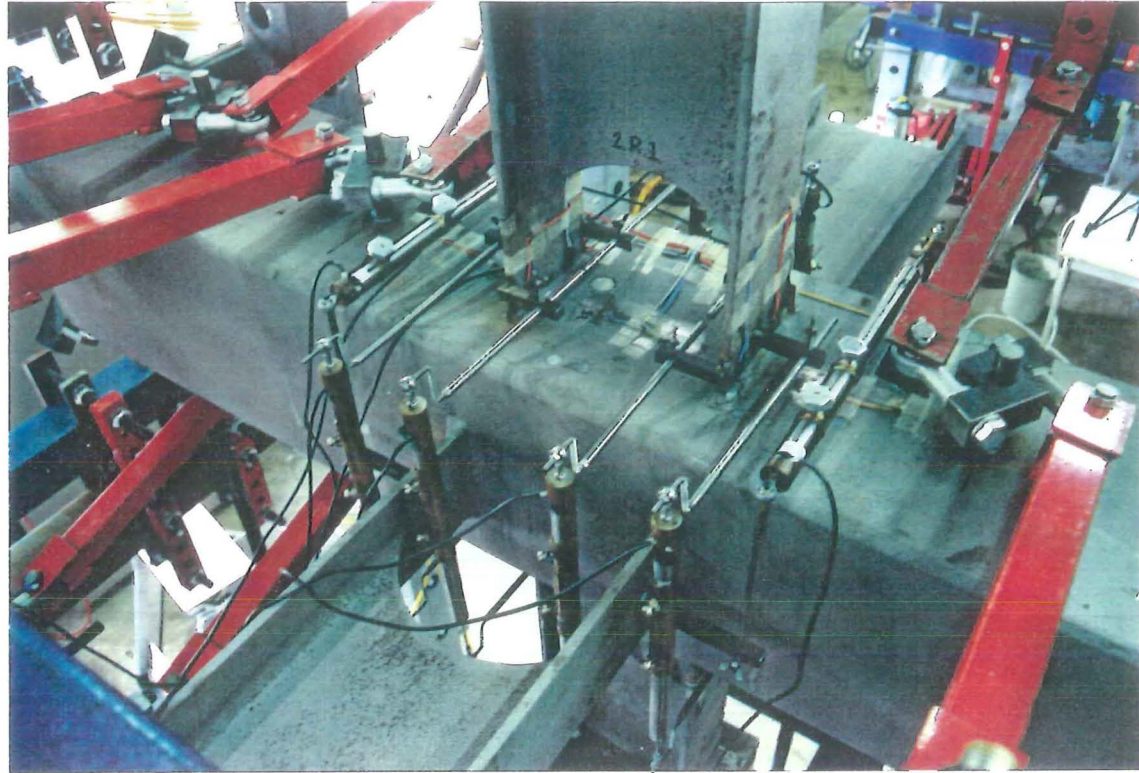


Photo 4-30 : 2R1 showing transducers

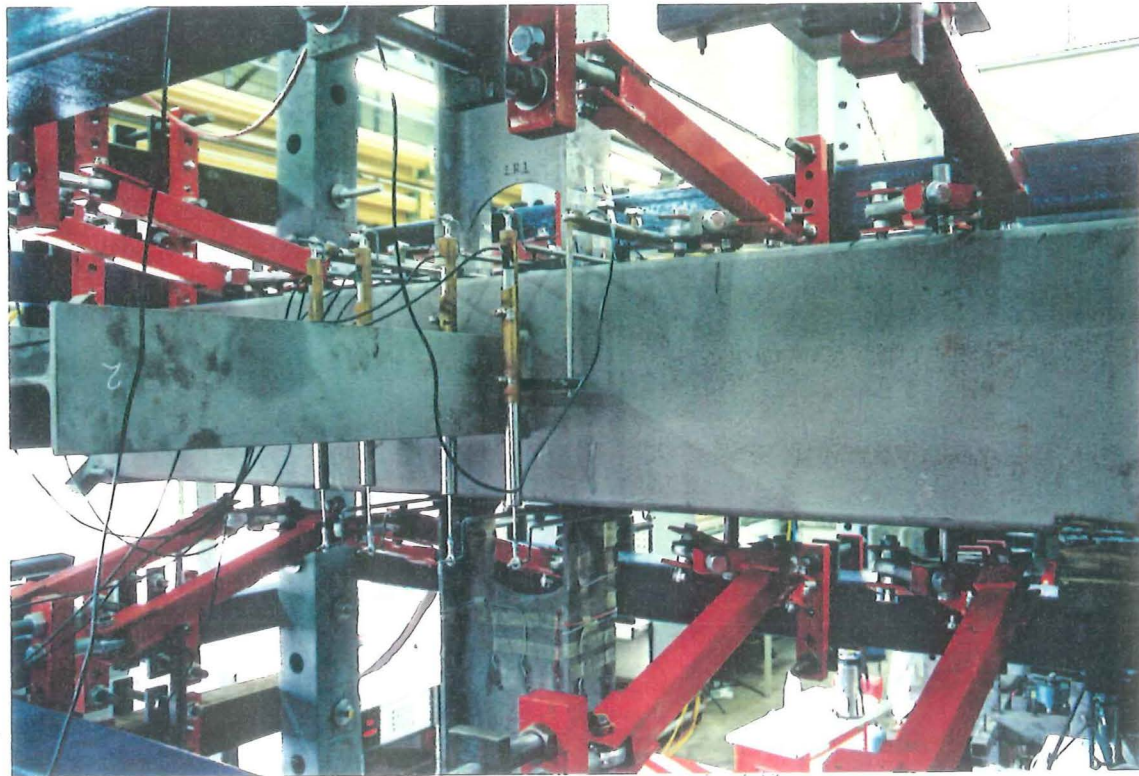


Photo 4-31 : 2R1 showing transducers

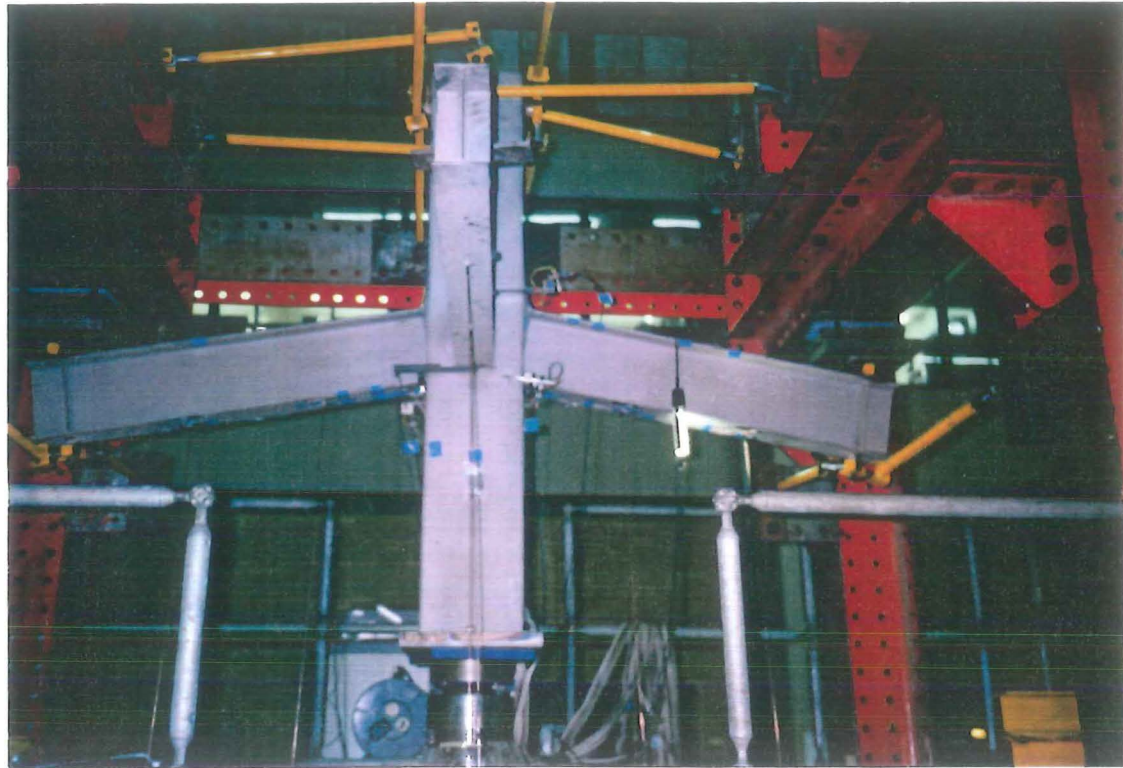


Photo 4-32 : Instrumentation on 3R1 at failure

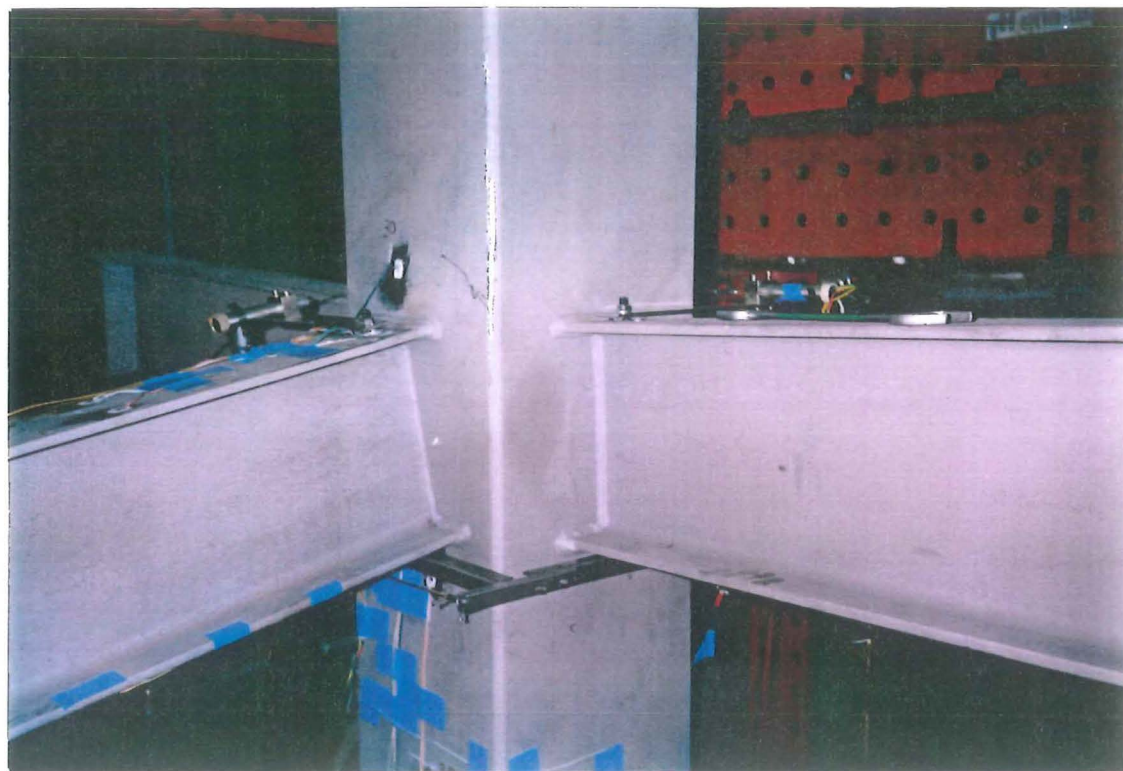


Photo 4-33 : Instrumentation on 3R1 at failure

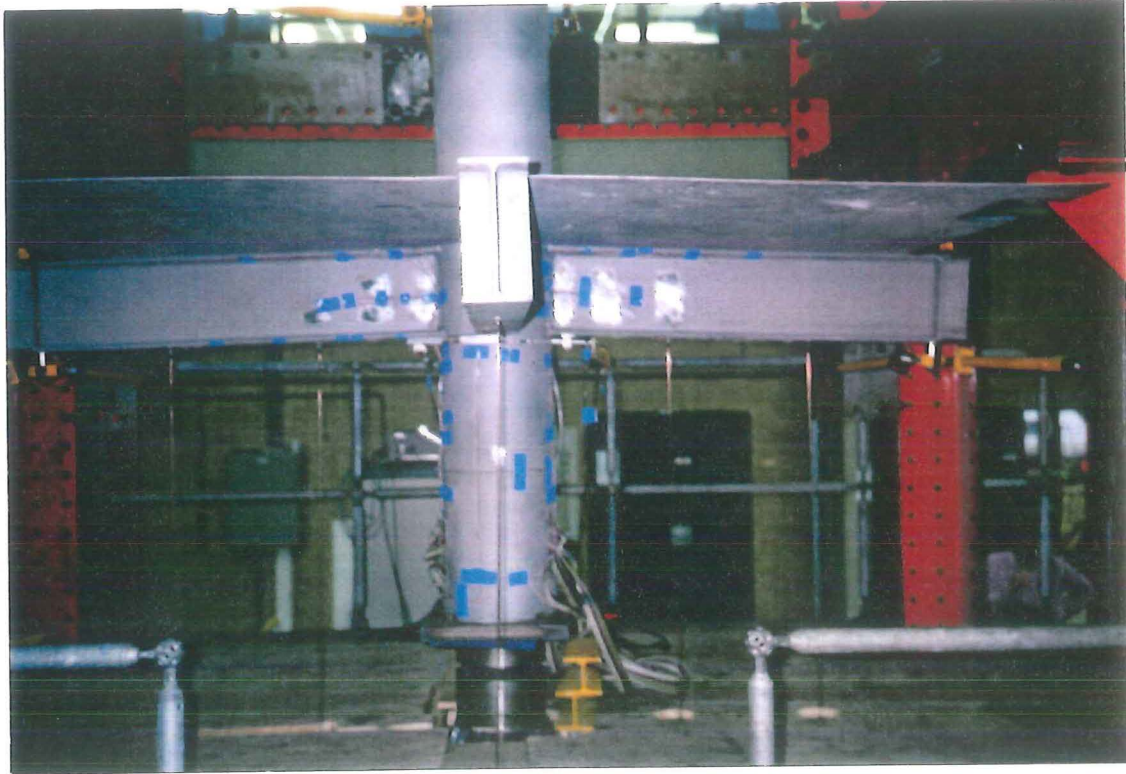


Photo 4-34 : Instrumentation on 3C2



Photo 4-35 :
Instrumentation on 3C2 and lateral
supports to column

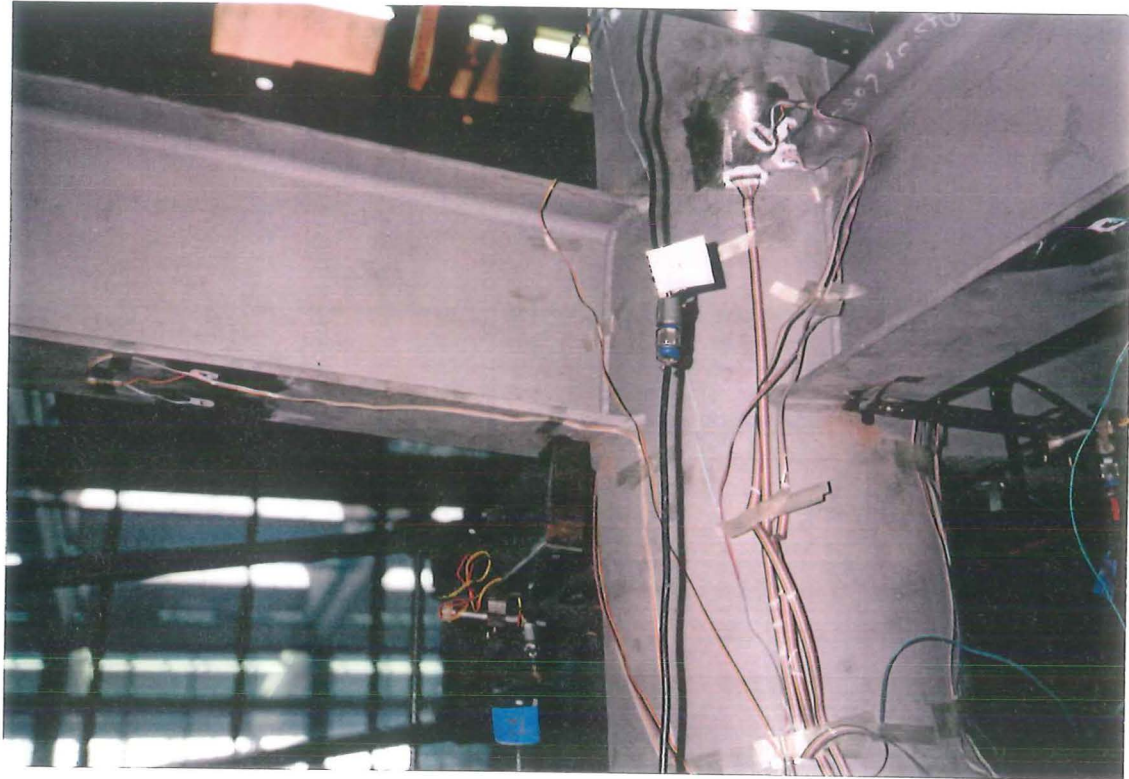


Photo 4-36 : Instrumentation on 3C3 and 3R3 at failure

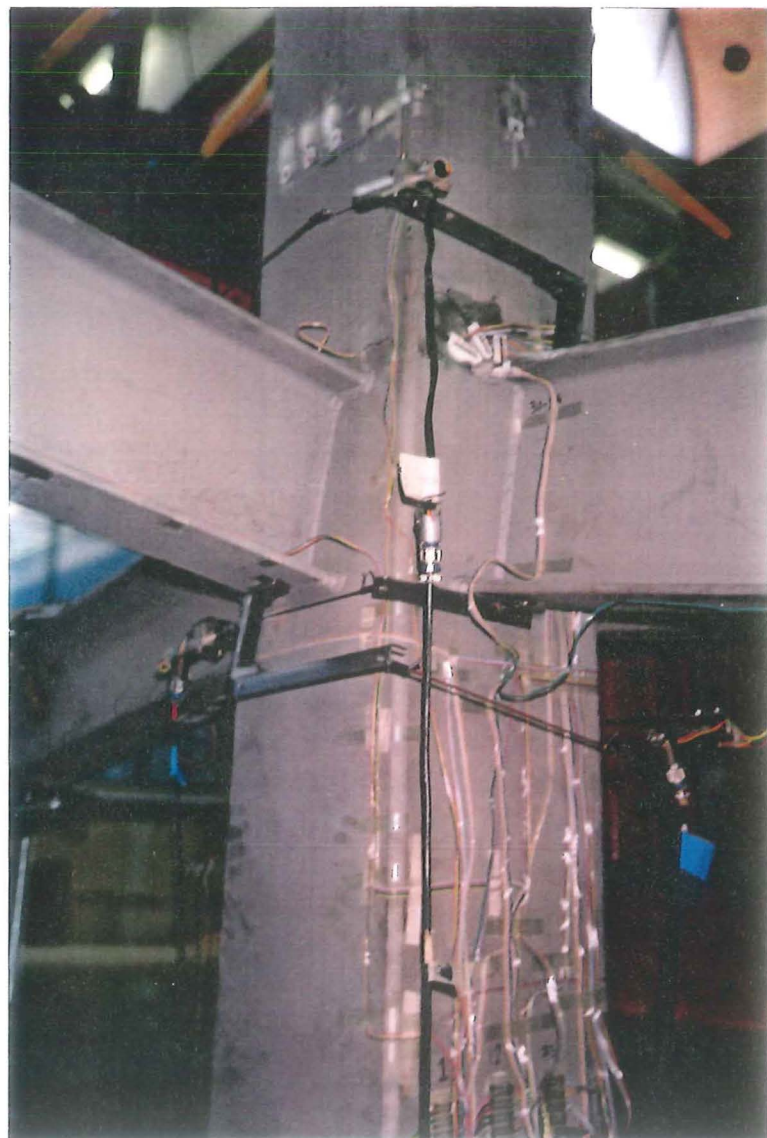


Photo 4-37 :
Instrumentation on 3C3 and 3R3
at failure

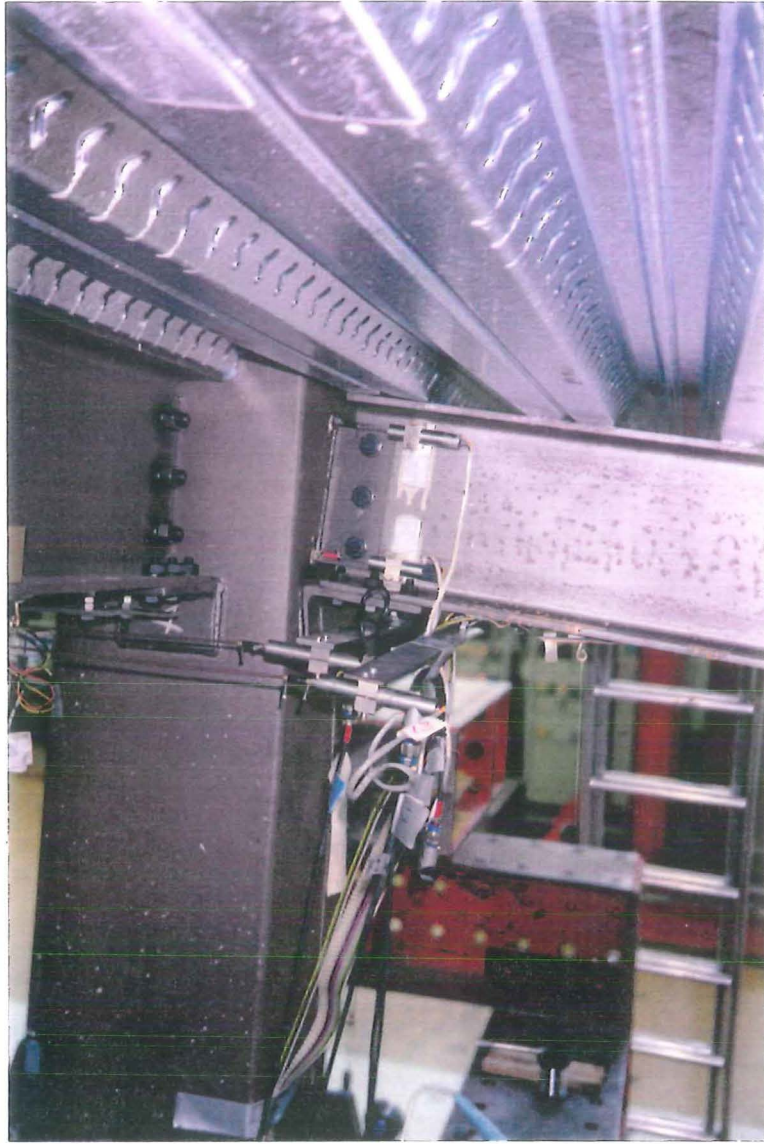


Photo 4-38 :
Instrumentation on 4R2 at failure

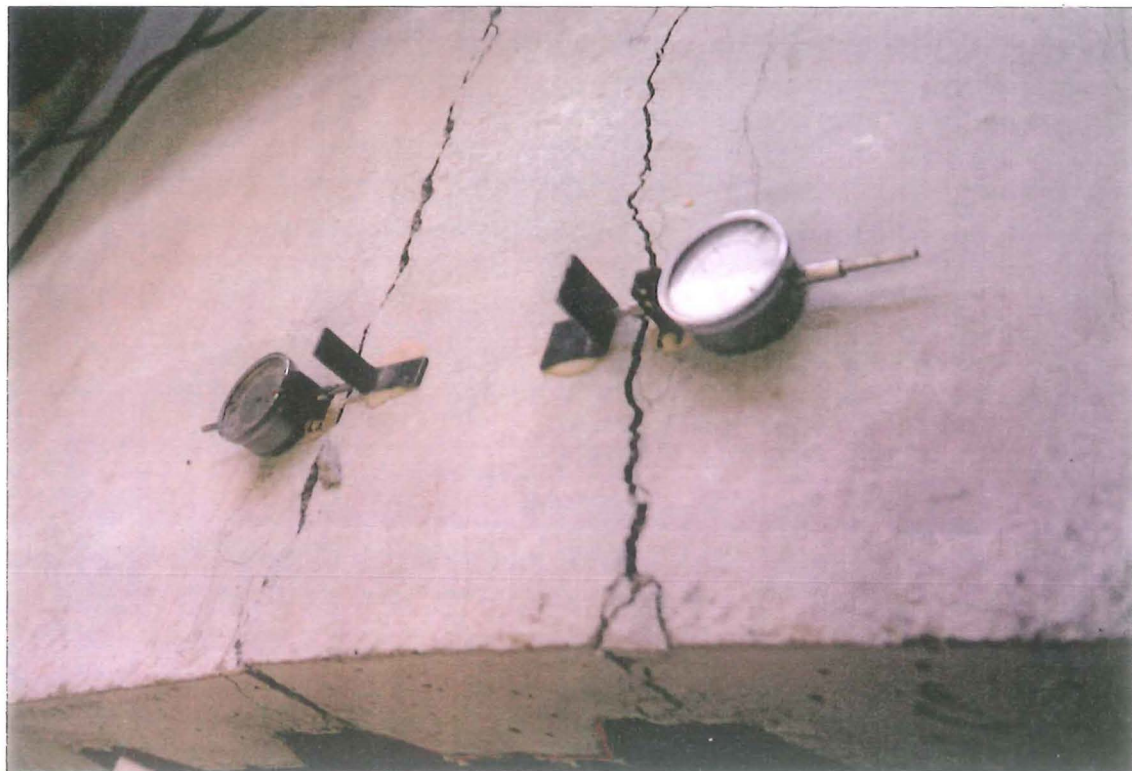


Photo 4-39 : Crack width meters on 4R2 at failure

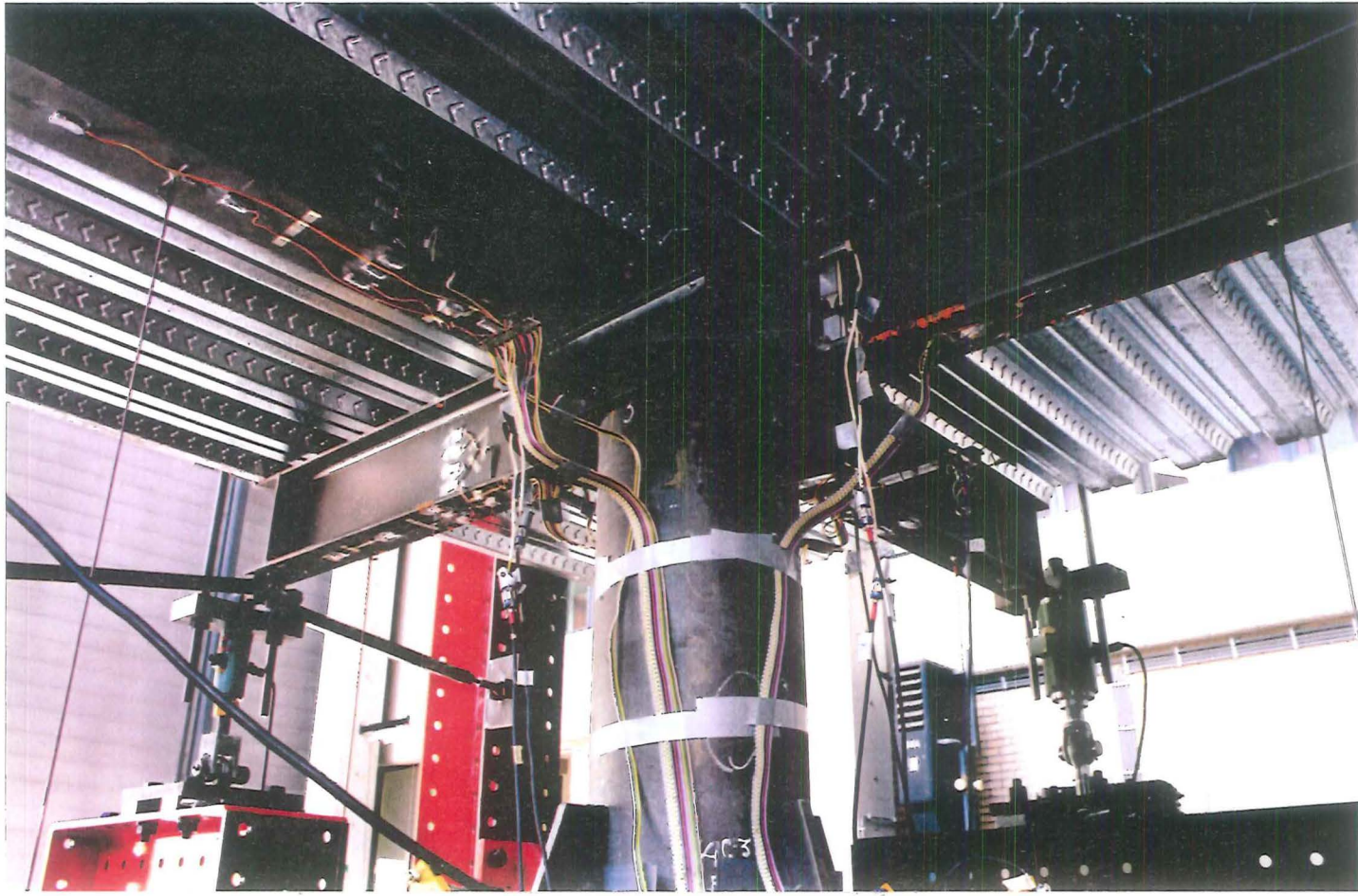


Photo 4-40 : Instrumentation below composite floor for 4C3

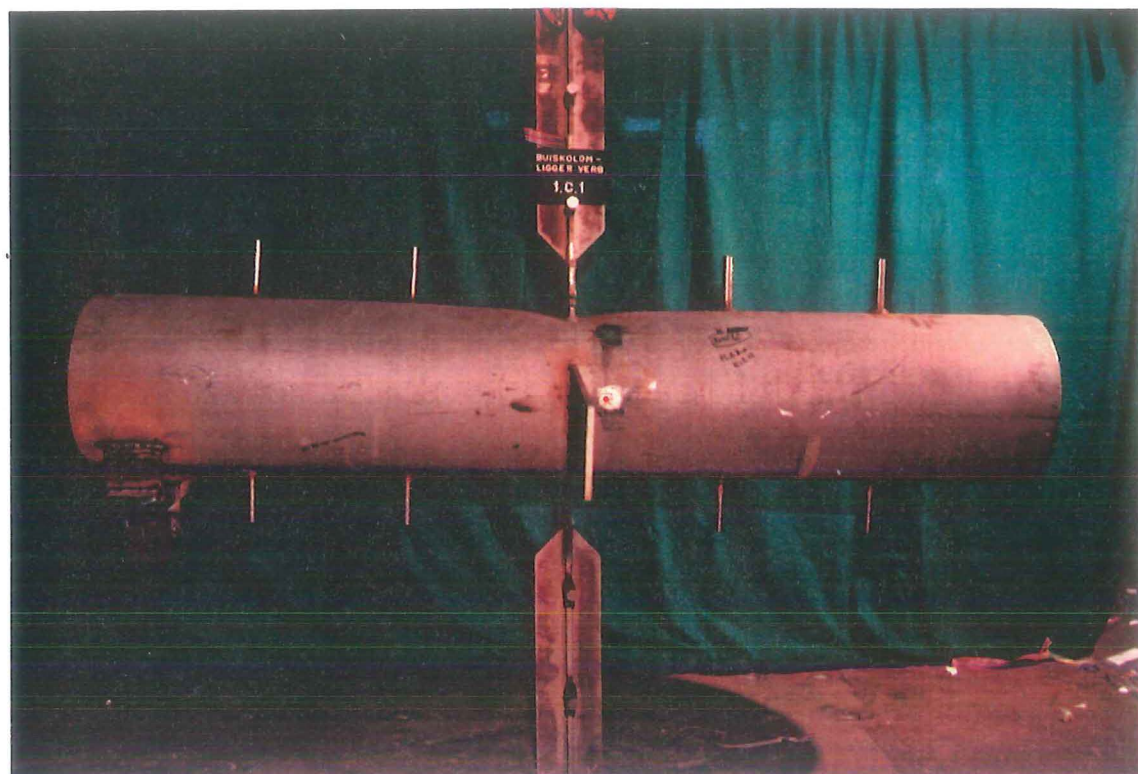


Photo 6-1 : Specimen 1C1 after failure

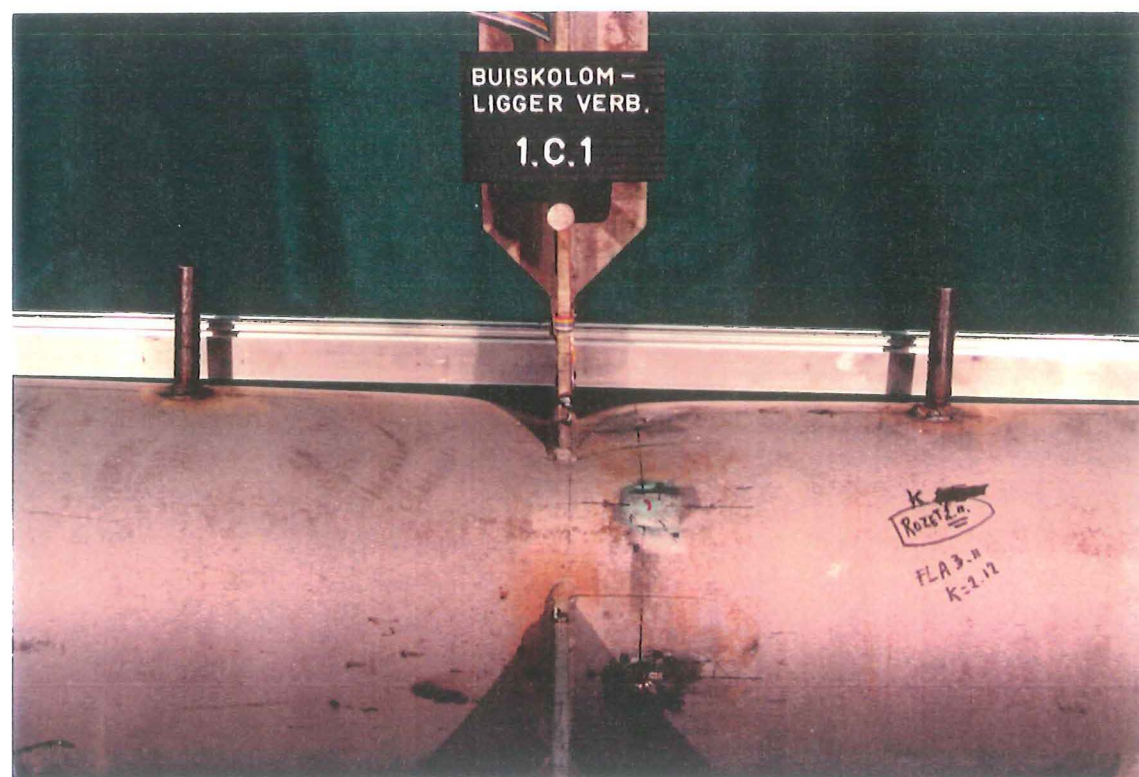


Photo 6-2 : Details of specimen 1C1 after failure

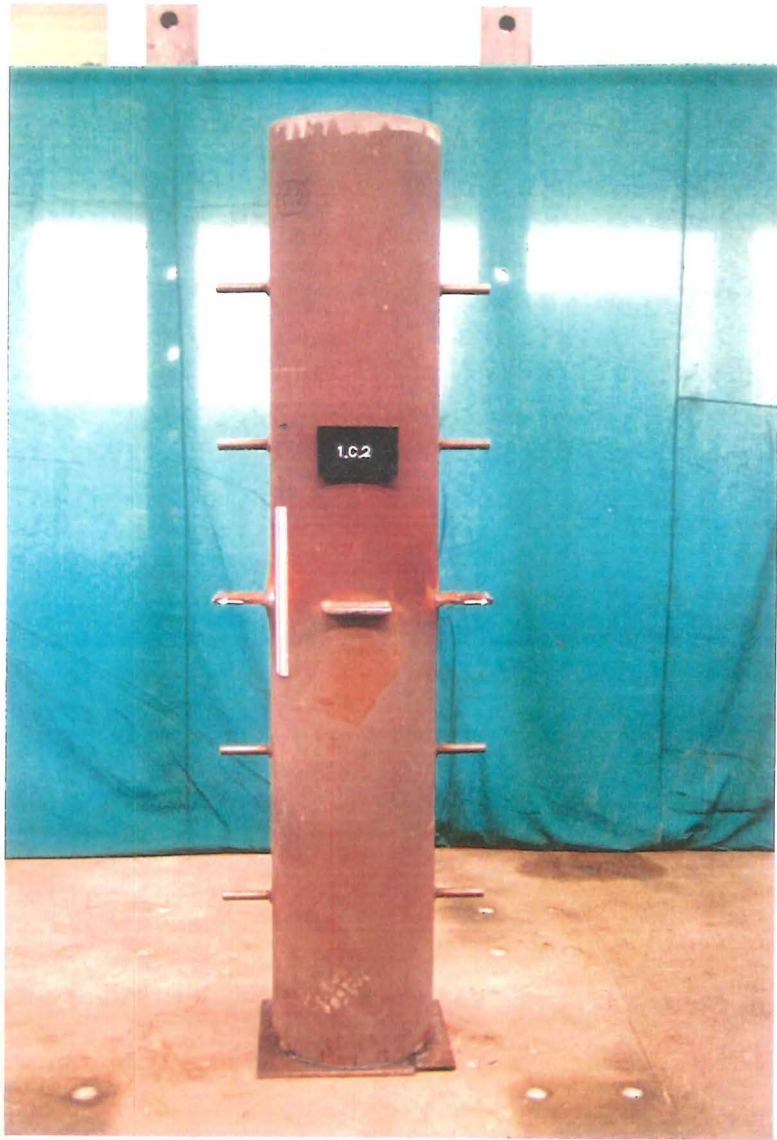


Photo 6-3 : Specimen 1C2 after failure

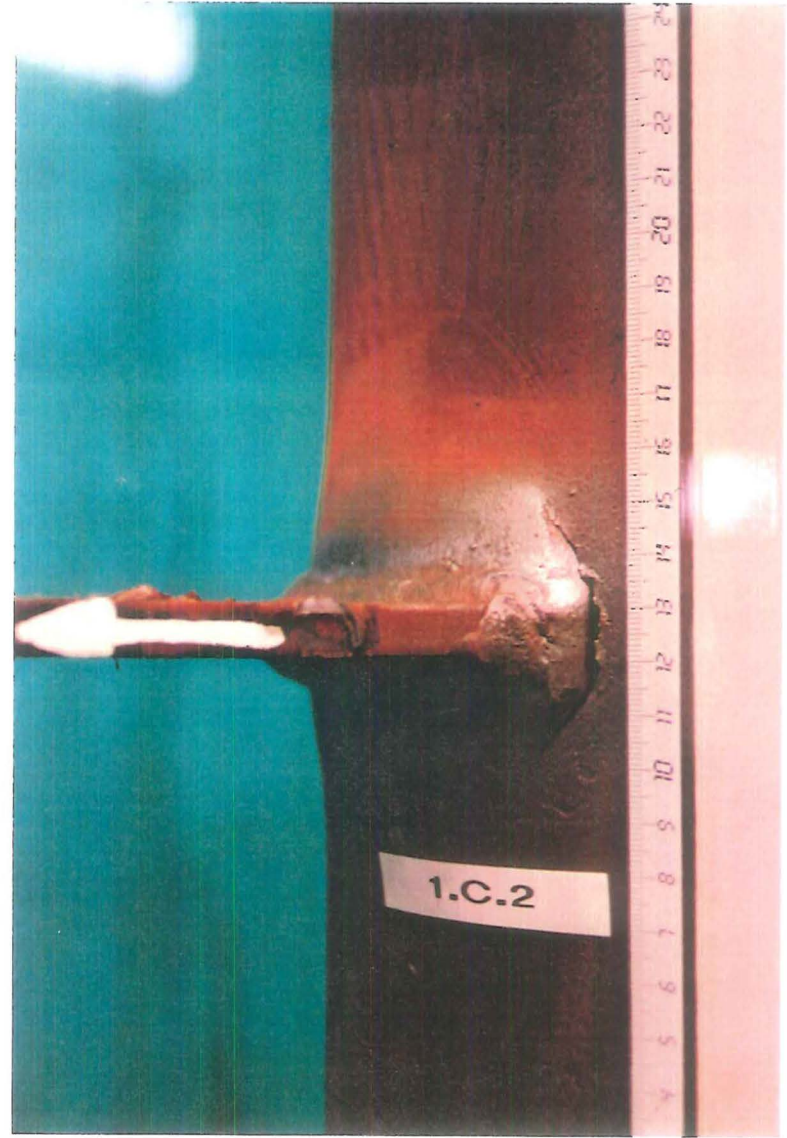


Photo 6-4 : Details of specimen 1C2 after failure

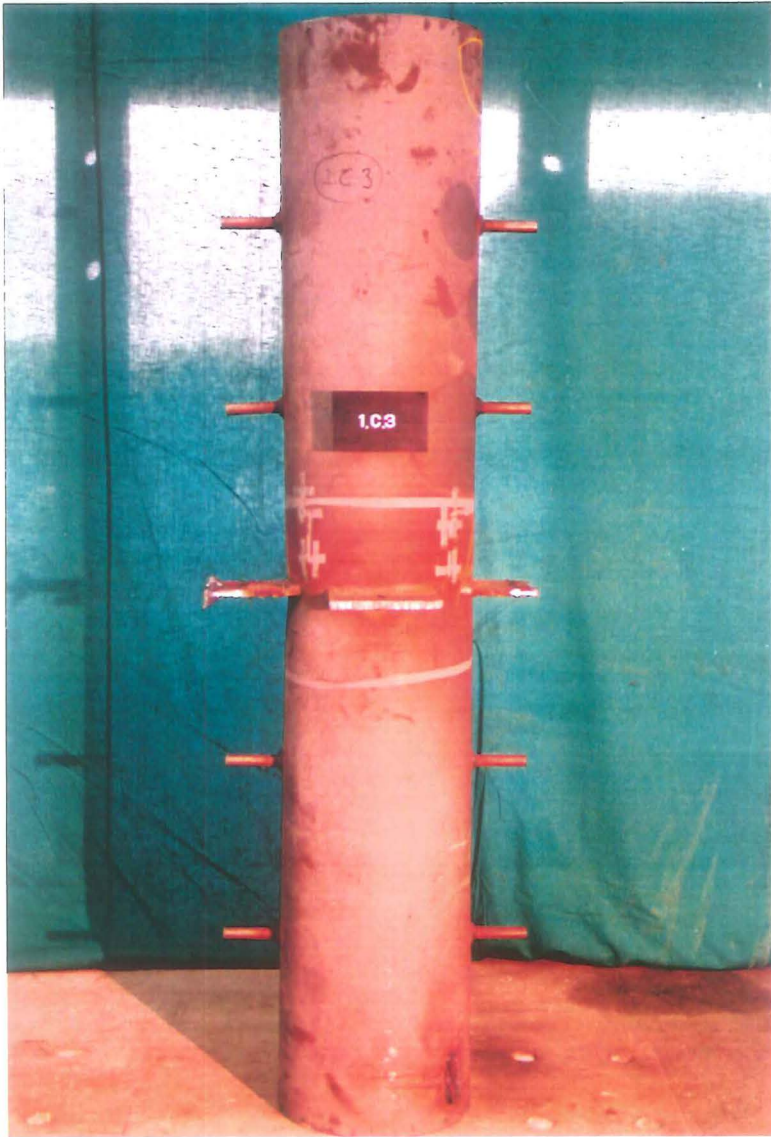


Photo 6-5 : Specimen 1C3 after failure

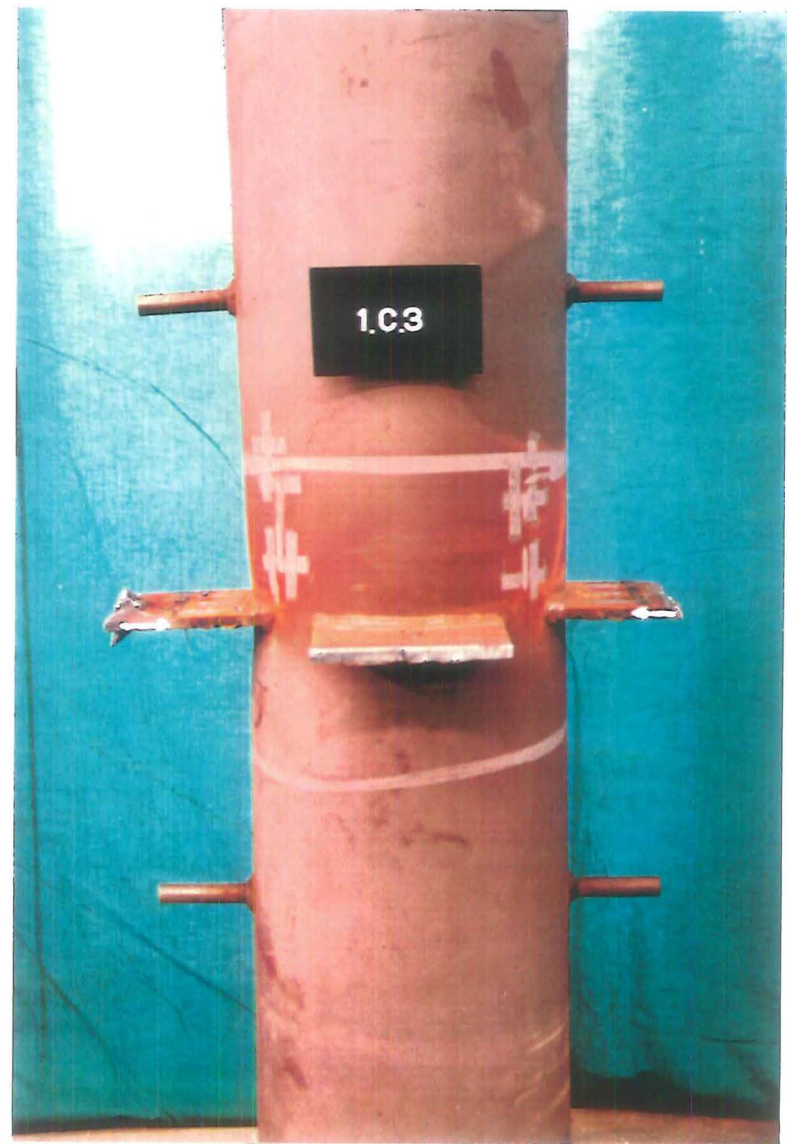


Photo 6-6 : Details of specimen 1C3 after failure

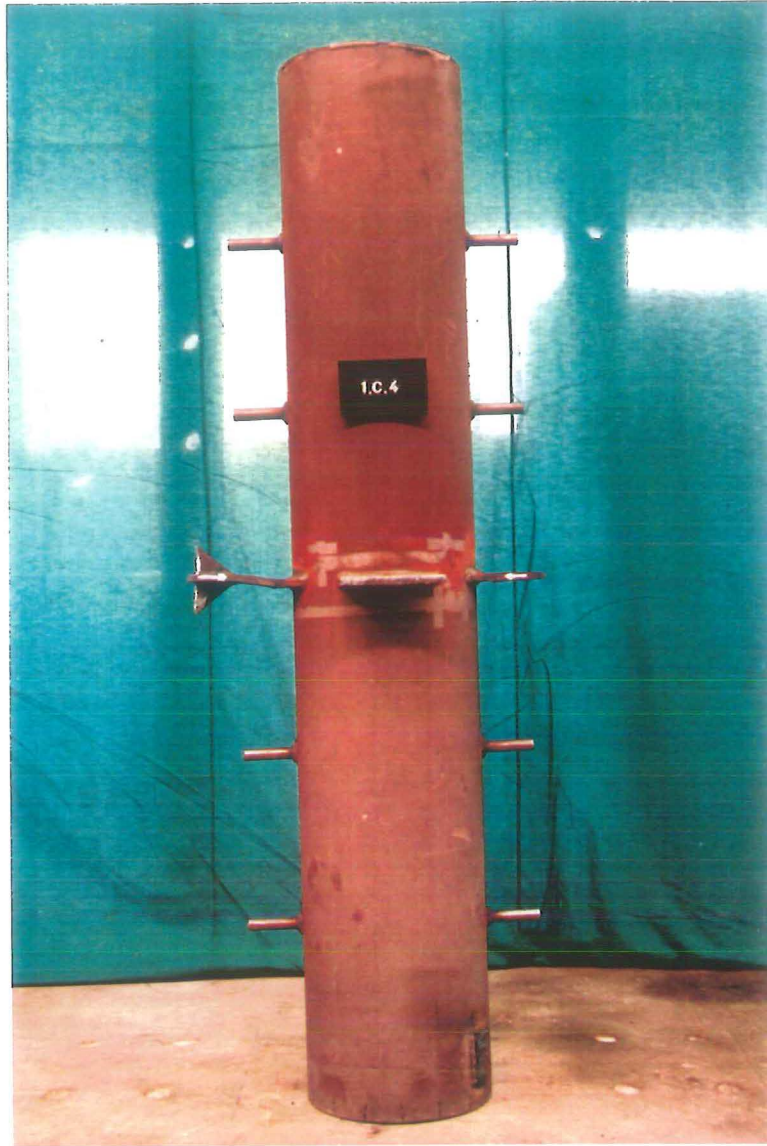


Photo 6-7 : Specimen 1C4 after failure

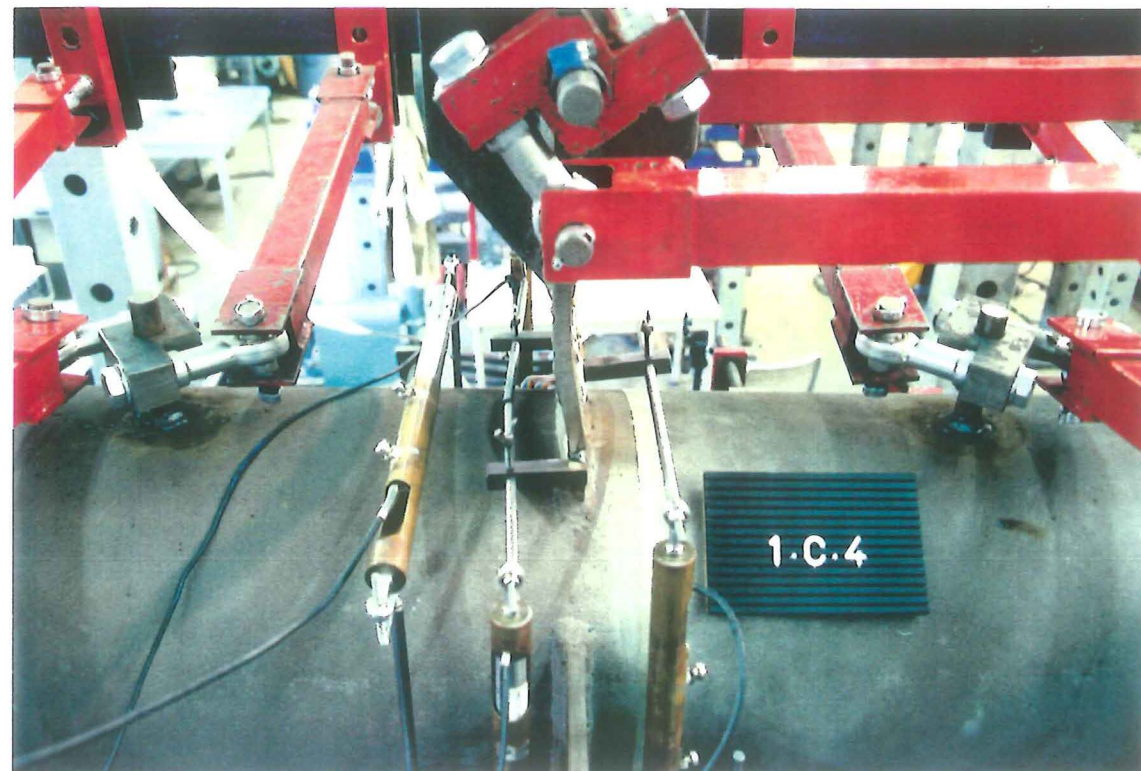


Photo 6-8 : Details of specimen 1C4 after failure

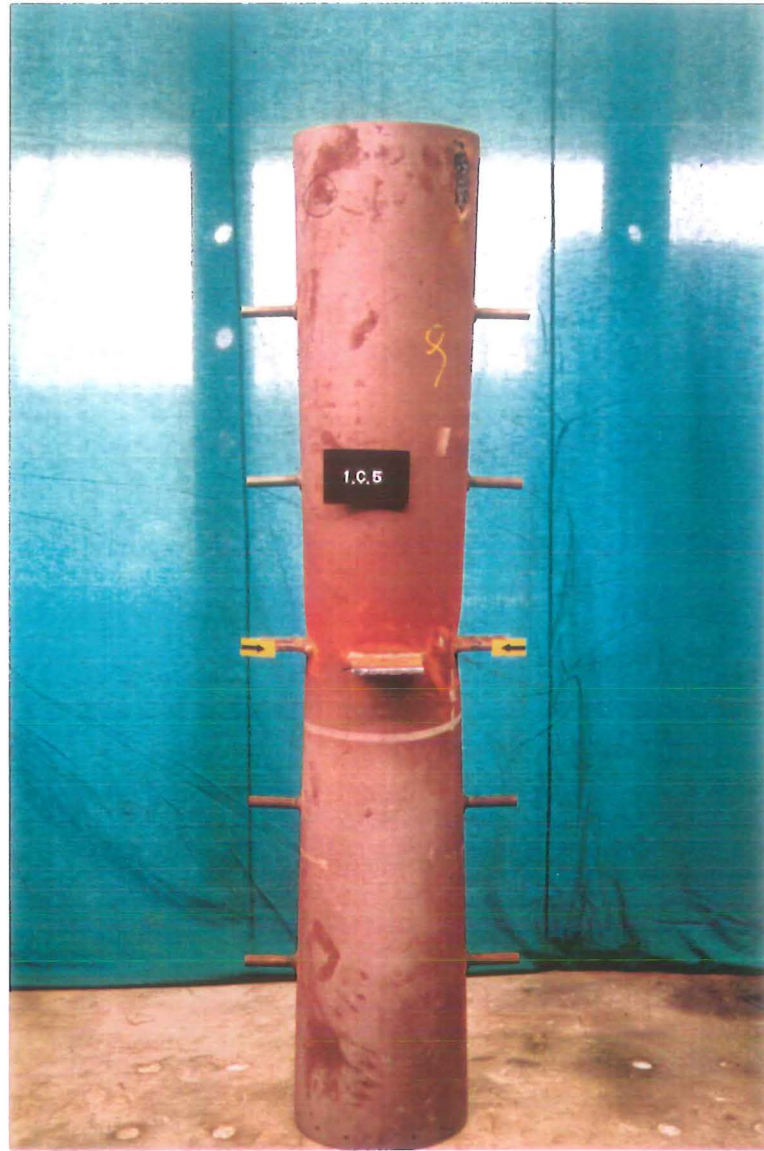


Photo 6-9 : Specimen 1C5 after failure



Photo 6-10 : Details of specimen 1C5 after failure



Photo 6-11 : Specimen 1C6 after failure

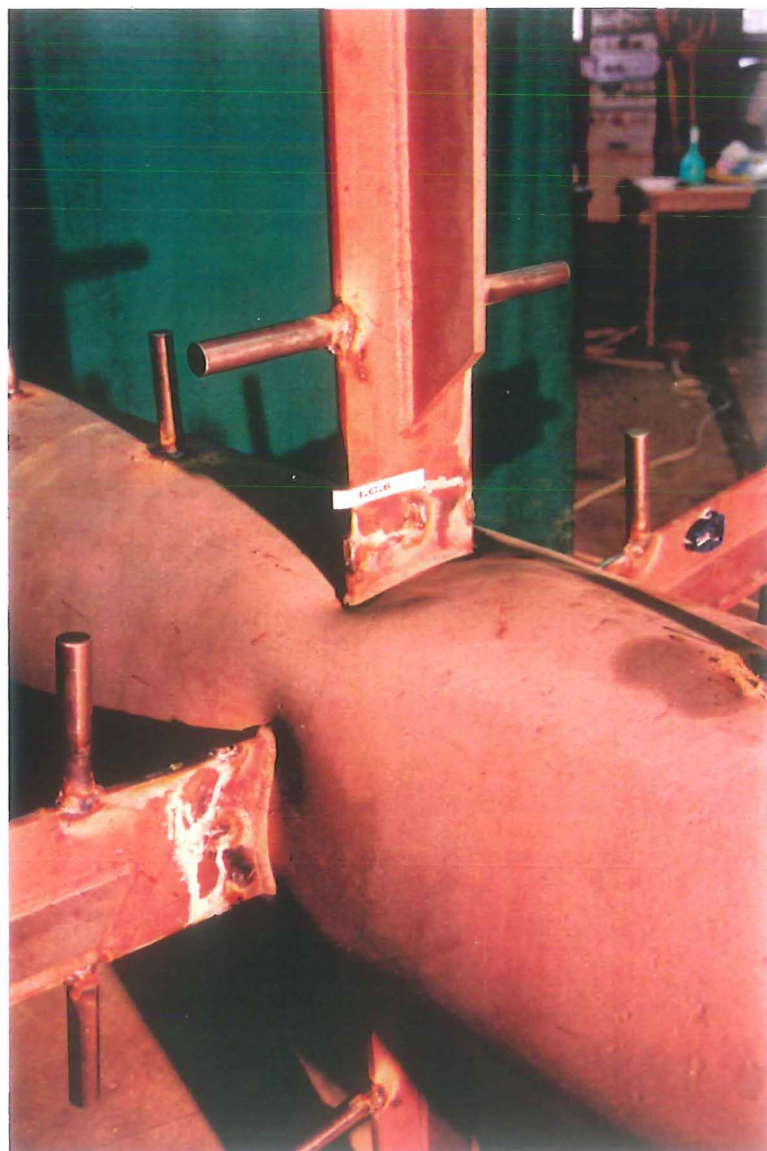


Photo 6-12 :
Details of specimen 1C6 after failure

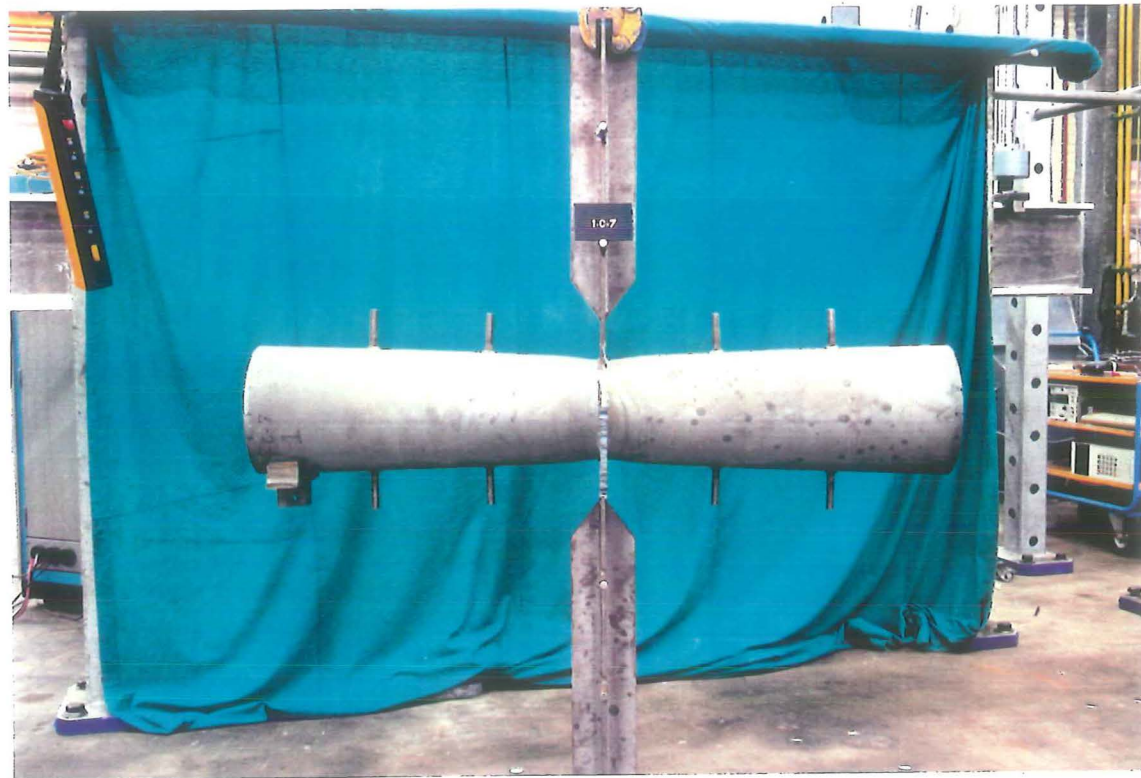


Photo 6-13 : Specimen 1C7 after failure

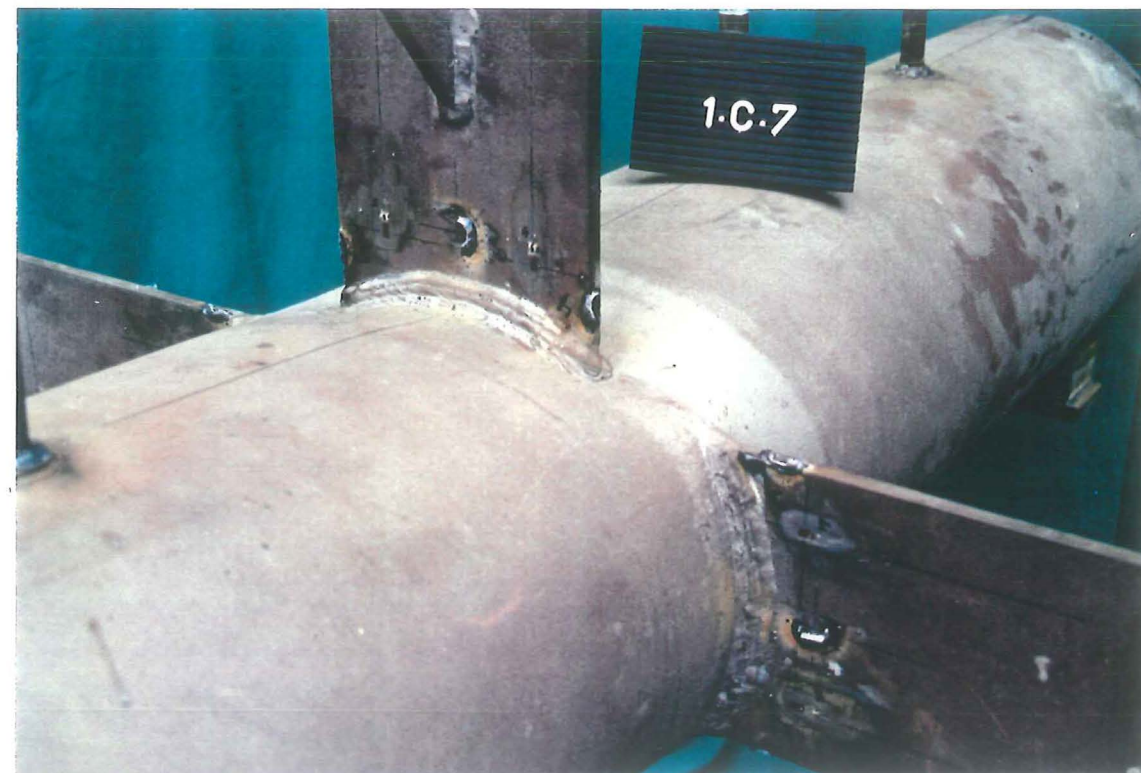


Photo 6-14 : Details of specimen 1C7 after failure

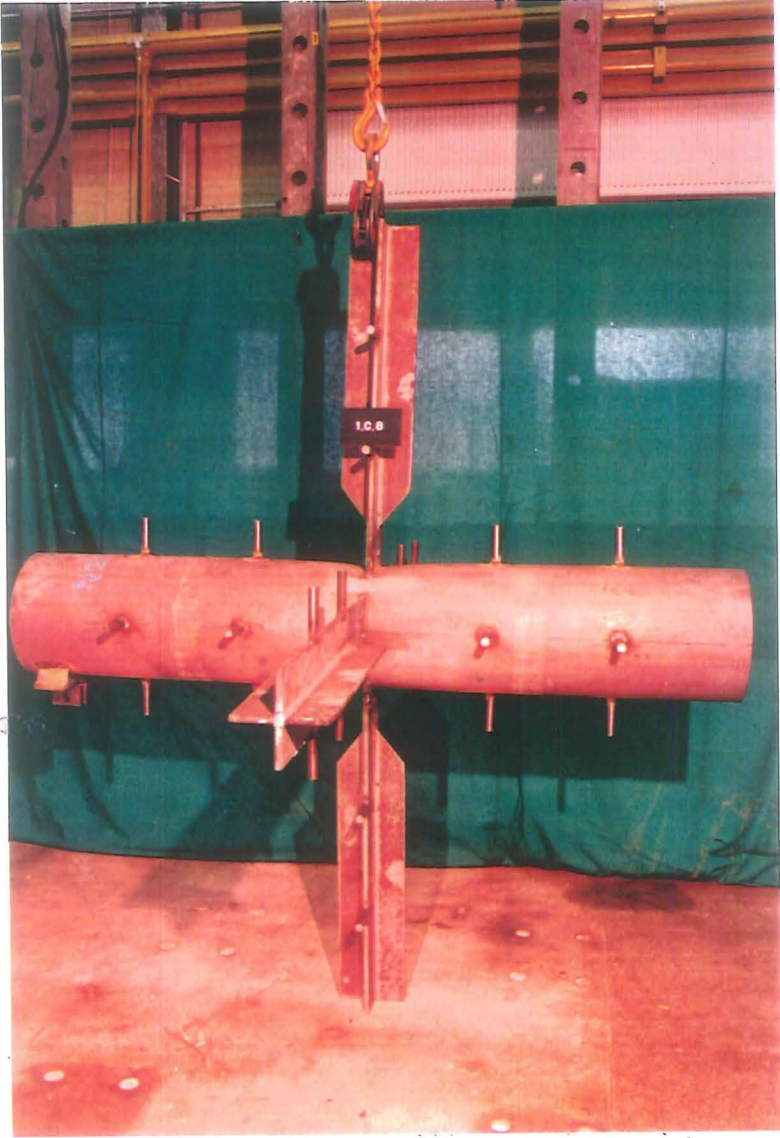


Photo 6-15 : Specimen 1C8 after failure



Photo 6-16 : Details of specimen 1C8 after failure



Photo 6-17 : Specimen 2C1 after failure

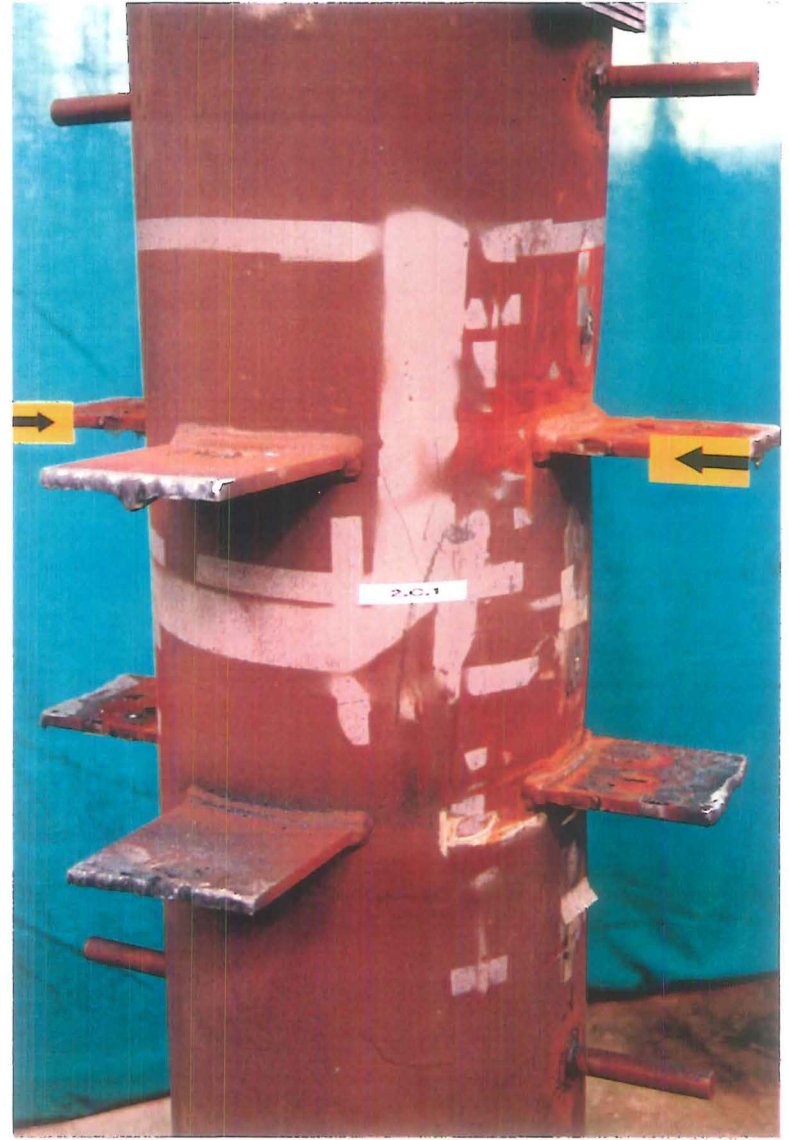


Photo 6-18 : Details of specimen 2C1 after failure

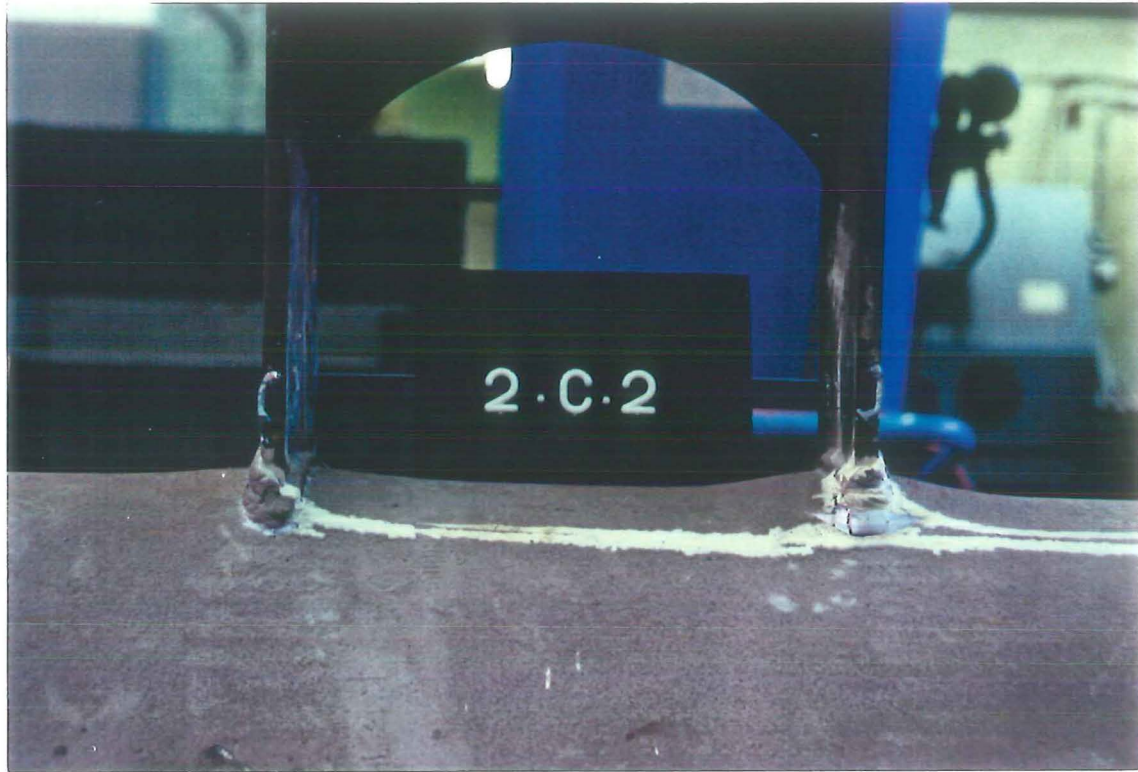


Photo 6-19 : Details of specimen 2C2 after failure

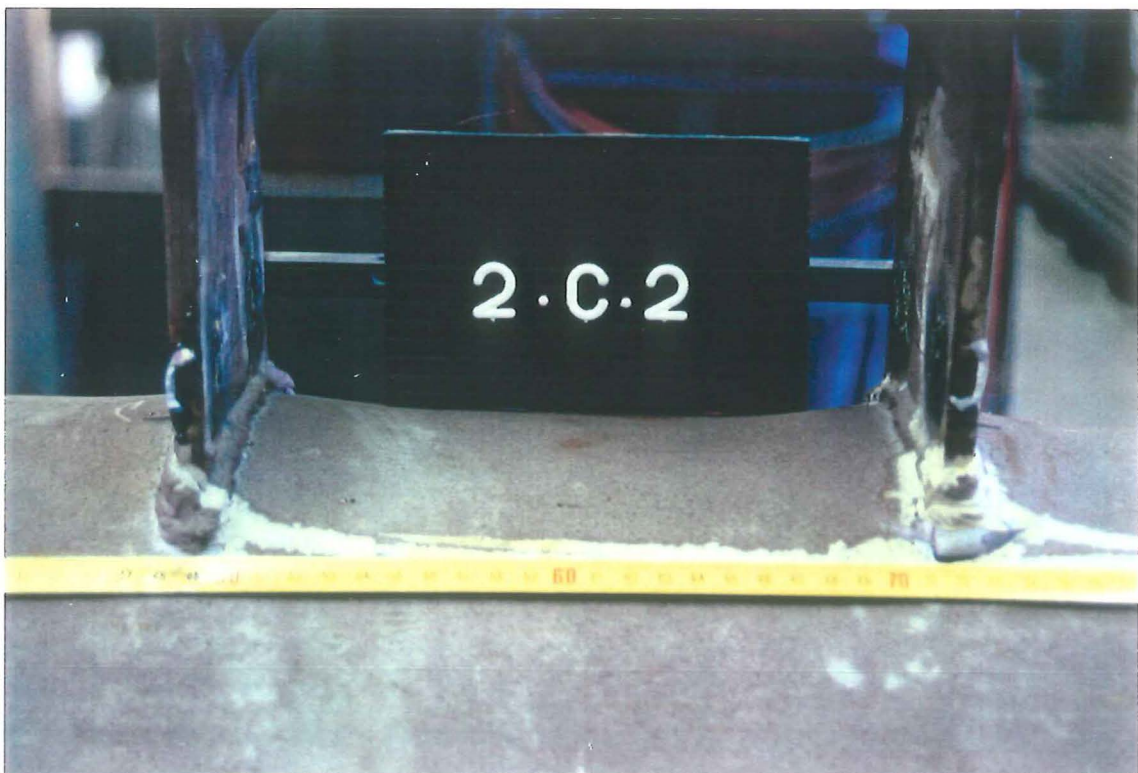


Photo 6-20 : Details of specimen 2C2 after failure



Photo 6-21 : Specimen 2C3 after failure

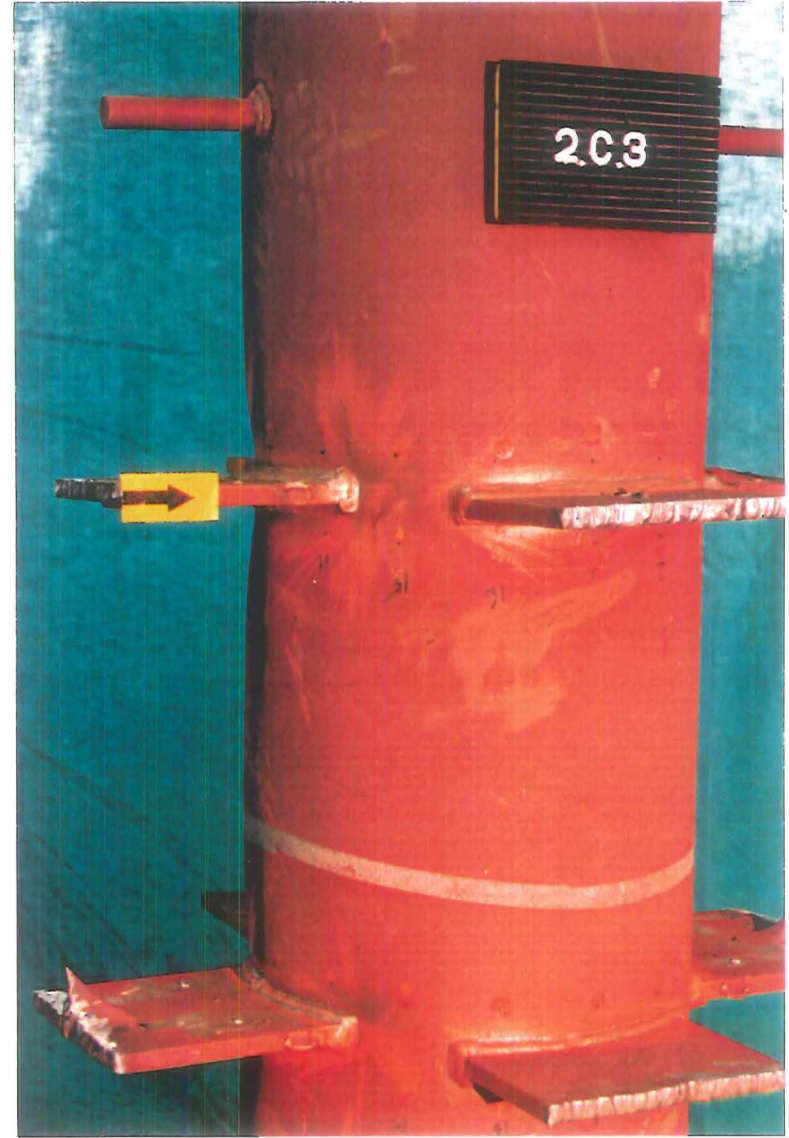


Photo 6-22 : Details of specimen 2C3 after failure

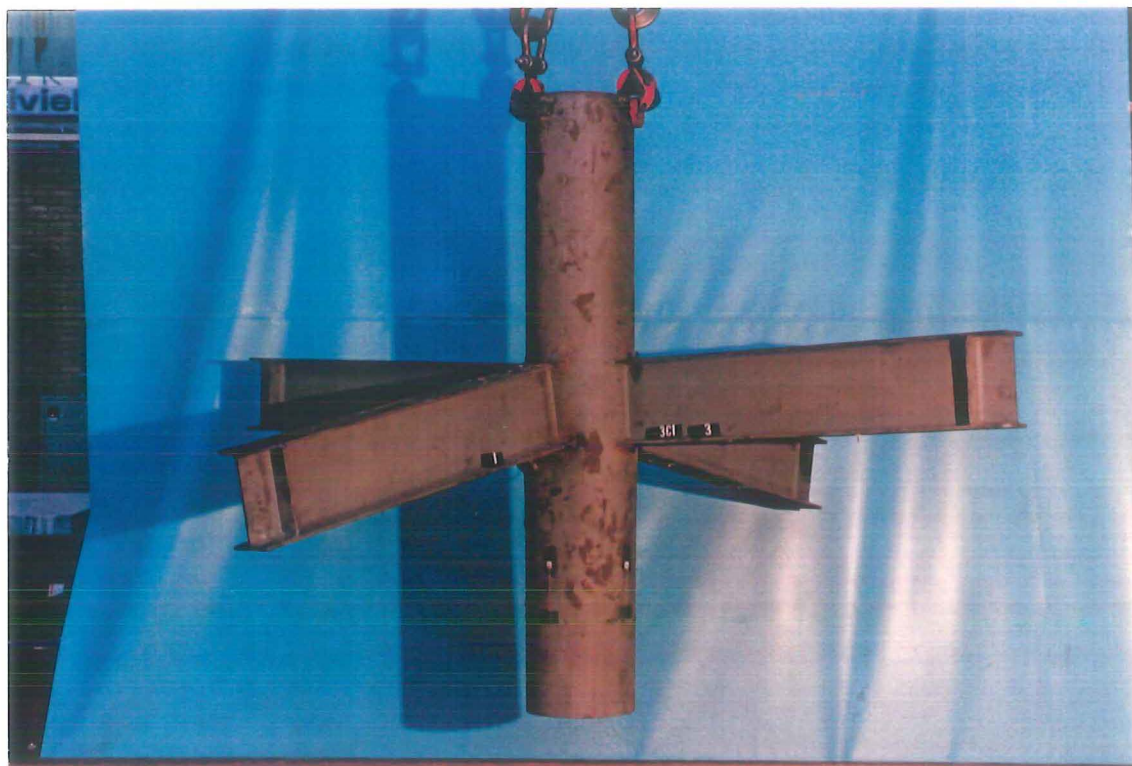


Photo 6-23 : Specimen 3C1 after failure



Photo 6-24 : Details of specimen 3C1 after failure

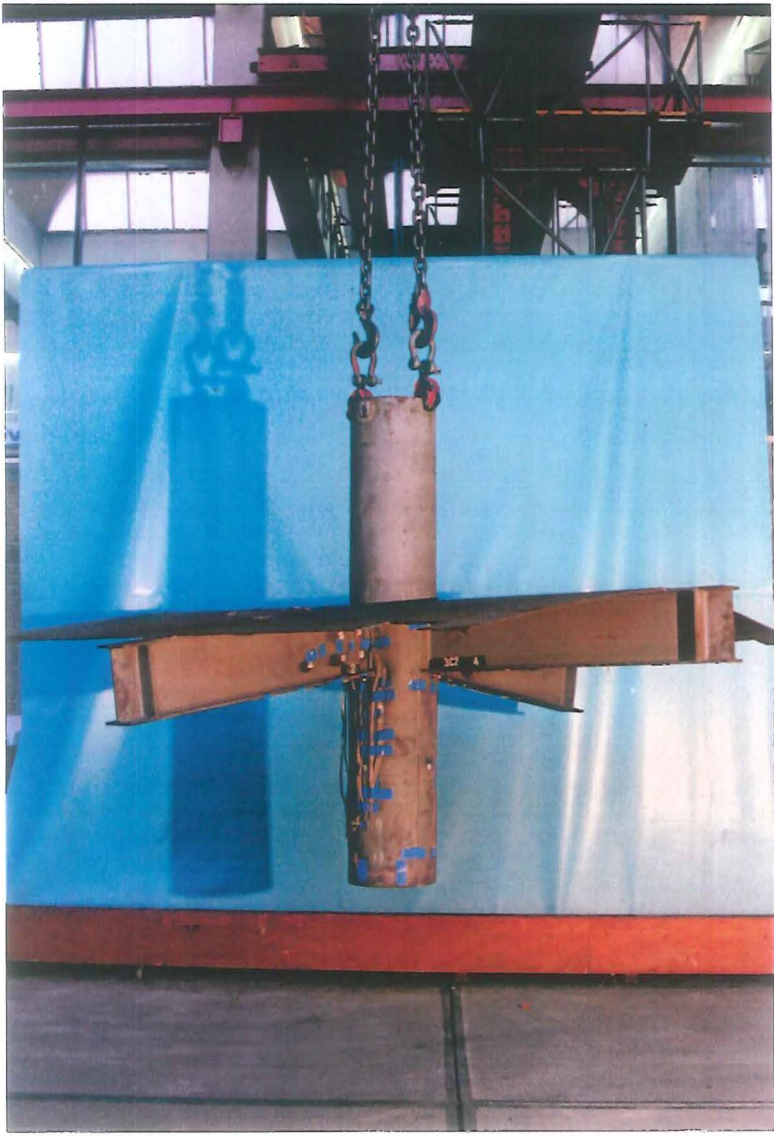


Photo 6-25 : Specimen 3C2 after failure

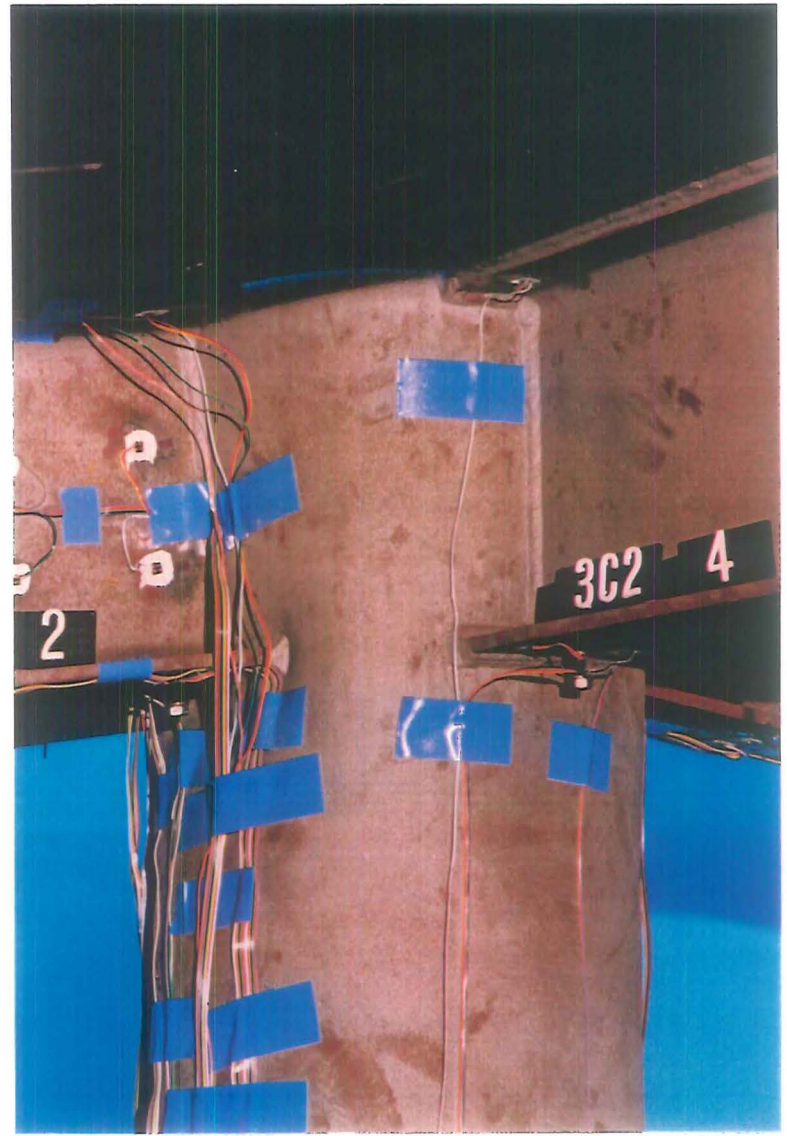


Photo 6-26 : Details of specimen 3C2 after failure



Photo 6-27 : Specimen 3C3 after failure

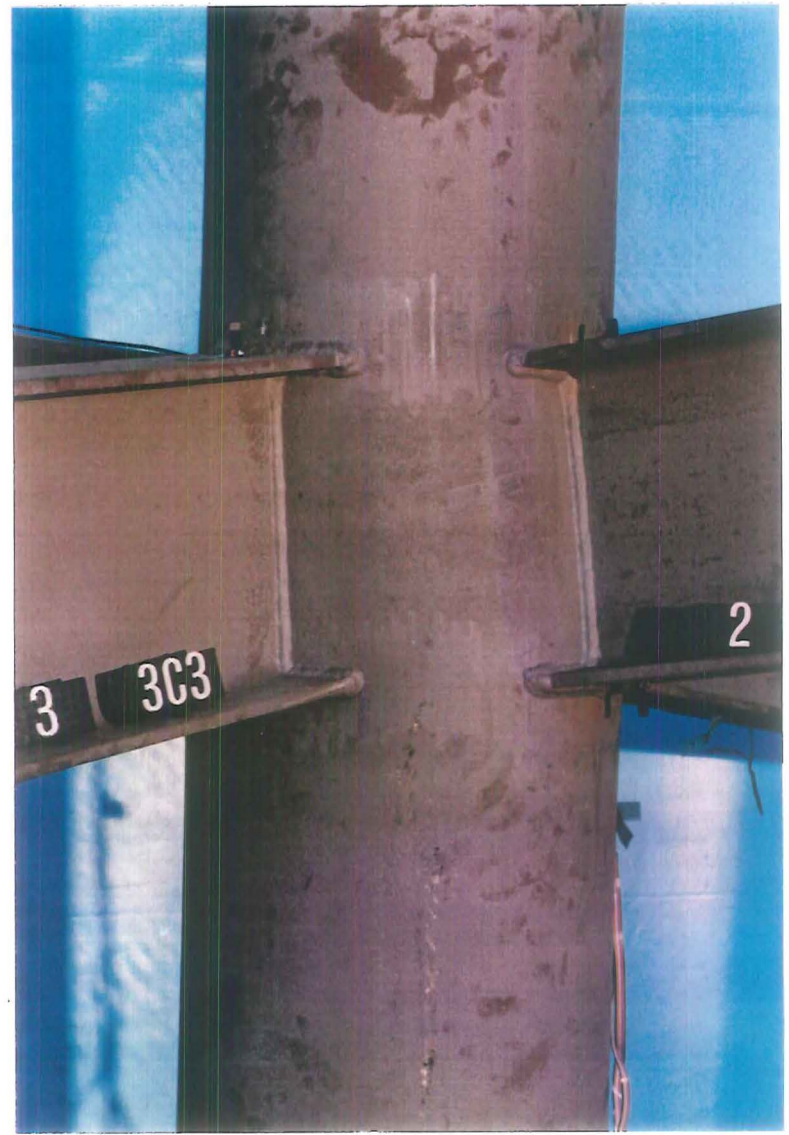


Photo 6-28 : Details of specimen 3C3 after failure

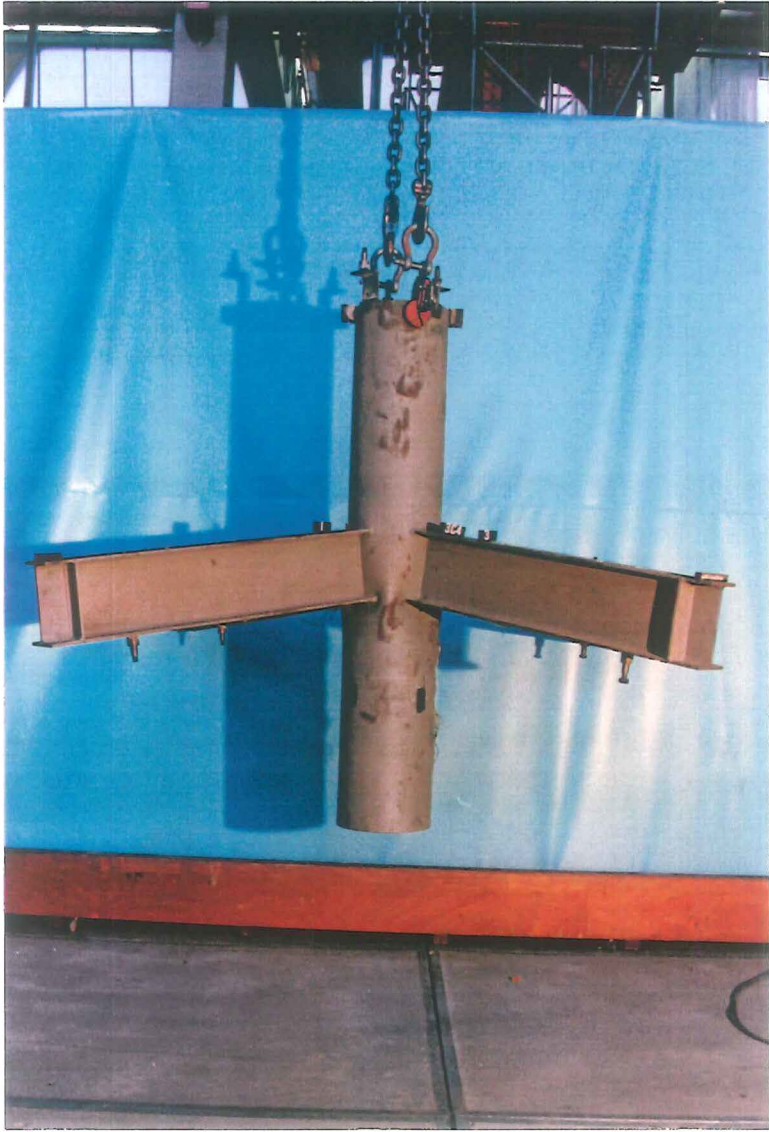


Photo 6-29 : Specimen 3C4 after failure

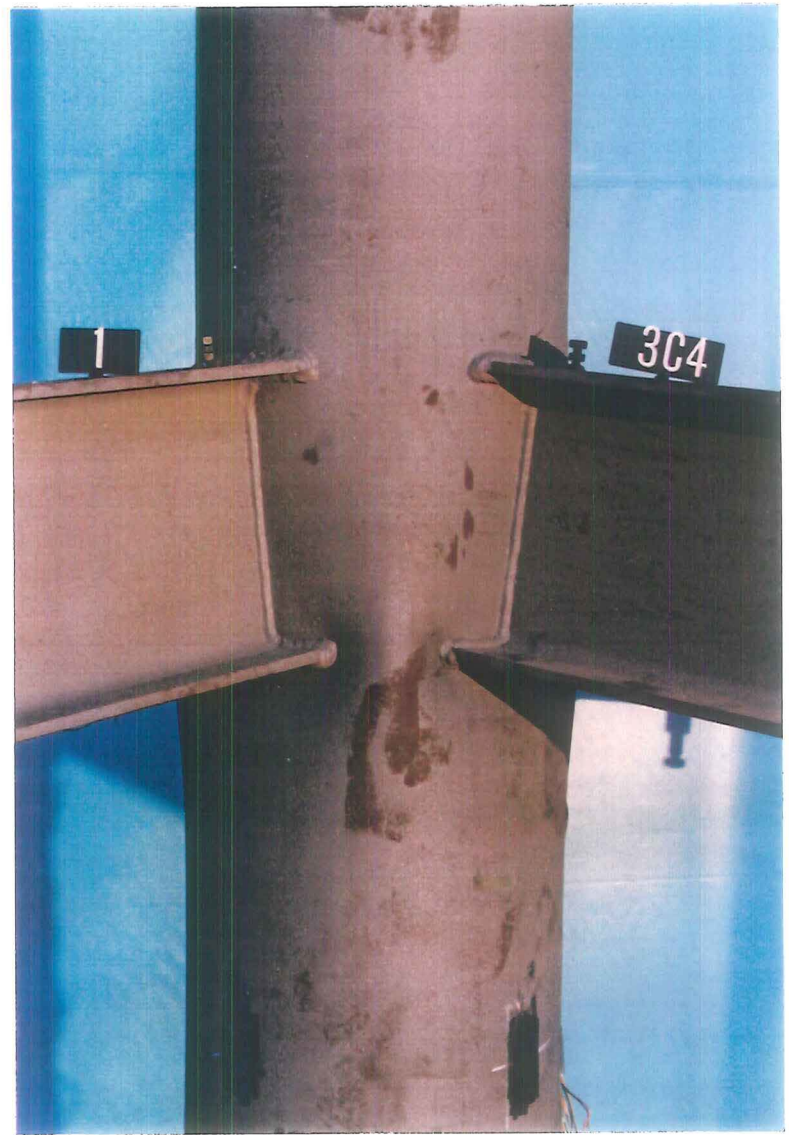


Photo 6-30 : Details of specimen 3C4 after failure

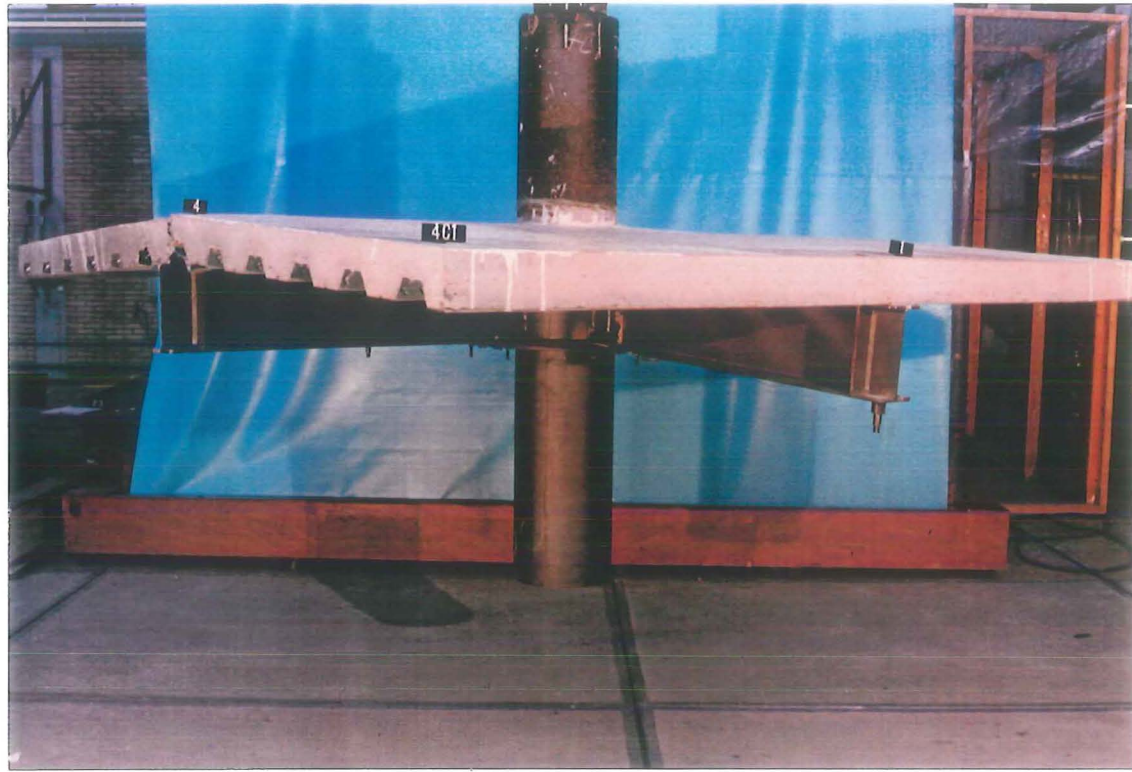


Photo 6-31 : Specimen 4C1 after failure

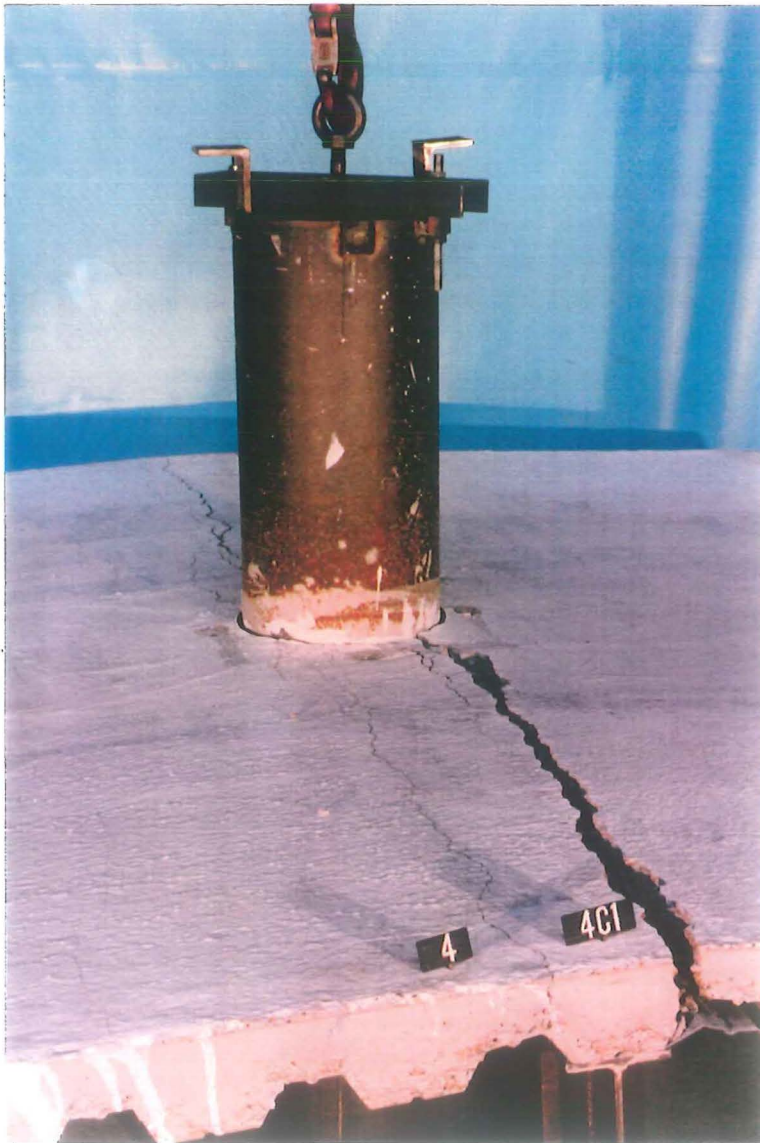


Photo 6-32 :
Details of specimen 4C1 after failure

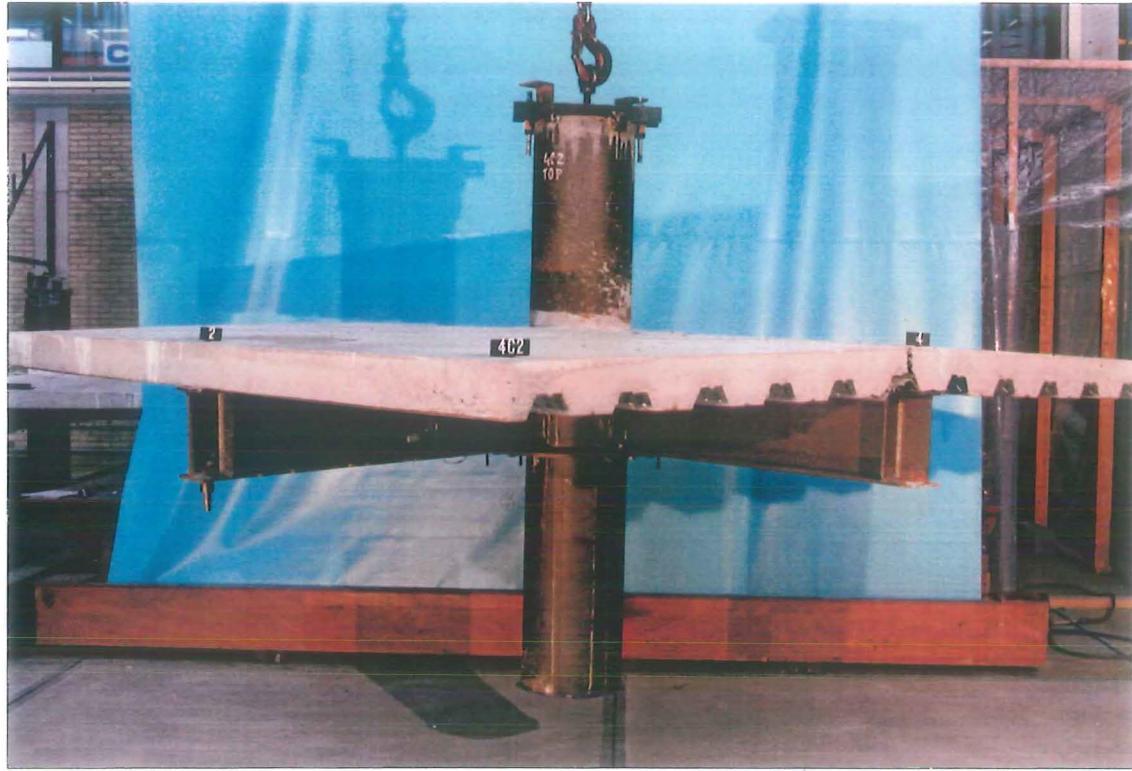


Photo 6-33 : Specimen 4C2 after failure



Photo 6-34 :
Details of specimen 4C2 after failure

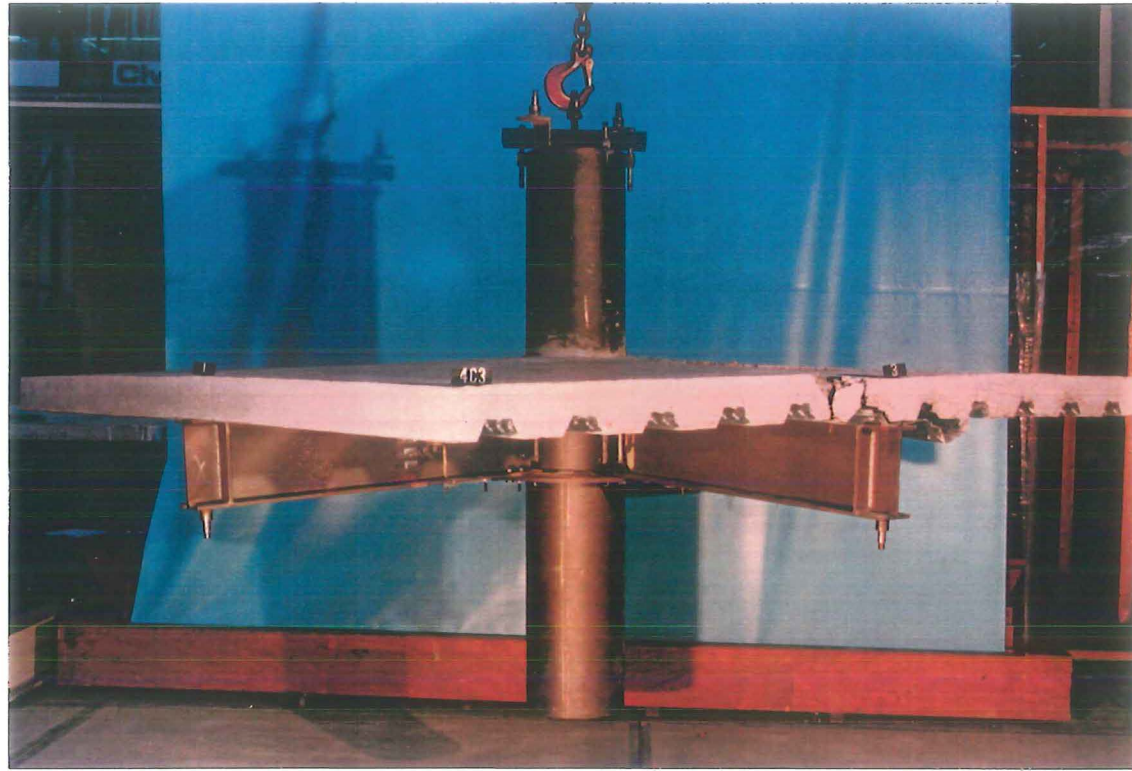


Photo 6-35 : Specimen 4C3 after failure

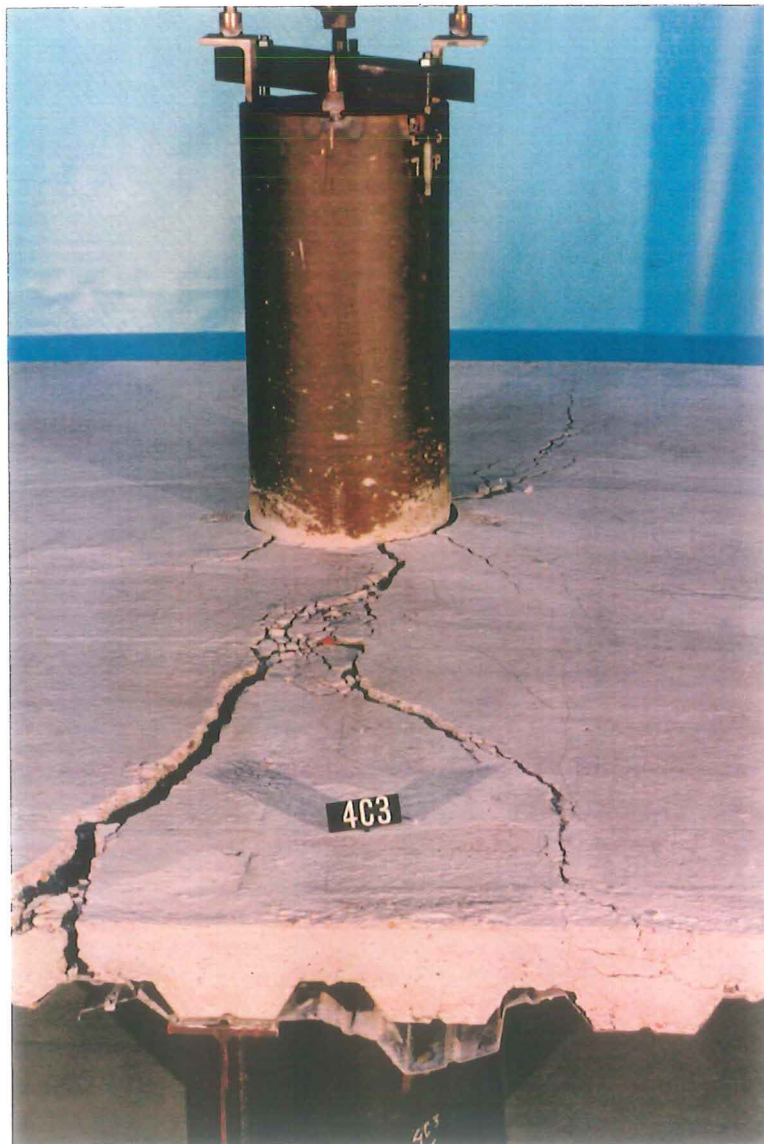


Photo 6-36 :
Details of specimen 4C3 after failure

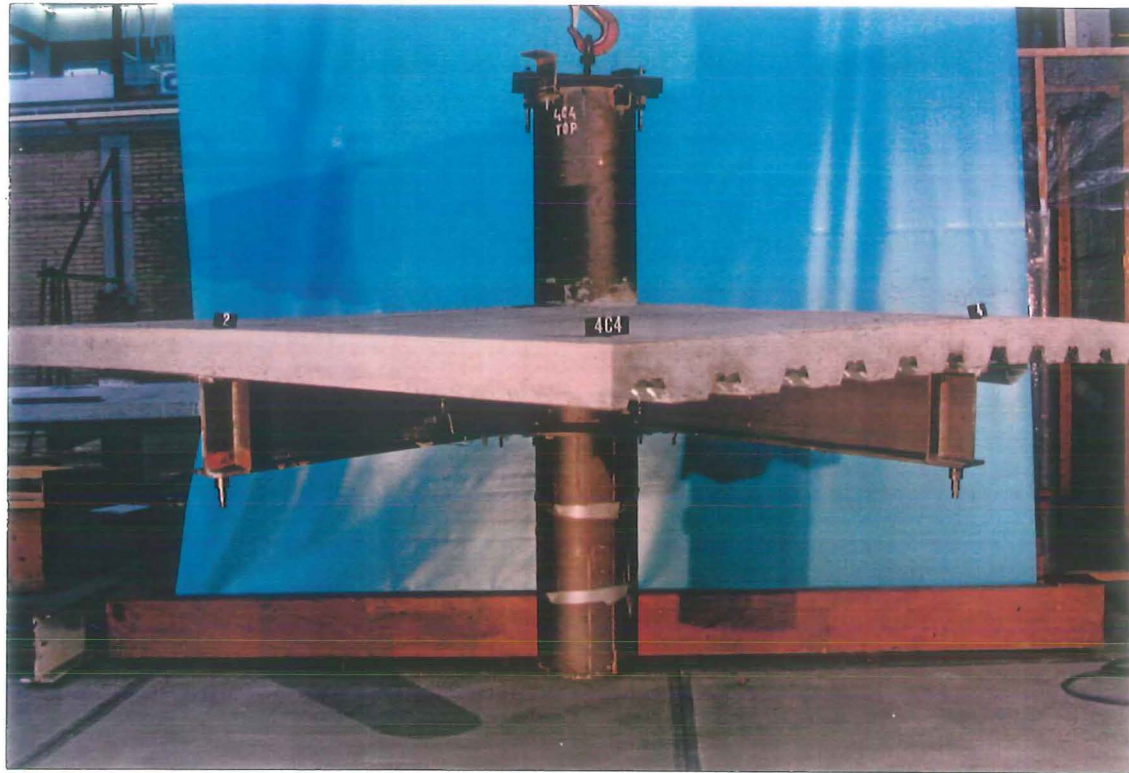


Photo 6-37 : Specimen 4C4 after failure



Photo 6-38 :
Details of specimen 4C4 after failure

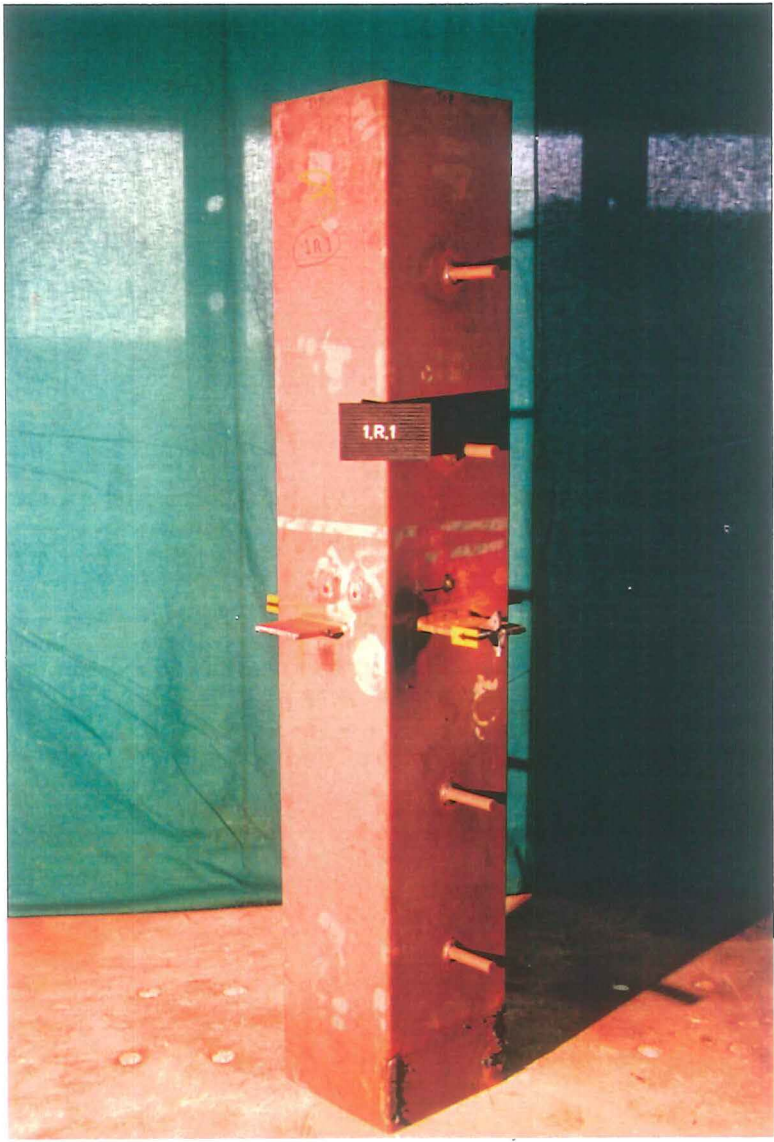


Photo 7-1 : Specimen 1R1 after failure

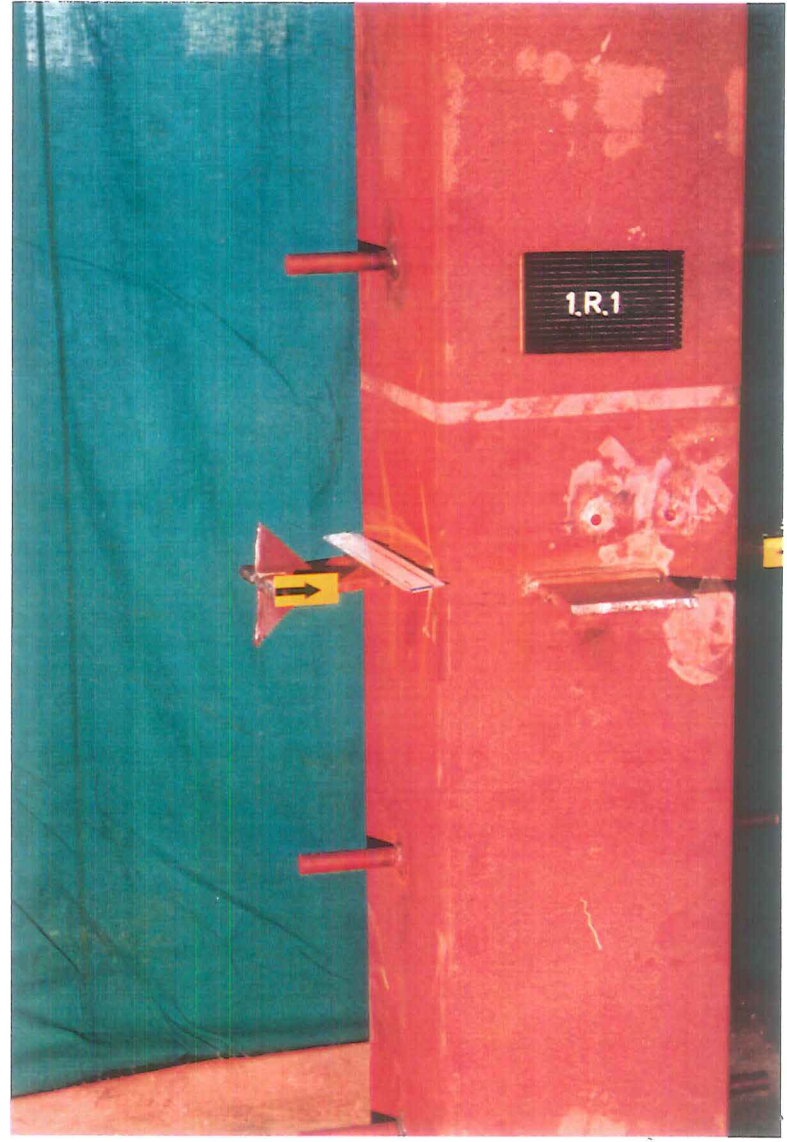


Photo 7-2 : Details of specimen 1R1 after failure

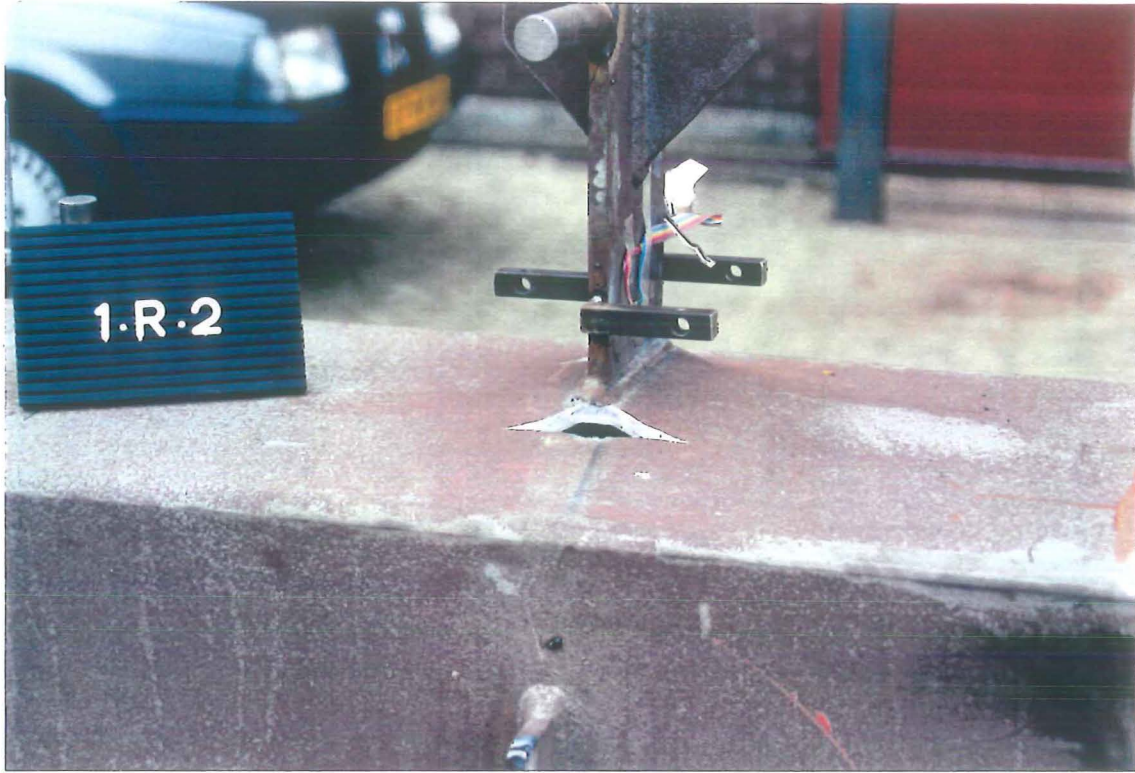


Photo 7-3 : Specimen 1R2 after failure

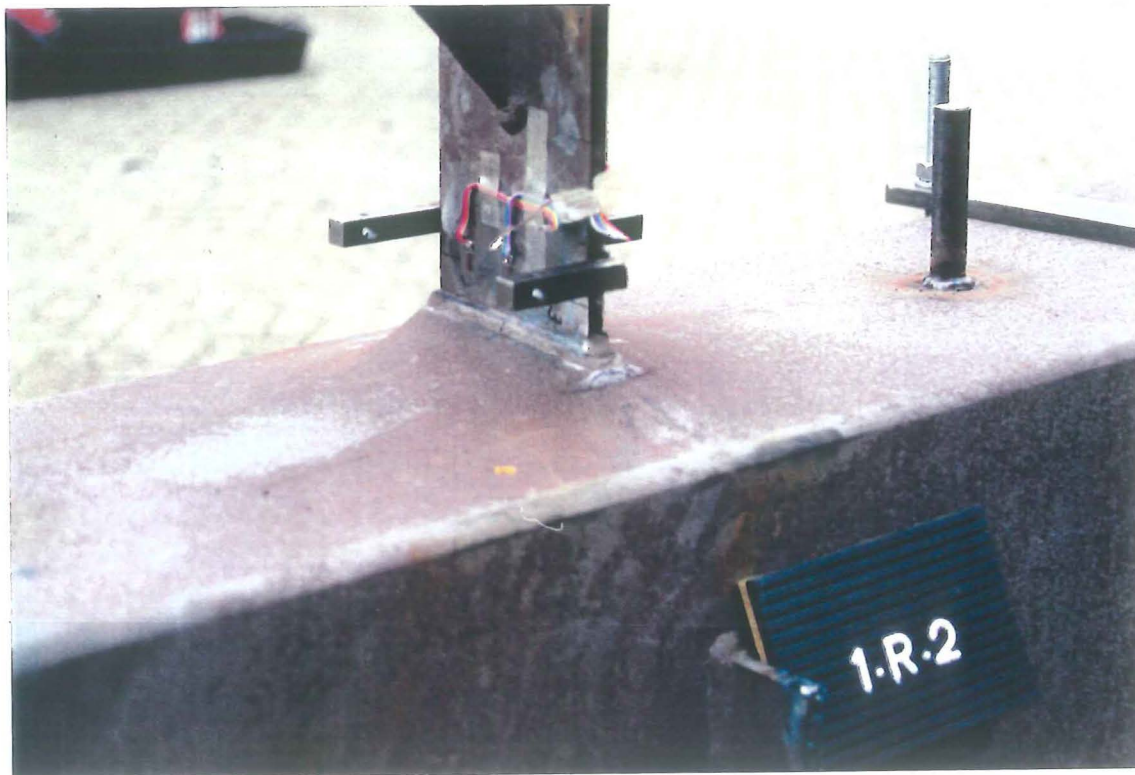


Photo 7-4 : Details of specimen 1R2 after failure

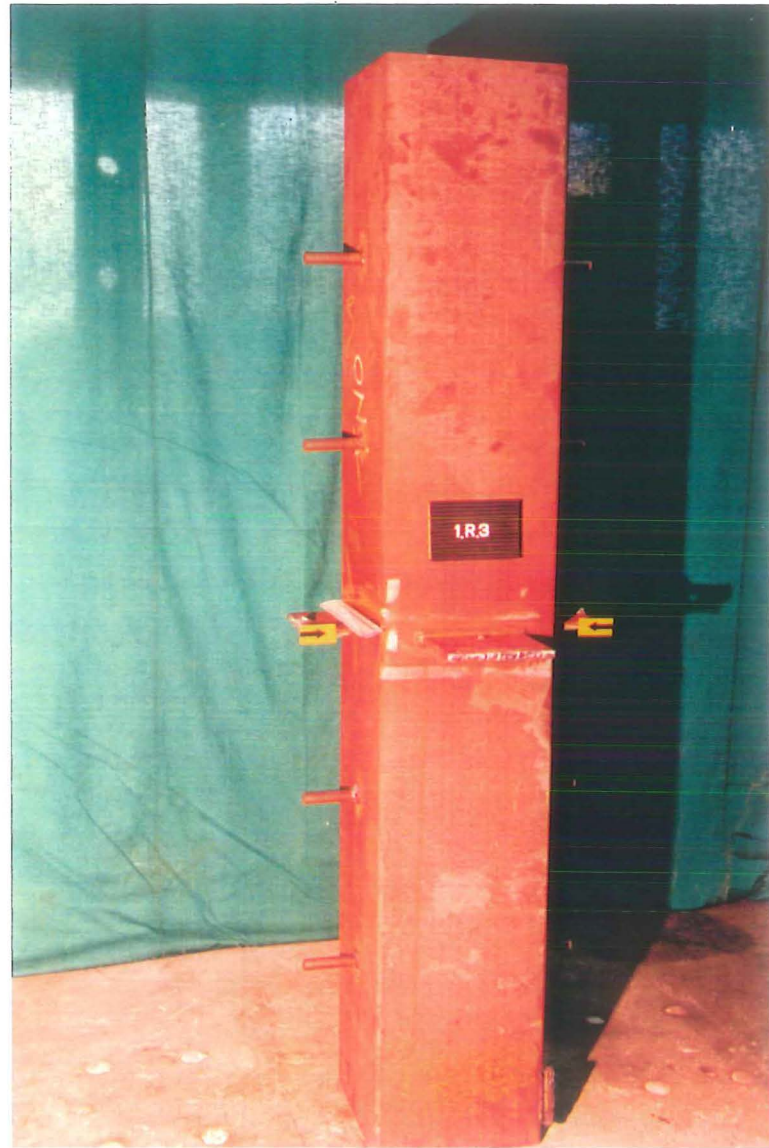


Photo 7-5 : Specimen 1R3 after failure

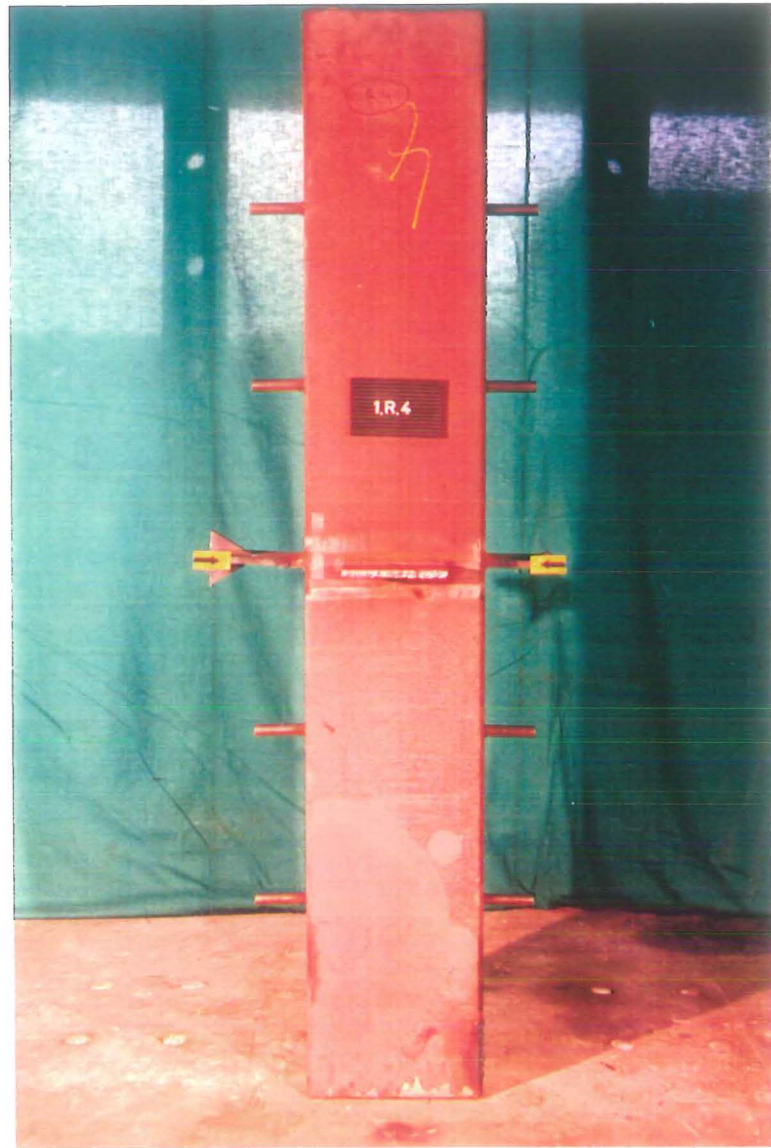


Photo 7-6 : Specimen 1R4 after failure

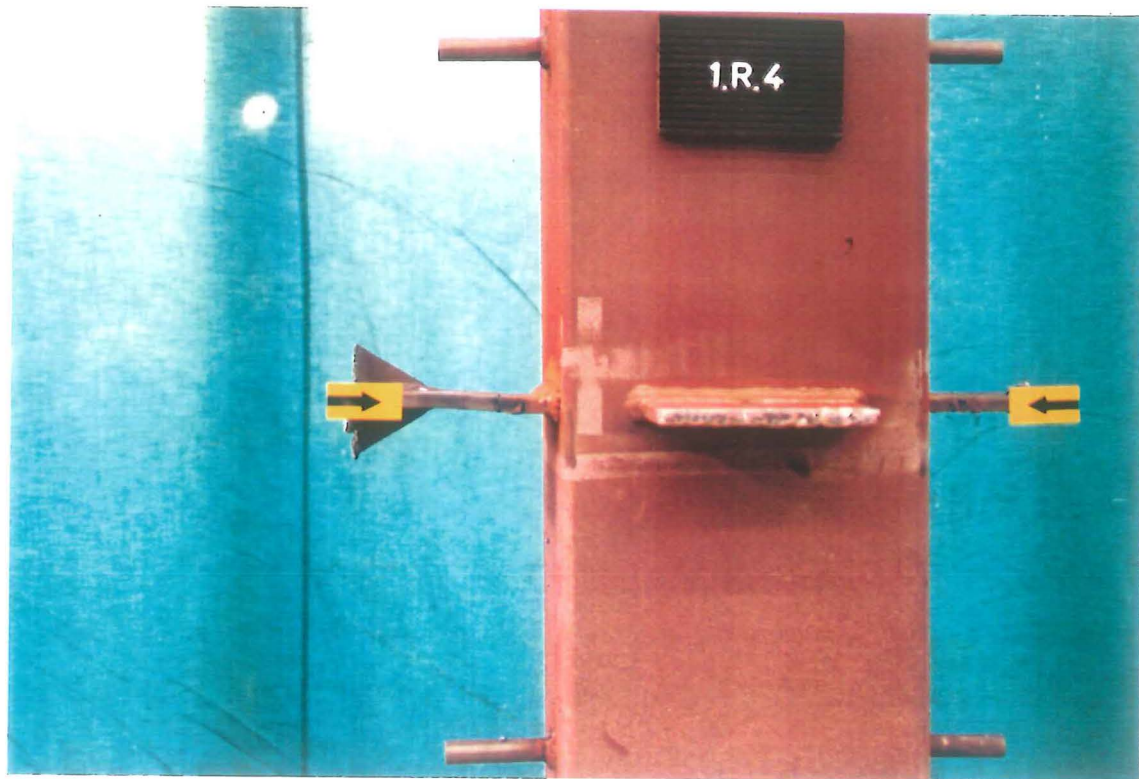


Photo 7-7 : Details of specimen 1R4 after failure

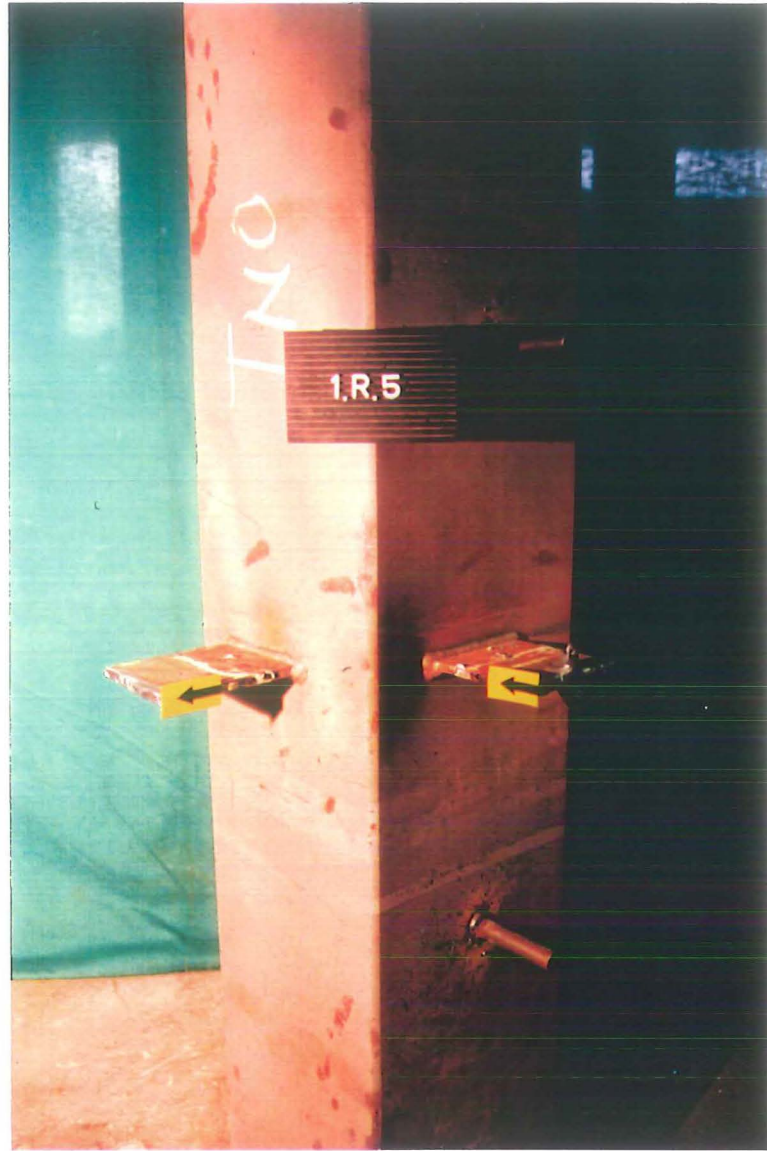


Photo 7-8 : Specimen 1R5 after failure

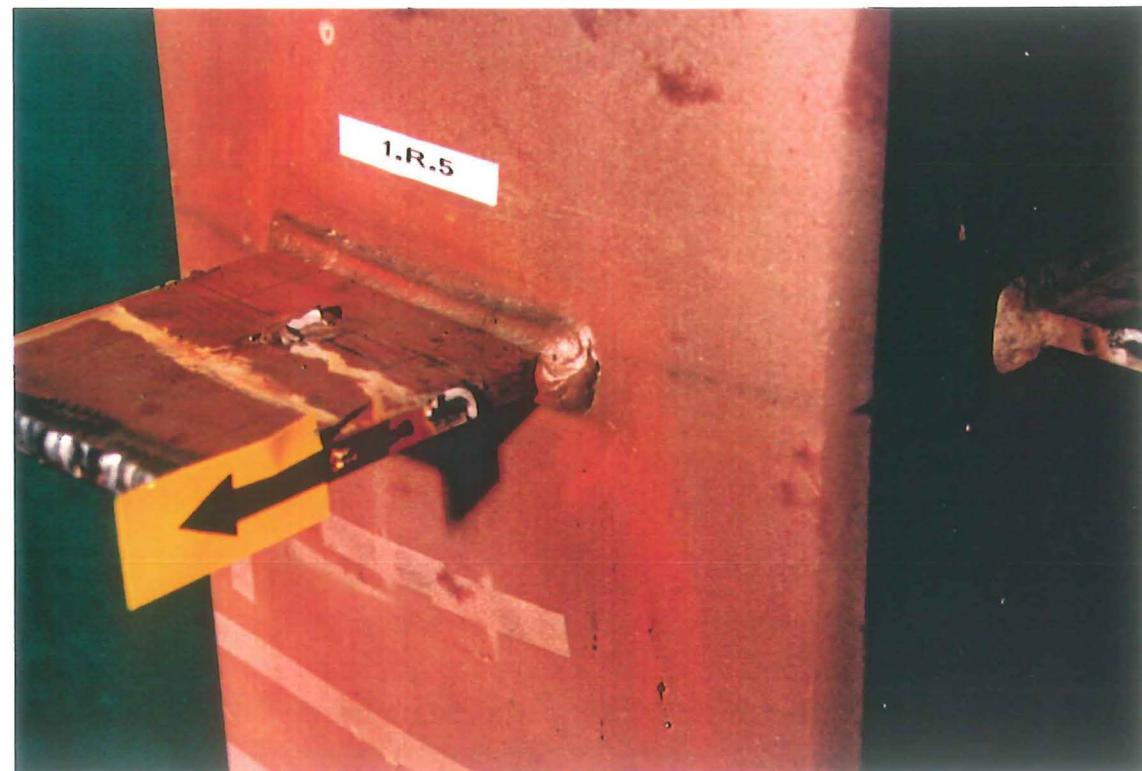


Photo 7-9 : Details of specimen 1R5 after failure

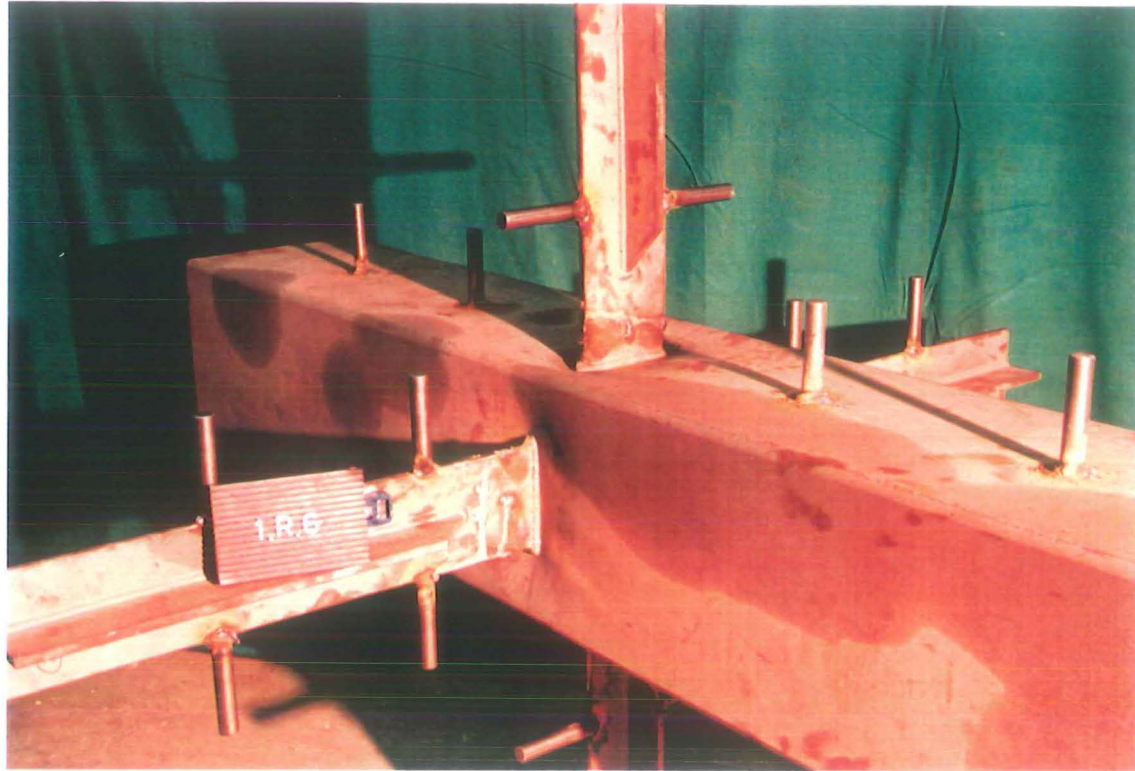


Photo 7-10 : Specimen 1R6 after failure

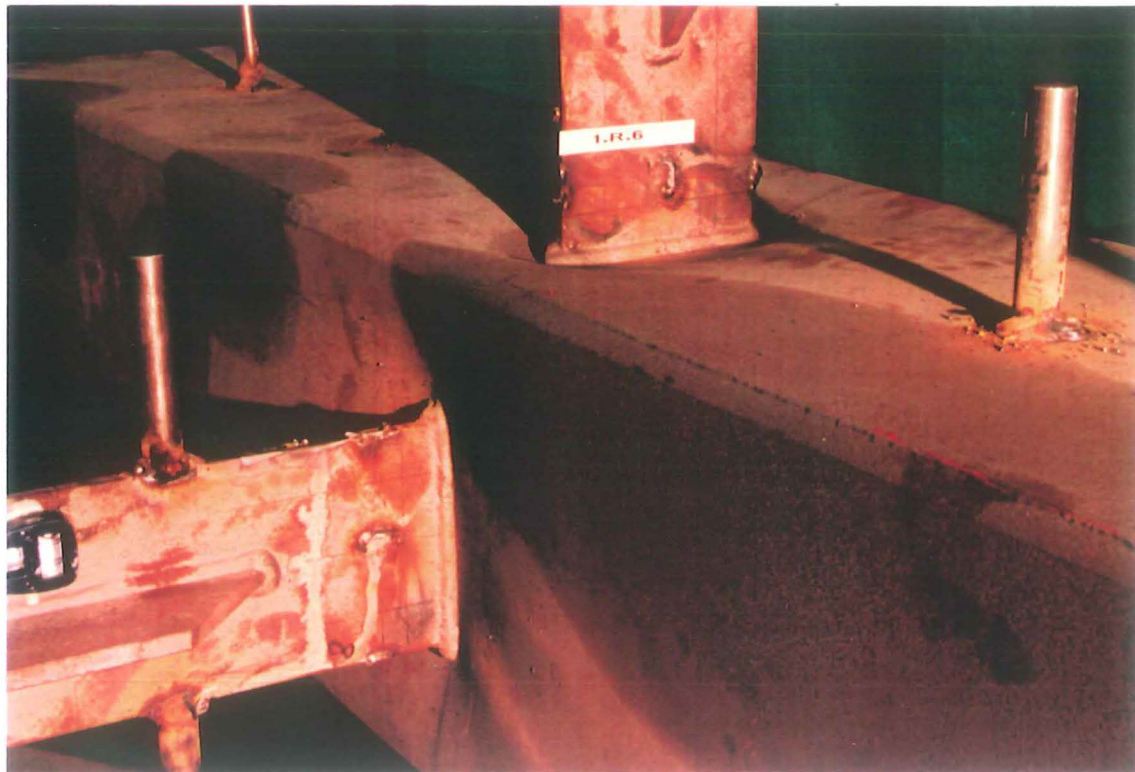


Photo 7-11 : Details of specimen 1R6 after failure

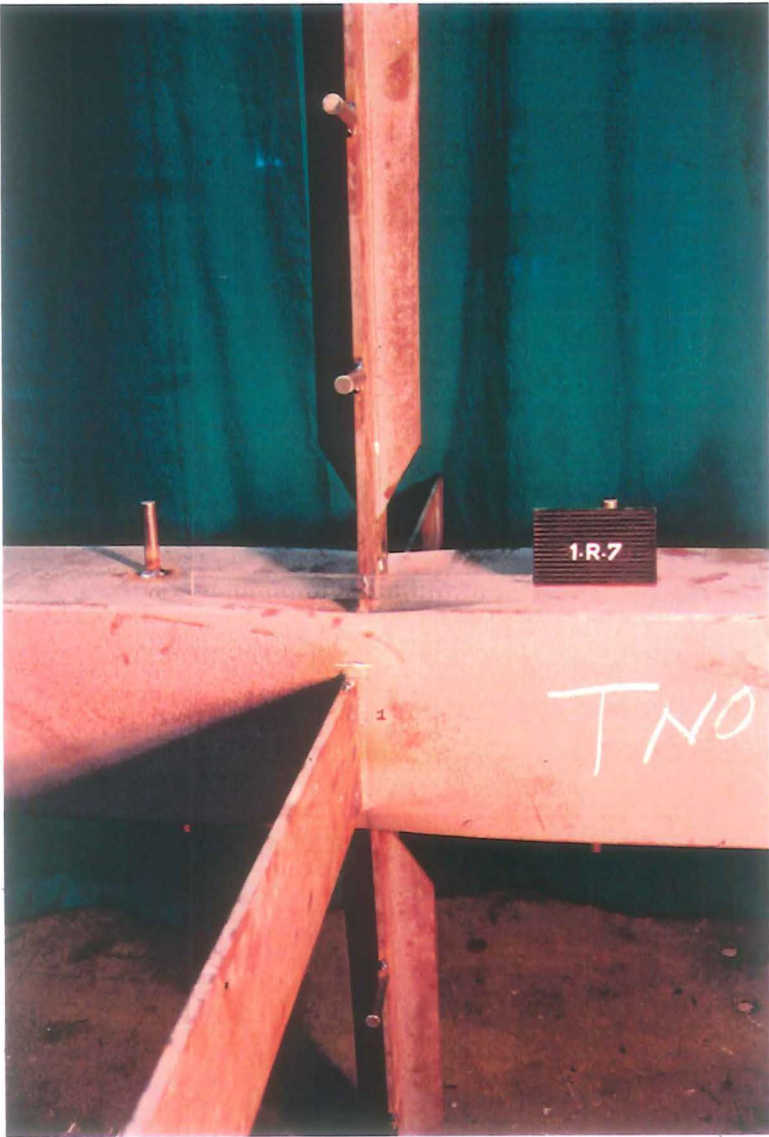


Photo 7-12 : Specimen 1R7 after failure

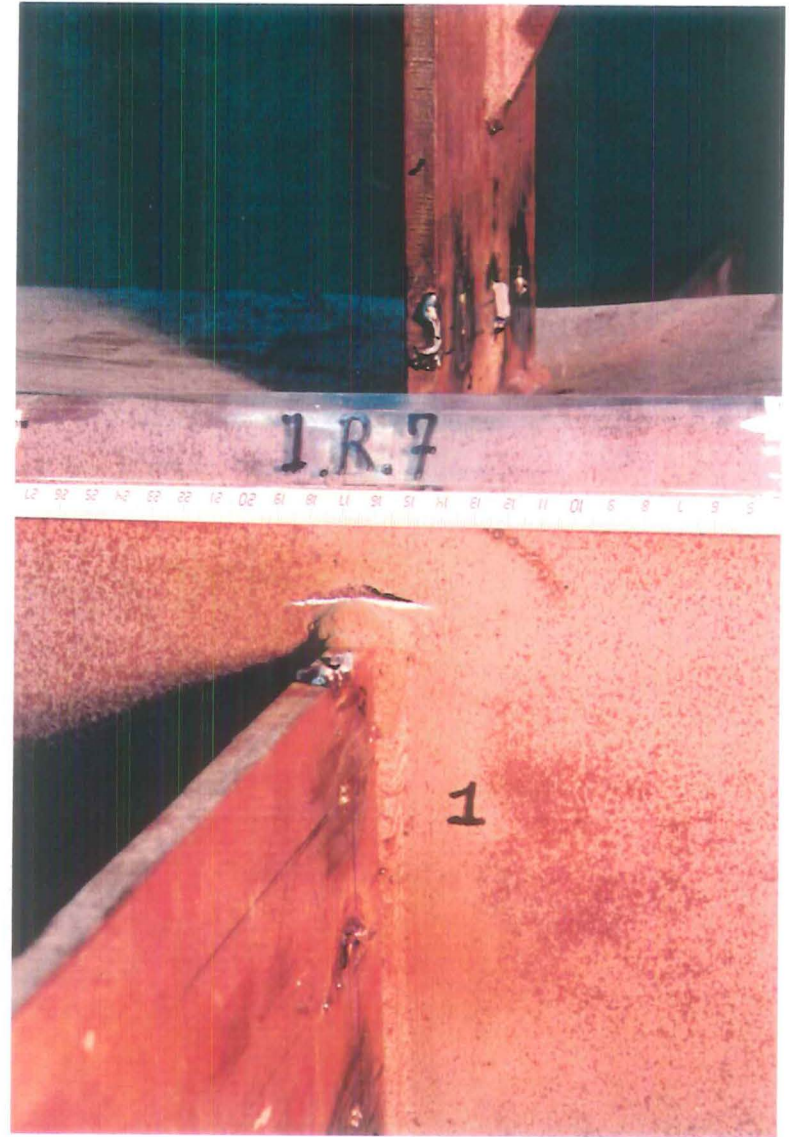


Photo 7-13 : Details of specimen 1R7 after failure



Photo 7-14 : Specimen 1R8 after failure

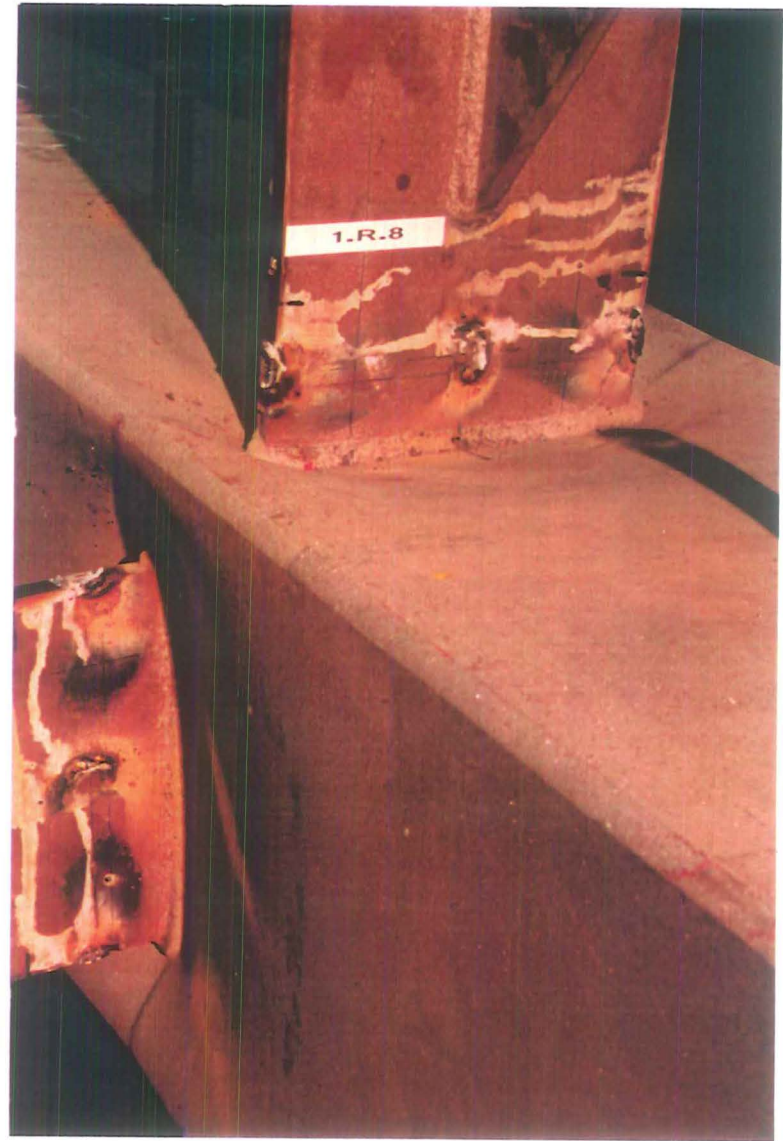


Photo 7-15 : Details of specimen 1R8 after failure



Photo 7-16 : Specimen 2R1 after failure



Photo 7-17 : Specimen 2R1 after failure

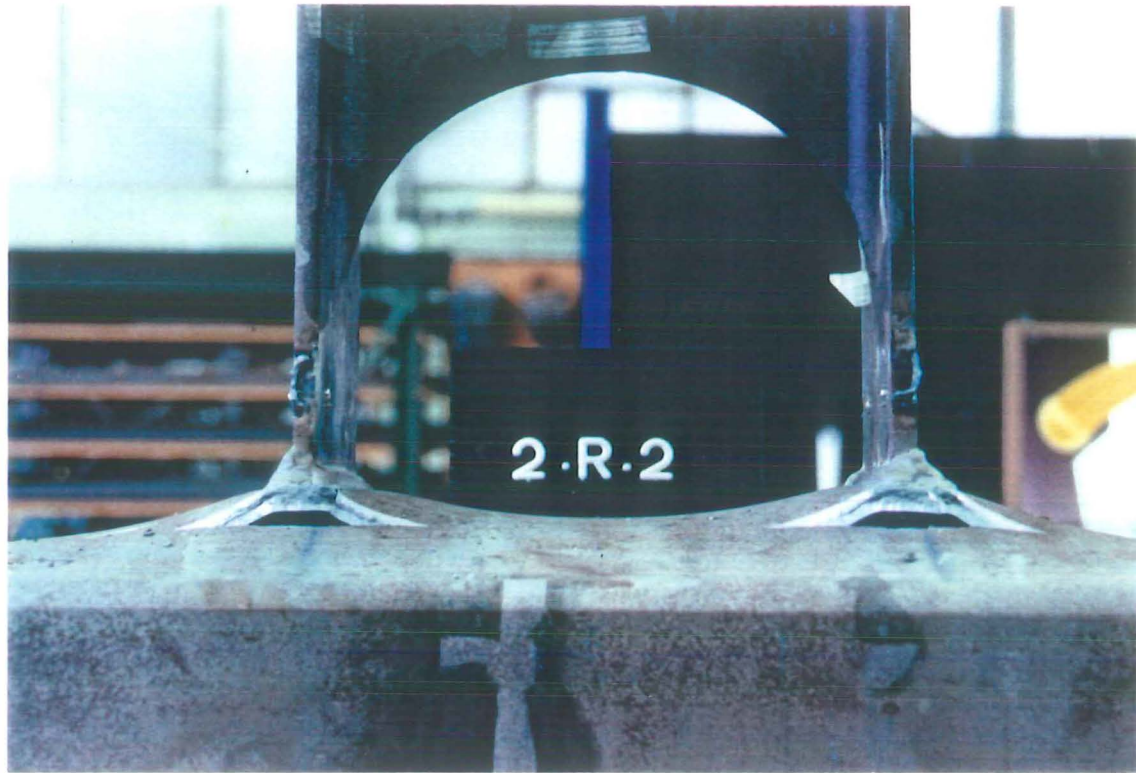


Photo 7-18 : Details of specimen 2R2 after failure

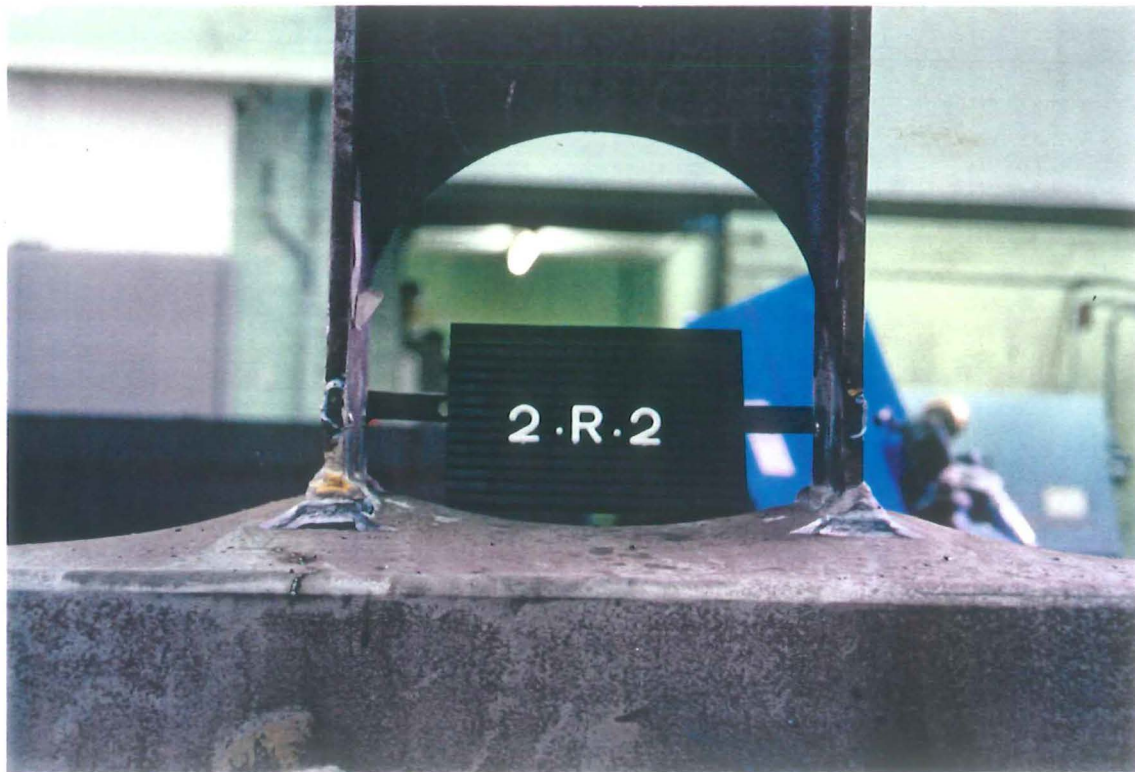


Photo 7-19 : Details of specimen 2R2 after failure



Photo 7-20 : Specimen 2R3 after failure



Photo 7-21 : Details of specimen 2R3 after failure

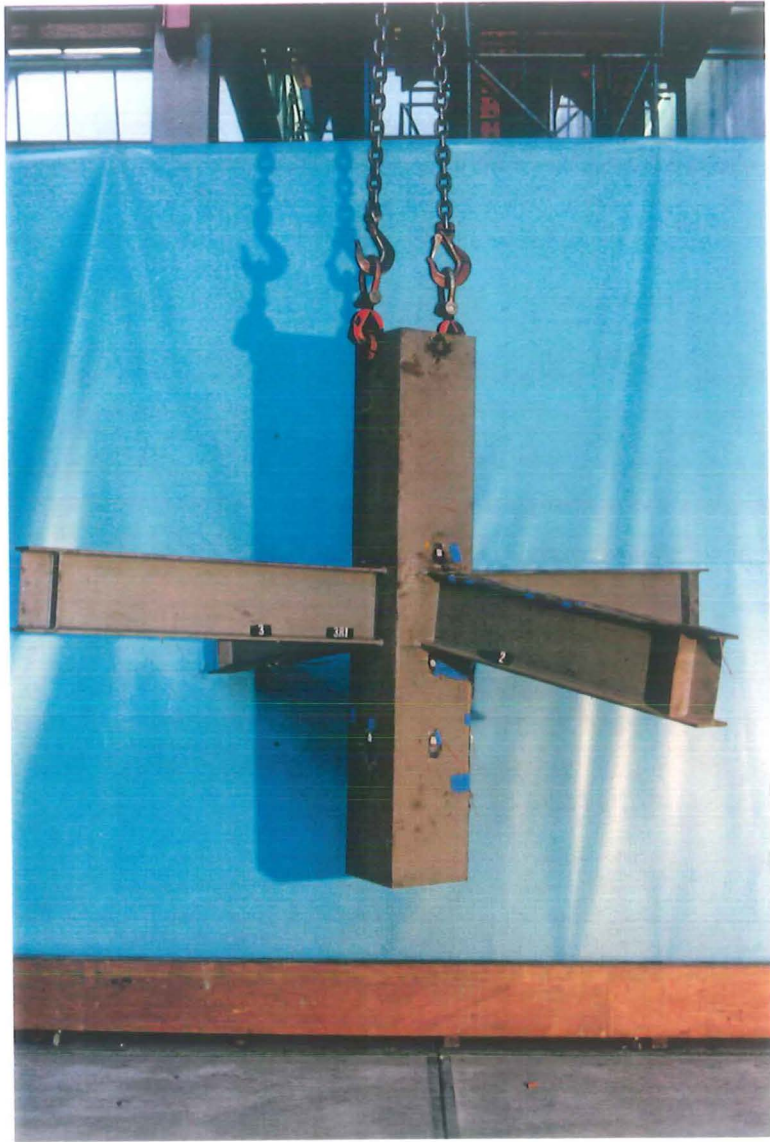


Photo 7-22 :
Specimen 3R1 after failure

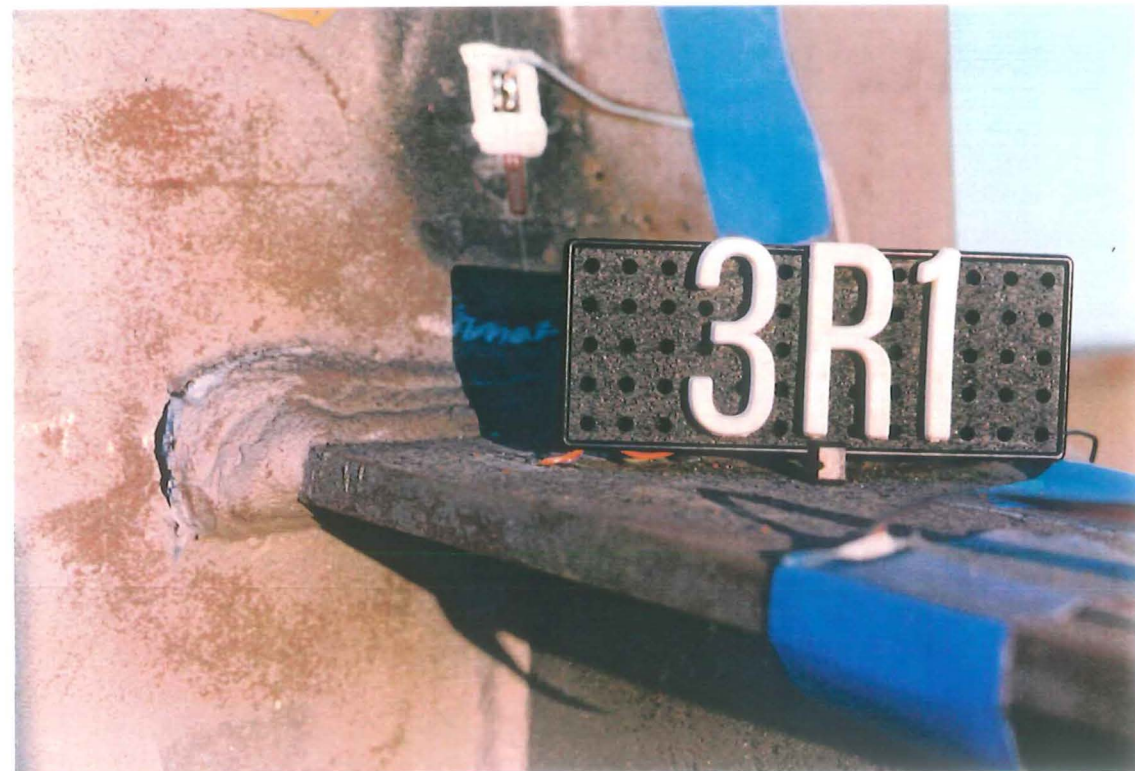


Photo 7-23 : Details of specimen 3R1 after failure

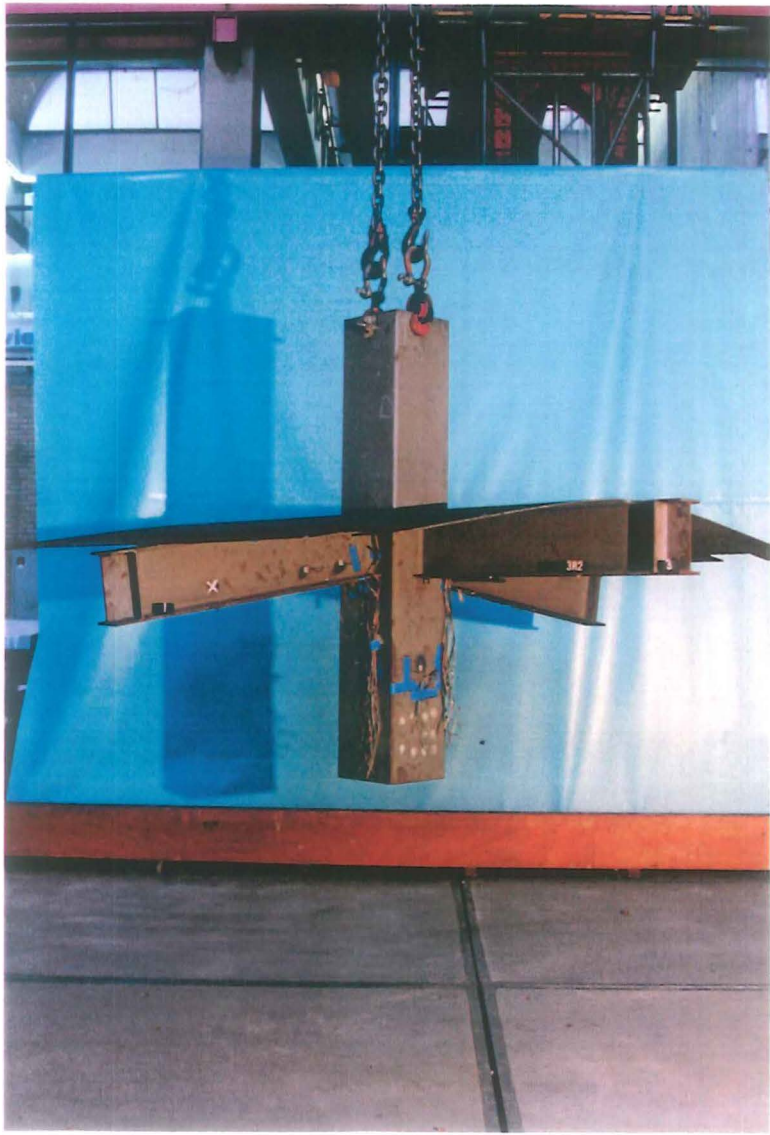


Photo 7-24 : Specimen 3R2 after failure

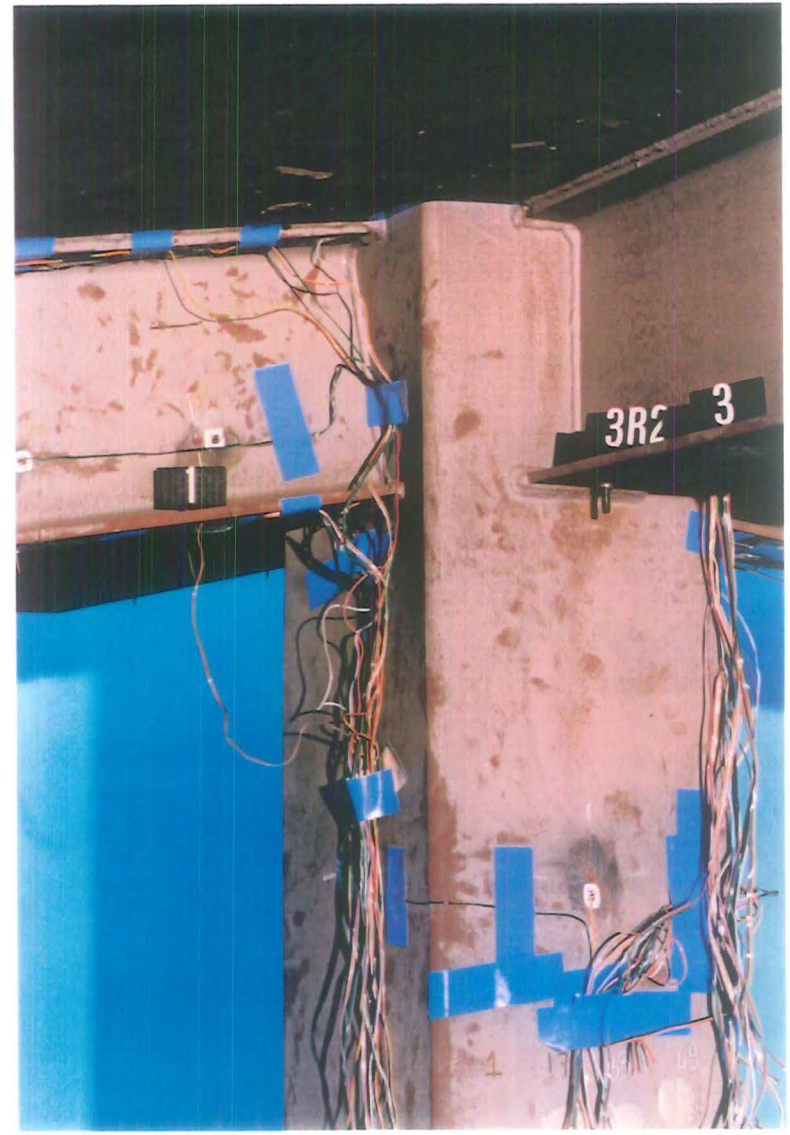


Photo 7-25 : Details of specimen 3R2 after failure

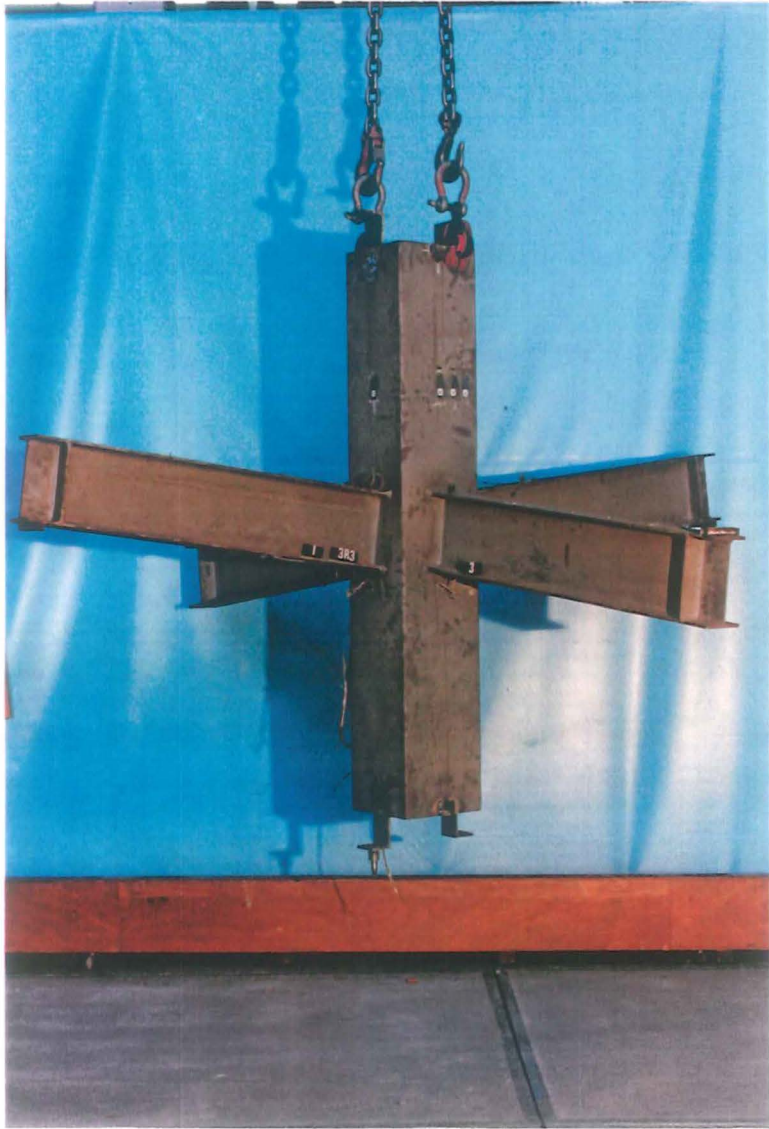


Photo 7-26 : Specimen 3R3 after failure

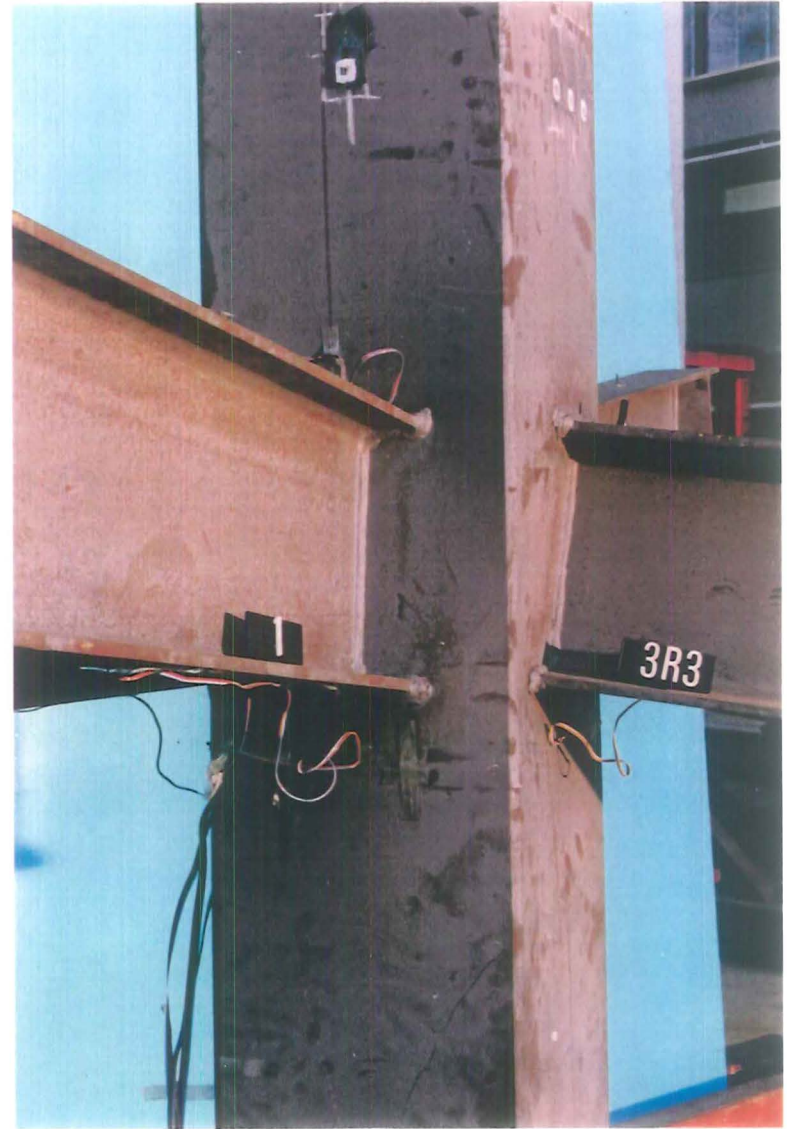


Photo 7-27 : Details of specimen 3R3 after failure



Photo 7-28 : Specimen 3R4 after failure



Photo 7-29 : Details of specimen 3R4 after failure



Photo 7-30 : Specimen 4R1 after failure

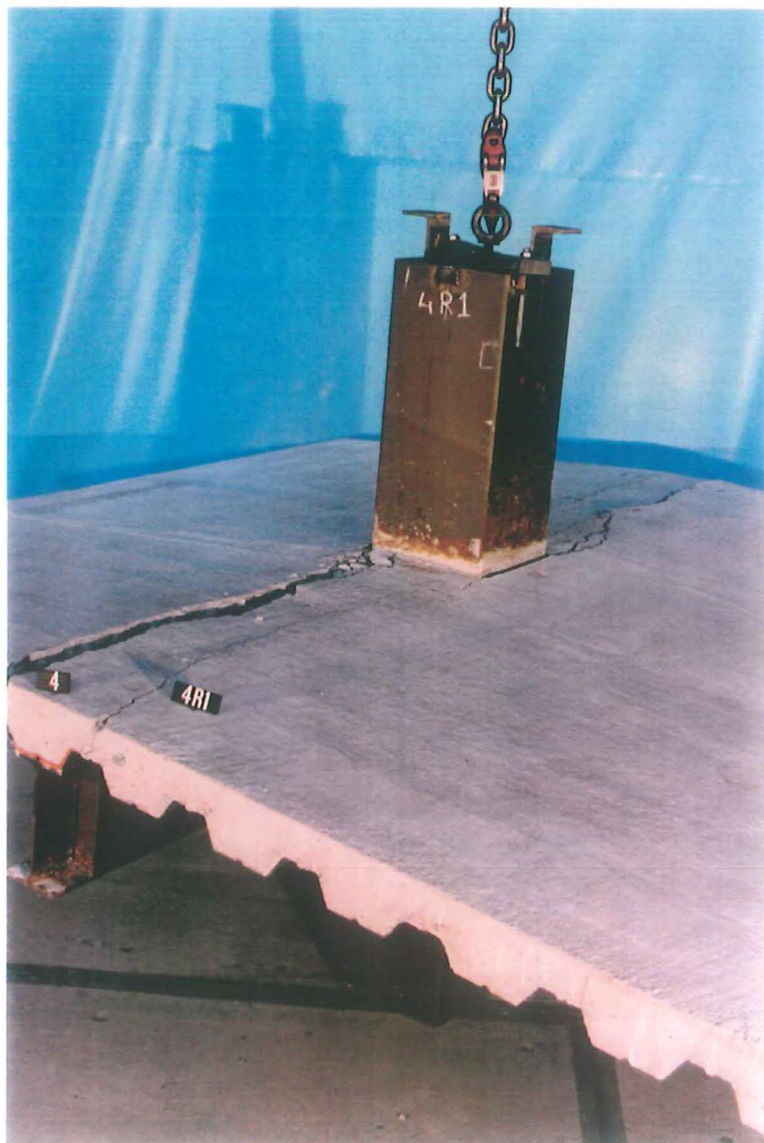


Photo 7-31 :
Details of specimen 4R1 after failure



Photo 7-32 : Specimen 4R2 after failure



Photo 7-33 :
Details of specimen 4R2 after failure

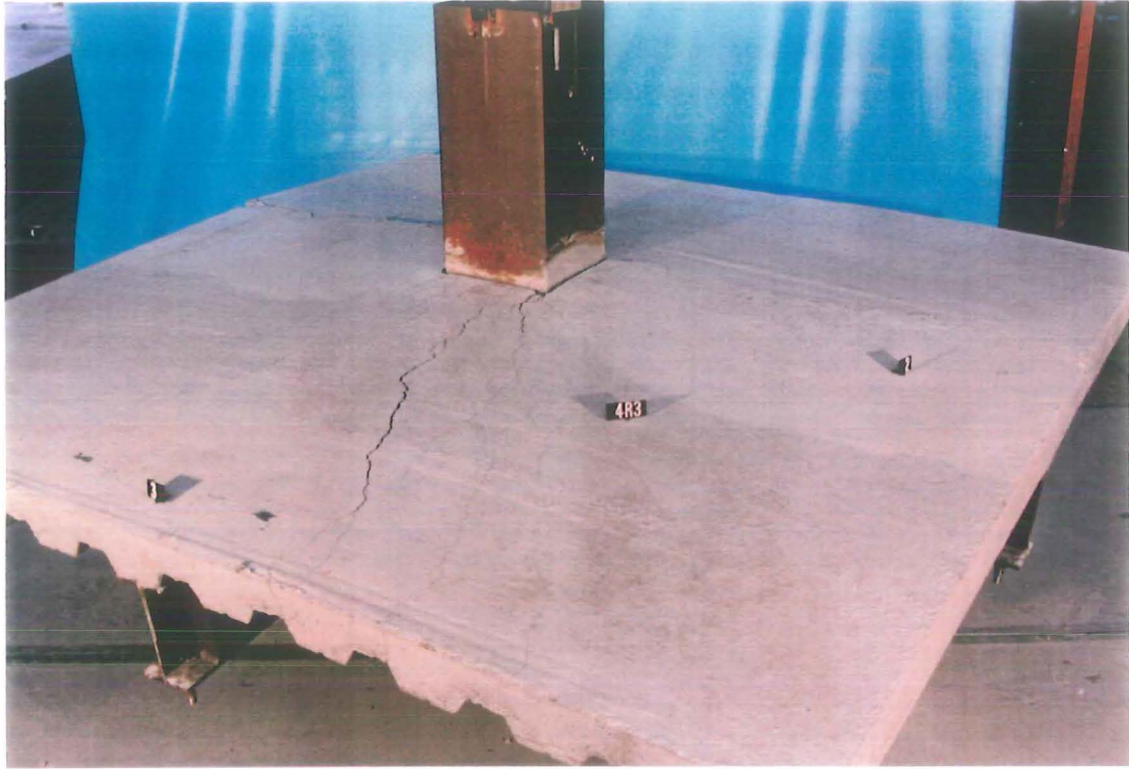


Photo 7-34 : Specimen 4R3 after failure



Photo 7-35 : Details of specimen 4R3 after failure

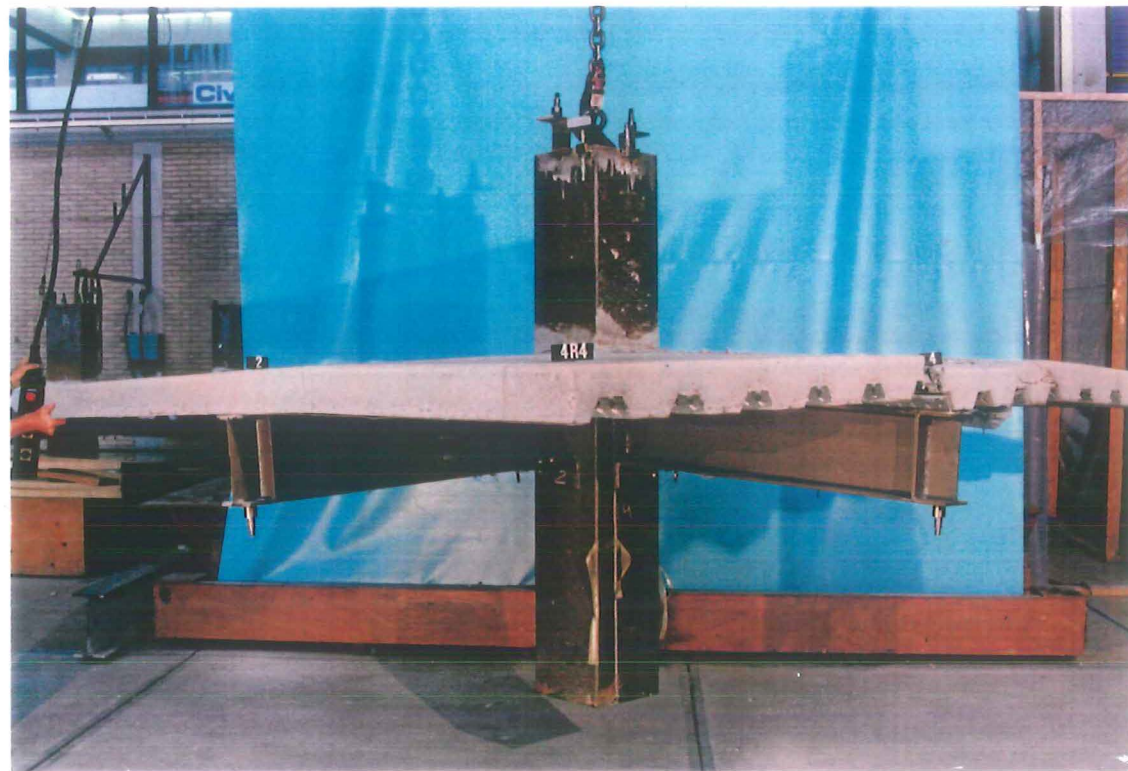


Photo 7-36 : Specimen 4R4 after failure



Photo 7-37 :
Details of specimen 4R4 after failure

